The University Of Sheffield.

Development of laser direct writing for fabrication of micro/nano-scale magnetic structures

By
Alaa Alasadi

A thesis submitted in partial fulfilment for
The degree of Doctor of Philosophy in

In the

Faculty of Engineering,
Department of Materials Science and Engineering

December 2018

Publications

1- Journal Paper

A. Alasadi, F. Claeyssens, and D. A. Allwood, "Laser direct writing (LDW) of magnetic structures," AIP Adv., vol. 056322, 2018.

2- In preparation

A. Alasadi, F. Claeyssens, and D. A. Allwood, "Rapid fabrication technquie of 2 D micro-scale magnetic structures by laser direct writing (LDW-)" (working title).
B. Alasadi, F. Claeyssens, Tom Hayward, Georgios Sarris and D. A. Allwood, "fabrection of AMR sensores by laser direct writing (LDW)" (working title).

3- Conferences

A. Alasadi, F. Claeyssens, and D. A. Allwood, "*Laser direct writing (LDW) of magnetic structures*" Magnetism and Magnetic Materials. Pittsburgh, PA. USA, November 2017. (Oral presentation)
B. Alasadi, F. Claeyssens, and D. A. Allwood, "*Laser Induced Forward Transfer for 1 and 2D magnetic micro/nanostructures fabrication"* The First Iraqi Conference at the University of Sheffield*,* University of Sheffield*,* sheffield, UK*, september 2017. (poster)*
C. Alasadi, F. Claeyssens, and D. A. Allwood," *Rapid fabrication of magnetic microstructures by laser direct writing (LDW).* Magnetism 2018, University of Manchester, Manchester, UK, April 2018. (poster).

Abstract

Traditional lithographic techniques used to fabricate a magnetic structure are often complex, time consuming, dependent on other techniques and expensive. Laser direct writing (LDW) can potentially overcome many of these drawbacks and may be a cheaper, faster and easier route to fabricating technique micro-/nano-magnetic structures. The main aim of this project is to fabricate magnetic structures through LDW. Two types of LDW were used to fabricate magnetic structures: subtractive LDW (LDW-) and laser-induced forward transfer (LIFT). LIFT was used to transfer permalloy ($Ni_{81}Fe_{19}$) using three laser systems. Numerous parameters were varied, including thin film thickness, scanning speed, pulse energy, distance between donor/acceptor and acceptor material. These attempts did not succeed in transferring the magnetic materials as a uniform shape. The differences of heat conductivity between the permalloy and acceptor substrate (glass and silicon), shock wave effects and the landing speed of material on the acceptor are the most possible reasons that the uniform structures and the magnetic properties were lost. LDW- was used to successfully pattern 90nm thick Permalloy into 1-D and 2-D microstructures. Magnetic wires with a range of widths, arrays of squares, rectangles with a range of aspect ratios and rhombic elements were patterned. These structures were fabricated using an 800-picosecond pulse laser and a 0.75 NA lens to give a 1.85µm diameter spot. Scan speeds were controlled to give 30% overlap between successive laser pulses and reduce the extent of width modulation in the final structures compared with lower levels of pulse overlap. Continuous magnetic wires that adjoined the rest of the film were fabricated with widths from 150 nm - 6.7µm and showed coercivity reducing across this range from 47 Oe to 10 Oe. Squares, rectangles and diamonds These elements demonstrated shape-sensitive magnetic behaviour with increasing the shape aspect ratio. Wires of different width were also fabricated by LDW- and their anisotropic magnetoresistance (AMR) determined to show a simple width-dependent magnetic field response, making them interesting as magnetic field sensors. This approach is extremely rapid and does not requires masks or chemical processing as part of the patterning procedure. The time required to patterned 1-D area of 4 x 0.18 mm was 85 s and the average fabrication time per element of

2-D structures was 4.7×10^{-4} s. The microstructures may be of use for AMR sensors or for biological applications, such as cell trapping.

Dedication

To: The greatest man in my life, the prophet Muhammad

قلبت كل العالمين فلم أجد

من يستحق الذكر الا محمدا

Acknowledgments

In Arabic there is proverb that says “whoever does not thank the creature will not thank the creator”, so, after thanking God Almighty, I would like to bow modestly to my beloved country, ***Iraq***, to its land and sky, to its trees and rivers, for each grain of its soil and to its great heroes and I say, there are not words enough to express my love and thanks.

I would like to express my thanks to Al-Furat Al-Awsat Technical University for giving me this opportunity to study for my PhD.

My supervisor Professor Dan Allwood; I thank you from my heart, it was great honour to work with you throughout my PhD, thanks for your support and your understanding. You are the best supervisor.

My appreciation and thanks should also go to my DDP supervisor, Dr. Frederik Claeyssens and to all members of the SCAMMED group with special thanks to Dr. Rene Dost and Dr. Colin Sherborne and Mr. Georgios Sarris.

For my mother and my late father, I am so pleased that your dreams for me have been realised.

To my sons, Mohammed, Dhurgham and Haidarah, you were a beacon of light on the long road of the PhD journey.

And finally, to my dear wife Inaam, who bore the burden of this journey with me, thank you for all the love, patience and support you provided me, you were a wonderful wife and mother.

Contents

Abstract..iii

Dedication...v

Acknowledgments..vi

Contents vii

Chapter 1: Introduction and Synopsis... 1

1.1 Introduction 1

1.2 Laser Direct Writing (LDW) 3

1.3 Project aims.. 4

1.4 Thesis contents 5

Chapter 2: Magnetism and magnetic materials... 7

2.1 Ferromagnetism 7

2.2 Domains 11

2.2.1 Exchange energy 12

2.2.2 Magnetostatic energy 13

2.2.3 Magnetocrystalline anisotropy energy 14

2.2.4 Magnetostrictive energy... 15

2.2.5 Zeeman energy... 16

2.3 Hysteresis loops 17

2.4 Ferromagnetic materials types 18

2.4.1 Permalloy.. 19

2.5 Magnetic anisotropy 22

2.5.1 Shape anisotropy.. 22

2.6 Small magnetic elements 24

2.7 Summary 25
Chapter 3: Fabrication techniques of micro/nano-magnetic structures 26
3.1 Introduction 26
3.2 Micro/nano-fabrication techniques 28
3.2.2 Non-resist-based lithography 42
3.3 Summary 47
Chapter 4: Laser Direct writing 48
4.1 Introduction 48
4.2 LDW system 48
4.3 Laser-material interaction 50
4.4 Ablation 53
4.5 *LDW* types 57
4.5.1 Laser Direct Writing Subtraction *LDW-* 58
4.5.2 Laser Direct Writing Modification (*LDWm)* 58
4.5.3 Laser Direct Writing addition (*LDW+)* 58
4.6 Summary 63
Chapter 5: Experimental methods 64
5.1 Introduction 64
5.2 Thin Film Deposition 64
5.3 Laser Direct Write (LDW) Systems 66
5.3.1 350 picosecond Q-switched laser system 66
5.3.2 800 Picosecond Q-switched laser system 71
5.3.3 System of femtosecond Ti: sapphire laser 73
5.3.4 Overlap of laser pulses on samples 75
5.4 Fabrication of magnetic structures 77
5.4.1 LDW- of magnetic structures 78
5.4.2 LIFT for magnetic structures 85
5.5 Measurements and characterisation 88
5.5.1 Focused Magneto-Optic Kerr Effect (fMOKE) magnetometry 89

5.5.2 Anisotropic magneto resistance (AMR) system. 91
5.5.3 I-V test system 93
5.5.4 Optical microscopy 94
5.5.5 Atomic force microscopy (AFM) 94
5.5.6 Scanning electron microscopy (SEM). 95

5.6 Summary 96

Chapter 6: Laser induced forward transfer (LIFT) of magnetic structures................ 97

6.1 Introduction 97

6.2 LIFT with 350 ps pulse length DPSS- Q-switched laser system..................... 97

6.3 LIFT with 100 fs pulse length Ti: sapphire laser system...............................103

6.4 LIFT with ps pulse length DPSS- Q-switched laser system...........................104
6.4.1 Transfer material using “Dwell” command 105
6.4.2 Transfer material using “Linear” command 109

6.5 Summary 120

Chapter 7: Laser direct writing subtraction (LDW-) fabrication of magnetic structures 123

7.1 Introduction 123

7.2 One-dimensional magnetic structures 123
7.2.1 Initial attempts of 1D structure fabrication...124
7.2.2 Width variation of magnetic wires 130

7.3 Two-dimensional micro/nano-scale magnetic structures...............................141

7.4 Anisotropic magnetoresistance (AMR) measurements of LDW- structures...150
7.4.1 Anisotropic Magnetoresistance Measurements 156

7.5 Summary 164

Chapter 8: Conclusions and Future Work...166

8.1 Conclusion 166

8.2 Future work 168

Appendix A 170

Appendix B 171
Appendix C 173
Appendix D 175
References 176

Chapter 1: Introduction and Synopsis

1.1 Introduction

Although magnetism was discovered earlier than 600 BC, the real breakthrough took place in the last century to understand and employ it for invention, and create and develop technologies based on this understanding. This revolution of magnetism came as a result of measurement of the behaviour of magnetic materials. Their response to magnetic field can be used to classify magnetic behaviour into five categories: diamagnetism, paramagnetism, ferrimagnetism, anti-ferromagnetism and ferromagnetism. Ferromagnetism will be explored further in chapter 2. Magnetism is present in nature, for example it is known in geology and geophysics from the response of sedimentary rocks [1]; but artificial magnetic structures are also now used in applications, such as in medicine: control of magnetically-tagged cells to achieve magnetic separation [2], drug delivery [3], immunoassays [4], magnetic resonance imaging (MRI) [5], and magnetic hyperthermia [2], or trapping of magnetically-labelled cells [5]; to actuators [6], sensors [7], [8] and production of various types of recording media [9] and data storage units [10]. Therefore, it's not surprising to find the applications based on magnetic materials are used every day around the worldwide in many of applications and devices. Consequently, billions of devices based on magnetic structures are traded in international markets, for example, the global market size of magnetic sensors alone reached USD 1.91 billion in 2017, for an estimated demand of 3.1 million units [11]. The compound annual growth rate (CAGR) of this market is expected to achieve 6.8% [11] because of progress in sensing technologies combined with increasing usage of sensing devices in numerous industry sectors.

New markets for magnetic sensors are opening up as automotive technology develops rapidly. Predictions of global revenue for this sector are that it will expand to \$2.3 billion in 2030 compared with \$1.1 billion in 2017 [12]. Fig 1.1 shows the predicted global market value of

different types of sensor in the automotive market from 2016 to 2030. This is predicted to be dominated by Hall effect sensors throughout the period considered but that anisotropic magnetoresistance (AMR) sensors will have the second largest market share, approaching $0.5 billion in 2030.

Figure 1.1 *Predicted global magnetic sensor market from 2016 to 2030 [12]. Technologies include Hall effect, anisotropic magnetoresistance (AMR), tunnelling magnetoresistance (TMR), 3D Hall effect, and giant magnetoresistance (GMR).*

The majority of applications listed above have been established based on nano- and micro-scale magnetic structures which can exhibit new and improved properties compared to their bulk equivalents. Accordingly, the development and discovery of the properties of magnetic structures have often arisen from developments in our ability to miniaturise the materials through micro/nano-fabrication processes. Various micro/nano-fabrication techniques are used to fabricate magnetic structures, such as: electron beam lithography, ion beam lithography, soft lithography, photolithography, X-ray lithography, focused-ion-beam milling and scanning probe lithography; and these will be discussed in chapter 3. In general, these techniques can be classified into resist-based lithography and non-resist-based lithography. Each fabrication technique brings particular advantages and drawbacks,

particularly in terms of flexibility, speed, complexity and cost. For example, commercial photolithography typically includes tens or even hundreds of separate steps which can take weeks or even months to complete. The majority of fabrication techniques require high costs, which can have capital costs reaching millions of dollars for fabrication systems for electron beam or X-ray lithography, and expensive consumable materials such as masks and frequent maintenance.

1.2 Laser Direct Writing (LDW)

LDW is an uncomplicated and mask-less technique for creating structures of one to three dimensional through a one-step process. This can often be carried out under atmospheric conditions, at room temperature and with no chemical processing, and under computer control to allow flexible structure design.

In general, LDW describes three approaches in which material is either modified (LDWm), removed (LDW-), or added (LDW+) [13], [14]. LDWm is employed to change the properties of materials using laser fluence below the ablation threshold, while material removal in LDW- requires an applied fluence higher than the ablation threshold. LDW+ requires a fluence just above threshold to transfer material from a carrier of a donor thin film to an acceptor substrate. LDW+ includes two procedures: Laser Induced Forward Transfer (LIFT) and Laser Induced Backward Transfer (LIBT).

All types of LDW system share the same three main parts: a laser source, a laser beam delivery system and a sample/platform scanning system, as shown in Fig 1.2.

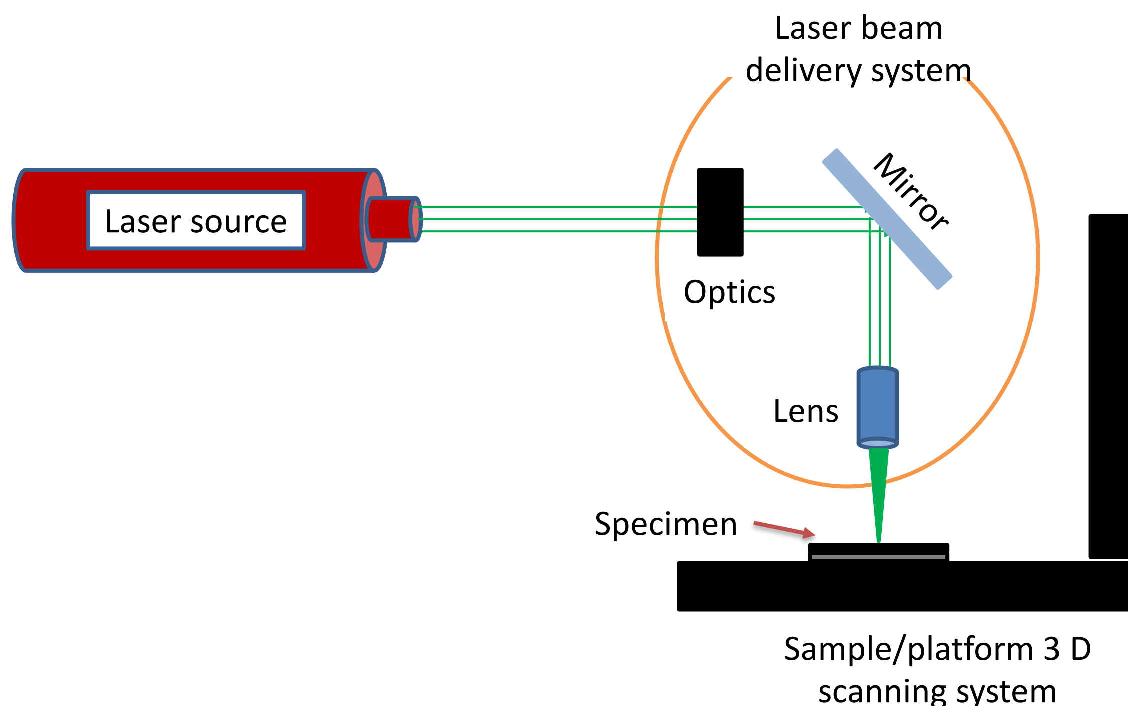

Figure 1.2 *General schematic of main parts of all types of LDW systems: laser source, laser beam delivery system and sample/platform scanning system.*

Though laser direct writing is a well-established technique and one of the most important in the family of direct writing techniques, it has not been used to fabricate magnetic structures so far.

1.3 Project aims

This thesis reports on attempts to use the unique characteristics of LDW to fabricate magnetic structures and explore how this might overcome some of the inherent drawbacks of traditional techniques otherwise used to fabricate magnetic structures. Two techniques of laser direct writing, LDW- and LDW+, were used to pattern micro/nano-scale magnetic structures. This may allow LDW to be realised as an easier, cheaper and faster way to fabricate micro/nano-scale magnetic structures.

1.4 Thesis contents

Chapter 2 of this thesis covers the basics of ferromagnetism and considers how the formation of domains depends on magnetic energies, before reviewing the types of ferromagnetic materials and the effect of shape anisotropy on the magnetic response of structures.

The fabrication techniques used for patterning micro/nano-scale magnetic structures are reviewed in chapter 3. The history of lithography is covered, from the first attempt in 1796 by Aloys Senefelder to transfer an engraved image onto paper to modern lithographic techniques. This review will evaluate each technique in terms of its speed, cost, resolution and complexity.

Laser direct writing will be discussed in chapter 4. The interaction between laser radiation and materials, ablation processes using short and ultra-short pulsed lasers, types of LDW and the important factors that effect the transfer processes in LDW+ are covered in this chapter.

Chapter 5 describes the experimental procedures used here to achieve LDW- and LDW+. The equipment and experimental setup used for preparation, fabricating and characterizing the magnetic structures, and all subsequent LIFT and LDW- experiments are presented. This chapter consists of two parts: preparation of thin films and patterned structures; and measurements and characterisation.

Chapter 6 present the attempts to fabricate magnetic structures using LIFT. These attempts were made by varying numerous experimental factors to transfer magnetic materials from a donor film to an acceptor substrate.

Chapter 7 present the results of one-dimensional, two-dimensional magnetic structure patterned by LDW-. These structures include arrays of squares, rectangles with

various aspect ratios and rhombic elements as well as MR magnetic structures achieved using LDW-.

Chapter 8 gives the main conclusions from the project and the plans to develop the techniques in the future.

Chapter 2: Magnetism and magnetic materials

2.1 Ferromagnetism

Magnetism results from the sum of atomic magnetic moments in a material. Each magnetic moment, $\boldsymbol{m}$, arises from the spin and orbital motion of electrons in an atom. The magnetization, $\boldsymbol{M}$, of a material is the volume average of the constituent magnetic moments [10]:

$$M = \frac{\sum \mathrm{m}}{V} \qquad (2.1)$$

In general, the response of the material to an external applied magnetic field (H) is called magnetic induction (B) and is given by [15]:

$$B = \mu_0 (H + M) \qquad (2.2)$$

where μ_0 is the permeability of free space.

The magnetic response of linear magnetic materials, including ferromagnetic materials under low fields, can be described by the magnetic susceptibility (χ) by [10]:

$$\chi = \frac{M}{H} \qquad (2.3)$$

The different responses of magnetic materials to externally applied magnetic field are usually summarized into five categories of behaviour: diamagnetism, paramagnetism, ferrimagnetism, anti-ferromagnetism and ferromagnetism.

Diamagnetic behaviour arises from electron orbitals within atoms subject to an applied magnetic field adjusting to repel the applied field, as described by Faraday's law. In the absence of an applied field, diamagnetic atoms have zero magnetic moment. The magnetization of diamagnetic materials is always opposite to the direction of applied magnetic field. This is a weak effect though so χ is small and negative, typically close to 10^{-5}. The exception to this is where materials are superconductive, in which case χ = 1. All materials show this effect but other magnetic responses are often present and dominate the diamagnetic behaviour.

Paramagnetic materials consist of atoms that have a spontaneous (i.e. present without the applied of a magnetic field) magnetic moment but that are each randomly oriented. In the absence of an applied magnetic field, this random orientation leads to net zero magnetization. However, the magnetic moments gradually align to an applied magnetic field, although the response is weak resulting in values of χ typically of 10^{-3} – 10^{-5}.

The strongest response to magnetic field comes from ferromagnetic materials, in which all atomic magnetic moments (m) can be readily aligned towards an applied magnetic field. However, ferromagnetic materials exhibit parallel alignment of moments resulting in large net magnetization even in the absence of a magnetic field. The magnetic moment comes from the spin and orbital motion of electrons in atoms. The magnetic moment of the ferromagnetic transition metals (Ni, Fe and Co) arises from unpaired 3d-orbital electrons of identical spin direction (e.g. for nickel in Figure 2.1).

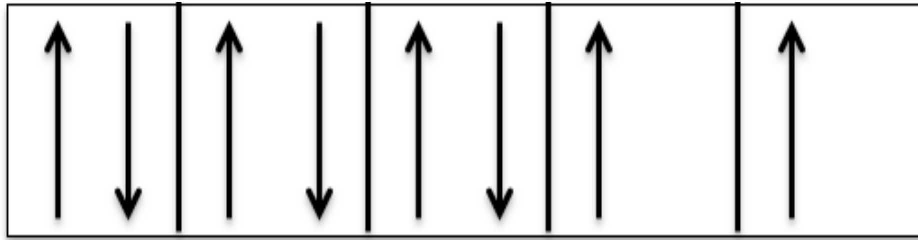

Figure 2.1: *The spin structure d-block electrons in nickel.*

The magnetic moments of atoms across large regions (called 'domains') of ferromagnetic material spontaneously align, resulting in large local values of spontaneous magnetization. Fig 2.2 shows a schematic of the alignment of atomic dipoles (magnetic materials) within a ferromagnetic domain.

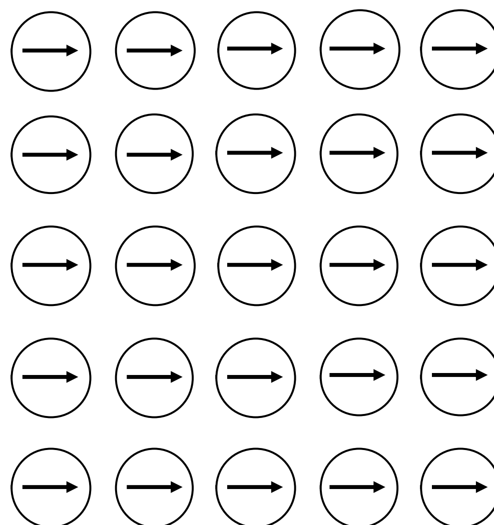

Figure 2.2: *Schematic of the alignment of magnetic moments in ferromagnetic material (adapted from ref.*[16]*).*

This behaviour comes as a result of the exchange interaction between adjacent atoms. However, not all materials with unpaired electrons in external orbitals are ferromagnetic, since the crystal structure of materials contributes to determine the type of magnetism exhibited by the elements. For example, manganese has five unpaired electrons but is not ferromagnetic because the magnetic moments of such magnetic atoms are oriented randomly under no applied field and the material is paramagnetic [17].

Anti-ferromagnetic materials are similar to ferromagnetic materials but neighbouring atoms have oppositely aligned magnetic moments. This results in zero spontaneous magnetization. Applied magnetic field gradually rotates the two spin lattices into the field directions to give typical values of χ of 10 – 100.

Ferrimagnetism arises from a similar spin structure to that of anti-ferromagnetic materials but with spin lattices made up of atoms with unequal magnetic moment. This results in a non-zero spontaneous magnetization and, at low fields, a similar response to applied magnetic fields as ferromagnetic materials. At high fields, the spin lattices gradually align into the field direction, as with antiferromagnetic materials. The magnetic susceptibility can be very high but the weaker magnetization of ferrimagnetic materials compared to ferromagnetic materials means that χ doesn't reach the high values seen with some ferromagnets.

$M = \mathrm{m}/\mathrm{V}$ Magnetization is often plotted as function to applied field to show the response of materials. For diamagnetic, paramagnetic, and antiferromagnetic materials the M–H characteristics are linear as shown in fig 2.3, but ferrimagnets and ferromagnets have a different behaviour, as will be explained in §2.3.

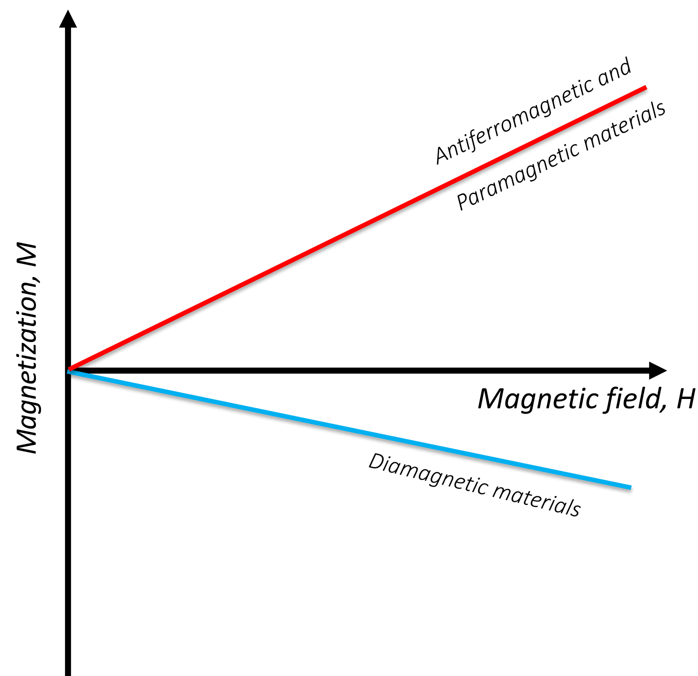

Figure 2.3: *The curve of magnetization as function to applied field for diamagnetic, paramagnetic, and antiferromagnetic materials (adapted from* [10], [16]*).*

2.2 Domains

As noted above, regions of ferromagnetic materials in which magnetic moments are aligned parallel are called domains. The orientation of domains depends on the demagnetised or magnetised state of ferromagnetic materials [10], [15]. In the demagnetised state, the vector summation of all the domains is equal to zero due to their different orientations, but in the fully magnetised state domains are oriented in the same direction and the vector summation of the dipoles produces an overall magnetic dipole of the material. The regions between neighbouring domains are called domain walls. An applied magnetic field causes domains aligned parallel to the field direction to grow by motion of domain walls, as will be discussed in section 2.3.

The configuration of domains in materials can be complex and is often observed by techniques such as the Bitter method, transmission electron microscopy, scanning tunnelling microscopy (STM), and magneto-optic Kerr effect imaging [10], [15].

The spatial configuration of magnetization within a ferromagnetic element is determined by five magnetic energies: exchange energy, magnetostatic energy, magnetocrystalline energy and magnetostrictive energy and Zeeman energy (from an applied magnetic field). Magnetostatic energy is the principal driving force for the formation of domains while others energies influence the shape and size of domains. These will be considered here in turn.

2.2.1 Exchange energy

The exchange interaction between neighbouring atoms creates an energetic dependence on the relative alignment of adjacent atomic moments. In ferromagnetic materials, parallel alignment reduces the exchange energy to a minimum value and results in the behaviour described above. With no other considerations, the most stable state of ferromagnetic materials will therefore be a single magnetic domain.

The exchange energy forms an important component of the total energy of ferromagnetic materials. The exchange energy of two adjacent atoms i and j can be calculated by the Heisenberg form of equation [15]:

$$E_{ex} = -2JS_iS_j \cos\phi \tag{2.4}$$

where J is an exchange integral, $\boldsymbol{S_i}$ and $\boldsymbol{S_j}$ are the spin angular momentum of the two atoms respectively and ϕ is the angle between the spins. J has a positive value for ferromagnetic materials, so that parallel alignment of adjacent spins results in a negative contribution to exchange energy. Conversely, J in antiferromagnetic and ferrimagnetic materials has a negative sign and is responsible for the anti-parallel alignment of neighbouring atomic moments that characterize these materials.

2.2.2 Magnetostatic energy

The exchange energy in ferromagnetic materials reaches a minimum when there is a single magnetic domain. This results in strong surface magnetic poles that generate a magnetic field around the material, as shown in fig 2.4(a). The poles also generate an internal field that opposes the magnetization, i.e. in the demagnetizing direction; this internal field is, therefore, called the 'demagnetizing field' and causes 'magnetostatic energy' to arise. Magnetostatic energy depend on the shape of the sample as will be discussed in §2.5.1.

In order to reduce the magnetostatic energy, the demagnetizing field must be minimized. Fig. 2.4(b) shows that this can be partially achieved by the single domain dividing into two oppositely oriented domains. However, this still leaves a reduced but non-zero demagnetizing field in the sample (and also a reduced stray field externally). Further increases in the number of (smaller) domains offer further reductions in demagnetizing field, and the formation of 'flux closure domains' at the object's ends (Fig. 2.4(c)) can reduce the demagnetizing field (and the magnetostatic energy) to zero.

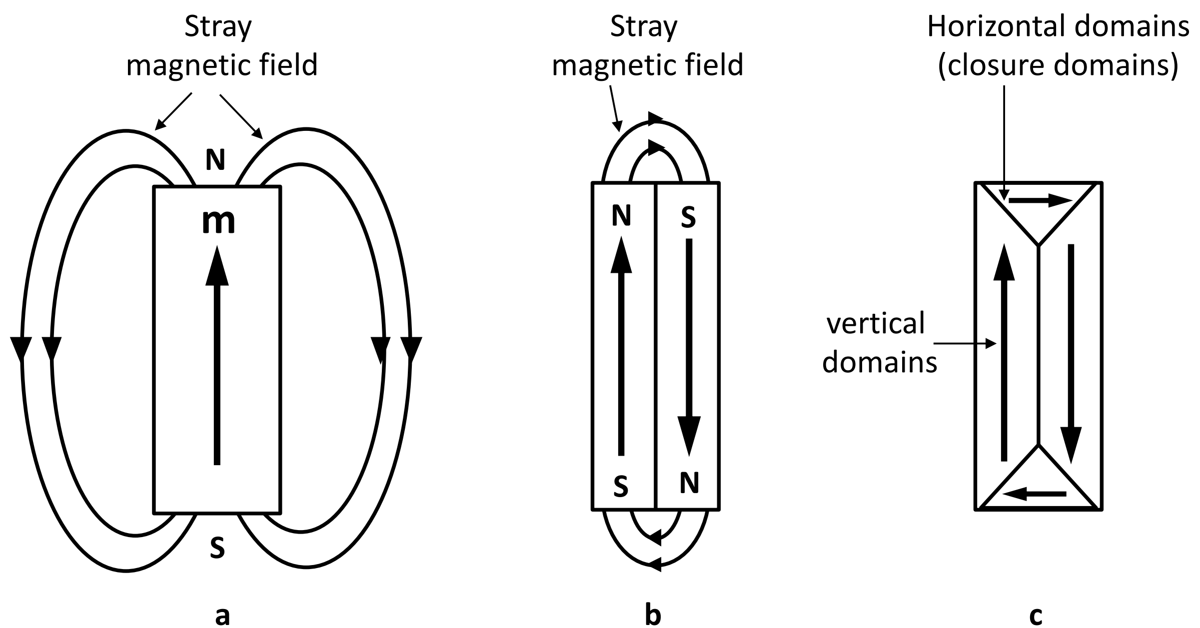

Figure 2.4: *Schematic of how external stray field depends on magnetic domain structure of a ferromagnetic element (adapted from ref* [18]).

2.2.3 Magnetocrystalline anisotropy energy

The magnetization of most ferromagnetic materials tends to align to particular crystallographic directions; this phenomenon of alignment is called "magnetocrystalline anisotropy". The origin of magnetocrystalline anisotropy is spin-orbit interactions. In fact, there are three significant types of coupling between spin, orbit and lattice, and one of these is important for causing magnetocrystalline anisotropy [17].

Spin–spin coupling (exchange coupling) is very strong and attempts to keep adjacent spins parallel or anti-parallel to one another, as described in §2.2.1. Exchange energy is isotropic, however, depending only on the angle between neighbouring spins (equation 2.4) and not on individual magnetic moment directions. Therefore, this type of coupling does not contribute to magnetocrystalline anisotropy[17].

The second type of coupling is orbit-lattice interactions. However, electron orbitals define the crystal structure and the orbitals and lattice are very strongly connected and even large external fields cannot break this coupling. Therefore, this interaction does not create magnetocrystalline anisotropy[17].

Finally, the interaction between the magnetic moments of an electron's spin with the magnetic field from the electron's orbital motion produces spin-orbit coupling. The spin of electrons reorients in an applied magnetic field and is, therefore, affected by the electron's own orbit. The strength of the orbit-lattice coupling means it resists rotating in externally applied magnetic fields but the spin-orbit coupling is not as strong and can be overcome by applying a magnetic field to reorient the spin system of a domain away from the easy direction. The strength of the field required to do this depends upon the strength of the spin-orbit interaction. This also means that magnetization is more easily saturated along the preferred or 'easy' axes as defined by the crystal structure. The least preferred crystallographic directions are known as 'hard axes'. Accordingly, the energy required to reach saturation along easy axes will be less than along hard axes. This difference in energy between magnetizing along easy and hard axes is called the magnetocrystalline anisotropy energy E_K and in uniaxial materials is given by [10]:

$$E_K = K_1 sin^2\theta + K_2 sin^4\theta + \cdots \qquad (2.5)$$

where, K_1, K_2 are anisotropy constants and θ the angle between the magnetization vector and the easy axis.

2.2.4 Magnetostrictive energy

The phenomenon of magnetostriction describes the change in length seen in most ferromagnetic materials when they are magnetized in response to applied magnetic field. This change is referred to as positive magnetostrictive for increases in length parallel to the applied field (e.g. in iron), or negative magnetostrictive when the length parallel to applied field decreases (such as in nickel). The fractional change in length is a strain and can be calculated by [15]:

$$\lambda = \frac{\Delta l}{l} \qquad (2.6)$$

where λ is the magnetostrictive strain and $\Delta l/l$ is the fractional change in length. The values of the magnetostrictive strain (λ) change with increase of applied magnetic field up to a saturation value, as shown in fig 2.5. This value of strain is called saturation magnetostriction λ_s.

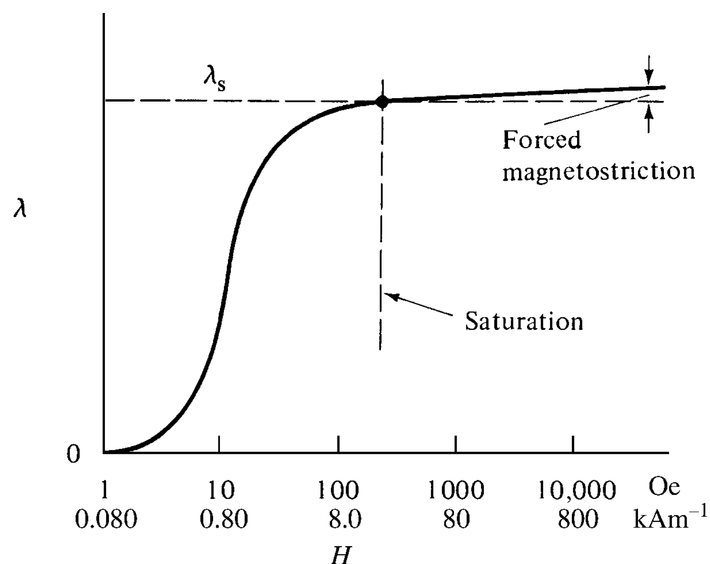

Figure 2.5: *The fractional magnetostrictive strain (λ) as function of an applied magnetic field, used with permission from* [15].

This change in length is very small, typically of the order of 10^{-5} regardless of it being positive or negative, but the associated energy is significant enough to rearrange the domain structure.

However, if the lattice is changed by strain the distances between the magnetic atoms is altered and hence the interaction energies are changed. This produces magneto-elastic anisotropy. The magneto-elastic effect arises from the spin-orbit interaction.

For an elastically isotropic medium, with isotropic magnetostriction, the magneto-elastic energy per unit volume is given by[15]:

$$E = -\frac{3}{2}\lambda\sigma cos^2\theta \qquad (2.7)$$

Where σ is stress and θ is the angle between the magnetisation and stress directions.

2.2.5 Zeeman energy

The Zeeman energy, E_Z, arises from the interaction between the applied field and the magnetic moment of the material and is given by:

$$E_z = -\mu_0 MHcos\,\theta \qquad (2.8)$$

Where; θ is the angle between the applied field and the sample's magnetisation.

The Zeeman energy is minimised when the magnetic field and magnetization are parallel, and hence is responsible for the tendency of magnetization to align to an externally applied magnetic field. "

2.3 Hysteresis loops

When a magnetic field is applied to a ferromagnetic material, the magnetic domains start to rearrange to become parallel to the field. The domains parallel to the field start to grow at the expense of other domains. As mentioned before, the growth of domains happens by the motion of domain walls. The growth of domains continues with increase of magnetic field until a single domain is achieved in which all of the magnetic moments are aligned in the same direction. This is often accompanied by a degree of domain rotation to bring the magnetization perfectly parallel to the applied field. When the applied magnetic field is reduced gradually to zero, the magnetization of the ferromagnetic material usually reduces in magnitude but doesn't reach zero, remaining instead at a value called the remanence magnetization (M_r). This ability to remember magnetic history is known as " hysteresis"; therefore, plots of *M*-*H* or *B*-*H* are called "hysteresis loops". By continuing to reduce the magnetic field beyond zero, the magnetization can eventually be reduced to zero; the magnetic field required to achieve this is called the coercivity (H_c). Fig 2.6 illustrated this process and illustrates the various stages of domain growth from multiple domains through to single domains at high fields.

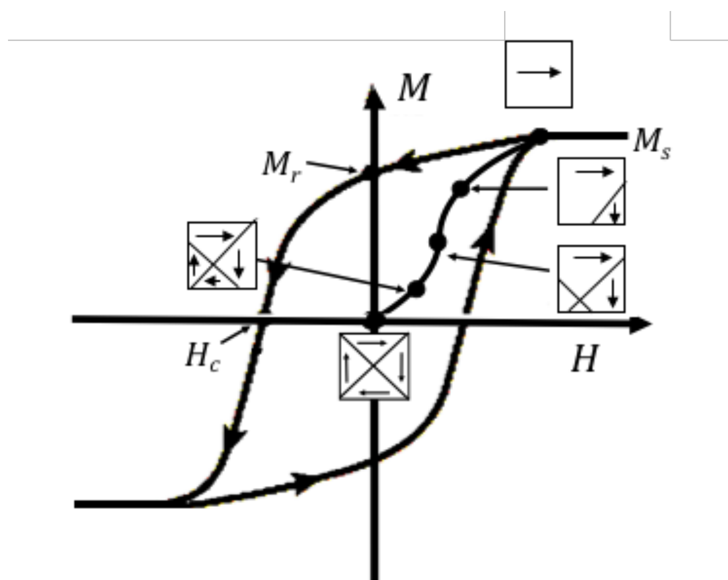

Figure: 2.6: *General schematic of magnetization hysteresis loop of ferromagnetic materials with points of M_s (saturation magnetization), M_r (remanence) and H_C (coercive field). Examples of domain configurations at various points in the hysteresis loop are also shown.*

2.4 Ferromagnetic materials types

Ferromagnetic materials include iron, cobalt, nickel and many alloys which contain one or more of these elements. These can be divided approximately into two categories based on their response to magnetic field: materials with a narrow (low coercivity) hysteresis loop (due to low spin-orbit interactions and, therefore, magnetocrystalline anisotropy) are referred to as 'soft' ferromagnetic materials while those with a wide (high coercivity) hysteresis loop (due to low spin-orbit interactions and, therefore, magnetocrystalline anisotropy) are referred to as 'hard' ferromagnetic materials (fig 2.7).

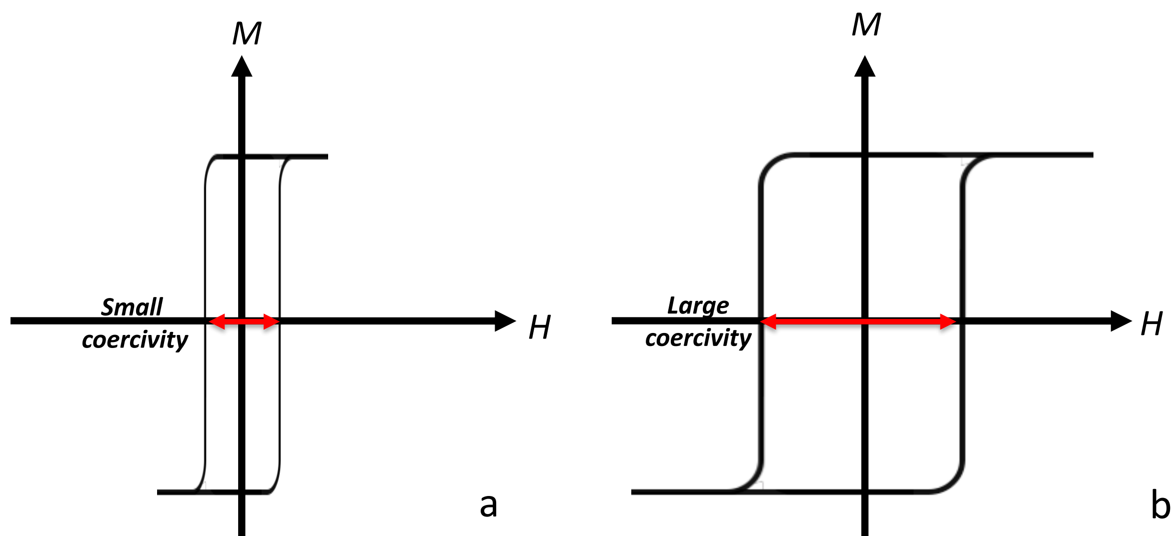

Figure 2.7: *Soft (left) ferromagnetic and hard (right) ferromagnetic material hysteresis loops (adapted from ref* [19]).

Hard ferromagnetic materials have high coercivity and often also have large values of remanence magnetization. Typical hard ferromagnetic materials include certain ferrites (e.g. barium ferrite BaO . $6Fe_2O_3$ and strontium ferrite $SrO.6Fe_2O_3$), AlNiCo and, most notably, rare-earth magnets such as Nd_2Fe_{14} and SmCo [17]. Consequently, they are often used as permanent magnets for use in applications such as motors and turbines.

Soft ferromagnetic materials are readily magnetized with small applied magnetic fields and hence have small coercive fields and often small remanence magnetization. Accordingly, soft ferromagnetic materials such as iron or silicon steel are used in solenoids, transformers electromagnets and sensors including in the write and read heads of magnetic hard disks.

2.4.1 Permalloy

A soft ferromagnetic alloy that contains nickel-iron to ratios close to 80:20 is called permalloy. Generally, these alloys exhibit high magnetic permeability and low coercivity [17], [19]. They are often used as thin films or foils and are generally of low cost. Permalloy has many applications, including in some designs of magnetic hard drive read/write heads (Fig 2.8).

Figure 2.8: *The main components of hard disk drive, including the write and read heads, which can contain permalloy.* [20]

The magnetocrystalline anisotropy of Nickel–iron is zero for a particular ratio [17]. M_s of permalloy depends on the nickel content as well as the degree of impurities and thermal history of the sample [17]. The saturation magnetization of Ni-Fe more generally increases with increasing Ni content contain up to 45%, and then reduces with further Ni additions. M_s is about $8x10^5$ A/m for $Ni_{81}Fe_{19}$ [17]. The Curie temperature increases with increasing nickel content to about 65% and then starts to decrease; for $Ni_{81}Fe_{19}$ it is about 450 ^oC. Figure 2.9 shows the variation of magentocrystalline anisotropy, Curie temperature and saturation magnetization with nickel weight percent. These properties make permalloy composites close to $Ni_{81}Fe_{19}$ very popular for use in magnetic structures, as will be discussed in sections below.

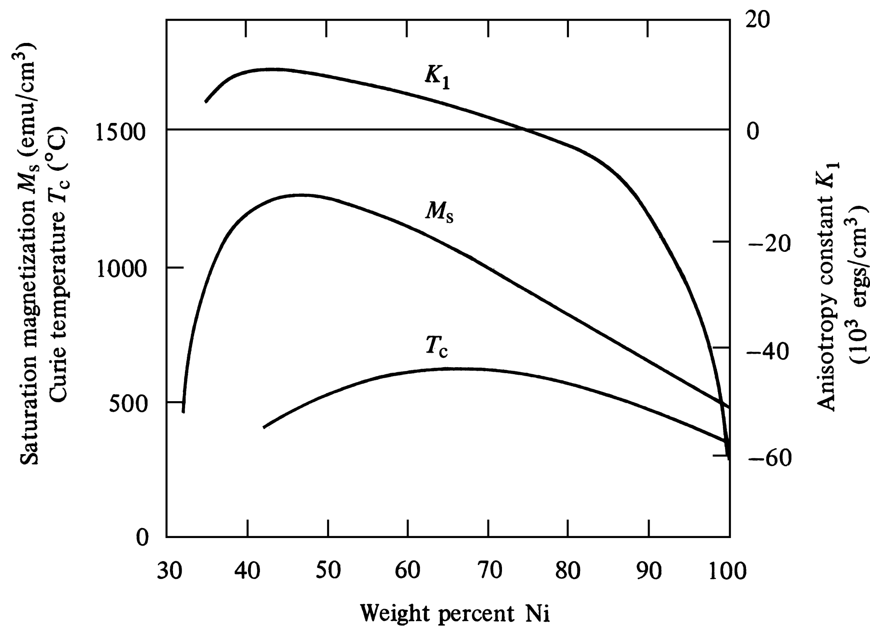

Fig 2.9: *The variation of magnetocrystalline anisotropy, curie temperature T_c and the saturation magnetization M_s with amount of nickel ratio, (used with permission from* [17]*).*

The magnetostriction of permalloy depends on the amount of nickel ratio but λ is zero for Ni content close to 80% as shown in fig 2.10.

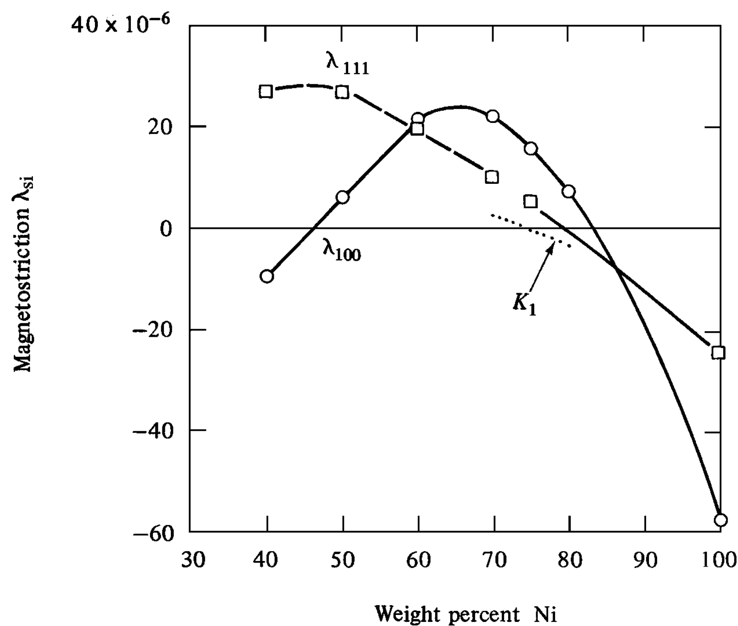

Fig 2.10: *The variation of saturation magnetostriction with amount of nickel ratio (used with permission from* [15], [21]*).*

2.5 Magnetic anisotropy

The observed magnetic response of ferromagnetic materials often depends on the direction in which measurements are performed. This also means that the magnetic energy terms and shape of hysteresis loop will be affected accordingly. Over and above the magnetocrystalline anisotropy discussed in §2.2.3, other anisotropy terms result from the shape of the magnetic element, or induced by several external factors such magnetic annealing, plastic deformation and irradiation. Here, we are most interested in shape anisotropy because the material used here, permalloy ($Ni_{81}fe_{19}$), has near zero magnetocrystalline anisotropy and was not subject to any processing that could induce anisotropic behaviour. Shape is, therefore, left as the primary term for dictating any magnetic anisotropic behaviour.

2.5.1 Shape anisotropy

Sample shape is a very important factor in the magnetic response of soft ferromagnetic materials. In the absence of any other source of anisotropy, a soft ferromagnetic object that is geometrically isotropic, i.e. a sphere, will have identical magnetic behaviour in any direction. This is because the demagnetizing field will be of equal magnitude when the object is magnetized in any direction. As soon as the geometry becomes anisotropic (non-spherical), the demagnetizing field magnitude depends on the direction of (saturated) magnetization; usually, the demagnetizing field is weaker when an object is magnetized along longer axes due to greater separation of magnetic poles. As explained below, this will affect the magnetic behaviour in different directions, e.g. requiring different magnetic fields to achieve saturated magnetization. Usually this results in magnetization along a long axis to be easier to achieve than along a short axis. Accordingly, the shape of the hysteresis loop is (in the ideal case) square when the magnetic field is applied along easy axes (fig. 2.11(a)), or linear with no hysteresis (fig. 2.11(b)) when the magnetic field is applied along hard axes.

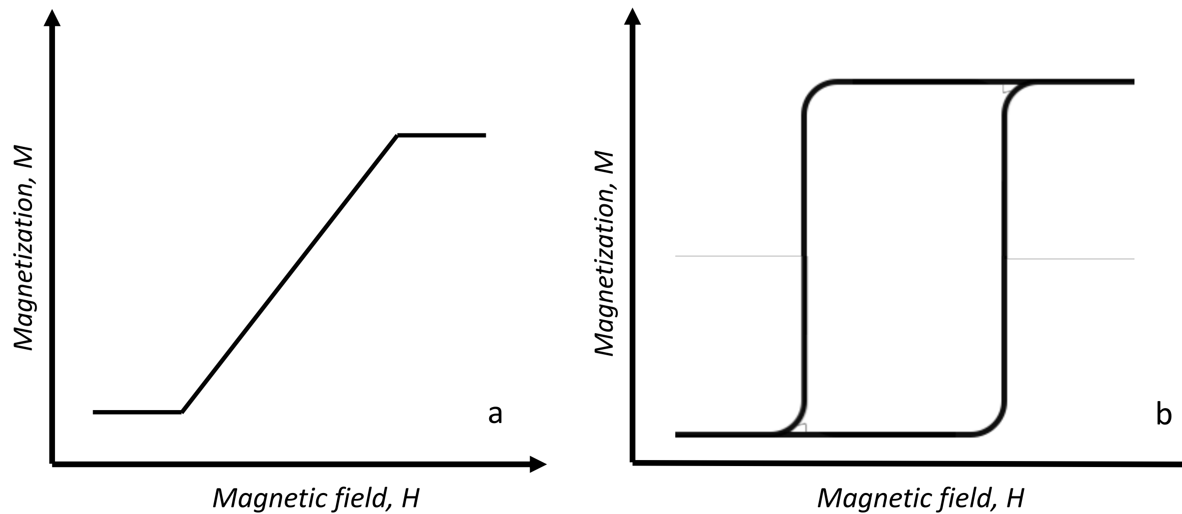

Figure 2.11: *The shape of hysteresis loop when applied the magnetic field along (a) hard axis and (b) easy axis, (adapted from ref.* [10]***).***

The internal demagnetizing field, H_d, noted in §2.2.2 opposes any magnetization, M. The magnitude of H_d depends on the shape of the magnetic element, i.e.

$$H_d = N_d M \qquad (2.9)\ [10]$$

where N_d is a directionally dependent value called the shape factor or demagnetizing factor.

The magnetostatic energy, E_{ms}, also uses the demagnetizing field and can be calculated as:

$$E_{ms} = \frac{1}{2}\mu_0 H_d M \qquad (2.10)\ [15]$$

By substituting Eq 2.10 into Eq 2.11 obtains:

$$E_{ms} = \frac{1}{2}\mu_0 N_d M^2 \qquad (2.11)$$

The demagnetizing factor N_d can be described as the sum of three orthogonal components N_x, N_y, N_z and equal to one, i.e.

$$N_x + N_y + N_z = 1 \qquad (2.12)\ [15]$$

For thin film in the x, y plane,

$$N_x = N_y = 0$$

$$N_z = 1$$

For long narrower object (such as wire) with its long axis in the x-direction

$$N_y = N_z = {}^{1}/_{2}$$

$$N_x = 0$$

2.6 Small magnetic elements

In addition to the influence of the shape anisotropy, the size of magnetic particles has a strong effect on magnetic properties, often becoming different from the bulk [22]. The radius of magnetic particles strongly influences magnetization structure due to non-uniformities creating high exchange energy contributions at the small dimensions concerned [10]. There is also a material-dependent critical radius below which a particle cannot readily support domain walls and is inherently single domain. The critical radius of particles depends on their magnetization and exchange constant, and typically lies between 10 nm to 100 nm [22]. A single domain particle needs a small magnetic field to reach the saturation point and results large coercivity compared to multi domain particles [10] as shown in fig 2.11.

The unique properties of small magnetic particles and the need to produce devices with smaller, faster, more efficient and higher memory densities has pushed the development of fabrication techniques to pattern micro/nano-scale magnetic structures.

2.7 Summary

This chapter has reviewed the fundamentals of magnetism and magnetic materials, focussing on the phenomenon of ferromagnetism. The five principal energies that govern magnetic behaviour: exchange energy, magnetostatic energy, magnetocrystalline energy, magnetostrictive energy and that from applied magnetic field (Zeeman energy) were discussed in relation to their effect on magnetic behaviour. The concept of a ferromagnetic domain was introduced, as well as the formation of multi-domain magnetic configurations and the motion of magnetic domain walls. Hard and soft ferromagnetic materials were discussed in terms of their response to applied magnetic field, and the material permalloy introduced. The concept of magnetic anisotropy was introduced, and especially shape anisotropy, which is relevant to the magnetic structures studied here.

Chapter 3: Fabrication techniques of micro/nano-magnetic structures

3.1 Introduction

Micro/nano-fabrication describes the methods that are used to design and produce structures with dimensions measured from micrometres to nanometres. This chapter reviews the methods and techniques used to design and fabricate micro/nano-magnetic structures.

Humankind has created patterns of materials for thousands of years, usually for writing, decorative and artistic purposes. Patterning has assumed greater technological importance in more recent history though. Fabrication techniques to produce objects with micro/nano-scale features are employed to produce lots of modern applications and devices, for example: integrated circuits, solar cells, microfluidics, micro-optics, and MEMS [23], [24] as well as magnetic structures for applications such as data storage (e.g. in computer hard disks) [10], [17] (Fig 3.1).

Figure 3.1: *Some products that include components fabricated by micro/nano-fabrication processes: (a) solar cells and (b) integrated circuits.*

However, the significant developments in production of micro/nano-scale applications and devices are a consequence of progress in the development of patterning processes that can make smaller and smaller objects. The study of small-scale elements has driven the development of fabrication techniques that offer higher spatial resolution (or reducing the power consumption, cost and time of fabrication), which in in turn feeds further research of nano/micro-scale elements.

The introduction of integrated circuits gave huge impetus to miniaturization research and today sees billions of electronic devices on one semiconductor chip. This has driven an orders-of-magnitude reduction in cost, size and operating speed of electronic devices, and forms the backbone of the modern computing revolution.

This project aims to develop a novel micro/nano-fabrication process and investigate the properties of the resulting miniature structures. Fig 3.2 explains the research-production cycle and the main aim of this project.

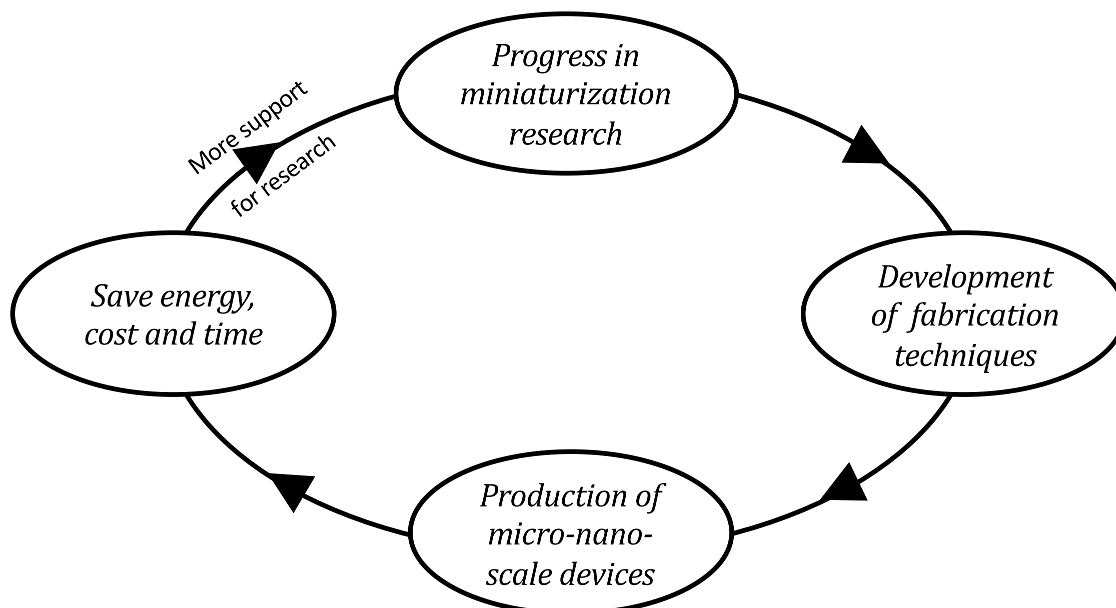

Figure 3.2: *Typical cycle of research and production development relevant to micro/nano-fabrication.*

3.2 Micro/nano-fabrication techniques

The word 'lithography' is often used to describe micro/nano-scale patterning techniques and yet originally referred to writing on the surface of stone, being derived from two Ancient Greek words: *lithos*, meaning stone, and *graphine*, meaning to write [24]. The lithography process was invented in 1796 by Aloys Senefelder to transfer an engraved image onto paper if inked and treated with appropriate chemicals [24]. Since then, there has been a steady development of other approaches to lithography, leading to today's nanofabrication techniques. However, the lithography process remains the most difficult, time-consuming and expensive of all the stages of device fabrication [25] and patterning techniques continue to be developed to try to alleviate the constraints of lithography.

Magnetic structures are used in many applications and devices such as: magnetic recording [26], data storage[10], [26], actuators[6], sensors[8], [27], [28], and control of

magnetic particles[29], [30] or magnetically-labelled cells[5], [26]. Various types of micro/nano-fabrication techniques are used to patterned micro/nano-magnetic structures, for instance, photolithography, electron beam lithography, ion beam lithography, X-Ray lithography and soft lithography.

The following sections review common lithographic techniques that are used to fabricate micro/nano-magnetic structures and evaluate each in terms of their speed, cost, resolution and complexity. Micro/nano-scale patterning techniques fall broadly into two categories of (a) resist-based lithography and (b) non-resist-based lithography and will be introduced here under these classifications.

3.2.1 Resist- based lithography

Resist-based lithography refers to lithographic techniques that use a sacrificial layer (the 'resist') in order to transfer the desired pattern onto a substrate. This ensures that lithographic processes can be optimised for a resist and used to pattern many different thin film materials, including multilayers. Resist-based lithography is well-suited to multi-level lithography to create multiple layers of patterns.

Resist–based lithography can be further divided into techniques that use a mask to project a pattern onto the resist, and adaptive or 'direct-write' techniques that allow the pattern to be controlled and changed as desired for each exposure. Masks allow identical exposures to be performed highly efficiently but direct-write techniques offer greater flexibility and are often preferred for prototyping and low volume fabrication. Photolithography will be discussed first and, in some depth, because it includes many of the processes relevant to other techniques, with only minor differences. X-ray, electron beam, ion beam lithography and soft lithography techniques will then also be discussed.

Generally, micro/nano-fabrication can be divided into pre-lithography, lithography and post-lithography processes. Fig 3.3 shows a basic flow chart giving more detail of these main stages for resist-based lithography.

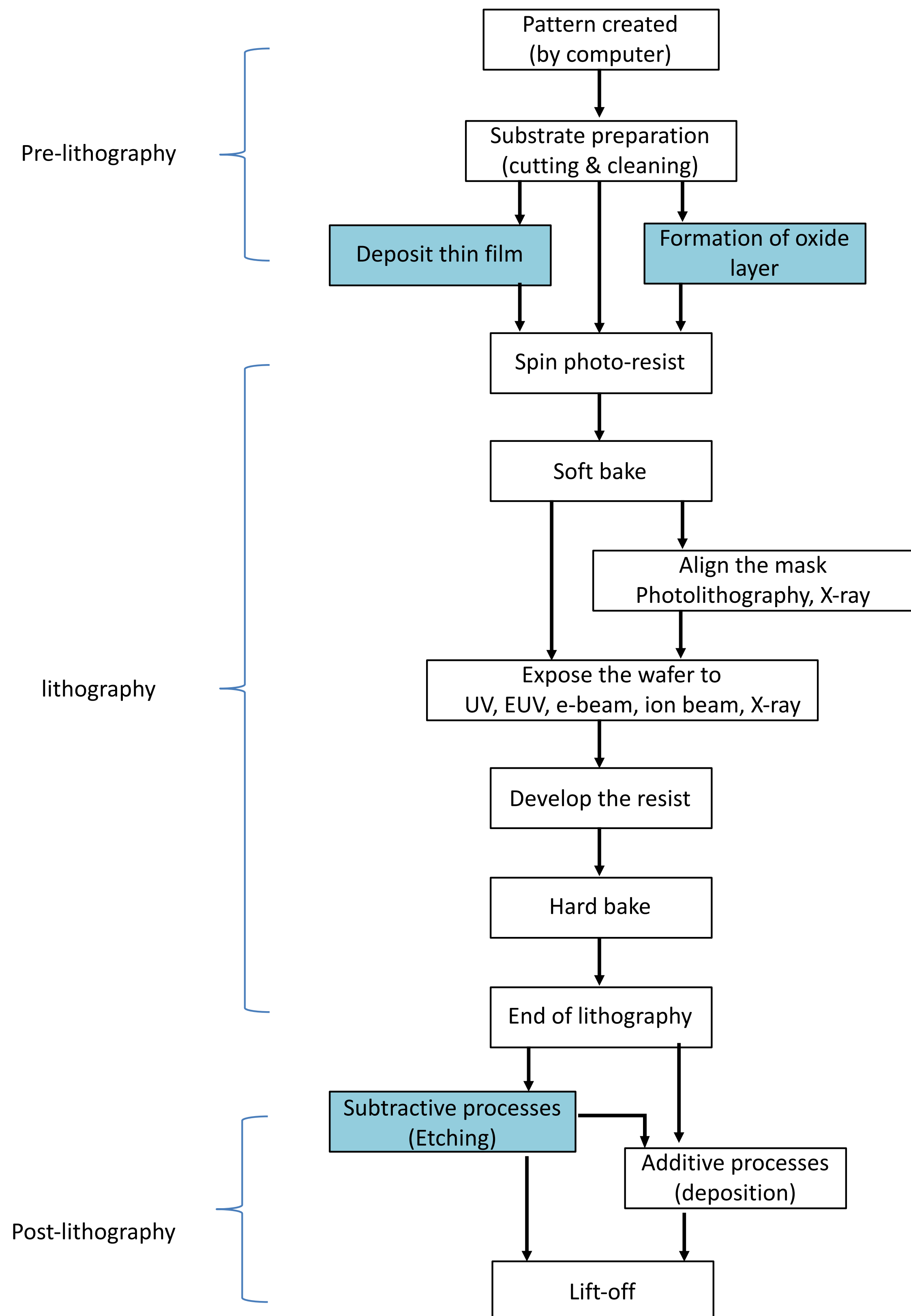

Figure 3.3: *A simple flow chart of standard resist- based lithography micro/nano-fabrication processes, where UV (ultraviolet) and e-beam (electron beam) are abbreviations.*

3.2.1.1 Photolithography

Photolithography is the most common fabrication technique used to pattern structures at the micro/nano-scale [23]. Photolithography usually includes 10 - 100 separate steps [23] and usually follows the steps shown in Fig. 3.3. Pre-lithography starts with creating the desired pattern by computer and, for standard mask-based photolithography, fabrication of the mask. Choosing the proper substrate depending on the application and fabrication technique. Various types of materials are used as substrate to build micro/nano-system such as: amorphous silicon/silicon dioxide, crystalline silicon, quartz and glass [23], [31]. Each substrate material has advantages and disadvantages but silicon is the most common and the mainstay of micro/nano-fabrication due to its electrical properties, cost, smoothness and availability in various sizes [23], [24], [31], [32]. Substrate cleaning is crucial in order to remove all organic and inorganic contaminants from the surface as these can affect the fabrication process and lead to unwanted resist removal or retention. The cleaning is ideally carried out in a cleanroom [23] using a chemical ultrasonic treatment with solvents suitable to the substrate [24], [33], e.g. acetone followed by ethanol. Insulating barrier layers for later processing (e.g. as an etch stop) [23], [32] commonly uses a deposited layer of SiO_2 [23]–[25], Si_3N_4 [23], [34] or $TiSi_2$ [23], [35]. In some cases, layers of the final materials are deposited first and etched after patterning of the resist material, as discussed below.

The lithography process then begins with addition of the photo-sensitive polymer (photoresist) to the substrate. Photoresist films are deposited onto the surface of substrate, usually by one of three approaches: electrochemical coating, spray coating and casting, and spin-coating [23], [24]. Of these, spin-coating is the most common method for low-volume prototyping on small (sub-cm) substrates. For spin-coating, the substrate is spun at speeds of up to 10,000 rpm [23] after the resist solution is added to achieve a uniform layer. The thickness of the photoresist is controlled by the spinning speed, solvent evaporation rate and photoresist viscosity [23], [32], [36] and is typically between 0.1μm and 2.5μm[24], [32]. After spinning, the resist is soft baked (typically at 60-100 ^{0}C for (5-30 min [[25], [32]) to drive off any remaining solvent and improve the adhesion of the resist to the substrate.

In general, there are two types of photoresist; positive and negative [24], [32]. The two types of resists need to be sensitive to the UV light that is applied in photolithography or to the other type of radiation that they are exposed to for patterning such as: visible, infrared or ultraviolet light, X-rays, electron beams and ion beams. Organic polymer resists such as polymethylmethacrylate (PMMA) are commonly used. The incident radiation causes the degree of polymerisation in the resist to change. In the most commonly used resists (known as 'positive' resists), exposure results in bond breaking to reduce the polymer chain length (e.g. with PMMA)[32], [36]. Conversely, negative resists become more polymerised during exposure. In either case, exposure is then followed by a development step that removes the more soluble smaller-length polymer chains. With positive resists, this removes the exposed regions while with negative resists it is only the exposed regions that remain. A choice of positive and negative resist widens the range of subsequent processing techniques that may be used to create patterns of the final material. Examples of negative resist materials include SAL-601, AZ-PN-100, while positive resists include PMMA, ZEP-520 and MMA [24], [37]. Fig (1.4) [25], [38] shows a comparison of positive and negative photoresist processes.

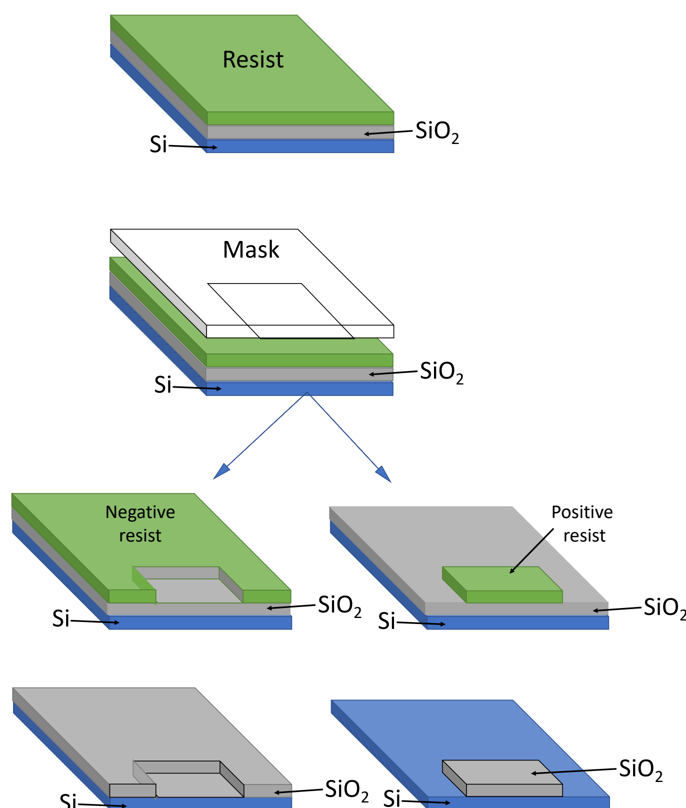

Figure 3.4: *Photolithography using negative or positive photoresists (adapted from ref.* [38]*).*

The lithography stage can now begin and pattern transfer take place. This is often achieved using a mask containing a copy of the desired pattern. The pattern transfer can be accomplished either by bringing the mask into contact with the resist in close proximity or using projection optics [23], [24], [32]. The light is most commonly ultraviolet (UV) [32] but extreme UV [32], [39] sources and optics have been developed over the past 20 years and this short-wavelength radiation is now commonly used to define state-of-the-art CMOS architectures [40], [41].

Masks are typically transparent plates of quartz or glass covered with pattern defined with a chromium layer (typically 100-Å thickness) [7], [17] to absorb or reflect light. while the transparent mask areas allow the light to pass through and reach the photoresist.

Simple masks offering sub-micrometre resolution are available commercially for under $1000. However, fabrication sets for (what was) state-of-the-art computer chip fabrication typically include 15 individual masks cost more than $500,000 in 2005 (offering 130 nm resolution) [23], [42] and up to $2 million in 2006 (for 65 nm resolution) [42], [43]. An order of magnitude improvement in resolution (14 nm [44] and 10nm [45]) has since been achieved but will require higher costs still..

The resolution ***R*** of mask-based lithography is given by [23], [25]:

$$R = k\lambda \tag{3.1}$$

where k is a constant and λ the wavelength of the light used. The value of k depends primarily on the numerical aperture (NA) of the lens system used for exposure and the dimensions and diffraction at the edges of mask. Accordingly, k can be reduced to improve the resolution by choosing the appropriate exposure system or reducing the gap between the wafer and mask in proximity exposure [23], [25], [32].

Equation 3.1 also shows how pattern resolution with masks is related to λ . Reducing λ has been a key part of improving resolution in state-of-the-art semiconductor fabrication facilities and the emergence of EUV systems [25].

Photolithography can also be achieved using point-by-point exposure of the resist to a scanning focussed laser beam [46], [47]. This offers considerable flexibility in pattern design in computer-controlled systems but at the expense of longer exposure times compared with mask-based lithography.

Once exposure is complete, the resist is developed by immersion in a developer solution to selectively remove short-chain photoresist, i.e. exposed positive resist or non-exposed negative resist (Fig. 3.4) [24], [32]. The developed resist is then hard baked to increase its hardness and adhesion to the substrate, a process that typically involves heating the sample to 120-180°C for 20-30 min [24], [32], [48]. The resist patterning process is now complete.

The final stage of the fabrication process (post-lithography) may contain a number of subtractive or additive processes or both. Etching processes are subtractive and in lithographic patterning remove regions of the sample not covered by the resist. Wet etching can be isotropic or anisotropic, is very rapid [23], [24], low cost and uses etchants such as NH4F:CH3COOH:C2H6O2 (ethyleneglycol):H2O for removing SiO2 [23]. Isotropic etches tend to make round sidewalls but anisotropic etches makes vertical sidewalls. However, wet etching limits the resolution that can be achieved [23], [24], [36]. Figure 3.5 shows the difference between isotropic and anisotropic wet etching.

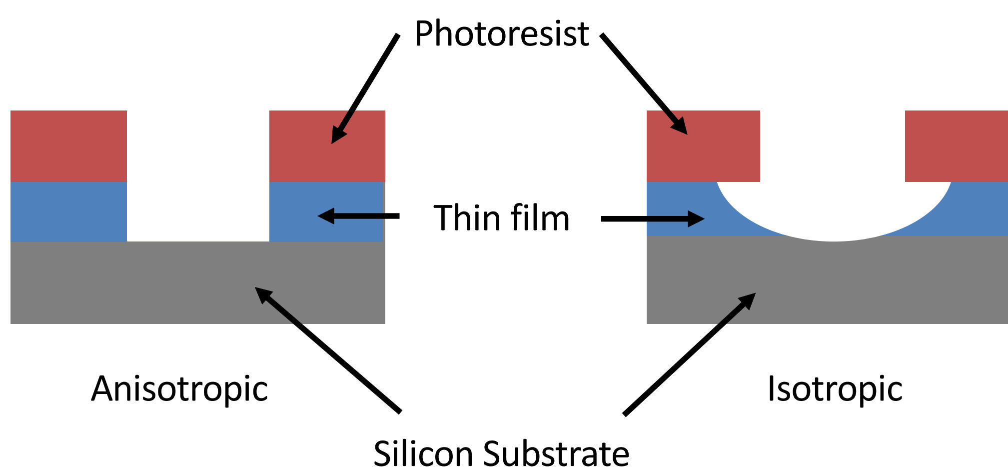

Figure 3.5: *The material profile obtained after isotropic and anisotropic wet etching (adapted from ref.* [25]*).*

Dry etching techniques are based mostly on using plasmas [23], [24], [32]. The main dry etching approaches are: high-pressure plasma etching, in which the highly reactive species of plasma etchers are created that react with the material that is to be etched; ion milling, where ions are accelerated towards a substrate and remove atoms by sputtering; and reactive-ion etching (RIE), in which plasma ions (typically SF_6/Ar) react with atoms in the (solid) sample to create gaseous molecules [25], [32], [36]. Dry etching techniques have numerous advantages compared with wet etching, such as supporting higher resolution fabrication, creating less undercutting, higher anisotropic (less uniform material removal) and maintaining greater cleanliness. However, dry etching techniques are often more expensive, relatively slow and (except RIE) offer low selectivity [24], [32].

Deposition processes are used to deposit the desired material on the resist pattern after development [23] to realise the required pattern (note that etching can also be used to pattern a previously deposited layer – see §3.2.1.4 below). There are numerous types of deposition techniques can be used for this purpose; for instance:

1- Physical vapour deposition (PVD) [23], [32], [49].
   - a- Evaporation (discussed further in chapter 5).
   - b- Sputtering.
   - c- Cathodic arc deposition.
   - d- Pulse laser deposition.
2- Chemical vapour deposition (CVD) which uses the reaction chemicals open deposition [23], [32], [49].
3- Atomic layer deposition (ALD)[49].

The final step of photolithography is lift-off removal of the remaining photoresist and any deposited material above it. This process is carried out by soaking the sample in a remover solvent, often under ultrasonication and at temperatures of 80-120 ^{0}C to overcome the resist adhesion to the substrate. The lift-off process can take a few minutes to several hours depending on the resist material, resist thickness and pattern design [6], [7].

The key advantages of photolithography are that is offers high throughput [23] due to its full-field exposure and can have high resolution, with sub-micrometre resolution using lab-based UV lamp systems [23], [36] to sub-10-nm resolution possible with the latest EUV sources in semiconductor fabrication plants [50]. However, photolithography also involves many complex steps [13], [36] so that it can be cumbersome and time-consuming [13], expensive to set up high resolution facilities [13], [31] and dependent on alternative techniques to pattern a photomask. It is also ill-suited to prototyping and being used in flexible design as new masks are required for each new design.

3.2.1.2 X-Ray lithography

X-rays were first used expose photoresists instead of UV light by International Business Machines (IBM) in 1969 [51]. X-ray lithography is also called high-aspect-ratio micromachining process (LIGA; an acronym of the German words *LI*thographie, *G*alvanoformung and *A*bformung) due to short wavelength of x-rays that can penetrate through thick layers (from hundreds of micrometres to millimetres) of photoresist without scattering into transverse directions for several micrometres. Therefore, it can fabricate structures with aspect ratios of up to 100:1, lateral resolution reaching sub-micrometre dimensions and thickness extending to millimetres [32], [51]. The X-ray lithography process follows similar steps to contact or proximity photolithography with differences in mask and photoresist materials, and in preferred deposition technique. Thick layers of PMMA are required but thinner layers of high sensitivity photoresist are more commonly used [24], [32], [51]. X-ray lithography masks tend to be made of titanium (Ti) and beryllium and the preferred alignment type is proximity to avoid damaging the mask [23], [24], [51]. The high aspect ratios achieved with X-ray lithography mean many of the deposition techniques used in traditional photolithography are unsuitable. Instead, electrodeposition is often used to fill the regions where resist has been removed and relies on highly conductive underlayers. These features are summarised in Fig. 3.6.

The lateral resolution of X-ray lithography can reach 30 nm [52], [53] but the commonly used proximity exposure configuration leads to a reduction in resolution to near-micrometre dimensions [23], [24], [32], [54]. High aspect ratio structures with thicknesses up to the millimetre range can be achieved [23], [32], [51]. But, the throughput of X-ray lithography is

very low, therefore it used only for the purposes of research and development [24], [32], [51]. Also the damage of masks and the high cost of the X-ray sources causes this to be a relatively expensive technique [24], [32].

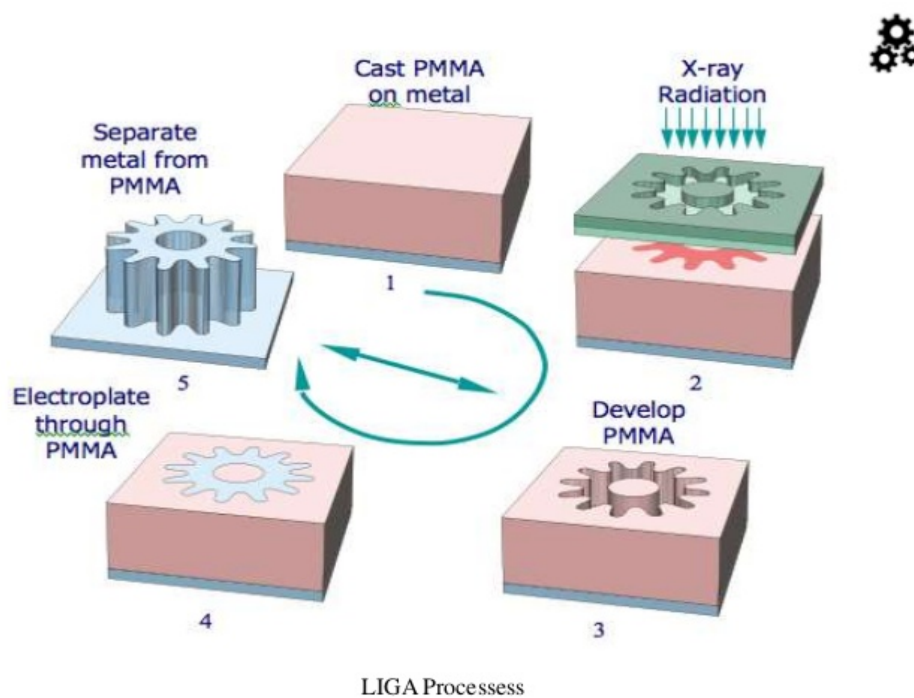

Figure 3.6: *The X-ray lithography process*[55]**.**

3.2.1.3 Electron beam lithography

Electron beam lithography (EBL) uses a focused electron beam to directly expose an electron-sensitive resist without the need for a mask[24], [52], [56]. Some consider EBL to be a 'direct write' technique [57] but here it will be categorized within resist-based lithography techniques as it mostly follows same processes of resist-based lithography shown in Fig. 3.3.

Electron beams are typically accelerated to 100 keV to 200 keV [58] for exposure, which gives the electrons de Broglie wavelengths of the order 1 nm. This short wavelength compared to those of UV or even EUV radiation means that very high lateral resolutions of sub-10-nm are possible [58], [59]. The electron beam is scanned across the resist to expose regions designed by the user, making it highly suitable for prototyping and low-volume fabrication. For these reasons it is very popular within device research. Numerous materials can be patterned using

EBL although patterning of resists on dielectric underlayers often necessitates an additional conducting layer to be deposited on the resist in order to create a conduction pathway for the incoming electrons [36], [58]. However, EBL is slow, since it marries the pixel-by-pixel scanning with the large number of steps shown in Fig. 3.3. It also requires expensive capital equipment, with cost often several millions of dollars [52], [60]. These systems (e.g. Fig. 3.7) tend to be highly complex and sensitive and, consequently, often require frequent maintenance to ensure good performance [24].

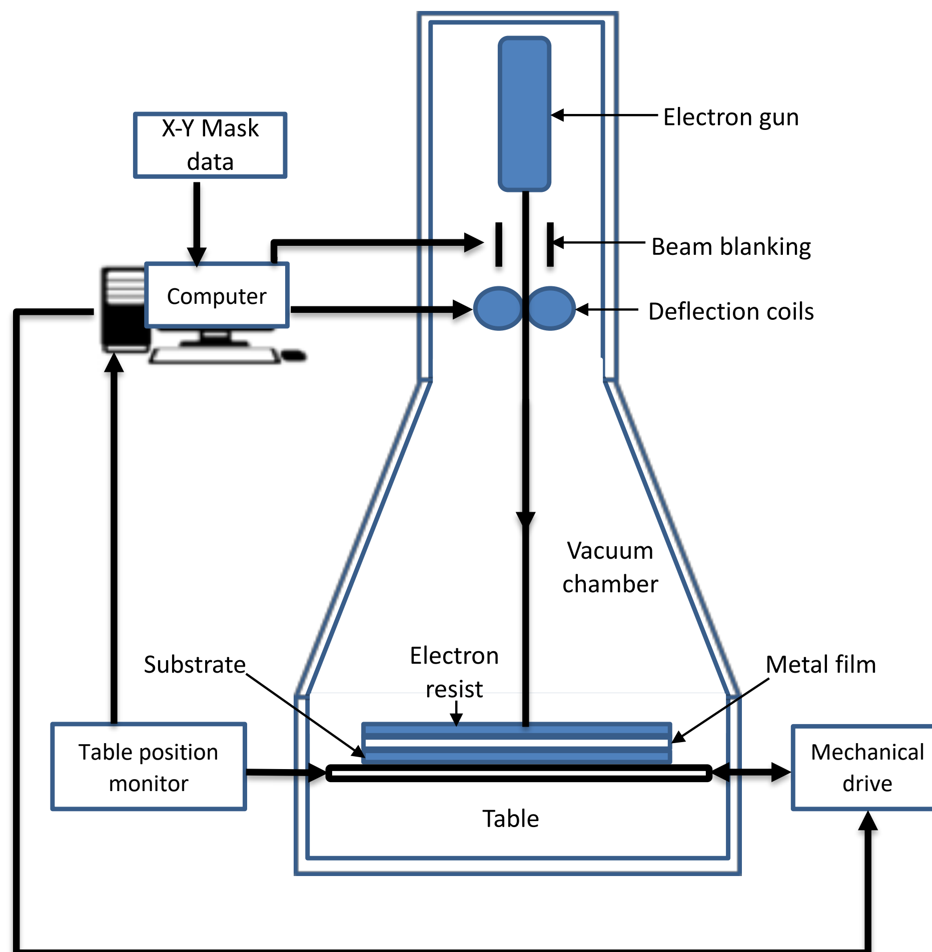

Figure 3.7: *Schematic of a basic E- beam lithography system (adapted from ref* [52]*)*.

3.2.1.4 Ion beam lithography

Ion beam lithography includes three main techniques: ion projection lithography (IPL), focused ion beam (FIB) exposure and proton beam writing (p-beam writing) [24], [61]. All three approaches are used in vacuum and expose a resist to change its solubility, ready for subsequent processing as described in §3.2.1.1 above [24]. FIB writing is also often used to pattern a material directly without the use of a resist therefore, FIB will be categorised within (non-resist-based lithography) because it most common to use as a direct etch tool (see §3.2.2.1).

In IPL, an ion beam passes through a mask in proximity before patterning a region of resist, similar to proximity photolithographic processing [62]. Ions are typically protons, H_2^+, He^+ or Ar^+ [62] and resist materials commonly TiO_2 or TiO_2/ Al_2O_3 [63].

3.2.1.5 Soft lithography

Soft lithography describes a range of micro/nano-scale fabrication techniques that use elastomeric stamps and moulds [24], [64], therefore, the key element in soft lithography is the stamp. This techniques include micro-contact printing (µCP), micro-transfer moulding (µTM), replica moulding (REM), solvent-assisted micro-moulding (SAMIM) and micro-moulding in capillaries (MIMIC) [31], [37], [65].

In general, soft lithography processes start with making a master template by photolithography or EBL, and dry etching or lift-off [31], [37], [66] as explained in §3.2.1.1.

The stamp materials are then poured in the template to produce the stamp. The most common materials used to produce the stamps are rubber or silicone (also called PDMS; polydimethylsiloxane) [67]. The stamp is peeled off from the template carefully. The stamp is coated with a solution ink that contains alkanethiol on gold or a trichloroalkylsilane on silicon oxide [66] before being brought into contact with a substrate in order to transfer the ink and create a pattern [37], [65]. After application of the stamp, the transferred material has to be

left to dry. The drying time is dependent on the material and feature size, but the typical time is between 20 to 30 min [67].

Soft lithography also used to pattern resist for fabricating submicron ring magnets[68].

Figure 3.8 explains the process of soft lithography [69]. The resolution of soft lithography is limited by many factors including: contraction or pairing of features of stamp during working, where it is impossible to isolated the dot-type structure each other[64], [67]; hydrophobic interactions, because it is difficult for inks based on water to flow through the channel because stamps are hydrophobic [66], [67]; and thermal expansion of the mould [37], [66].

Soft lithography techniques are relatively fast, e.g. requiring a few hours to produce a structure [37], [64], [65], compared to other techniques. The mould and stamp can be used up to 40 times [31], [37], [66], which makes soft lithography relatively inexpensive compared with other techniques, although it becomes important (and challenging) to avoid damage to the mechanically soft mould during use [37], [65]. However, the mechanical flexibility of the mould material means soft lithography can be used on curved substrates [31], [66]. Soft lithography can achieve resolutions better than 100 nm [37], [65] and is being extended to 30 nm [31], [67].

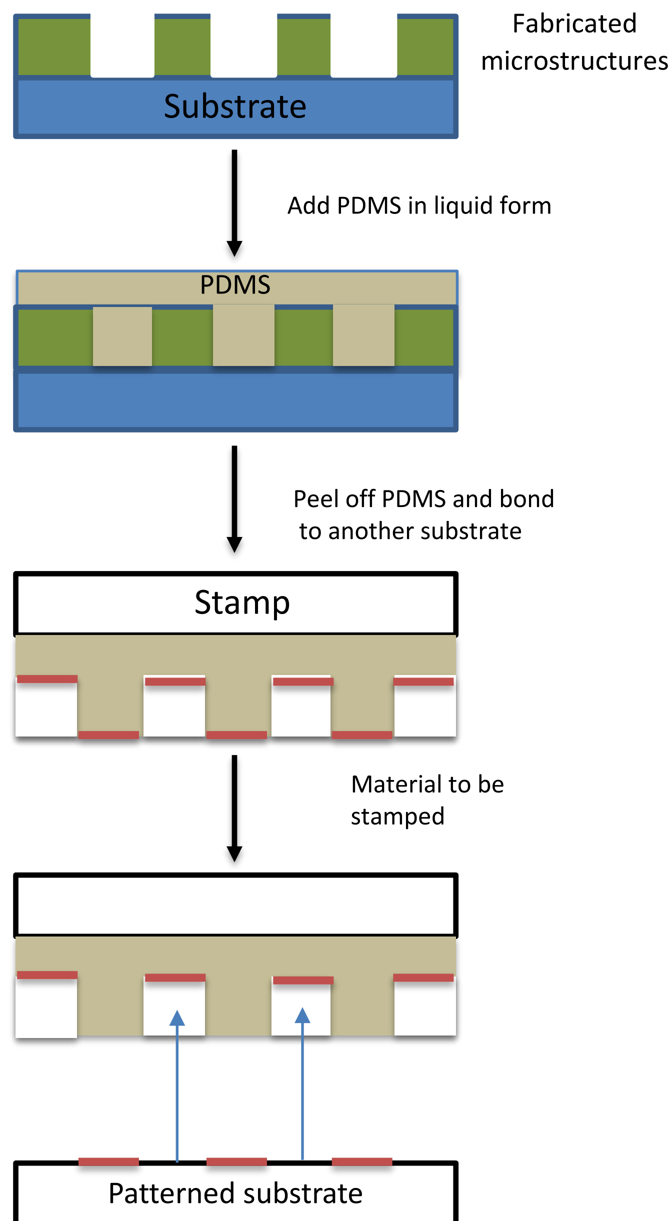

Figure 3.8: *Soft lithography process(adapted from ref* [65]*).*

3.2.1.6 Other techniques

There are further of resist-based lithography techniques such as interference or holographic lithography that follow similar processes to those described. These techniques are used to pattern structures of fine features without need to use of photomasks in processes similar to those used in electron-beam or X-ray lithography [36]. In interference lithography, a laser beam is divided using a beam splitter into two coherent beams, then the split beams are

recombined at different angles onto a photoresist. The resulting structures will reflect the sinusoidal laser intensity resulting from the interference of the beams.

3.2.2 Non-resist-based lithography

A number of lithographic techniques create patterns without the use of a resist or mask. These are known as 'direct write' techniques and will be introduced briefly here.

3.2.2.1 Focused ion beam (FIB)

Focused ion beam (FIB) writing controls a focussed beam of ions to create a user-defined pattern. FIB most commonly uses Ga^+ ions (since Ga is a liquid at room temperature, which makes possible continual replenishment of the ion source) accelerated to several keV but other ions such as Au/ Si, Au/Si/Be or Pd/As/B are also sometimes used [24], [70], [71]. Although FIB techniques can be used to alter the local solubility of a resist [24], they can also be employed to create local patterning by milling a resist [24], [70], milling a thin film of the desired final material (including magnetic materials) [72] or change the magnetic nature of a thin film by Ga implantation, e.g. change regions from being ferromagnetic to paramagnetic [72]. Focused ion beam milling (FIBM) can be categorized as a direct write process.

FIB systems often have a spot size below 10 nm. Therefore, it they offer higher resolution than photolithography and X-ray lithography [24], [61] but lower than EBL. Ion beam lithography tends to be very slow so throughput is also very slow and, according to some sources, slower than EBL [24], [73]. Also, the system can frequently damage the underlying sample because of the high energy ions [24], [73]. Ions can often become embedded in the material through scattering processes over many tens of nanometres laterally, which can limit the resolution of the technique [43]. Ion beam lithography is also expensive [24].

3.2.2.2 Scanning probe lithography (SPL)

Scanning tunnelling microscopy (STM) was invented in 1985 by Binnig and Rohrer [74] and was quickly followed in 1986 by Binnig and Quate inventing atomic force microscopy (AFM)

[75]. These approaches fall under the more general terms of 'scanning probe microscopy' (SPM) [54], [76].

SPM can be adapted to create patterns on a surface, in a process known as 'scanning probe lithography' (SPL), rather than just providing an image of a surface. SPL methods use a sharp probe tip to create patterns on a substrate [77] by local heating [54]. In general, the desired materials are coated on the sharp probe (tip) then induced to transfer from the tip to a surface of substrate. This process is realised by one of two methods: flowing very small electric current between the tip and substrate, which generated from applied voltage pulse or by applying a laser beam to melt the material on the tip to allow it to flow onto the adjacent substrate [77]. Figure 3.9 shows a schematic of SPL with the two methods to transfer the desired materials from the tip to substrate.

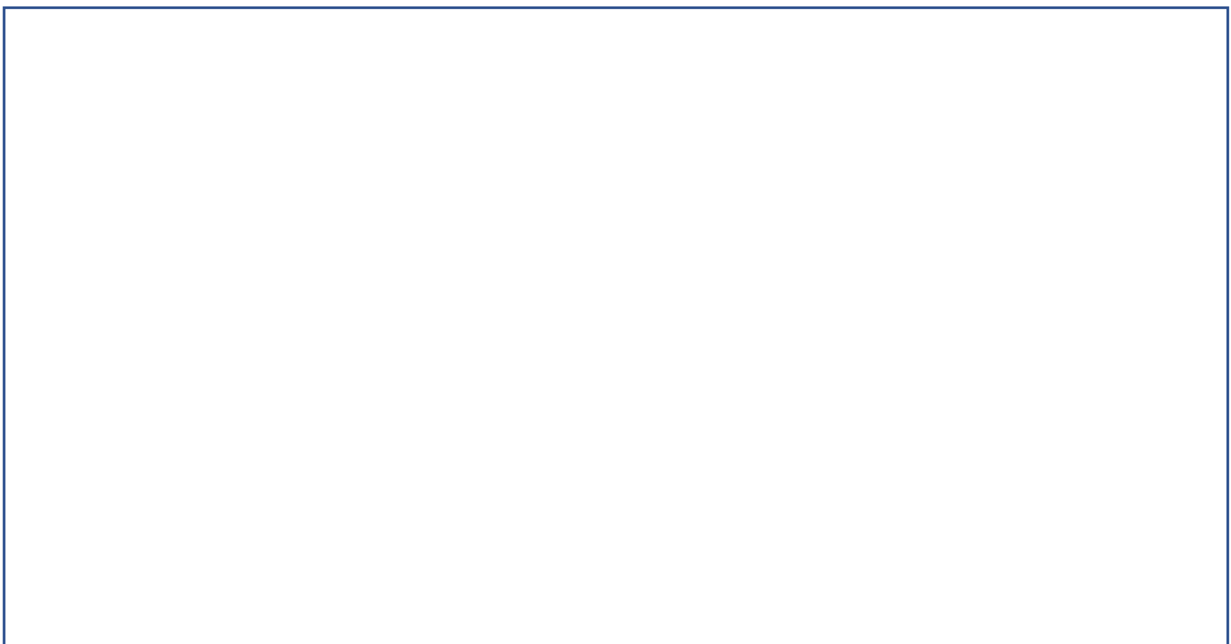

Figure 3.9: *The schematic of the two methods for heating material on a scanning probe tip to create transfer to substrate: a, laser heating* [77]*; b, applied voltage pulse* [54].

SPL techniques offer high resolution (sub-10-nm) single-step direct write fabrication [77]. However, they tend to be slow, with poor throughput and small work areas (a few μm^2) [36],

[54], [77]; consequently, SPL tends to only be used in research activities. SPL also suffers from frequent damage to the probe [36], [77].

The capability and limitations of each technique that discussed in this chapter are summarised in table 3.1, also table 3.2 involve some examples images of structures fabricated these techniques.

Table 3.1: *Capability and limitation of miniaturization techniques.*

No.	*Criteria* / *Technique*	*Complex*	*Process Time*	*Throughput*	*Cost*	*Resolution*	*Rely on other techniques*
1	Commercial Photolithography	High	Long	High	High Expensive	Good <100nm	Depended
2	Electron-beam lithography	High	Long	Low	High Expensive	Very good <10nm	Depended
3	Ion-beam lithography	High	Long	Low	High Expensive	Very good better than E-beam	Depended
4	X-ray lithography	High	Long	Low	High Expensive	Very good <17nm	Depended
5	Soft lithography	Medium	Long	Medium	Expensive	Good 30nm	Depended
6	Scanning probe lithography	Low	Long	Low	Expensive	Good >50	Independent
8	Interference lithography	High	Long	Low	?	Good 30nm	Depended

Table 3.2: *Samples of SEM and AFM images of 2-D and 3-D structures produced using lithographic techniques : a- AFM images of gold nanoparticles fabricated by photolithography* [78], *b- SEM images of 3D nanostructures fabricated by electron beam lithography demonstrated with less than 20 nm misalignment* [79], *c- Nano-gratings fabricated by focused ion lithography implantation* [80], *d- Photonic crystal made by X ray lithography*[81], *e- SEM image of an array of silver disks fabricated using soft lithography* [82], *f- SEM image of a 2-D array of hexagonal pits fabricated using scanning probe lithography* [83] *and g- SEM images of negative photoresist columns created by interference lithography* [84].

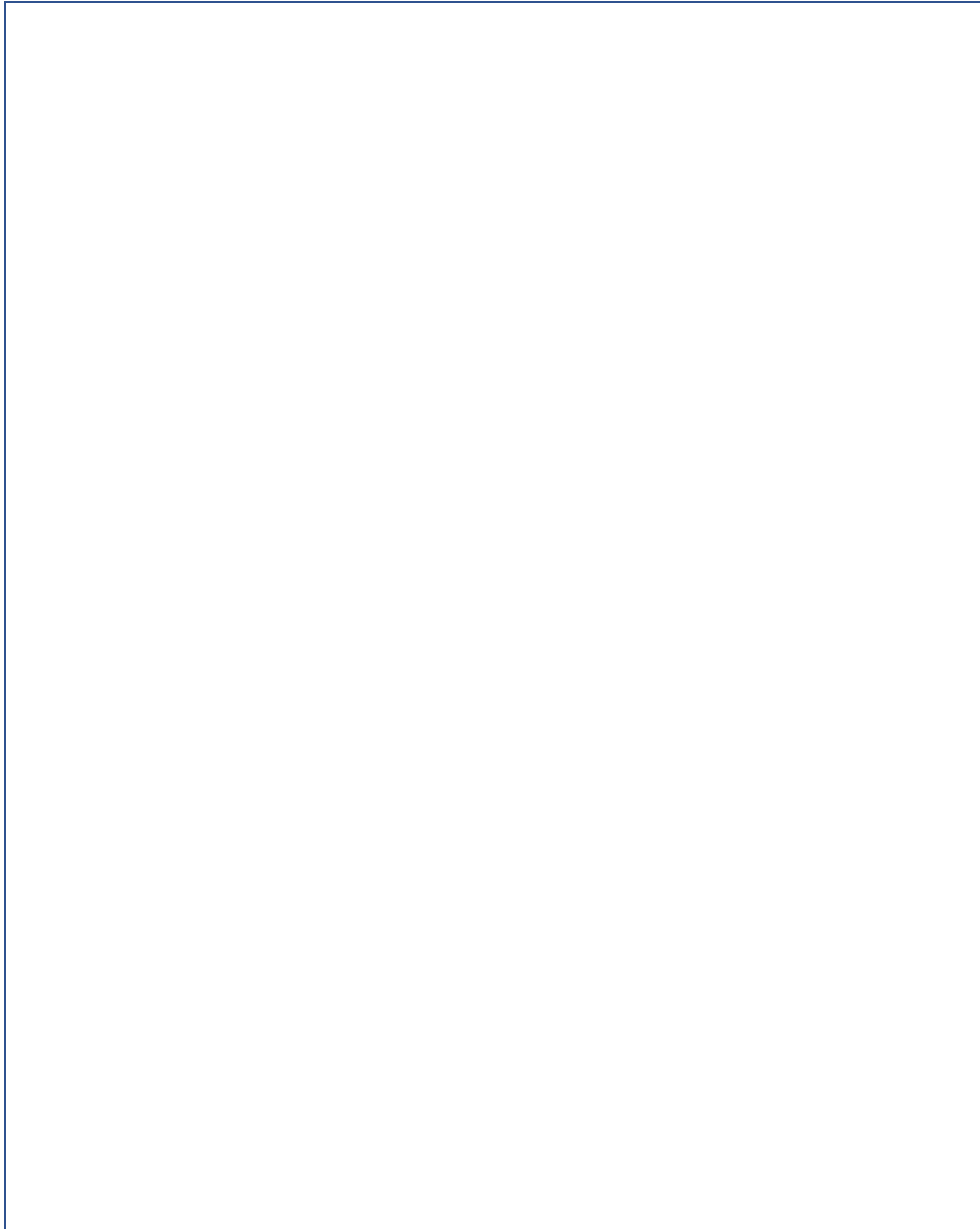

3.3 Summary

The fabrication techniques used for patterning micro/nano-scale magnetic structures were reviewed in this chapter. We have covered the history of lithography from the first attempt in 1796 by Aloys Senefelder to transfer an engraved image onto paper through to modern lithographic techniques. Techniques have been compared in terms of their speed, cost, resolution and complexity, with each offering advantages and disadvantages, and no single technique is appropriate to all situations.

Chapter 4: Laser Direct writing

4.1 Introduction

Laser direct writing (LDW) is an important category within direct write technologies [57]. LDW has become popular due to its unique ability to add, subtract, or modify materials, an ability to apply very precise amounts of energy to small, accurately defined areas and the flexibility to produce 1D to 3D complex structures with high resolution under computer control [57], [85]. Structures are designed and written directly in a single step without the need for masks and the associated long, complex process of traditional lithography techniques discussed in the previous chapter [13], [85]. These characteristics of LDW often result in reduced production costs and fabrication time, which of course creates increased productivity [85]–[87].

AT&T Bell Laboratories and Lawrence Livermore National Laboratory introduced LDW in 1980 by to produce one and two dimensional micro-scale structures for electronic circuits [57]. Joint work of the Max Plank Institute in Germany and the US Naval Research Laboratory in 1990 saw the first use of LDW to pattern three-dimensional structures for wider applications such as photonic crystals and MEMs[57].

4.2 LDW system

A typical LDW system contains three main parts of a laser source, optics to deliver the laser beam and a sample/platform scanning system (Fig. 4.1).

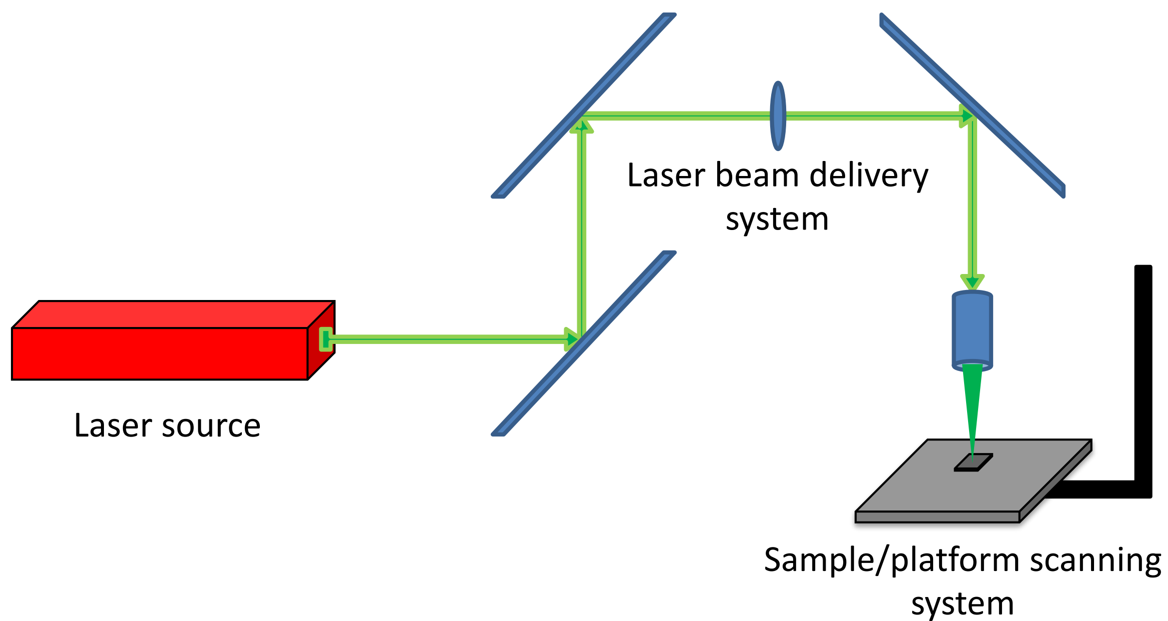

Figure 4.1: *Schematic of the main three parts of a laser direct write (LDW) system: laser source; laser beam delivery system; and sample/platform scanning system.*

The key part of any LDW system is the laser source. These are usually pulsed lasers but high power continuous wave (CW) lasers can be used [85], [86]. A wide variety of lasing media can be used in LDW, including solid state, gas-based and liquid state [14], [88]. There is a corresponding range of laser wavelengths used, from ultra-violet (e.g. 193 nm ArF excimer laser light [89]) to mid-infra-red (10.6 µm wavelength from CO_2 gas lasers) [89], [90]. The material used and process requirements determine the most suitable choice of laser in terms of pulsed or CW, wavelength, pulse energy or continuous power, and pulse duration [85], [88].

A range of optical components can be used to deliver the laser to the working head as well as control the required average power, spot size and wavelength. Optical components may include conditioning lenses, objective lenses, mirrors, filters, prisms, shutters, masks and optical fibres [86].

The third element of any LDW system is the scanning stage. This is usually achieved using galvanometric scanning mirrors to steer the laser beam across a sample or sample motion stages to move the sample beneath a stationary laser beam. The sample motion stages

usually allow linear control of the sample in either two- or three-dimensions [85], [86]. The resolution of the LDW-generated patterns is governed by both the focal spot size and scanning system resolution.

4.3 Laser-material interaction

Pulsed laser beams can be used to remove very small areas of material from a substrate (workpiece) with high accuracy in a process called ablation [88]. The ablation process results from various light-matter interactions but, principally, from a material absorbing sufficient laser energy in a short period of time.

Light that is incident upon a material can be reflected, absorbed and/or transmitted by the material. The manner in which laser light interacts with the material is dependent upon the laser wavelength and frequency, the material's optical properties, surface finish and, for thin films and structures, and sample dimensions (e.g. film thickness) [88].

The reflectivity of normal incidence light is governed by the Fresnel equations [88]:

$$R_s = \left[\frac{E_r}{E_i}\right]^2 = \left[\frac{n_1 \cos(\theta_i) - n_2 \cos(\theta_t)}{n_1 \cos(\theta_i) + n_2 \cos(\theta_t)}\right]^2 \quad (4.1)$$

$$R_p = \left[\frac{E_r}{E_i}\right]^2 = \left[\frac{n_1 \cos(\theta_t) - n_2 \cos(\theta_i)}{n_1 \cos(\theta_t) + n_2 \cos(\theta_i)}\right]^2 \quad (4.2)$$

where R_s and R_p are the intensity reflection coefficients of *s*- and *p*-polarized light, respectively, E_i and E_r are the incident and reflected optical electric fields, respectively, n_1 and n_2 are the refractive indices of the initial and final material, respectively, and θ_i and θ_t are the angles of incidence and transmission, respectively.

The effect of light absorption by a material is described by the Beer-Lambert law [88]:

$$I(z) = I_0 e^{-\alpha z} \quad (4.3)$$

where $I(z)$ is light intensity at depth z in the material, I_0 is the non-reflected incident light intensity and α is the absorption coefficient (usually expressed in units of cm^{-1}) of the material at the incident wavelength of light. Eq. 4.3 shows that $I(z)$ will decay exponentially with depth z, leading to highly non-uniform deposition of energy within a material. However, the laser energy can be approximated to be deposited into a depth of $1/\alpha$ [91].

With metals, the incident photons are most commonly absorbed by conduction electrons causing them to become excited by an amount equal to the photon energy [88], [92]. This excitation energy is then transferred rapidly to the lattice as heat via internal conversion processes [92], [93]. The time required to convert the energy of exited electrons into heat depends on the specific material and the mechanisms it undergoes [88], [94]. However, thermalization times in most metals are typically between 10^{-12} s and 10^{-10} s [88], [95]. Given this and the strong thermal diffusivity of most metals, their response to laser light depends very strongly on the laser beam dwell time or temporal pulse width [88], [92], [96]. Two principal mechanisms can be identified, described as the photothermal mechanism and the photochemical mechanism [96]–[99]. The photothermal response occurs when the pulse width is longer than thermalization time, i.e. for metals a laser pulse width on the order of 10^{-9} s and longer (nanosecond, microsecond and millisecond lasers). In this case, the laser energy is converted into heat before or during any ablation process, with the absorbed laser energy ΔE, fully converting to internal energy ΔU in the material in order to increase the temperature of system, as given by [100].

$$\Delta E = \Delta U = cm\Delta T \qquad (4.4)$$

where c is the heat capacity and m is the mass of the heated target material and ΔT is the resulting increase in temperature.

Photochemical (non-thermal) mechanisms occur in materials irradiated by laser pulses of width 10^{-10} s and shorter (picosecond, femtosecond lasers). In this case, the pulse width is shorter than the thermalization time of the electronic excitation. Therefore, sufficient

absorbed pulse energy will lead to bonds in the material being broken directly without significant change in the system temperature.

The incident laser pulse energy, or rather the incident laser fluence, *F* (optical energy delivered per unit area of sample – in units of J/cm^2), is also very important in determining the nature of the material's response to its irradiation [94]. Making the approximations of negligible lateral thermal diffusion and uniform heating, and using $\rho = m/(At)$, where ρ is density, ***A*** is area and ***t*** is thickness through the sample, Eq. 4.4 can be written as:

$$\Delta E = \Delta U = c\rho A t \Delta T \qquad (4.5)$$

so that

$$F = \frac{\Delta E}{A} = \frac{\Delta U}{A} = c\rho t \Delta T \qquad (4.6)$$

Even when the incident fluence is below the threshold for melting the sample, numerous temperature-dependent processes can be activated, such as reorganization of the crystal structure, sintering of porous materials and rapid transformations to high-temperature crystal phases [88]. These processes can 'pattern' materials by creating local variations in material properties (i.e. LDWm).

When the fluence is at or above the threshold for melting the material, the molten pools can solidify rapidly (quench) without removal of material [88]. Rapid solidification can lead to a variety of results, such as freezing in of defects and supersaturated solutes, formation of metastable material phases, recrystallization of larger grains than in the original material, and redistributed and/or reshaped material [101], [102].

The material can also be removed (ablated) by fluences above another threshold fluence, as will discussed in the following section.

4.4 Ablation

Ablation processes occur at fluences above a threshold that depends on laser parameters such as wavelength and pulse width, and on the thermal and optical properties of the irradiated material [88], [95], [103]. The ablation threshold is the minimum energy needed to remove material from its surface; however, it can be reduced using multiple pulses, due to the cumulative creation of defects [88] as shown in fig 4.2.

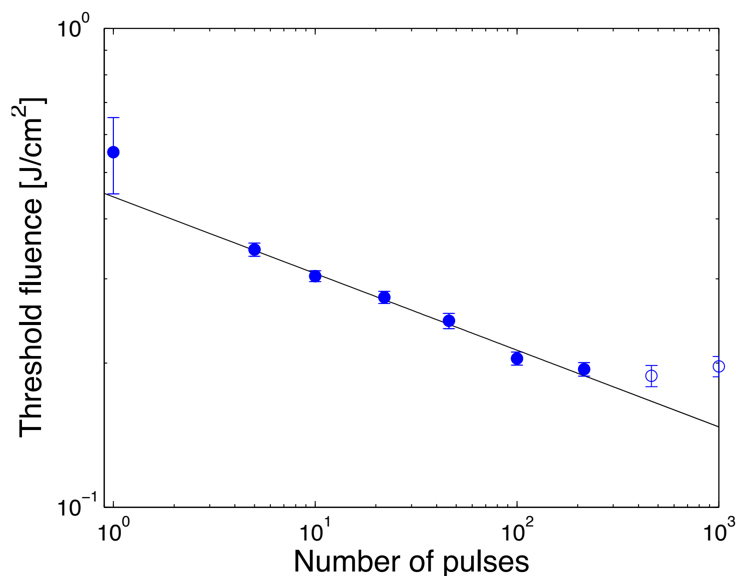

Figure 4.2 *Threshold fluence for ablation of tungsten as a function of the number of 100 fs laser pulses (used with permission from ref* [104]).

The ablation (or etch) rate of material removal also depends on the material and the characteristics of the laser pulse. For example, using a KrF excimer laser (248 nm wavelength, nanosecond-scale pulse length) the ablation rate of bronze and copper samples corresponds linearly with the laser fluence [105], but for silver and silver alloys the ablation rate increases exponentially with laser fluence, as predicted by the Beer-Lambert law (Eq. 4.3) [88], [105]. The depth to which laser energy is deposited is often approximated as $1/\alpha$ [91], but the ablation threshold fluence reduces approximately linearly with the logarithm of α. Using a Nd:YAG laser of similar wavelength but longer pulse length (256 nm wavelength, 23 ns pulse length) the ablation threshold shows different results [105]. However, the ablation rate using femtosecond laser pulses exhibits another type of behaviour, where it increases logarithmically

with applied fluence, typically from 1 J/cm^2 to close to 10 J/cm^2, before becoming linear with fluence [93]. The thickness of a thin film is an important factor in determining the threshold fluence (fig 4.3) [101].

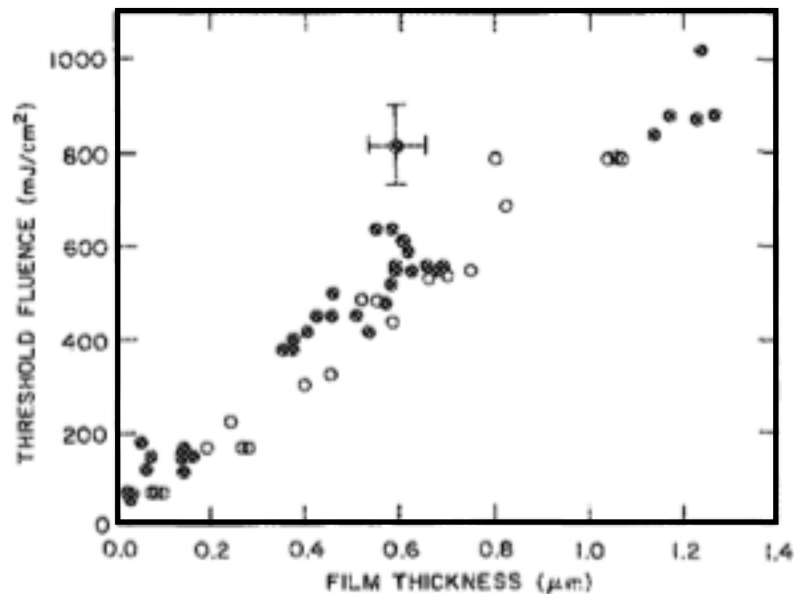

Figure 4.3 *Threshold fluence as function to the film thickness of gold (used with permission from ref* [106].

As described in the previous section, the ablation process using short (typically > 1 ns) pulse lasers (SPLs) of pulse lengths of the order of at least nanoseconds is based on the classical interaction between light and materials; the irradiated material absorbs sufficient optical energy to become heated and transform a volume from the solid to the gas state. The ablation process can be achieved by focusing laser beam on precise area of material surface under a vacuum condition or even at atmosphere. Ablation generally does not occur until the material is taken beyond its melting point [48], [88], [95], when rapid evaporation (ablation) can commence [88], [107]. Gas phase absorption and continued thermalization of electronic excitation can then lead to the formation of a plasma phase, which changes the dynamic reflectivity and absorption of the material system [95], [107]. Fig 4.4 shows the typical stages of ablation process of short pulse.

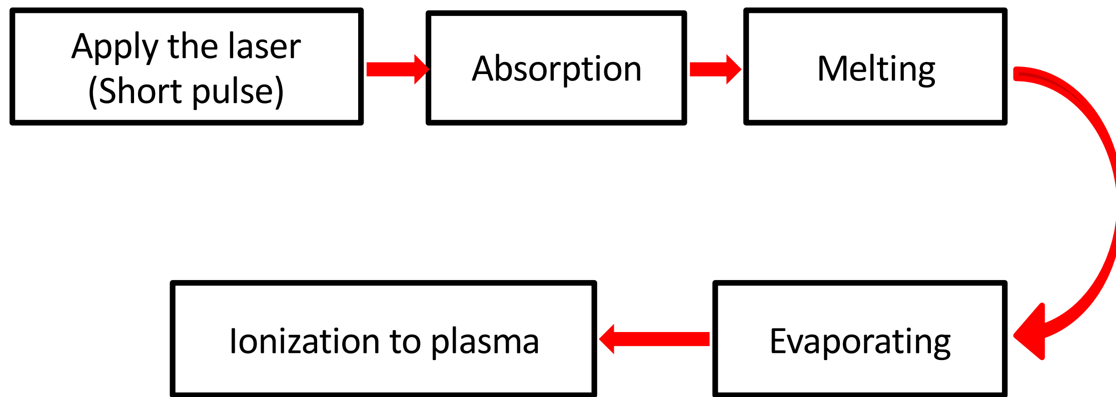

Figure 4.4 *Simple flowchart of the main stages of photothermal ablation with a short laser pulse.*

The mass of ablated material can be calculated as [107]

$$m = \frac{N.E_{pulse}}{c_p.(T_v - T_0) + \Delta H_m + \Delta H_v} \qquad (4.7)$$

where N is number of laser pulses, E_{pulse} the pulse energy, T_v the evaporation temperature, T_0 the ambient temperature, ΔH_m the enthalpy of melting and ΔH_v the enthalpy of evaporation.

In general, laser pulses of ns-µs pulse widths offer high ablation rates but often result in thermal damage to samples [13], [107]. Fig 4.5 shows images of example for the thermal damage around the hole and ablation area.

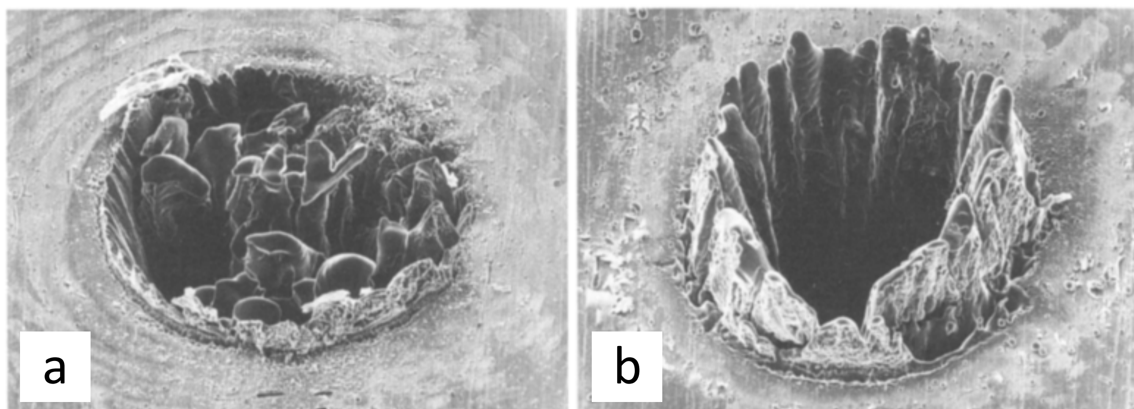

Figure 4.5 *SEM images of: a) ablation and b) drill a) 100 µm steel foil using a nanosecond pulse laser with different fluences (used with permission from ref.* [92]*).*

The ablation mechanism using ultra-short (< 100 ps) pulse lasers (USPLs) is different, being photochemical in nature, and the classical concept of light-material Interaction fails [61],[63]. Atoms in the material experience multi-photon absorption due to the extremely high intensity of ultra-short laser pulses [34],[58],[60],[62]. This results in bonds being broken directly without causing heating [88], although a degree of thermalization occurs on a longer timescale. However, we can understand the material transformation from solid to gas state in step-by-step processes. As in the photothermal mechanism, the material melts in the first step and can boil if the vapour pressure of the molten state exceeds the ambient pressure. Therefore this process will produce a homogeneous mixture of vapour and drops of molten material up to an explosive boiling event, a so called "phase explosion” [95], [107]. The explosively ejected material includes solid and liquid material fragments [88], [107]. The phase of plasma can be reached by optical ionisation of ablated metal. Also, sublimation can occur by heating above the critical temperature[95]. Fig 4.6 shows the typical stages of ablation process of ultrashort pulse.

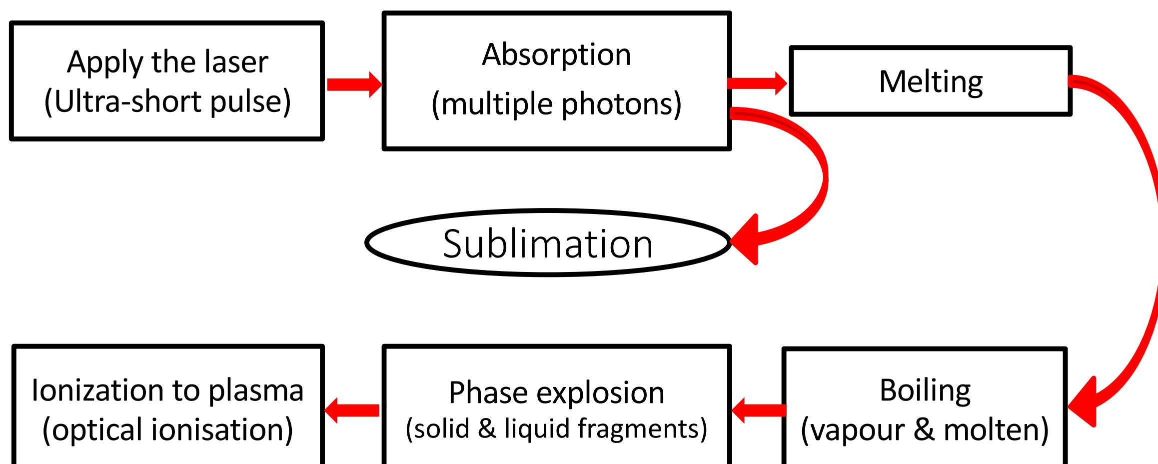

Figure 4.6 *A simple flowchart of the main stages of photochemical laser ablation with an ultra-short laser pulse (typically < 100 ps).*

The mass of ablated material ***m*** can be calculated from the equation which derived from Chichkov’s formula [92], [107];

$$m = N.\rho.A.\alpha^{-1}.ln\left(\frac{F_a}{F_{th}}\right) \qquad (4.8)$$

where: N is the number of laser pulses, ρ the density, A the focal spot area, α the absorption coefficient, F_a the laser fluence and F_{th} threshold fluence for ablation.

The ablation thresholds with ultra-short laser pulses are typically lower than for nanosecond width pulses but with higher instantaneous intensities [109]. The reduced thermalization with ultra-fast ablation processes means that there is a corresponding reduction in heat-affected zones (HAZs) [109] and better control over the ablation region (Fig 4.7).

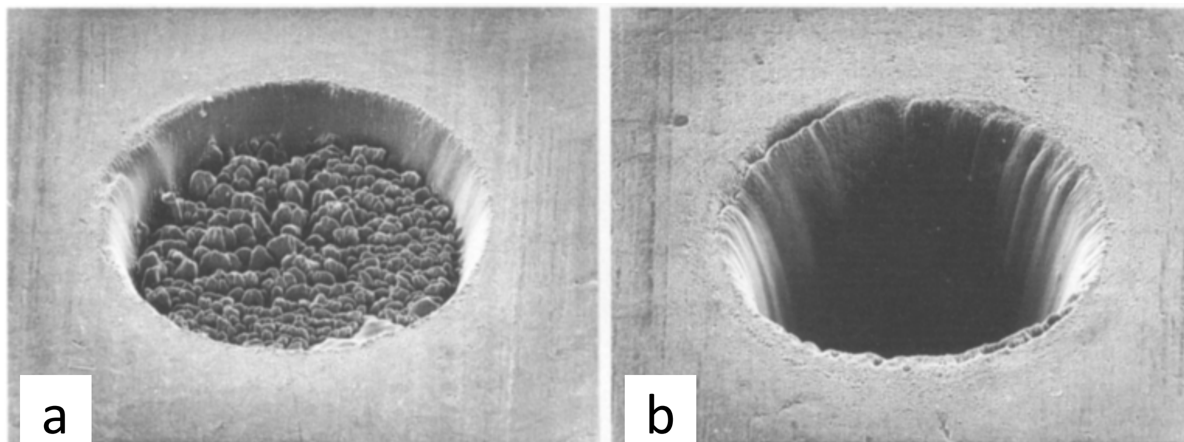

Figure 4.7 *SEM images of: a) ablation and b) drilling of 500 µm steel plate using femtosecond pulse length laser pulses with different numbers of pulses (used with permission from ref.* [92]*).*

4.5 LDW types

LDW can be categorised to three main classes depending on whether material is removed (LDW-), modified (LDWm) or added (LDW+) [13], [14]. In this work, the main processes of relevance are LDW- and LDW+ but all three processes are discussed below.

4.5.1 Laser Direct Writing Subtraction *LDW-*

LDW- is the most common type of LDW and uses either photochemical or photothermal ablation to remove precise areas/amounts of material in cutting [110], [111], drilling [112], [113], scribing and etching [14], [86], [114] applications. LDW- is employed in a wide range of industrial applications, including high-throughput steel fabrication, fabrication of high resolution structures and creation of implantable biomaterials [85]. LDW- can be used to remove all types of material, including organic or inorganic materials, metals or plastic, thin films or bulk. This thesis concerns fabrication of one-dimensional (1D) and two-dimensional (2D) micro/nano-scale magnetic structures from metallic thin films and uses *LDW*- as the primary fabrication route. The parameters that affect this type of LDW are those discussed above for laser ablation (e.g. the laser repetition rate, wavelength, pulse width, pulse energy and spot diameter) as well as the optical and mechanical properties of the thin film and carrier substrate (e.g. glass, quartz or silicon).

4.5.2 Laser Direct Writing Modification (LDWm*)*

Materials properties can be changed permanently in LDWm techniques by application of sufficient fluence to modify morphology or to achieve chemical changes but without removing material. Consequently, the incident fluence used is less than the threshold for ablation. The most common example of LDWm is to expose a photoresist in traditional lithographic techniques [14], [115], [116] as well as to carry out surface modifications such as microstructural, mechanical and morphological changes of metals [117] and polymers [118], and in biological applications [119].

4.5.3 Laser Direct Writing addition (LDW+)

LDW+ describes processes used to form structures by transferring material from a donor sample to a receiver or acceptor substrate [120]. Achieving this requires careful control of pulsed laser properties, the conditions of the transfer process and the mechanical and optical properties of the various materials.

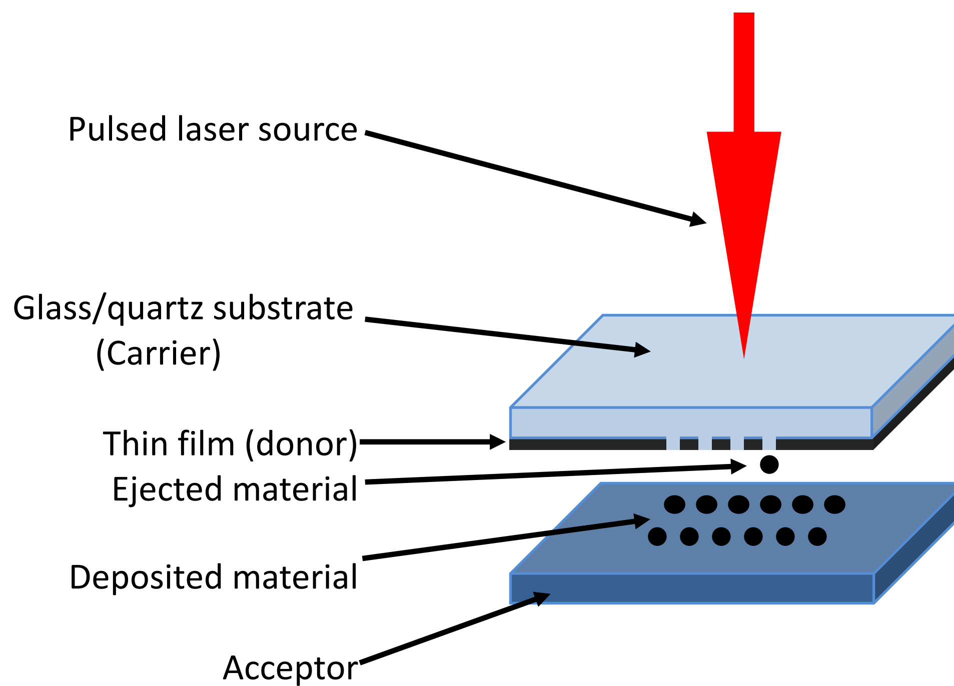

Figure 4.8 Laser induced forward transfer (LIFT) *process.*

The *Laser Induced Forward Transfer* (LIFT) configuration of LDW+ (Fig. 4.8) promotes transfer of ablated material from a donor film to a nearby acceptor/receiver substrate in the direction of the incident laser pulse. Prior to patterning, a donor layer of the required final material is deposited on one side of a transparent substrate (the carrier), which is typically glass or quartz depending on the wavelength of using laser. The donor layer is then positioned in contact or in close proximity to a receiver or acceptor substrate either under a vacuum or in an appropriate atmosphere [13], [121], [122]. The laser beam is focused through the transparent carrier onto the donor layer, where the laser pulse energy is absorbed. The exposed donor material then ablates towards the acceptor substrate, either by evaporation (photothermal ablation) or phase explosion (photochemical ablation) depending on the pulse duration of the laser (see §4.4), and condenses on the acceptor surface. Computer controlled motion of laser beam/sample by a scanning stage or galvanometric scanning mirrors between laser pulses then allows structures to be defined on the acceptor surface.

The first appearance of LIFT was in in 1970 when Levene, M. L. Scott, R. D. Siryj, B. W. transfer black ink from typewriter to a recording medium [123]. But in 1986, J. Bohandy, B. F.

Kim, and F. J. Adrian [121] reemployed *LIFT* to transfer a metal. They transferred accurate amounts of 410 nm thin film of copper from a transparent substrate (donor) to a silicon substrate (acceptor) [121], the narrower wire was achieved in this attempt 40 µm. This was used to repair defects in photomasks and has since become a strong competitor to traditional techniques for applications such as electronic and sensor materials [124] and high viscosity nano-pastes [125].

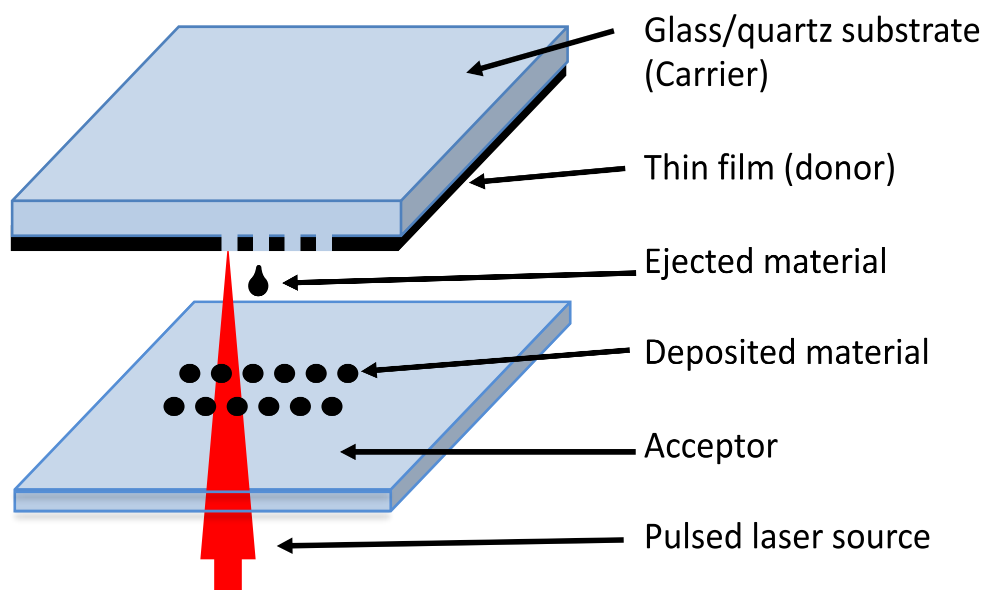

Figure 4.9 Laser induced backward transfer (*LIBT*) *process.*

Alternatively, *Laser Induced Backward Transfer* (*LIBT*) (Fig. 4.9) reverses the direction of material transfer seen in *LIFT*. In this arrangement, the laser pulse passes through a transparent acceptor substrate and is incident on a donor thin film layer or bulk material in contact or close proximity. Ablated donor material is then directed opposite to the laser direction and is deposited on the acceptor substrate. *LIBT* was first demonstrated in 2005 by Mir-Hosseini, N. Schmidt, M. J J and Li, L.[126] to pattern conducting SnO_2 films onto a glass substrate.

Laser Induced Transfer (*LIT*) processes (both *LIFT* and *LIBT*) have been used to transfer a wide range of materials, including metals such as Cu [121], Ag [120], Au [101], [127], [128], Zn [127], Cr [127], [129], Al, Ti, W, Pt and Ni [13], [130], oxides [13], [130], [131], polymers [13], superconductors and semiconductors [13], [130], and diamond and carbon nanotube field emission cathodes [13]. *LIT* has also been used to deposit biomaterials such as DNA [98], cells, tissue and proteins [13], [99], [130]. In 1993, Lee, I., Tolbert, W., Dlott, D., Doxtader, M., Foley, D., Arnold, D., and Ellis, E. [132] transferred PMMA/coloured dyes using the LIFT arrangement with a sacrificial laser layer between the carrier (glass substrate) and donor material to absorb the laser energy and avoid damaging the sensitive biomaterials during the transfer process. The sacrificial layer is called a "*Dynamic Release Layer*" (DRL) and can be a polymer, metal or ceramic [13], [122], [132].

The influence of many experimental parameters was discussed above in §4.3 and §4.4 but there are further consequences of these with *LIT* processes. The laser intensity and fluence must of course be greater than the ablation thresholds to achieve transfer. However, these must be carefully controlled since intensities very close to the threshold result in separated islands or non-adherent particles being deposited while intensities that are significantly above the threshold result in a loss of resolution and increase in unwanted debris being deposited [121], [130].

The laser pulse width dictates whether the ablated process is photothermal processes seem (SPLs) or photochemical (USPLs) (see §4.4) [13], [128], with the former generating molten or gas-phase ablated material and the latter producing a mixture of liquid and solid material (Fig. 4.10). Thus, transferring material using photochemical ablation (with USPLs) offers the benefits of transfer of solid material and reducing the size of Heat-Effected Zones (HAZs) in the donor material.

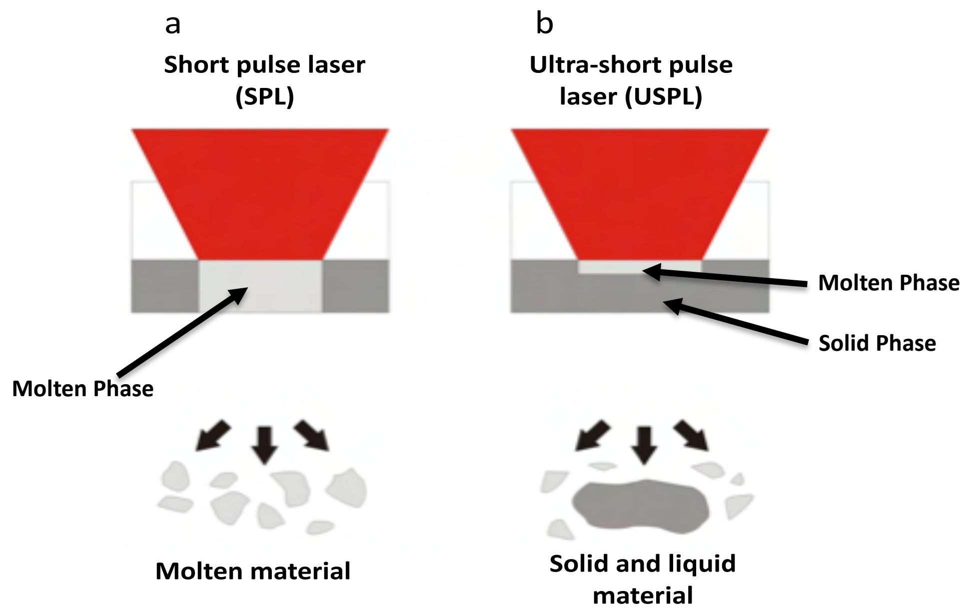

Figure 4.10 *The transferred material: a) molten using SPLs and b) mixture of solid and liquid material fragments using USPLs (used with permission from ref.* [13]*).*

The importance in selecting an appropriate laser wavelength, λ, is not just to ensure that the material has a sufficiently strong optical absorption coefficient to achieve ablation at reasonable laser intensities. Laser wavelength also dictates the smallest focussed laser spot diameter that can be achieved, with the resolution (*R*) of an LDW system given by [65], [133].

$$R = \frac{0.61\lambda}{NA} \qquad (4.9)$$

where *NA* is the numerical aperture of objective lens. Using a laser with a shorter wavelength will, therefore, allow smaller sized features to be created.

The distance between the donor to acceptor strongly affects the shape of transferred elements. Donor-acceptor separations are usually is between zero to 100 μm but larger gaps result in deformed final structures, especially if the transfer process is carried out in a gaseous atmosphere, which leads to a short of mean free path [134], [135]. The velocity of ablated species can be tens to thousands of metres per second but high velocities can result in damage

to the acceptor substrate [98]. The velocity depends on laser parameters such as fluence and pulse width as well as donor material parameters such as film thickness and elastic properties [94], [98]. The thermal conductivity of the acceptor material can have a marked effect on solidification of transferred (molten) material [101]. A low acceptor thermal conductivity will slow down the solidification dynamics of ablated material and may result in splashing and an increase in post-ablation debris. This can be mitigated by increasing the thermal conductivity of the acceptor substrate.

A significant challenge to LIT processes can be the effects of a shockwave generated in the donor material [94], [98], [129]. The shockwave can be generated from explosive loading during ablation (see §4.4), plate impact or application of the laser on one side of the donor substrate [94]. If the shockwave reaches the acceptor it can often result in removal of transferred material. In order to avoid this, LIT processes can be carried out under vacuum with a gap between the acceptor and donor of few micrometres, although the low pressure results in an increase in the velocity of material transferred.

4.6 Summary

This chapter has introduced the key aspects of laser direct writing. A short review of the history of LDW was followed by a discussion of the common elements of any LDW system. Understanding the interaction between the laser beam and target material is very important access to understand the ablation process and the key processes were discussed here. This included considering the ablation processes using either short and ultra-short pulse length lasers and their mechanisms. The three types of LDW a were reviewed and the significant factors that effect on the materials transferring process of LDW+ and LIFT were also covered.

Chapter 5: Experimental methods

5.1 Introduction

This chapter describes the equipment and experimental setups that were used to fabricate and characterize the magnetic structures of interest. The first part deals with sample preparation, including thin film deposition using thermal evaporator. The specific laser direct write (LDW) systems will be illustrated in the third part. The fourth section covers characterization methods, including focussed Magneto-Optic Kerr Effect (fMOKE) magnetometry, optical microscopy, atomic force microscopy (AFM) and scanning electron microscopy (SEM).

5.2 Thin Film Deposition

Thin films of permalloy ($Ni_{80}Fe_{20}$) were deposited on substrates before the later laser processing using a custom-built Wordentec thermal evaporator (Fig. 5.1).

First, substrates of BK7 glass, silicon ((001) orientation n-type doped with native oxide) or quartz were cut to approximately 5 mm x 5 mm and cleaned with acetone (SLS, 95%) and then IPA (SLS, 95%), both in an ultrasonic bath, before finally being dried with N_2 gas. These samples were mounted on the thermal evaporator sample holder using a small droplet of polymethylmethacrylate (PMMA) solution. Once the PMMA was dry, the holder was loaded into the evaporator's sample carousel, which has space for six samples to be coated in separate deposition runs (Fig. 5.1).

Crucibles in the evaporator that hold powders were made of alumina-coated tungsten wires (MegaTech Ltd). The Wordentec thermal evaporator has three positions for crucibles, allowing different source materials to be deposited in one process. Permalloy powder

(Goodfellow, max. particle size: 45micron) was loaded into one of these.

The evaporator was evacuated using a turbomolecular vacuum pump (Leybold Vacuum, TURBOVAC 361, pumping speed 340-370 $l.s^{-1}$) backed by a rotary pump (Pfeiffer Vacuum, UN0 016 B). A bake out was performed during each deposition run by passing electrical current through the permalloy-containing crucible until the permalloy powder melted and started to evaporate. This was used to heat the chamber for 16 to 20 minutes before the current was removed and the pumping continued, achieving a high vacuum (< 10^{-7} mbar).

For deposition, the relevant crucible was again heated with electrical current until evaporation commenced. The sample carousel was used to position the substrate of choice behind an opening in a mask, in line with the evaporated material, and a shutter opened to commence the deposition. The thickness of the deposited material was monitored using a quartz crystal microbalance, with the quartz crystal held adjacent to the substrates in order to ensure exposure to vapour at the same time and distance from the source. Deposition rates of between 0.3 $Å.s^{-1}$ and 0.5 $Å.s^{-1}$ were used throughout this work, which raised the chamber pressure during deposition to approximately 10^{-5} mbar.

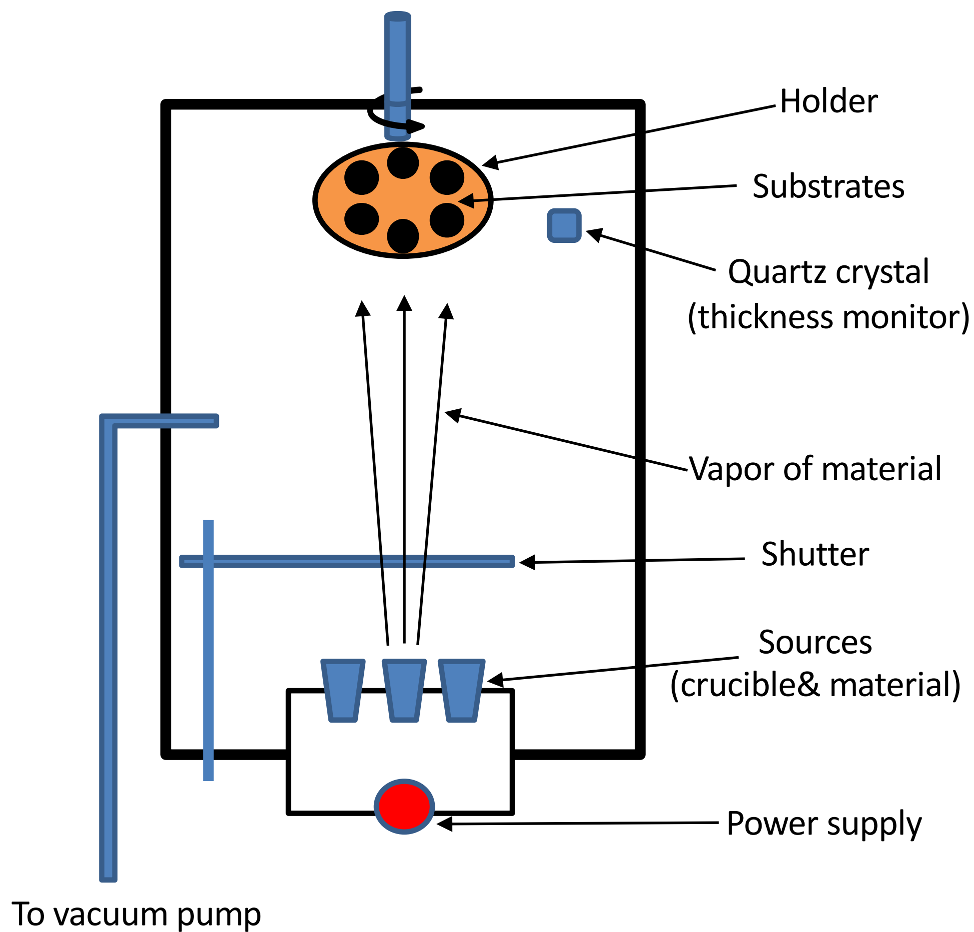

Figure 5.1: *General schematic of Wordentec thermal evaporator*.

5.3 Laser Direct Write (LDW) Systems

Three laser systems were used to produce patterned elements and are described here.

5.3.1 350 picosecond Q-switched laser system

A 350 picosecond pulse-length Q-switched laser system used for direct writing consisted of a diode-pumped solid-state semiconductor laser (Alphalas; PULSELAS-P-355-300), laser beam delivery optics, and a three-axis (x,y,z) scanning stage (Fig 5.2).

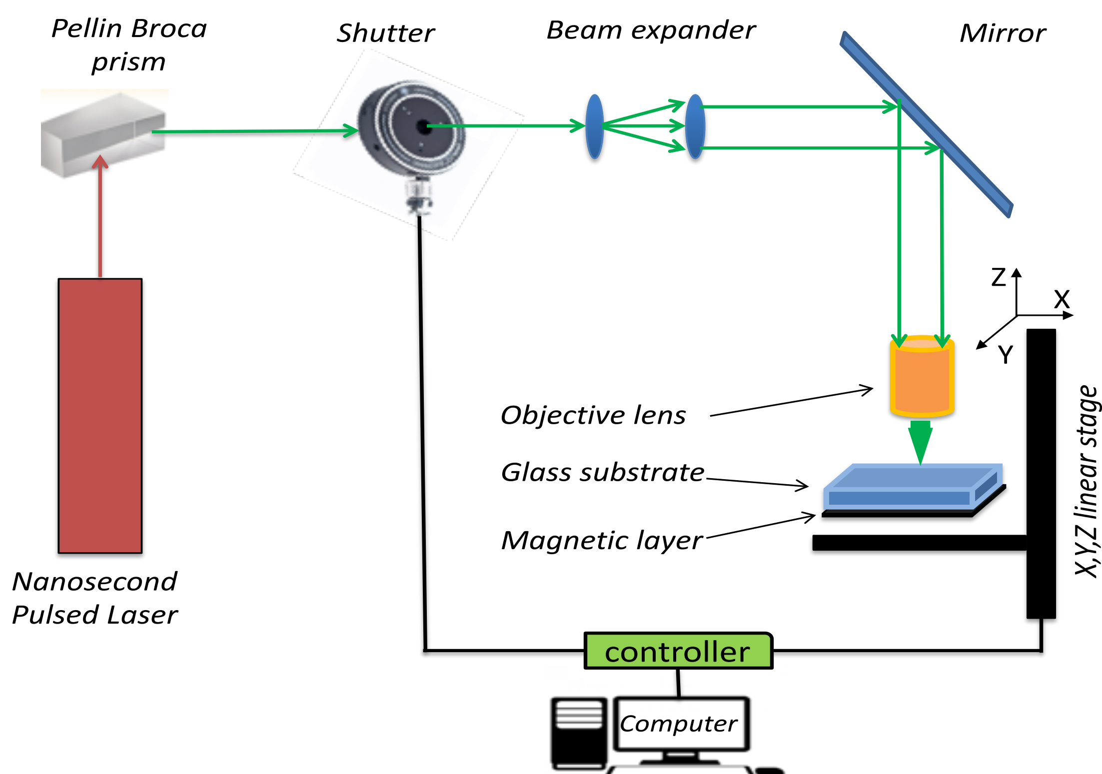

Figure 5.2: *Schematic of the 350 picosecond Q-switch LDW system with main three parts: laser source, laser beam delivery system and sample/platform scanning system.*

The pulsed laser source is passively Q-switched and had three wavelengths available (355 nm, 532 nm, 1064 nm) but this work used only the 355 nm and 532 nm wavelengths. The repetition rate of the laser was 14.2 kHz, the pulse width 350 ps and the beam profile TEM_{00}. The peak power and pulse energy of each wavelength are contained in table 5.1. The pulse energy and the repetition rate were controlled through controlled laser diode driver.

Table 5.1: *Parameters of 350 picosecond Q-switch LDW laser.*

Wavelength (nm)	Peak power (kW)	Pulse energy (μJ)
355	3.43	1.2
532	16.86	5.9
1064	37.14	13

The laser beam delivery optics and sample scanning system consisted of:

a- A Pellin Broca prism (Fig. 5.3) used to separate the required wavelength from the laser beam harmonics.

Figure 5.3: *The Pellin Broca prism and the rotation mount*[136].

b- A shutter (UNIBLITZ Laser shutter LS6ZM2-nl with UNIBLITZ® VCM-D1 shutter driver) used to control the exposure time of the laser beam at appropriate sample positions in order to fabricate the required patterns (Fig. 5.4).

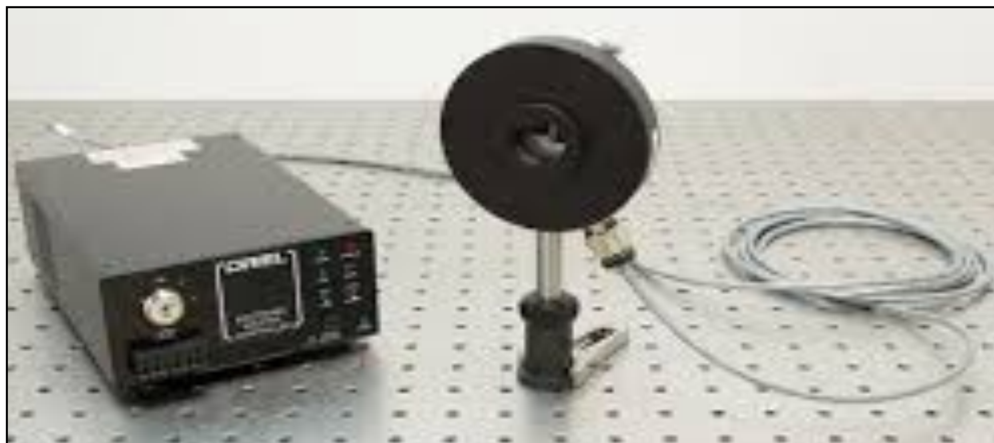

Figure 5.4: *The UNIBLITZ Laser shutter and its driver.*

c- One of two objective lenses were used with the system, having numerical apertures of 0.50 (Zeiss, Objective EC Plan-Neofluar 20x/0.50 M27) with a working distance of 2.0 mm or 0.30 (Zeiss, Objective EC Plan-Neofluar 10x/0.30 M27) with a working

distance of 5.2 mm. The lenses focused the laser beam directly onto the magnetic thin film or through a glass substrate to concentrate laser intensity within spot diameter of <5 µm as discussed in §4.5.3.

d- A scanning stage to move the sample under the laser beam and bring it to the laser focus. A three-axis (x, y, z) system of motorized linear stages (Aerotech ANT130-XY for lateral (x, y) directions and PRO115 for the optical axis (z) direction) allowed the sample to be scanned under computer control to 5 nm precision and at speeds of up to 2 m. s^{-1}. Computer control using the "A3200 Software-Based machine controller" allowed a minimum achievable increment of movement 0.10 µm and a maximum (hardware limited) stage velocity of 300 mm. s^{-1}.

The motion along the optical z axis is used to focus the laser beam, while, the in-plane (x, y) stage was used for scanning the sample to pattern the desired structures.

There was significant sample vibration and deformation in the resulting pattern during the motion of stage especially with high scanning speed (20 mm/s and higher), fig 5.5 shows an image of deform sample because the vibration during the scanning stage motion.

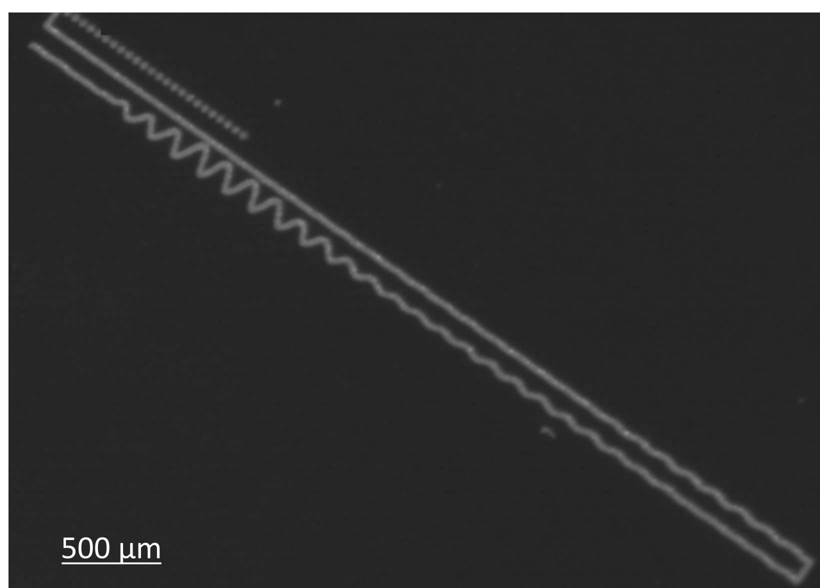

Figure 5.5: *Optical microscopy images of donor substrates for a double wire and 25 separated dots. The zigzag structures resulted from vibrations during sample motion.*

In order to reduce the vibration, a substrate holder (Fig. 5.6) was designed and constructed to hold the substrates (5x5 mm) in place and ensure the correct separation distance along the optical z axis from the lens was maintained in order to preserve a good laser focus. Also, thin layer of rubber was added between the holder and scanning stage to absorb vibration during working. A substrate (or 'donor' in LIFT – see §4.5.3) was placed on two supporting edges and, for LIFT experiments, the 'acceptor' placed inside a polymer sample holder of this platform.

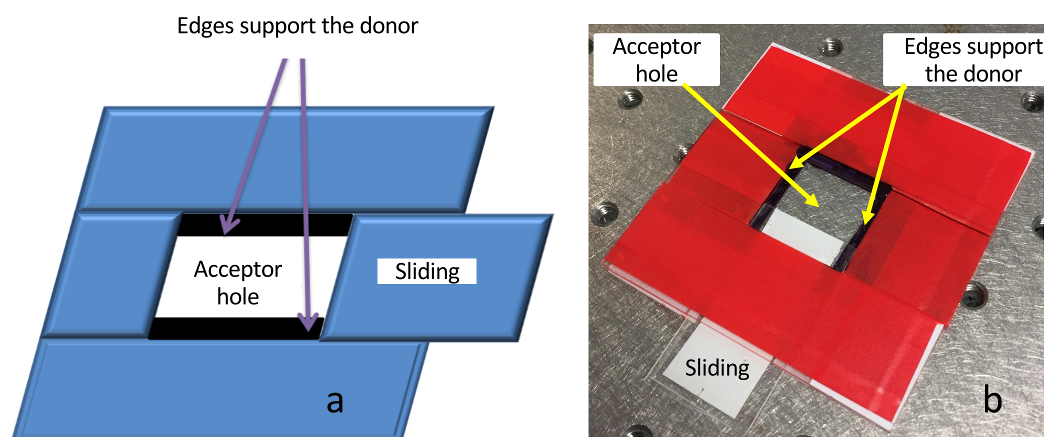

Figure 5.6: *a) The design of the substrate holder. Two edges support the substrates or LIFT donor and keep it at the correct distance from the focusing lens. The sliding piece helps to minimize vibration by hold the donor/acceptor and b) Actual photo of sample holder.*

e- A vacuum cell was designed and constructed to allow LIFT experiments under vacuum, even with the very short working distances of the lenses used (see above). The main parts of the vacuum cell were a metal spring, a vacuum chamber, a glass window, rubber tube and a valve (Fig. 5.7). The LIFT donor substrate (glass or quartz) was placed on the glass window inside the vacuum chamber and the LIFT acceptor mounted behind this on the metal spring. The rubber tube linked the vacuum chamber to the valve. The metal spring pushed the acceptor substrate against the donor substrate and any rubber O-ring used, while allowing the acceptor substrate to be withdrawn and replaced during evacuation.

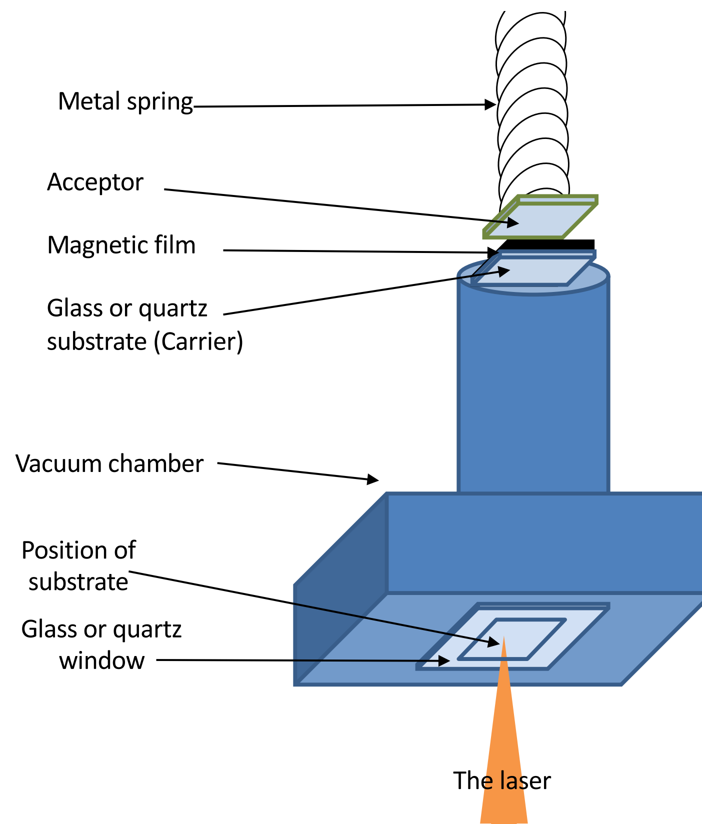

Figure 5.7: *The design and main parts of the vacuum cell.*

The glass platform and the vacuum cell were used for all three laser systems.

5.3.2 800 Picosecond Q-switched laser system

The second laser direct writing system consists of an 800 picosecond pulse-length diode-pumped solid-state semiconductor laser (Alphalas; PULSELAS-P-1064-700-HP), laser beam delivery optics and a three-axis (x, y, z) sample scanning stage (Fig. 5.8).

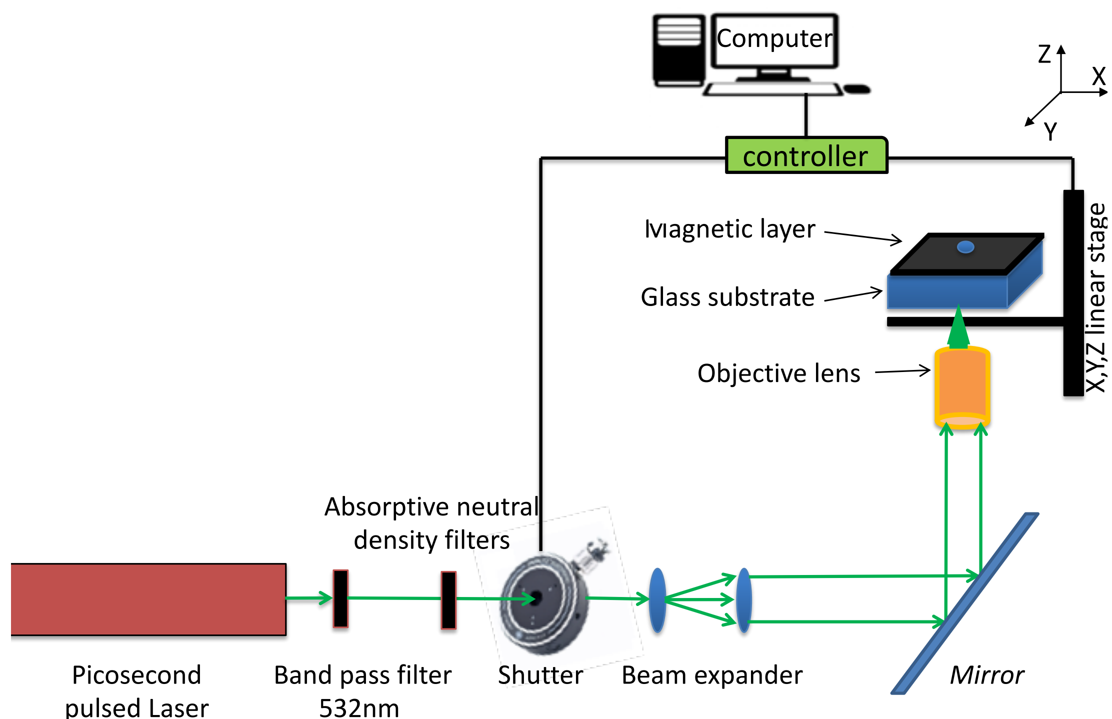

Figure 5.8: *Schematic of the 800 picosecond Q-switch LDW system with main three parts: laser source, laser beam delivery system and sample/platform scanning system.*

The laser has two wavelengths of 532 nm and 1064 nm but only the frequency-doubled wavelength of 532 nm was used. Indeed, experimental measurements showed good agreement with the manufacturing specification.

The pulse energy and the repetition rate were set by controlling the laser diode driver as well as (for pulse energy) using absorptive or reflective optics. The measured average power and repetition rate were controlled by the laser diode driver.

The measured repetition rate, pulse width, pulse energy, peak power and beam profile are shown in table 5.2.

Table 5.2: *Specified and measured parameters of 800 picosecond Q-switch LDW laser.*

Parameter	Specified	measured
Repetition rate	40 kHz	40 kHz
Pulse width	800 ps	632 ps
Pulse energy	5.1 nJ	8.2 nJ
Peak power	6.4 kW	13 kW
Beam profile	TEM_{00}	TEM_{00}

The optics and sample scanning system used to deliver the laser beam consisted of:

a- Band pass filter used to select the frequency doubled 532 nm wavelength only (linewidth = 532 ± 2 nm). This dropped the average power from 225 mW to 5 mW due to removing all unwanted harmonics.

b- A continuously variable metallic neutral density filter was used to attenuate and control the pulse energy (Thorlabs, NDC-50C-4M-A).

c- A shutter, as described for the previous laser system above (§5.3.1).

d- Elliptical mirror (Thorlabs, PFE10-P01) to direct the laser beam to the objective lens and sample.

e- Objective lens with NA = 0.75 (Nikon CFI Plan Apo Lambda 20X/0.75 with working distance 1 mm) to achieve a smallest spot diameter of 1.85 µm.

f- The scanning stage used is same type and model that was described in the previous system (§5.3.1).

5.3.3 System of femtosecond Ti: sapphire laser

The third system used for laser direct writing was a femtosecond pulse length Ti: sapphire oscillator (Spectra-Physics Mai Tai). The system had a maximum pulse energy of 31 nJ, a repetition rate of 80MHz, pulse length < 100 fs and allowed tuning of the emitted wavelength between 690 nm and 1040 nm. The laser beam delivery system and sample/platform scanning system is shown in Fig. 5.9 and consisted of:

a- Variable attenuator to control the average power (Newport, VA-BB).

b- Laser shutter (as used in the systems described in §5.3.1 and §5.3.2 above).

c- Four mirrors to guide the laser beam towards the objective lens.

d- Objective lens with NA = 0.75 (Zeiss, Objective EC Plan-Neofluar 40x/0.75 M27) with working distance 0.71 mm.

e- Scanning stage (as used in previously described systems §5.3.1 and §5.3.2).

This system was used in LIFT experiments to transfer material from a donor to an acceptor substrate.

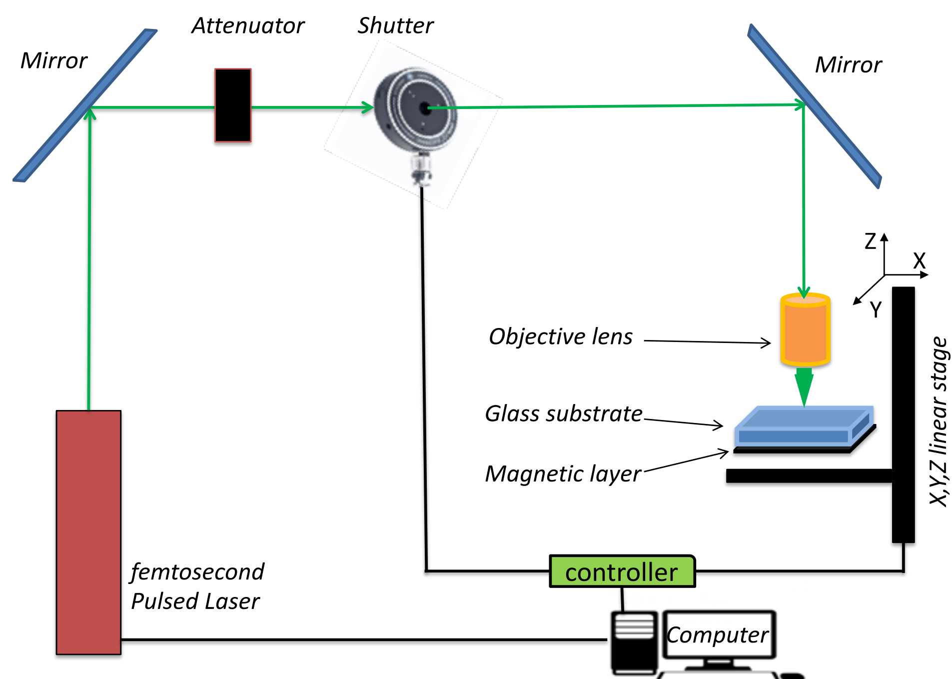

Figure 5.9: *Schematic of the femtosecond Ti: sapphire laser LDW system with laser source, laser beam delivery system and sample/platform scanning system.*

5.3.4 Overlap of laser pulses on samples

The pulses from laser systems with 350 picosecond (§5.2.1) and 800 picosecond (§5.3.2) pulse lengths were made to overlap on samples by controlling the pulse repetition rate and the sample scanning speed.

The laser repetition rate, f, was varied using the laser diode driver by controlling the electric current supplied to the laser's pump diodes. The maximum repetition rate and pulse energy was produced with the maximum laser diode current and reduced with decreasing laser diode current.

The second parameter to control the train of pulses was the sample scan speed ***v.*** The number of pulses per unit length, ***N***, can then be calculated by:

$$N = \frac{f}{v} \qquad (5.1)$$

The total length of exposed area per unit length (L) is given by:

$$L = N * d \qquad (5.2)$$

The total (T) separation (positive values) or overlap (negative values) of pulses per unit length is then:

$$T = -L + 1 \qquad (5.3)$$

With a laser ablation spot diameter, ***d***, the distance/overlap ***D*** between ablation spot edges can be calculated by dividing Eq. (5.3) by Eq. (5.1):

$$D = \frac{T}{N} \qquad (5.4)$$

Finally, by substituting Eqs (5.1), (5.2) and (5.3) into (5.4) obtains:

$$D = \frac{-(N*d)+1}{N} = \frac{1}{N} - d \qquad (5.5)$$

D can take one of the following values:

$$D = \begin{cases} > 0 & pulses\ separated \\ 0 & pulses\ contiguous\ (just\ touching) \\ < 0 & pulses\ overlap \end{cases}$$

The first case (*D* > 0) describes separated ablation spot regions. The second case (*D* = 0) describes ablation spots that just touch without separation or overlap. The final case (*D* < 0) denotes overlapping pulses. These three possibilities are illustrated in Fig. 5.10.

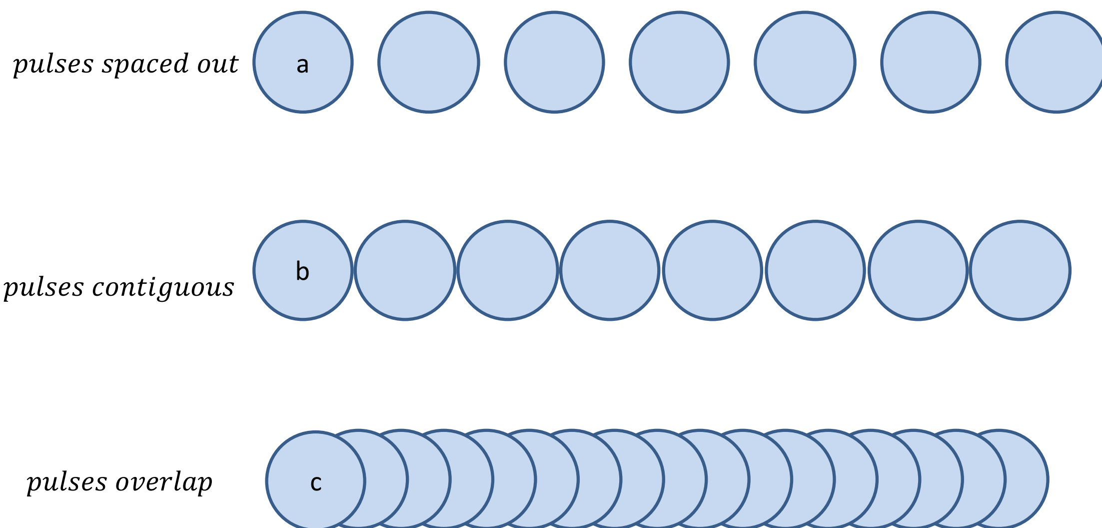

Figure 5.10: *The three possibilities of distances between ablated pulse edges: a) separated, b) contiguous and c) overlapping.*

Combining Eqs 5.1 and 5.5 allows the required scan speed to achieve a particular ablation spot separation or overlap:

$$v = f(d + D) \qquad (5.6)$$

For example, to achieve a separation of D= 5 µm between the spot edges with diameter of $\boldsymbol{d}$ = 4 µm and the repetition rate $\boldsymbol{f}$ = 20kHz, the required scan speed is $\boldsymbol{v}$ = 180 mm.s^{-1}, while to get overlap of 50% (distance between centres of 0.5$\boldsymbol{d}$; Fig. 5.11), the required scan speed becomes 40 mm.s^{-1} and for contiguous pulses the speed is 80 mm. s^{-1}.

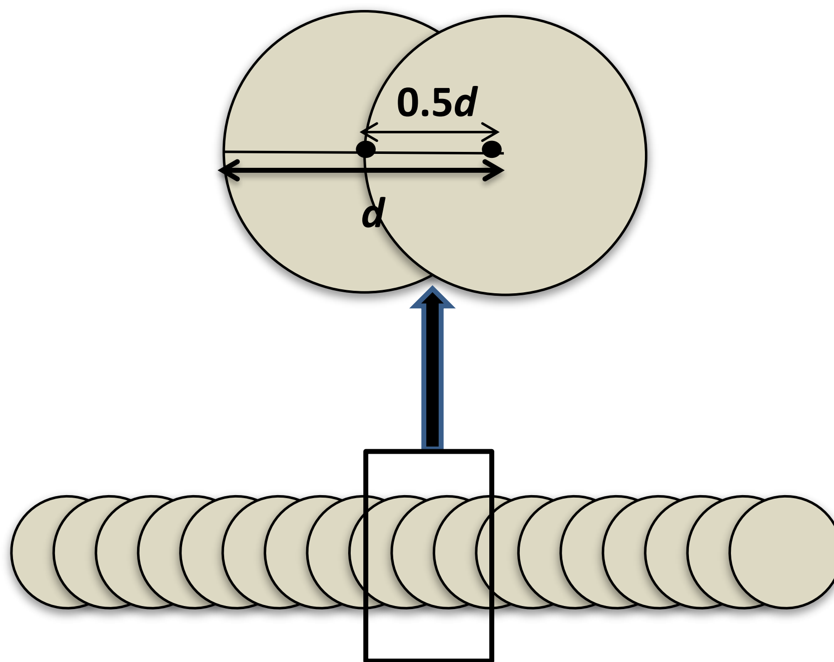

Figure 5.11: *Diagram of example for controlling the overlap between the laser pulses, here shown as 50% overlap by way of example.*

5.4 Fabrication of magnetic structures

Nano/micro-scale magnetic structures were fabricated using the three laser systems described in §5.3 for subtractive and additive laser direct writing (LDW- and LDW+, respectively). The approaches for achieving LDW- and LDW+ are described below.

5.4.1 LDW- of magnetic structures

LDW- was employed to fabricate 1D and 2D nano/micro-scale magnetic structures using the system of 800 picosecond Q-switch laser (§5.3.2). Substrates supporting a $Ni_{80}Fe_{20}$ (permalloy) 90 nm thin film were cut using a diamond scribe to approximately 5 mm x 5 mm to fit into the fabrication system sample holder (§5.3.1-d) and to allow it to be held in the focussed magneto-optical Kerr effect (fMOKE) magnetometer (see §5.5.1 below). The magnetic structures were designed using a computer script to control the sample scanning stage during laser exposure. In LDW- structures were patterned by removing unwanted areas of thin film material from the substrates by laser ablation. The remaining non-ablated material then formed the (magnetic) structures, e.g. as shown in Fig. 5.12. The magnetic structures were patterned with 30% overlap between laser pulses. Overlapping laser pulses meant that isolated magnetic structures could be defined; for example, a magnetic wire could be formed between separated ablation lines, as shown in fig 5.12. This resulted in an undulating edge profile definition in the patterned structures that depended on the pulse overlap ratio.

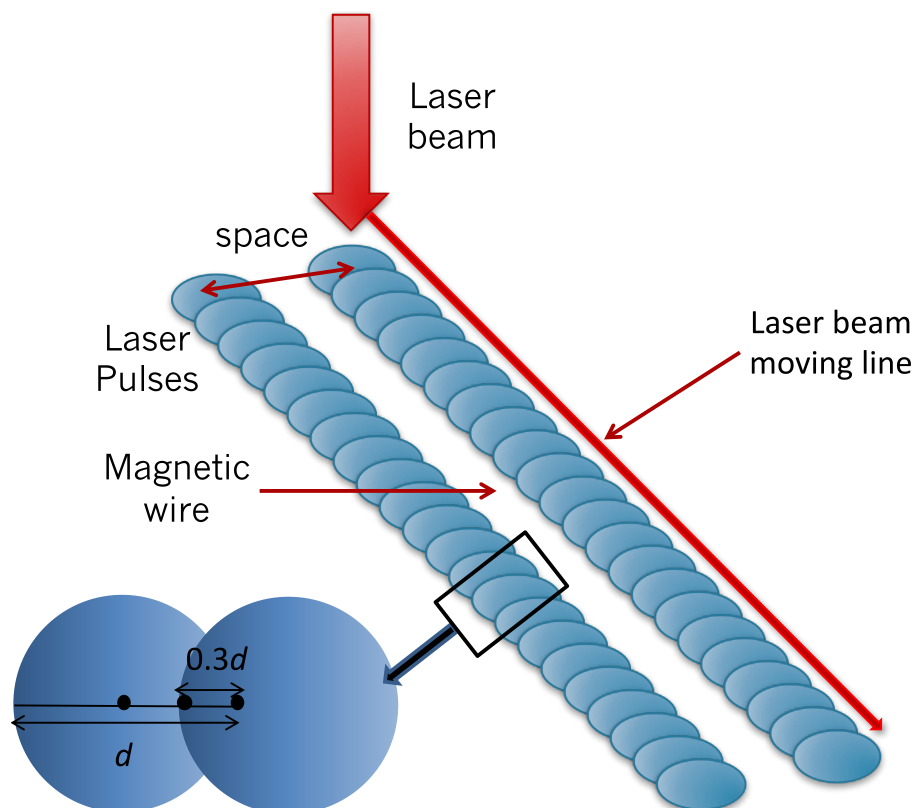

Figure 5.12: *Diagram of the formation of wires by removal of unwanted areas of a film with an overlap of 30%. Here, a wire is formed between the two (blue) ablation lines.*

The experimental conditions used to achieve LDW- were:

a. Pulse repetition rate approximately 6 kHz. The 800 picosecond laser was set at this frequency by selecting a laser diode driver current of 1.33 A.
b. Pulse energy (at a laser diode driver current of 1.33 A) was attenuated to 10 nJ using absorptive neutral density filters.
c. The 0.75 NA objective lens allowed and conditions *a* and *b* above achieved a laser ablation spot diameter was 1.85 μm and less with thin film thickness of 90nm (fig 5.13).

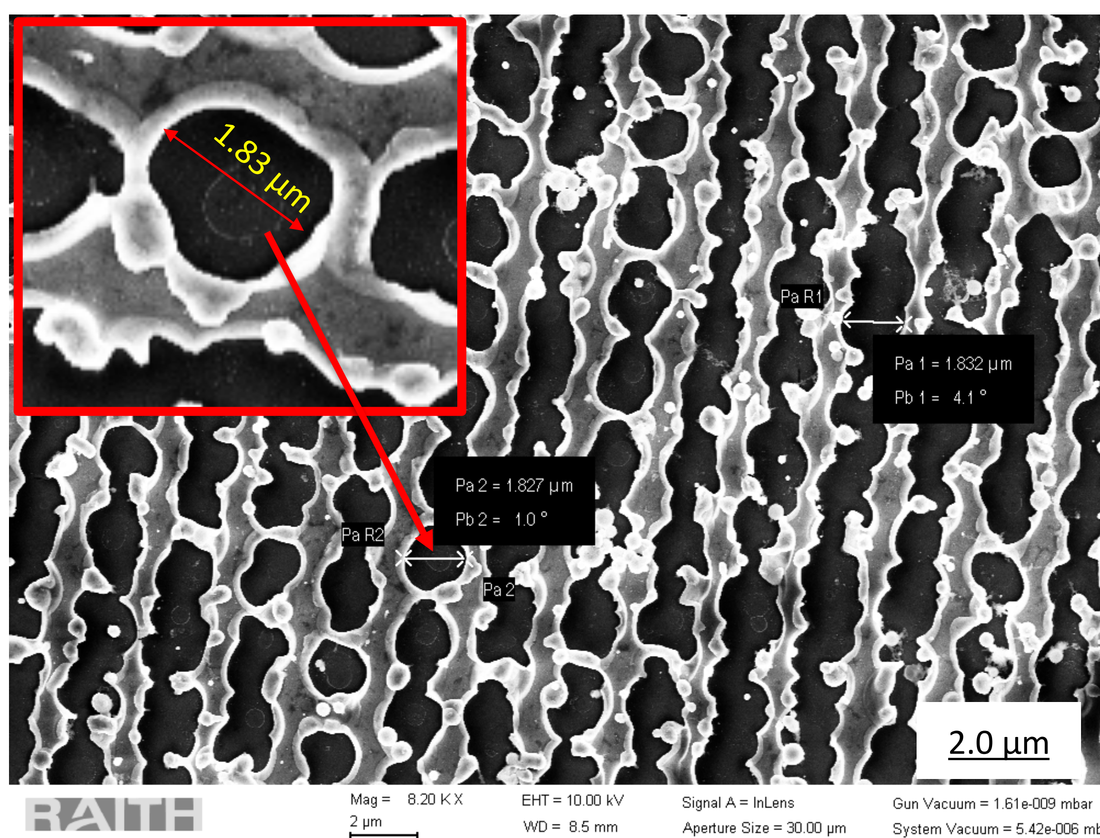

Figure 5.13: *Scanning electron micrographs of separated ablation spot achieve with a fluence of XX mJ.cm^{-2}. The inset shows a single ablation spot with diameter of 1.83.*

d. Sample scan speed of 7.5 mm. s^{-1}. This scanning speed have been used for all experiments of LDW- except the fabrication of structures for magnetoresistance (MR) measurements.

The magnetic structures were patterned in a single step under atmospheric conditions and room temperature, i.e. there were no special requirements for carrying out the fabrication process. The laser beam was applied through transparent (glass) substrates onto the rear of magnetic thin films, as shown in fig 5.14.

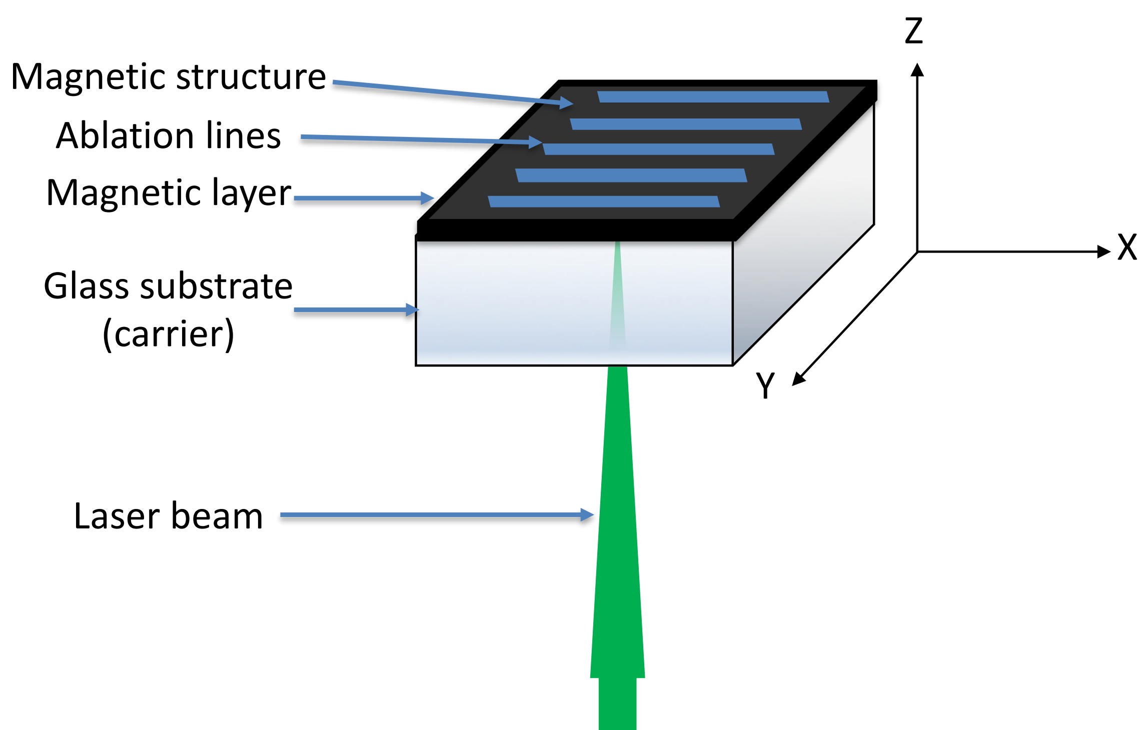

Figure 5.14: *Sample arrangement to achieve subtractive laser direct writing (LDW-). The focused laser beam passes through a glass substrate onto the rear of a magnetic thin film, where patterning takes place. Ablated lines (blue) and non-ablated regions (black) are shown to illustrate the patterning process.*

One-dimensional (1-D) structures were fabricated by creating arrays of 4 mm long magnetic (permalloy) wires of different widths. These wires connect at their ends to the wider film as shown in fig 5.14. The laser shutter was used to align the laser exposure to the sample movement, for example to allow the laser beam to pass during the motion of stage along the ablation line axis (the *x*-axis) but block it during motion of the transverse stage (the *y*-axis) between *x*-axis sweeps.

Wire width was controlled by varying the spacing between ablation lines along the ***y***-axis between 2 µm and 8.6 µm. 76 ablation lines were written for each structure to create an array of 75 magnetic wires. This large number of magnetic wires gave an array width of at least 150 µm and was selected to reduce sensitivity to the wider thin film during fMOKE measurements of the arrays.

Appendix A contains the A3200 software code for design and fabrication of the magnetic wire arrays.

Arrays of two-dimensional (2-D) magnetic structures included patterns of squares, rectangles with a range of aspect ratios, and rhombic structures. These were all fabricated under the same ablation conditions as described above.

The arrays of square magnetic elements with size of 1.9 µm x 1.9 µm (aspect ratio, *AR* = 1.0) were patterned using successive laser ablation scans in orthogonal directions. The patterning process started by creating 76 ablation lines along the ***x***-axis, as described above for the magnetic wire arrays. The sample was then moved along the ***y***-axis to obtain another 76 ablation lines in this direction, overlapping with the original ***x***-axis lines (Fig. 5.15). This required the starting point of ablation along the ***y***-axis to be from exactly the same point as the start of the ***x***-axis ablation lines to fill the array with the desired structures. The centre-to-centre spacing of the ablation lines along both the ***x***- and ***y***-axes was 3.75 µm (including the spot diameter of 1.85 µm) to leave separated square elements between the ablation lines.

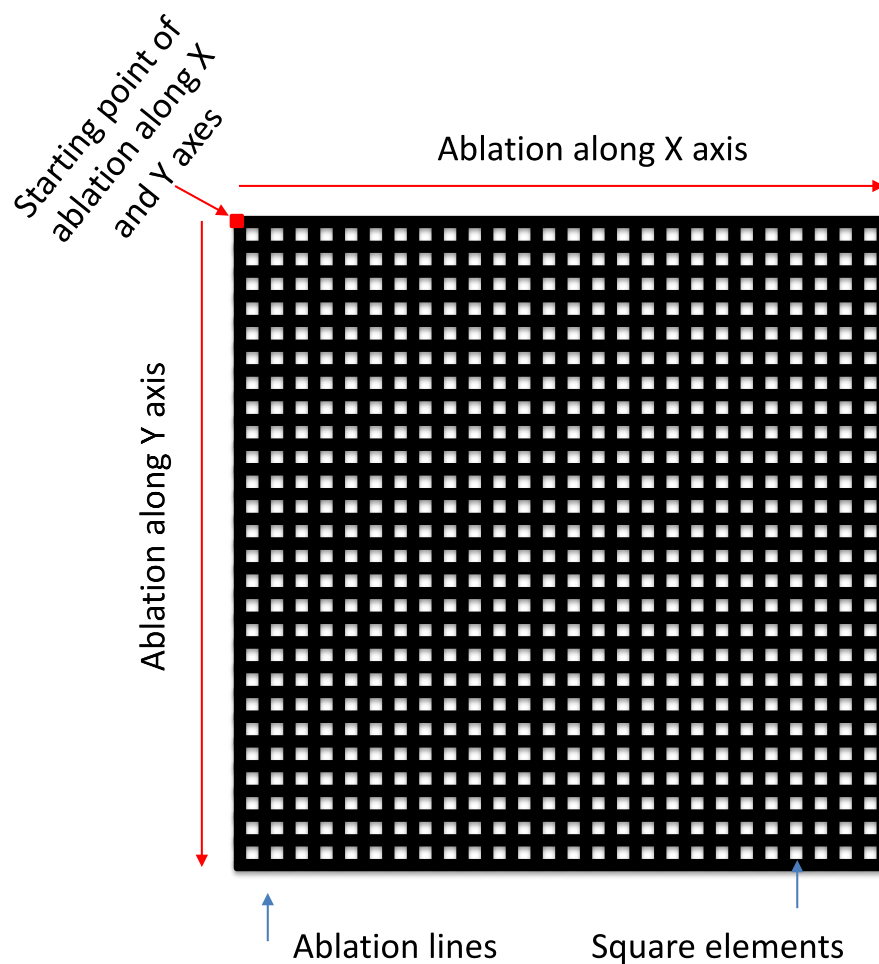

Figure 5.15: *Illustration of fabrication of array of square elements patterned by laser ablation lines along the x and y-axes. The red point shows the starting point for both scan directions. The black regions are ablated areas and the light regions are the non-ablated square elements (magnetic structures).*

Arrays of rectangular elements with range of aspect ratios, *AR* = 1.5, 2.1, 2.6, 3.1 and 4.2 were patterned by same method used for square structures described above but with a larger spacing between ablation lines along the *y*-axis, increasing by 1 μm for each increase in *AR*.

Appendix B contains A3200 software code to design and fabricate the arrays of square and rectangular elements.

Rhombic structures with aspect ratio of major-to-minor axes of 3.6 were patterned using laser ablation along two non-orthogonal directions (Fig 5.16).

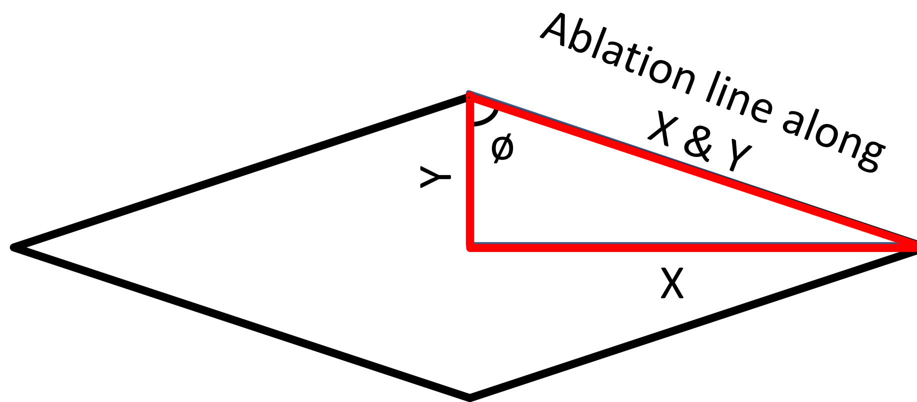

Figure 5.16: *The aspect ratio of rhombic magnetic structure.*

Neither scan direction was along the ***x***- or ***y***-axis exclusively, but required control of stage controllers along both directions simultaneously. The distance moved along the ***x***- and ***y***-directions defines the aspect ratio of the defined rhombuses and allows the internal angle, ϕ (defined in Fig. 5.16), to be defined given by:

$$tan\, \emptyset = \frac{x}{y} \qquad (5.7)$$

For example, to achieve rhombic elements with aspect ratio of 3.0 required sample movement during ablation of 1 unit along the ***y***-axis and 3 units along the ***x***-axis, giving an internal angle ϕ = 71.5°.

The patterning process started by creating 76 parallel angled ablation lines, similar to those created above for fabricating magnetic wires. The second step involved creating 76 ablation lines with the sign of the ***y***-axis movement reversed while maintaining identical ***x***-axis motion. The size of the rhombic elements was controlled with the separation between the ablation lines. This process is summarised in Fig 5.17.

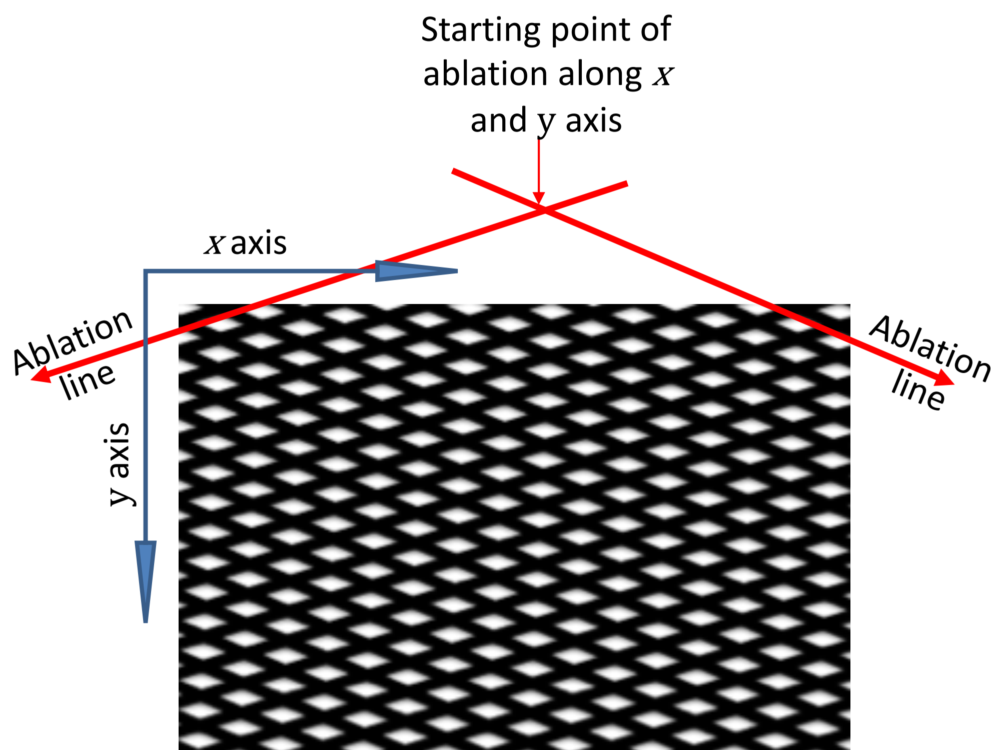

Figure 5.17: *The schematic of the patterning process of the rhombic structures, the black regions are ablation areas and light areas are the rhombic element (magnetic structure).*

Appendix C contains A3200 software code to design and fabricate the arrays of rhombic elements.

Finally, magnetic structures for anisotropic magnetoresistance (AMR) measurements were patterned from 25 nm thick permalloy thin films. The permalloy substrates were cut to 7.0 mm x 5.0 mm to fit the cell of the AMR measurement apparatus (see §5.5.2 below) to reduce the fabrication time. The fabrication process was carried out with the maximum laser pulse repetition rate (40 kHz), a pulse energy of 1.3 μJ and scanning speed of 6.0 mm. s^{-1}. This process was similar to process of fabricating one-dimensional (1-D) structures but by removal of all unwanted magnetic material between ablation lines except wire areas and contact regions at each wire end. This was achieved by removing 0.5 mm wide (along the x axis) segments of film with ablation lines separated along the y axis by 1.5µm (smaller than the focal spot diameter) to ensure removal of all unwanted material in this region, as shown in fig 5.18.

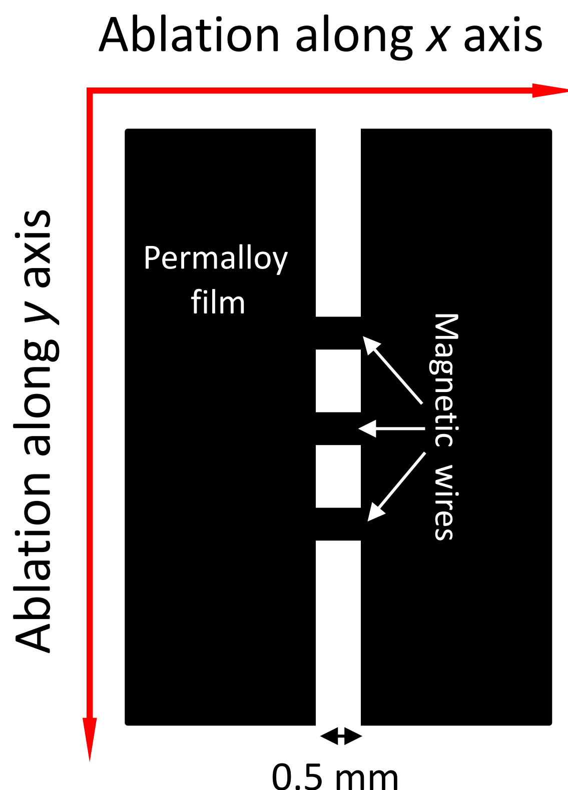

Figure 5.18: *The schematic of the patterning process of the magnetic sensors: a) with single wire and b) with multi wires. The long of all wires is 0.5 mm but with different widths (aspect ratio).*

The length of wires was selected to be 0.5 mm to allow shape anisotropy effects to be investigated while being sufficiently small to allow electrical contacts for AMR measurements to be applied (The AMR measurement system includes a linear array of four needle probes each separated by 1 mm). Variation of wire width was achieved by separating the ablated segments from each other by different amounts, and allowed wire aspect ratio to be explored, as will be discussed in chapter 7.

5.4.2 LIFT for magnetic structures

Laser-induced forward transfer (LIFT) was used to fabricate micro/nano-scale magnetic structures using the 350 picosecond Q-switched (§5.3.1), 800 picosecond Q-switched laser system 9§5.3.2) and femtosecond Ti: sapphire (§5.3.3) laser systems. The structures included arrays of dots and wires. The structures were designed and patterned using a similar process to that for LDW- described above (§5.4.1).

The structures were transferred directly from a donor substrate to an acceptor substrate in a single step under atmospheric or vacuum conditions and room temperature. The following experimental parameters could be varied:

1- Distance between the donor (D) and acceptor (A) substrates.

   Preliminary attempts using the 350 picoosecond pulse length laser system to transfer a permalloy thin film were made by varying the distance between D & A from 0 – 100 µm to determine the optimum substrate separation. For distances more than 40 µm, the separation was achieved by inserting tape between the substrates. Separations less than 40 µm were made by adding a layer of spin-on photoresist discussed in §3.2.1.1 or by drawing a frame around the acceptor using a permanent ink pen for distances less than 10 µm. The separation of 40 µm and above has been measured using Vernier and less 40 µm by AFM.

2- Thin film thickness

   Different thicknesses of permalloy thin films of 20 nm, 40 nm 50 nm, 70 nm or 90 nm were transferred with all laser systems.

3- Pulse energy

   Each thickness of thin film was transferred by varying the pulse energy to determine the transfer threshold. The ranges of pulse energy used to transfer permalloy films are contained in table 5.3.

Table 5.3 *The ranges of pulse energy used to transfer permalloy films for each laser system.*

Laser	P. E min (µJ)	P. E max (µJ)
350 picosecond	5.6	13
800 picosecond	0.060	3.5
Femtosecond	0.0065	0.0055

4- Material of acceptor

   The magnetic material was transferred onto glass and silicon acceptor substrates. Wire arrays were fabricated with wires either separate or continuous. The separate wires

were transferred using similar program code to that used for LDW- (§5.4.1; Appendix A) but for ten wires only. A continuous structure was transferred by keeping the laser shutter open throughout the whole fabrication process, including motion in the ***y***-direction between long wire definition, resulting in a serpentine-like structure (Fig. 5.19). For these structures, the movement along the ***y***-axis determined the distance between defined wires only and did not specify the width of the wires used with LDW-structures. Unlike with LDW- (§5.4.1), the width of LIFT wires was controlled directly by the laser spot diameter.

LIFT experiments used parameters of scanning speed = 1.5 mm. s^{-1}, laser pulse repetition rate = 14.2 kHz, and laser spot diameter ~ 5 µm, resulting in about 9.5 pulses/µm and a 98 % pulse overlap on samples.

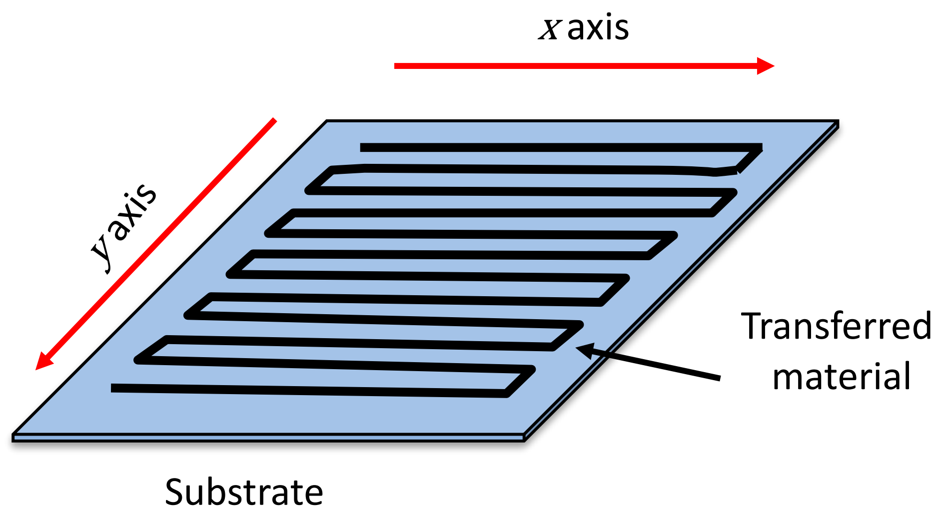

Figure 5.19: *Schematic of the continuous wire structures fabricated by the LIFT process. The black line indicates transferred material.*

Arrays of dots were fabricated by LIFT by applying a specific number of pulses on single points of a thin film. The number of pulses at each point was controlled using a 'Dwell' software command to maintain the sample position for a period of time, t. The number of pulses at each point, n, can be calculated as:

$$n = ft \qquad (5.8)$$

The shortest dwell time possible with the laser shutter and control software was 1 ms, which for f = 5 kHz gives 50 pulses at each point.

Movement along *x*- and *y*-axes was used to control the distances between the dot centres. Fig 5.20 shows the process of patterning arrays of dot structures.

Appendix D contains A3200 software code to design and fabricate the arrays of dots using "Dwell" command.

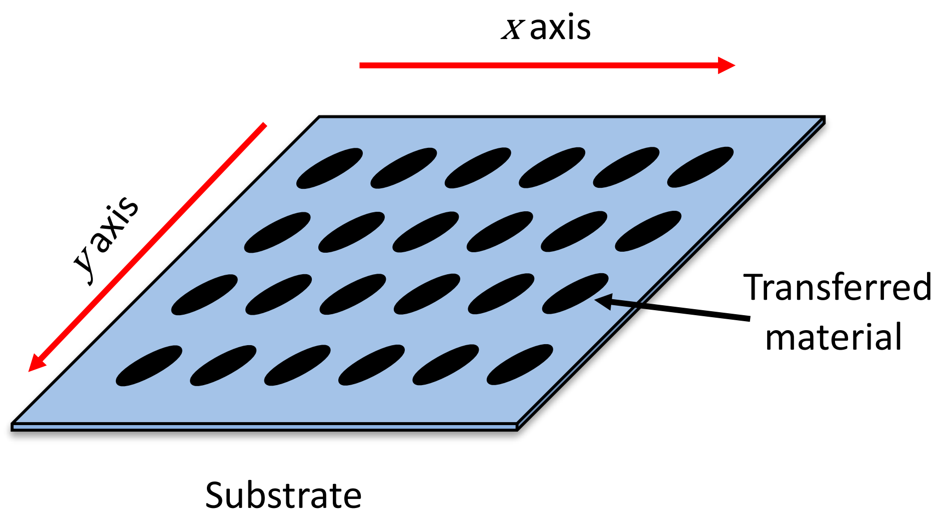

Figure 5.20 *Schematic of dot array patterning.*

5.5 Measurements and characterisation

The fabricated nano/micro-scale structures were subjected to magnetic characterisation by: focused magneto-optic Kerr effect (fMOKE) magnetometry and anisotropic magneto-resistance (*AMR*) measurements; and structural characterisation by: optical microscopy; atomic force microscopy (AFM) and scanning electron microscopy (SEM).

5.5.1 Focused Magneto-Optic Kerr Effect (fMOKE) magnetometry

The focused magneto-optic Kerr effect (fMOKE) system was used for obtaining magnetization hysteresis loops from thin films and structures.

In 1877, John Kerr discovered the magneto-optic Kerr effect (MOKE) [137] when describing the phenomenon of change of polarized light reflected from a magnetic surface [10], [138]. MOKE describes the rotation of polarization of light reflected from a magnetic surface. The degree of rotation depends on the strength and direction of the magnetization, as well as on material-specific optical constants. Generally, the extent of rotation is just a few tenths of a degree at most [10]. MOKE can be understood through three configurations: polar, longitudinal and transverse [137], [138] as shown in fig 5.21.

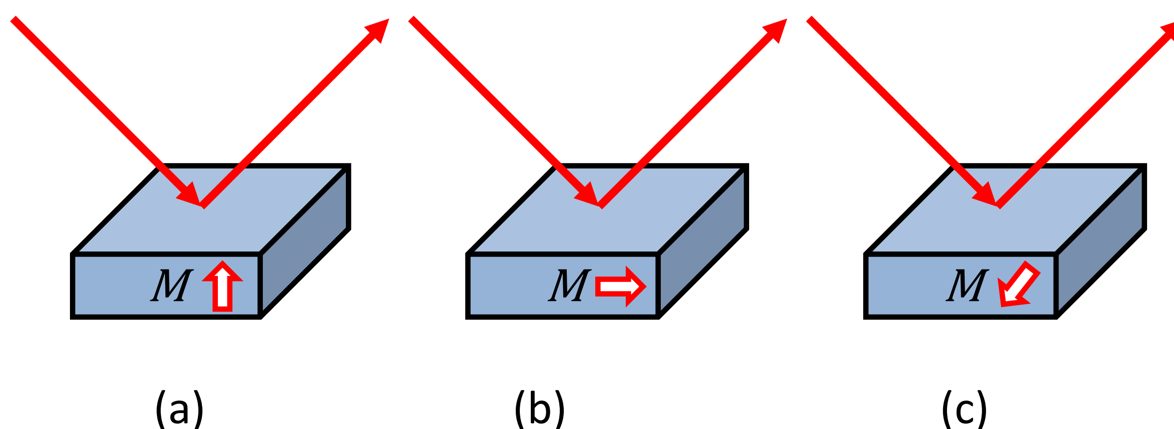

Figure 5.21: *Illustration of three different optical and magnetic geometries of MOKE measurements: a) polar configuration, b) longitudinal configuration and c) transverse configuration.*

In the polar configuration, the magnetization M is perpendicular to the sample surface. In the longitudinal configuration M is in the sample surface and parallel to the optical plane of incidence. In the transverse configuration, the M is in the sample surface and perpendicular to the optical plane of incidence (and in this case, MOKE results in a change in light intensity, not polarization rotation). The rotation of polarization (seen in the longitudinal and polar configurations) does not lead to a change in the reflected laser intensity directly but this may be detected via polarization optics.

The fMOKE system used detects these changes in polarization and pick up the changes

of intensity.

Figure 5.22 shows a schematic of the fMOKE system used here. In brief, a continuous wave (CW) laser beam (Coherent Verdi V-2, wavelength 532nm) was polarized with a Glan-Laser prism polarizer and focused to a full-width-at-half-maximum (FWHM) spot size of 4 µm x 7 µm on a magnetic sample. However, the spot had significant intensity beyond this, which is why the structure array samples were made with 75 wires to avoid significant signals from the surrounding thin films being detected (see §5.4.1).

Samples were mounted on a motion system for in-plane translation and positioned between electromagnet pole pieces to be subjected to an external magnetic field. The space between the two electromagnets poles is relatively small, therefore, samples are restricted to sizes no larger than approximately 5 mm x 5 mm (see §5.4.1). The reflected light from the sample surface passed through an objective lens to collimate the beam.

A 90:10 pellicle beam splitter allowed the majority of the reflected beam to pass through a quarter-wave plate to remove polarization ellipticity and an analyzer (to convert polarization changes into intensity changes) before detection by a Si photodiode. The lower intensity beam from the beam splitter passed through a low-pass filter (to remove most of the laser wavelength light) and, with a collinear white-light source, allowed the sample surface to be imaged on a CCD camera.

The optical (MOKE) signal was recorded during application of a time-varying magnetic field via the electromagnet using an oscilloscope. These signals were then plotted parametrically to obtain a magnetization hysteresis loop.

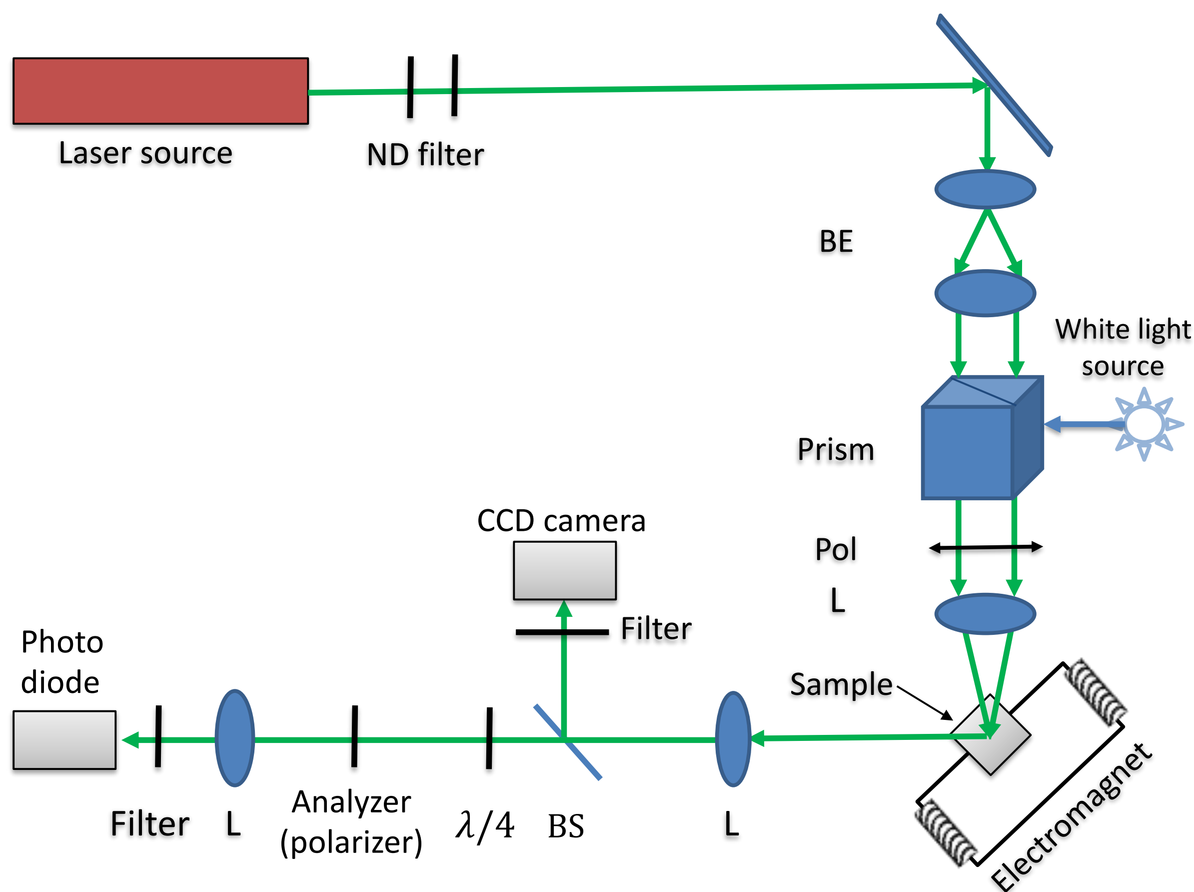

Figure 5.22: *Sketch of the optical layout of the fMOKE system. Abbreviations according to the precedence in the sketch are: ND, neutral density filters; BS, beam splitter; Pol, polarizer; L, lens; BS, beam splitter; and λ/4, quarter-wave plate respectively.*

5.5.2 Anisotropic magneto resistance (AMR) system.

Magnetoresistance (MR) describes the change of electrical resistance of a material when an external magnetic field is applied [17] and can be calculated as [10]:

$$MR = \frac{R_H - R_0}{R_0} \qquad (5.9)$$

where R_H is the resistance during application of the magnetic field and R_0 is the resistance without a magnetic field. Anisotropic magnetoresistance (AMR) is seen in ferromagnetic materials and depends on the alignment of a sample's magnetization to the electrical current direction [139], [140].

AMR can be described by:

$$R(\phi) = R_{\perp} + (R_{\parallel} - R_{\perp})cos^2\phi \qquad (5.10)$$

where $R(\phi)$ is the resistance of the material, $R_{\perp}$ and $R_{\parallel}$ denote the resistance when current and magnetization are perpendicular and parallel, respectively, and ϕ is the angle between current and magnetization. For most materials, $R_{\perp} < R_{\parallel}$ and so the maximum resistance is seen when current and magnetization are parallel, and the minimum resistance seen when current and magnetization are perpendicular. AMR was originally described by Lord Kelvin in 1850 [10].

AMR was measured using a "*GMW* Magnet System 5403AC" electromagnet, a KEITHLEY 6221 DC and AC current source and a "Stanford Research Systems SR830 DSP" Lock-in amplifier. The magnetic sample was mounted between the two electromagnet poles and contacted by a linear array of four needle probes, with probes separated by 1 mm. The outer two probes were used to applied AC current from the KEITHLEY current source and the inner two were used to measure the resulting potential difference across the magnetic wire while under magnetic field. An external field from -100 Oe to 100 Oe was applied during AMR measurement and the voltage was recorded using software designed in LabView.

This procedure was carried out with the magnetic field applied either parallel or perpendicular to the electrical current. Fig 5.23 shows the main parts of the AMR measurement system and MR sample cell.

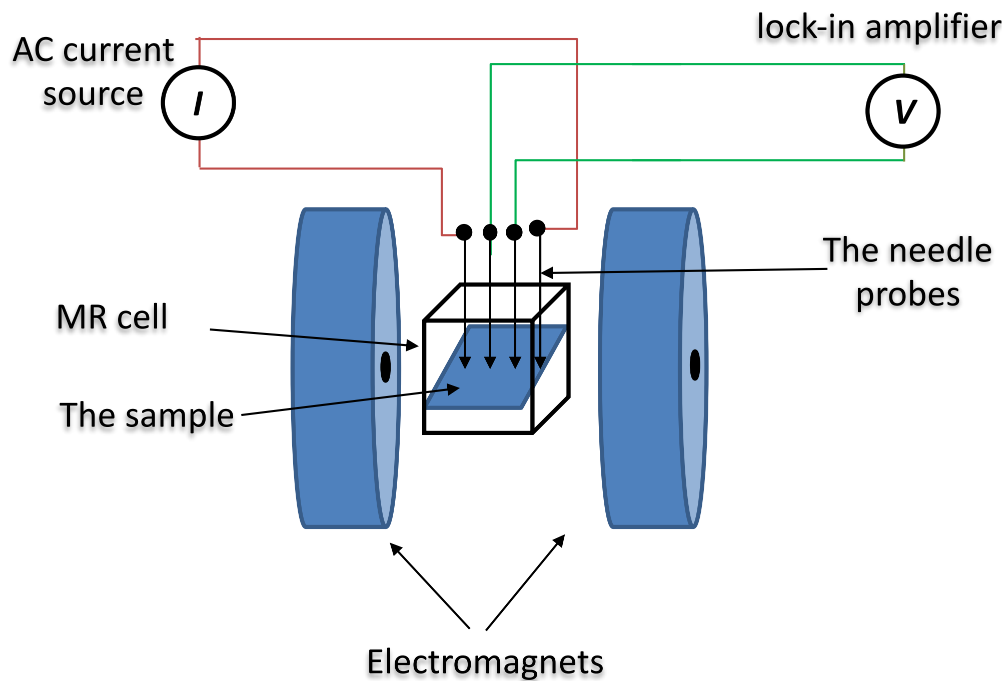

Figure 5.23: *Sketch of Anisotropic Magnetoresistance system (AMR).*

5.5.3 I-V test system

The basic current-voltage (I-V) characteristic of microstructures were tested using an a Keithley 2400 Source Meter with a two-contact arrangement (fig 5.24).

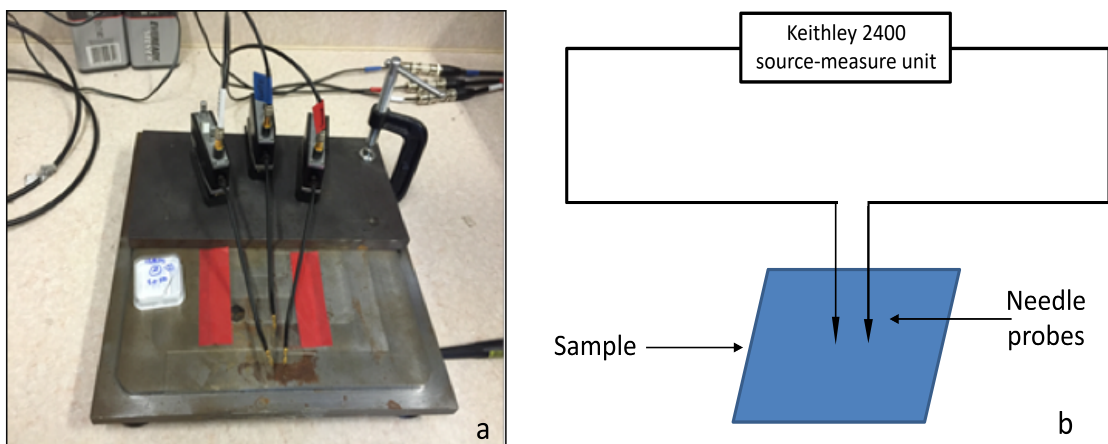

Figure 5.24: *The system of a I-V test system.*

5.5.4 Optical microscopy

Optical microscopy was performed using a "ZEISS Stemi 305" Greenough Stereo microscope with LED Integrated illumination. In-built optical zoom instead of changing objective lenses. Both reflection and transmission microscopy were used and a x5 zoom used for immediate observation of fabricated samples. ZEN-lite imaging software allowed simple image processing to be conducted. The Greenough microscope can give crisp 3D impressions, versatile object illumination. The 3 D images are achieved based on the double spot illumination with self-carrying goosenecks is optimal. It creates half-shadow effects that lead to a good 3D impression without overly dark shadows.

5.5.5 Atomic force microscopy (AFM)

Atomic force microcopy (AFM) was used to measure the lateral and out-of-plane dimensions of structures and ablated regions, as well as to measure surface roughness. AFM was performed using a "Veeco Dimension 3100" scanning probe microscope, which offers sub-nanometre resolution (20 nm in plane and 1 nm out of plane) and both contact and tapping mode AFM. The principle of AFM is that a cantilever with a sharp tip is used to scan the surface of a sample. The movement of stage along x and y axis are 150 mm with 2 μm resolution. Fig 5.25 shows the Veeco Dimension 3100 AFM.

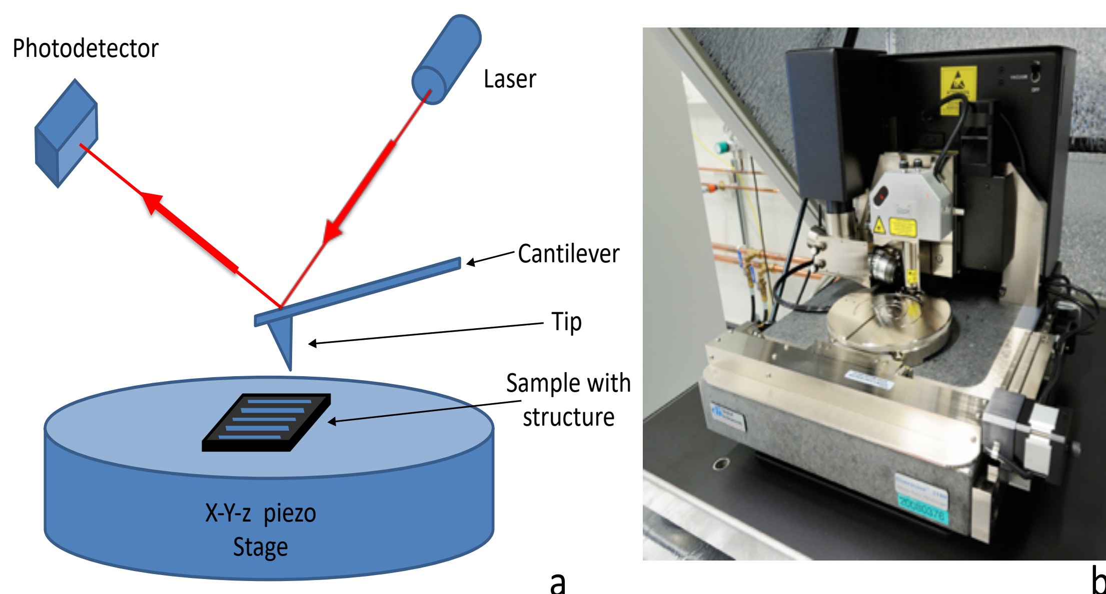

Figure 5.25: *a) Simple schematic of AFM system and b) The Veeco Dimension 3100 AFM.*

5.5.6 Scanning electron microscopy (SEM).

A scanning electron microscopy (Raith EO FE-SEM) system was used for imaging and characterizing the micro/nano-scale magnetic structures. The electron source of this system was a "Schottky Thermal Field Emission sources (TFE)" and the acceleration voltages (a.v.) used were 0.1kV - 30kV. This system can offer resolution: 1.3 nm with a.v. of 15 kV, 2.1 nm with a.v. of 1 kV and 5.0 nm with a.v. of 0.2 kV. Here, we used a.v. of 10kV and secondary electron imaging. Samples patterned on silicon substrates were imaged using SEM directly without any further preparation but structures on glass substrates were coated with 3-4 nm of a metallic (permalloy) thin film by thermal evaporation (see §5.2). This conductive layer prevented the accumulation of electrostatic charge during SEM imaging to avoid aberrations and failed scans.

Figure 5.25: *Raith 'EO' FE-SEM System.*

5.6 Summary

The experimental methods including thin film deposition, laser fabrication methods, and characterization techniques used in this project were covered in this chapter. This included production of single pulses and control of the overlap between successive laser pulses in pulse trains. This was achieved by tuning two parameters: the electric current supplied to the laser diode driver to control the repetition rate and the sample scanning speed to control the distances/overlap between pulses. This allows laser scan lines to be designed for fabrication of magnetic wires and arrays of two-dimensional elements. Fabricated structures were subject to focused Magneto-Optic Kerr Effect (fMOKE) magnetometry and measurement of anisotropic magnetoresistance (AMR). The structures were also imaged using scanning electron microscopy (SEM), atomic force microscopy (AFM) and optical microscopy.

Chapter 6: Laser induced forward transfer (LIFT) of magnetic structures

6.1 Introduction

In this chapter, the attempts to fabricate magnetic structure and the results that were obtained using LIFT are presented. The methodology of performing LIFT adopted here is described in detail in §5.4.2.

Three laser systems were used to pattern magnetic structures: a 350 picosecond pulse length Diode-Pumped Solid-State (DPSS) Q-switched laser system, 800 picosecond pulse length Diode-Pumped Solid-State (DPSS) Q-switched laser system and femtosecond pulse length Ti: sapphire laser system. The fabricated structures were tested by fMOKE magnetometry for magnetic properties and the I-V test system for electrical properties. These structures were also characterized by optical microscopy, AFM and SEM.

The patterned structures include sets of separated and continuous wires and arrays of dots. The results are presented based on the laser system that was used for fabrication. All details of the laser systems and the characterisation methods used can be found in the Experimental chapter (Chapter 5).

6.2 LIFT with 350 ps pulse length DPSS- Q-switched laser system

The initial attempts to use LIFT were made on 20 nm permalloy films on glass onto a silicon acceptor substrate using a 350 picosecond pulse length DPSS- Q-switched laser system. Fabrication of separate and continuous wires were attempted. The pulse energy used was 5.6 μJ with a repetition rate of laser about 14.2 kHz.

The laser beam was focused onto the donor substrate using a 0.30 NA objective lens. The laser ablation spot diameter was measured to be approximately 5.0 µm, giving an effective fluence of 28.6 J. cm^{-2}.These parameters were chosen depending on the optics available with the laser system

The structures were fabricated using the same code that was used to fabricate arrays of magnetic wires in LDW- (Appendix A) in §5.4.1 and §5.4.2 but with a much slower scanning speed of just 1.5 mm. s^{-1}. This gave an overlap between successive laser pulses of about 98%. The transfer was conducted with the donor (D) and acceptor (A) substrates in direct contact.

Two structures were created: separate wires 2 mm in length (shown in an array of ten wires in Fig. 6.1a) and a structure containing 1 mm long connected wires (Fig. 6.1b). Fig 6.2 shows the optical microscopy image of donor substrates following LIFT ablation of single isolated wire and SEM images (Fig. 6.3 for a single isolated wire) showed that each wire was 7.9 µm wide but suffered from a fragmented structure with additional debris on either side.

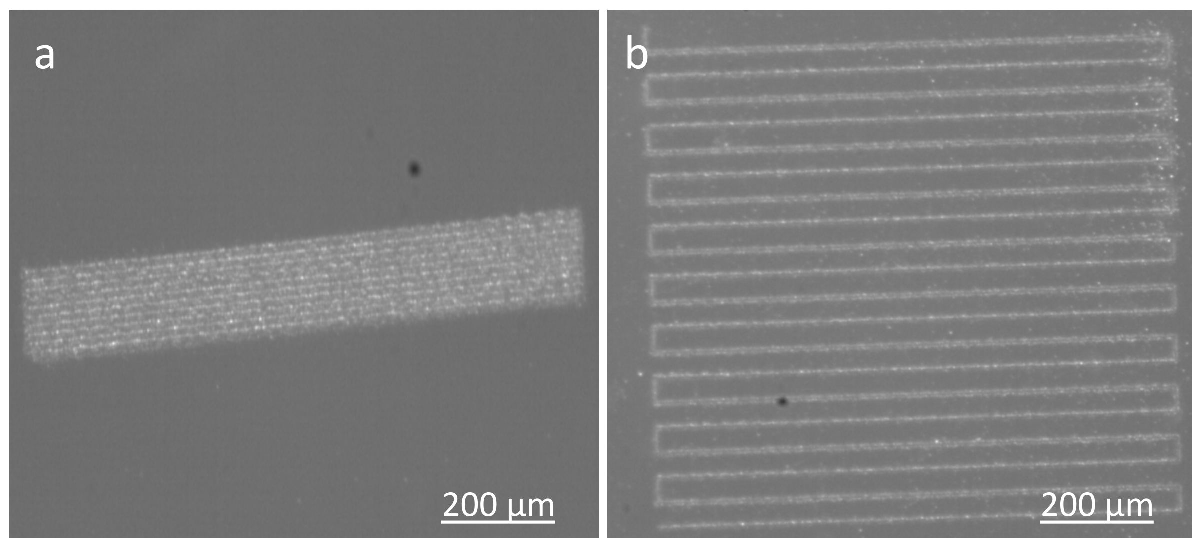

Figure 6.1: *Optical microscopy images of LIFT-fabricated permalloy wires: a) ten separate wires of 2 mm length and line separation of 10 µm and b) a continuous structure of 20 connected wires of 1 mm length and 50 µm line separation. Both images are of transferred material on the acceptor substrate.*

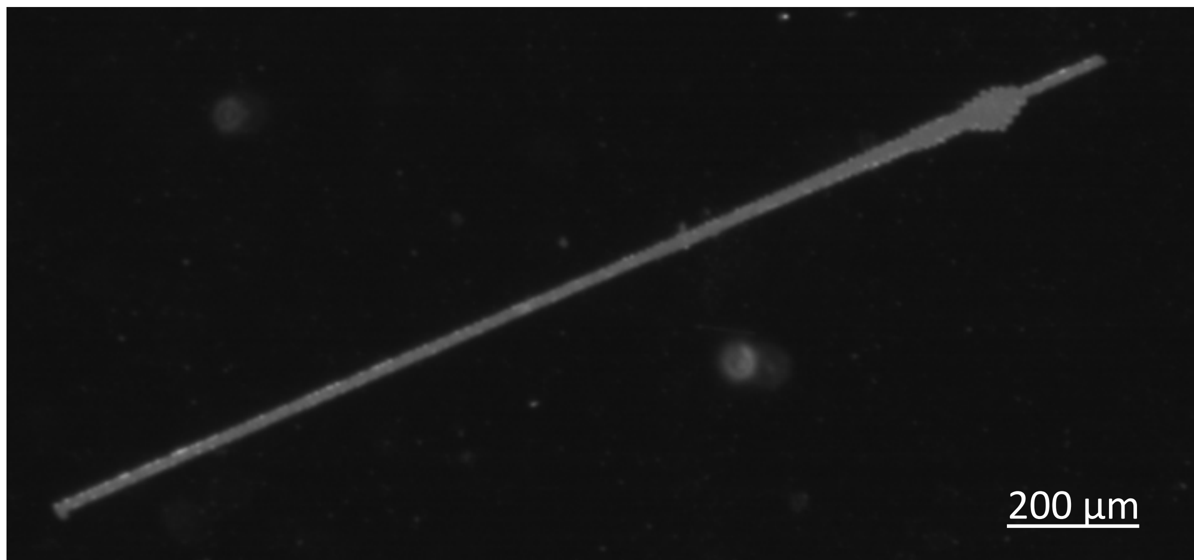

Figure 6.2: *Optical microscopy images of donor substrates following LIFT ablation of single isolated wire*

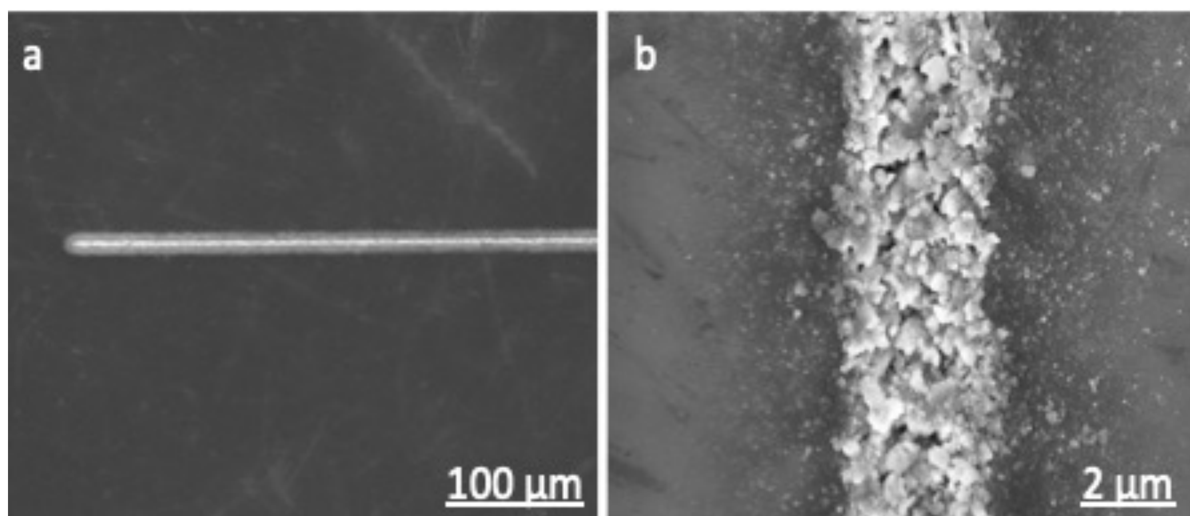

Figure 6.3 *Scanning electron micrographs of LIFT-transferred permalloy wire of width 7.9 µm at two magnifications.*

However, rotating the sample inside the SEM chamber (by 55° and 70° in Fig. 6.4) revealed that the structure visible was in fact a groove etched from the acceptor substrate. This groove and the scattered fragments seem to have resulted from the high intensity of the laser used here (far higher than the ablation threshold) and the very high overlap ratio between laser pulses used in this initial experiment.

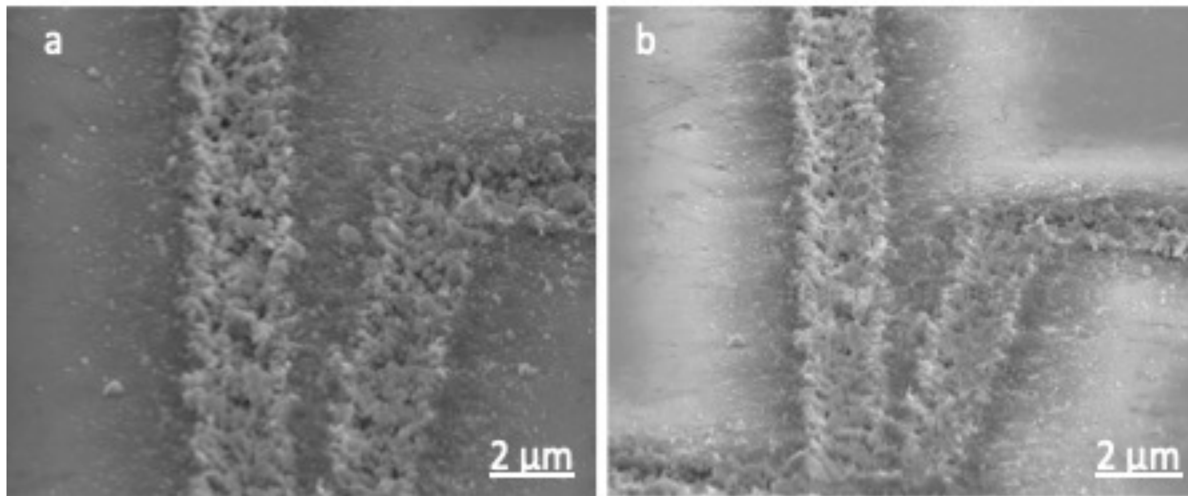

Figure 6.4: *Scanning electron micrographs of acceptor substrate at imaging angles of (a) 55° and (b) 70° following LIFT processing.*

The high overlap ratio was designed to create structures with smooth edges but the high number of pulses at each position appeared to cause problems with the final state of the acceptor substrate. While the first pulse in an area might have ablated/transferred the magnetic material from the surface of the donor, the successive pulses appeared to destroy any transferred structure and instead etching the deposited material and the acceptor substrate. The result of this process is mixture of transferred permalloy material and fragments of etched silicon.

Not surprisingly, the fragmented material on the acceptor substrate showed no magnetic response when measured by fMOKE (fig 6.5).

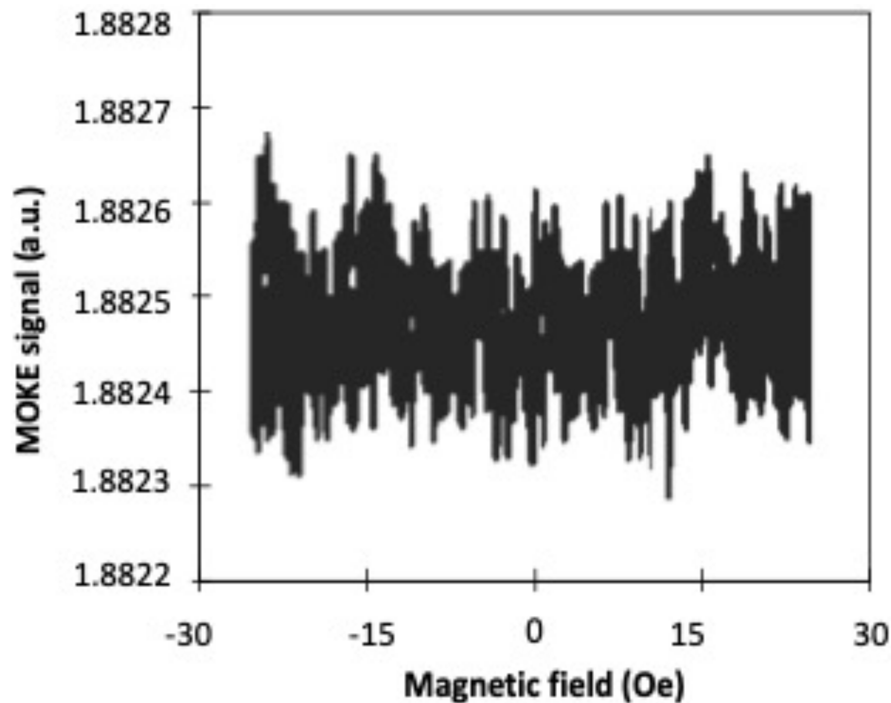

Figure 6.5: *fMOKE M-H characteristic of LIFT-transferred wires using high degree of spatial overlap of pulses from ns-pulse length DPSS- Q-switched laser.*

However, measurements of resistivity showed that very weak electric currents were able to pass through the wire (Fig. 6.6). An electric current between 10 nA and -25 nA was applied with voltages between -1 V and 1 V with a separation between needle probe contacts of approximately 0.5 mm. Some measurement attempts (with probes repositioned each time) resulted in a non-linear I-V characteristic (Fig. 6.6 attempts 2 and 3), which may be due to the Si content in the fragmented material. Analysis of the linear response region allowed a resistance of 1.3 GΩ to be measured.

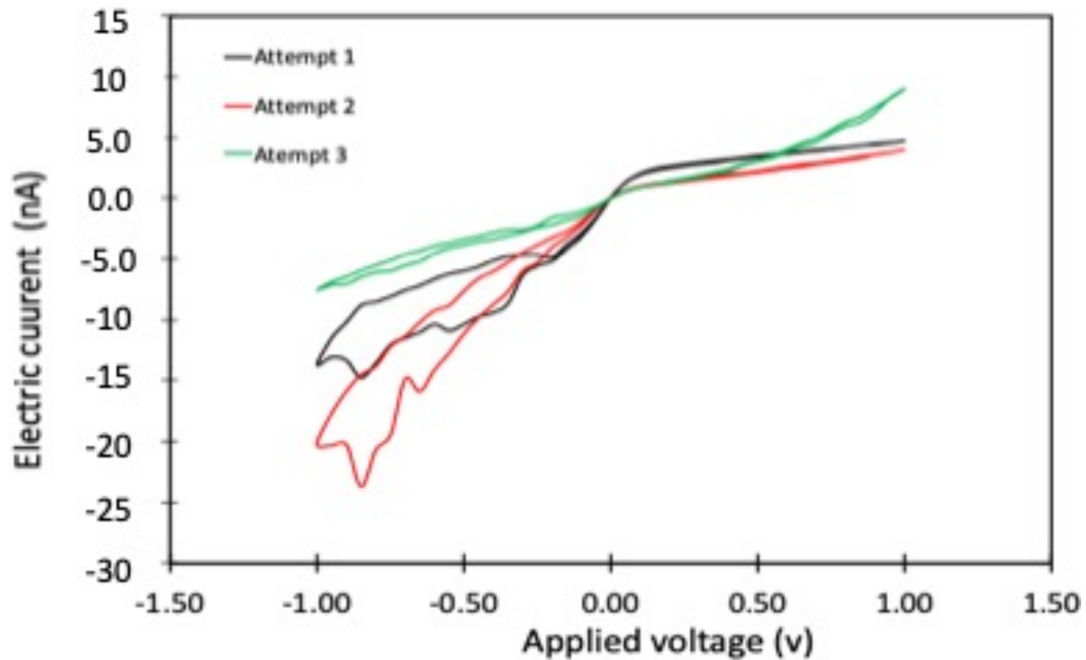

Figure 6.6: *The electric current passing through the wire with contribution of silicon substrate by applied voltage from 1V to -1V for three attempts.*

In order to check the accuracy of the initial measurements of conductivity of wire and to sort the contribution of silicon substrate than magnetic wire, this measurement was repeated after a week. The conductivity of the silicon substrate and wire were measured separately to determine their separate contributions (Fig. 6.7). The I-V characteristics are strongly non-Ohmic and show that the wire had a larger resistance than the forward bias resistance of the substrate. These results may suggest isolated elements through the wire because getting more oxidation between the two measurements.

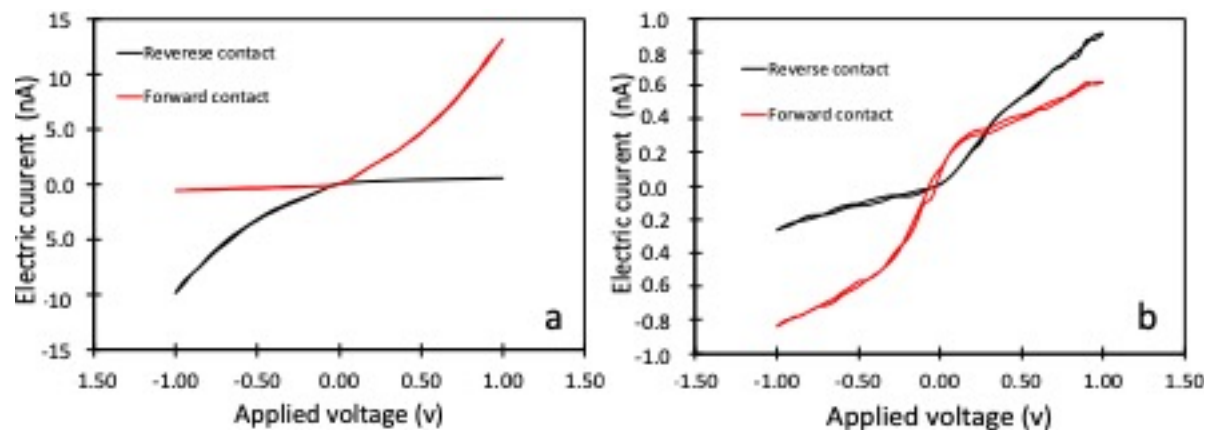

Figure 6.7: *The electric current passing through; a) silicon substrate and b) the wire by applied voltage from 1V to -1V with forward contact and reverse contact.*

6.3 LIFT with 100 fs pulse length Ti: sapphire laser system

LIFT processing using the 100 fs pulse length, 80 MHz repetition rate Ti: sapphire laser system with frequency-doubled 750 nm wavelength light. The laser beam was focused with a 0.75 NA objective lens onto the sample to achieve a focal spot width of approximately 3 μm, which resulted in a pulse overlap of 99.99 % with scanning speed of 10 mm.s^{-1}. Ablation of a 40 nm permalloy film could be achieved with a threshold fluence of about 110 mJ.cm^{-2} (intensity about 0.1x10^{13}W/cm^{2}). The permalloy film was on contact with the acceptor (silicon) substrate.

The donor substrate showed clear signs of ablation having taken place, for example, Fig. 6.8 shows images of the donor magnetic thin film with regions removed from various fluence, F(110 mJ.cm^{-2}, 120 mJ.cm^{-2}, 125 mJ.cm^{-2} and 130 mJ.cm^{-2}); the calculation of ablation threshold fluence was based on the continuous film removal observed with pulse energy = 6nJ (F= 125 mJ.cm^{-2}).

However, no magnetic material could be observed on the acceptor substrate for any value of pulse energy. This phenomenon occurred possibly due high intensity of femtosecond pulse which about 10^{13} W/cm^{2}. Where, the materials were possibly transferred as very tiny debris as powder because of difference of thermal conductivity between the permalloy and the material of acceptor as will discuss further next, especially with very high repetition rate

which apply one ultra-short pulse in each 12 ns in which might be destroyed all transferred material by applied new pulse on the same debris itself, where the pulses overlap 99.99 % as mentioned before.

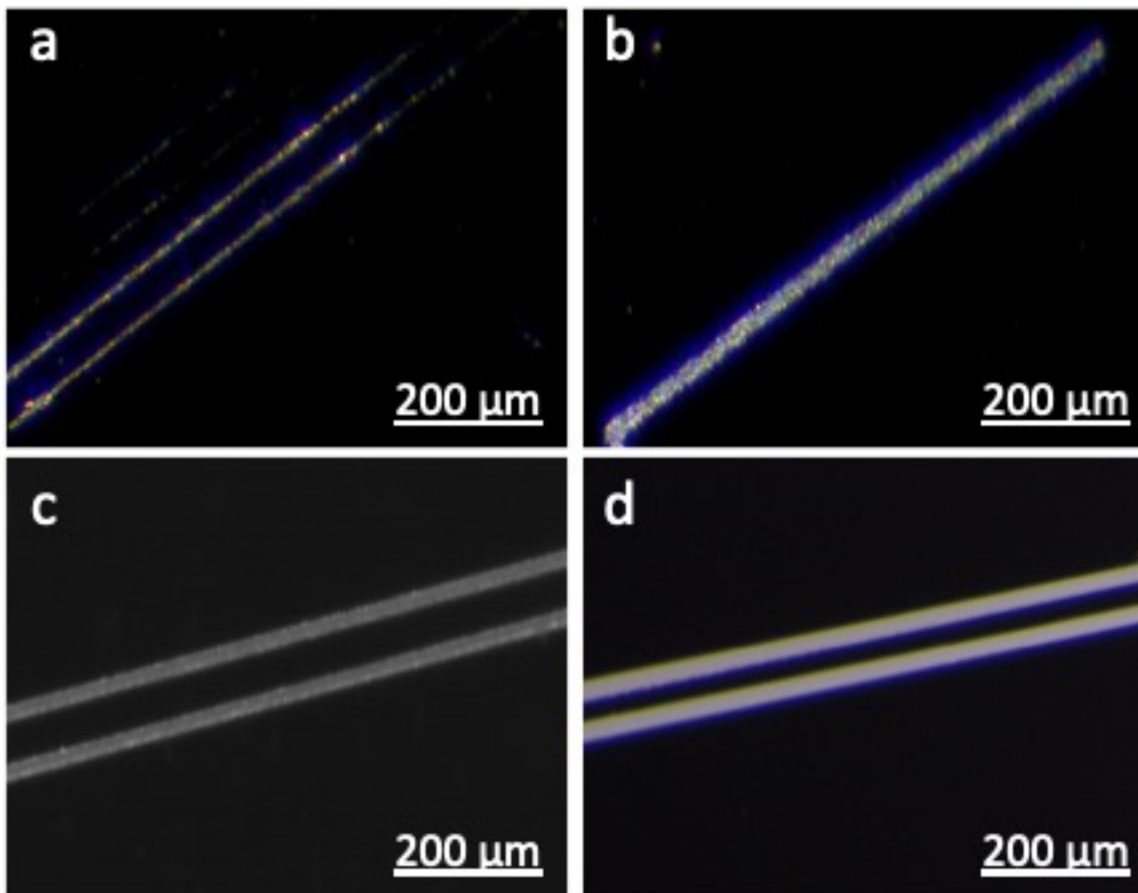

Figure 6.8: *Optical microscopy images of donor substrates following LIFT ablation using 750 nm wavelength laser light from a 100-fs pulse width Ti: sapphire laser using laser fluence, a) 110 mJ. cm^{-2}, b) 120 mJ. cm^{-2}, c) 125 mJ. cm^{-2} and d) 130 mJ. cm^{-2})*

6.4 LIFT with ps pulse length DPSS- Q-switched laser system

The DPSS- Q-switched laser system with 800 ps width pulses and 532 nm wavelength was used to investigate LIFT of permalloy films. As noted in §5.3.2, the laser pulses were focussed with a 0.75 NA objective lens to obtain a spot size of 1.85 μm diameter. Several parameters were adjusted in this study of transferring permalloy films, including thin film thickness, sample scanning speed, laser pulse energy, distance between donor/acceptor substrates, the acceptor materials and commands within the program code that control the sample motion. Results for

each parameter will be presented here. Control of the laser average power and pulse repetition rate by varying the laser diode driver current are shown in fig 6.9.

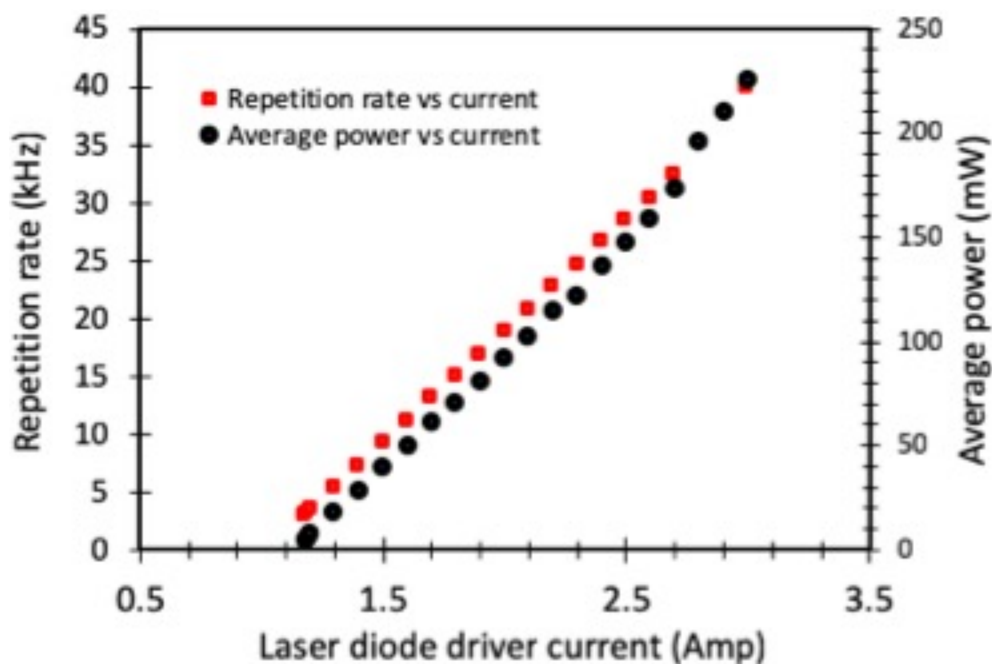

Figure 6.9: *The pulse repetition rate and average power of the 800 picosecond laser as a function of laser diode driver current.*

6.4.1 Transfer material using "Dwell" command

Arrays of dots were transferred using the "Dwell" command, which is used to pause the sample motion a specified time. Here, the Dwell command was used to control the number of pulses per dot. Delay times of 1s, 0.06s, 0.05s and 0.001 s were used with different repetition rates and various thin film thickness.

a- Effect of the delay time by Dwell

The initial attempts to use the Dwell command were with a 20 nm permalloy film, pulse energy of 3.5 µJ, pulse repetition rate of 13 kHz, silicon acceptor substrate and without separation between acceptor and donor substrates. An attempt to transfer a 5 x 5 array of elements with 60 µm between elements used a 1 s Dwell time to apply 13,000 pulses for each dot. The shape of this structures did not appear as separated dots but as a continuous structure (Fig. 6.10).

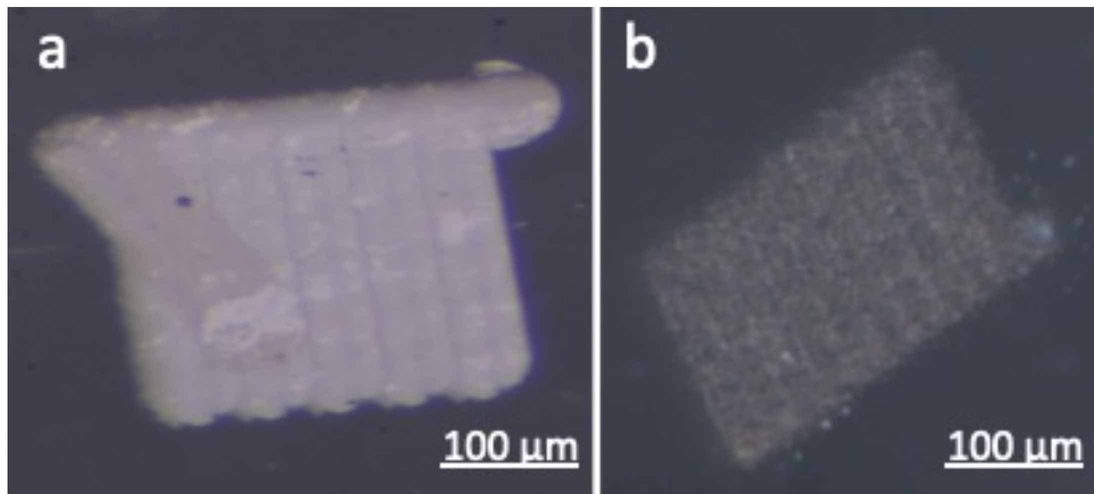

Figure 6.10: *Optical microscopy images of array of 5x5 elements separated (in the design) by 60 μm created with LIFT arrangement and ps-pulse length laser pulses with a sample Dwell parameter equal to 1 s. Images show a) donor substrate with 20 nm permalloy film (dark) and b) transferred structure deposited on silicon acceptor substrate (light).*

The transferred array on the acceptor substrate appeared powdery and could be removed mechanically very easily. The high pulse energy and large number of pulses per point resulted in the shape of transferred structures not matching designed shapes. Therefore, the Dwell time was reduced to 0.06 s to apply 780 pulses for each dot, with other parameters identical to those used previously. The transferred structures also appeared like a powder on the acceptor and were again removed easily but the elements were distinct from each other (Fig. 6.11).

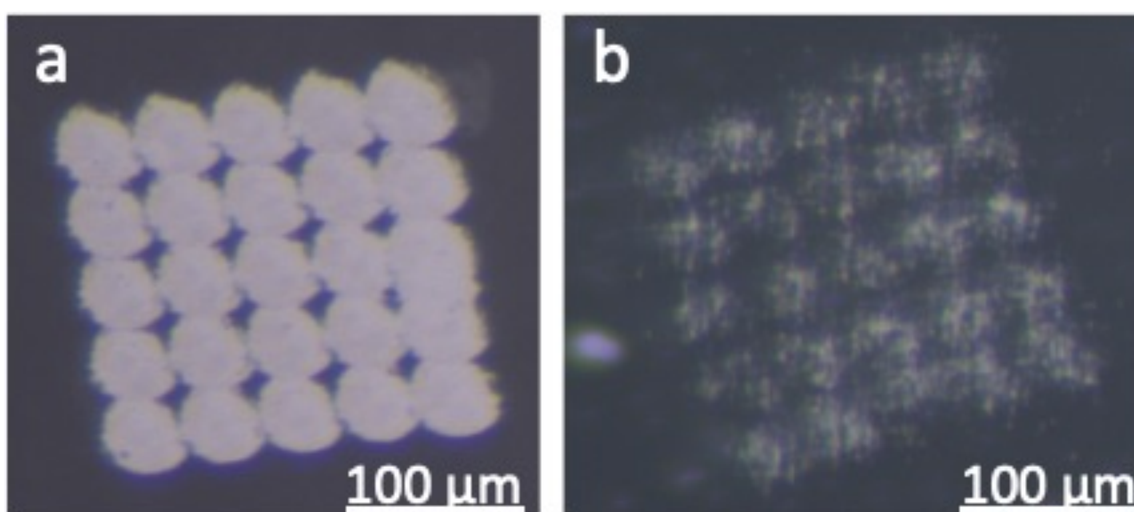

Figure 6.11: *Optical microscopy images of array of 5x5 elements separated (in the design) by 60 μm created with LIFT arrangement and ps-pulse length laser pulses with a sample Dwell parameter equal to 0.06 s. Images show; a) donor substrate with 20 nm permalloy film (dark) and b) transferred structure deposited on silicon acceptor substrate (light).*

Greater separation between the elements was achieved using a thicker (40 nm) film of permalloy and reducing the Dwell time further to 0.05 s, which reduced the number of pulses per dot to 650 shot. However, the transferred material again appeared as a powder on the acceptor substrate and was again removed easily (Fig. 6.12).

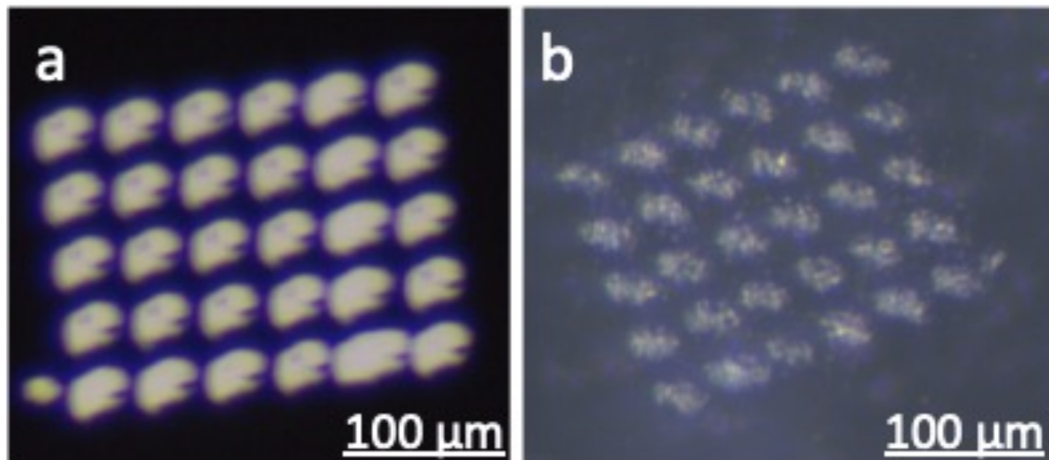

Figure 6.12: *Optical microscopy images of array of 5x6 elements separated (in the design) by 60 μm created with LIFT arrangement and ps-pulse length laser pulses with a sample Dwell parameter equal to 0.05 s. Images show a) donor substrate with 40 nm permalloy film (dark) and b) transferred structure deposited on silicon acceptor substrate (light).*

a- Effect of the repetition rate

Further reduction of the repetition rate to about 6 kHz and pulse energy to 2.5 µJ (F= 93 J.cm^{-2}) with a Dwell value of 0.001 s allowed just six pulses per dot to be used. This resulted in incomplete removal of material from the silicon substrate (Fig. 6.13).

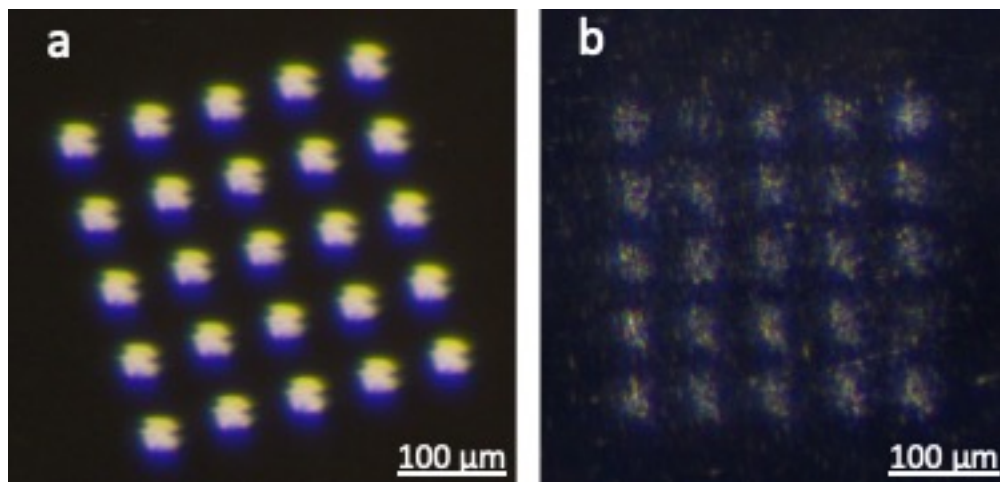

Figure 6.13: *Optical microscopy images of array of 5x5 elements separated (in the design) by 40 µm created with LIFT arrangement and ps-pulse length laser pulses with a sample Dwell parameter equal to 0.001 s. Images show a) donor substrate with 40 nm permalloy film (dark) and b) transferred structure deposited on silicon acceptor substrate (light).*

Consequently, to minimize the size of elements and obtain more regularly shaped elements, the number of pulses per dot were again reduced by lowering the repetition rate to about 4 kHz and using a pulse energy of 250 nJ. Setting the Dwell parameter to 0.001 s meant exposure became four laser pulses per dot position. An array of 10x10 elements with 3.5 µm between elements was transferred using a 70 nm permalloy film.

Despite the elements only having small separation, they remained clearly identifiable but in fact were deposited only as scattered debris (Fig. 6.14). The balled nature of the transferred material appears to show that it had melted and then formed spheres as a liquid.

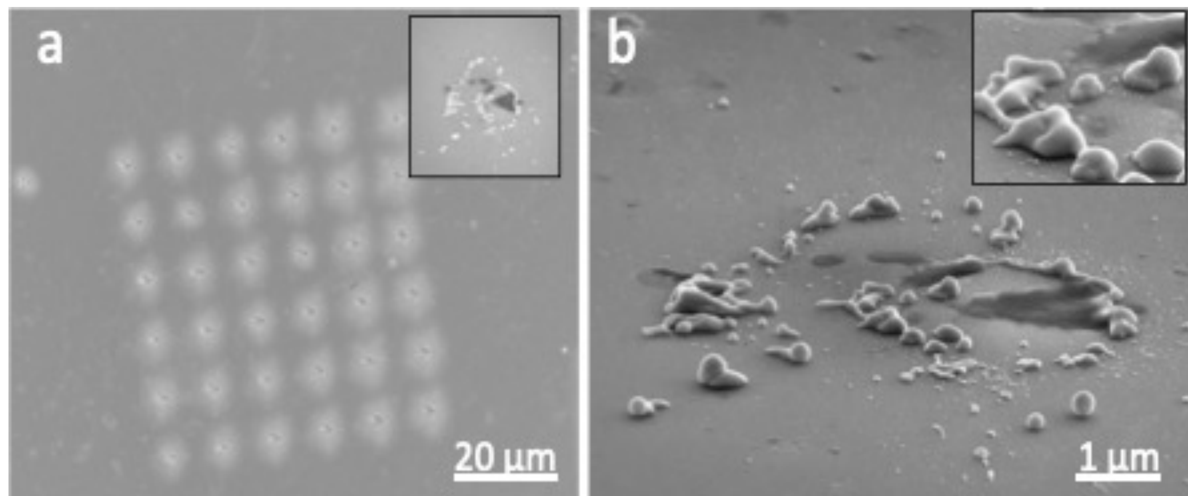

Figure 6.14: *Scanning electron micrographs of a) array of 10x10 elements transferred by LIFT using Dwell command of 0.001 s (four laser pulses per point) with spaces between elements 3.5 µm with thickness of 70 nm and b) image of single dot deposited on silicon substrate as scattered debris, with the inset providing an additional 362 x times magnification.*

6.4.2 Transfer material using "Linear" command

LIFT of permalloy was also attempted using a constant sample scanning speed obtained using the software's "Linear" command. Scanning speed was varied from 1 mm.s^{-1} to 300 mm.s^{-1} to avoid the problem of multiple pulses destroying the transferred structures as seen with the results shown above and instead to ensure a single laser pulse per position (i.e. no pulse overlap). This was investigated using a permalloy film of 40 nm thickness, pulse energy 1 µJ (laser fluence of 4.5 J. cm^{-2} compared to a threshold fluence of 2.2 J.cm^{-2}), a pulse repetition rate of 3.5 kHz, a silicon acceptor substrate and with the donor and abstract substrates in contact. These values produced a laser ablation spot about 6 µm diameter.

Fig 6.15 shows examples of optical microscopy images of transferred single ablation line on the silicon substrate using scanning speeds of 1 mm.s^{-1}, 5 mm.s^{-1}, 10 mm.s^{-1}, 40 mm.s^{-1} and 300 mm.s^{-1}. The use of 1 mm.s^{-1} scanning speed resulted in an unusual wire appearance, possibly due to re-ablation of deposited material by successive pulses. A more continuous single wire was generated with scan speeds from 5 mm.s^{-1} while using 300 mm.s^{-1} scan speed resulted in separated dots. The structures had diffuse debris deposited more widely but this reduced with increased scan speeds and could not be seen for scan speeds of 300 mm.s^{-1},

which is most easily understood as simple having fewer pulses per unit distance.

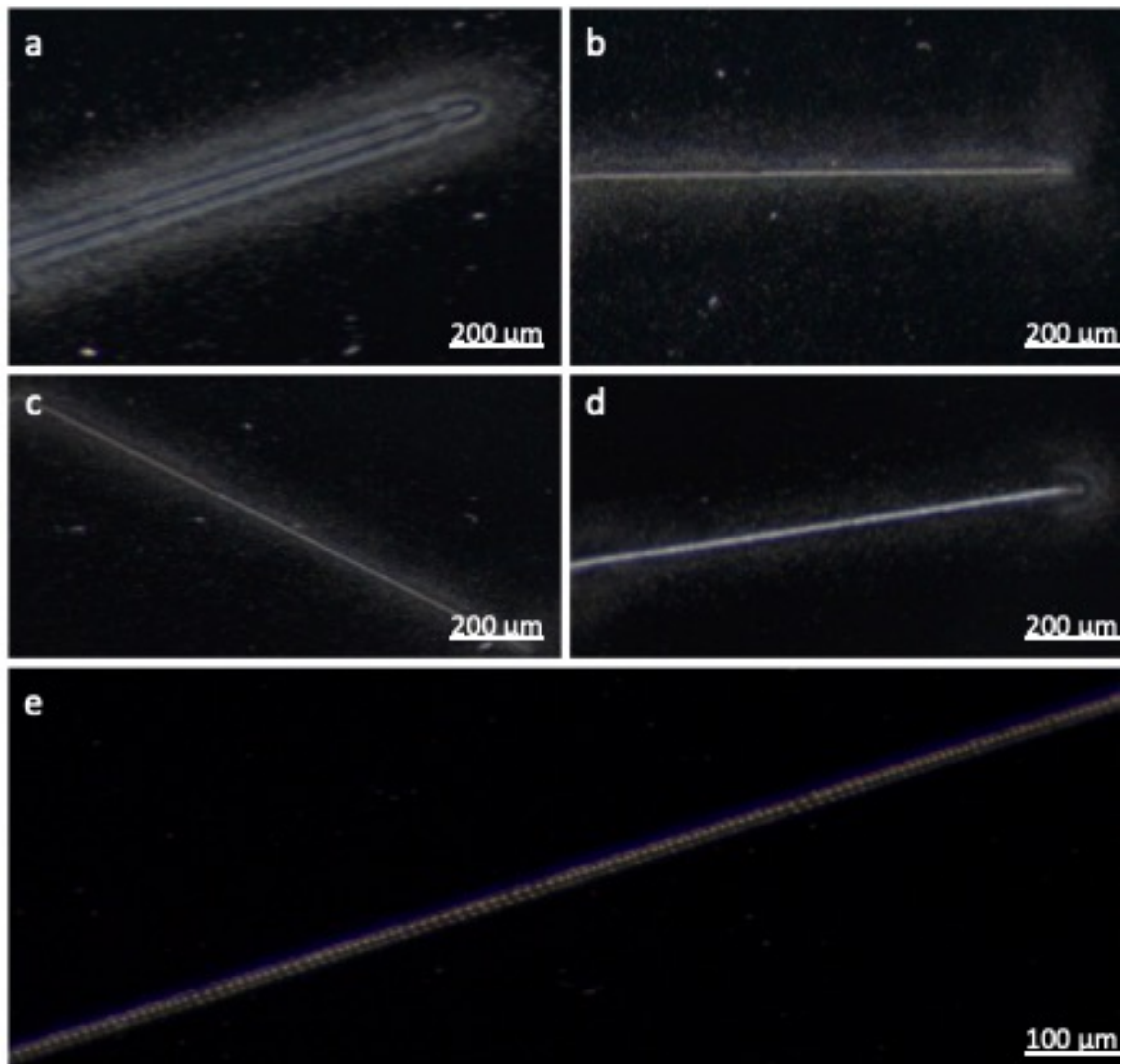

Figure 6.15: *Optical microscopy image of LIFT-fabricated single wires (60 nm thick permalloy) with scanning speeds of a) 1 mm.s^{-1}, b) 5 mm.s^{-1}, c) 10 mm.s^{-1}, d) 40 mm.s^{-1} and d) 300 mm.s^{-1}.*

The width of the structure in fig 6.15d was measured by AFM for other structures in fig 6.15 by analysis of optical microscopy. The structure width was found to decrease with increase in the sample scanning speed (Fig. 6.16), which reflects a reduction in pulse overlap.

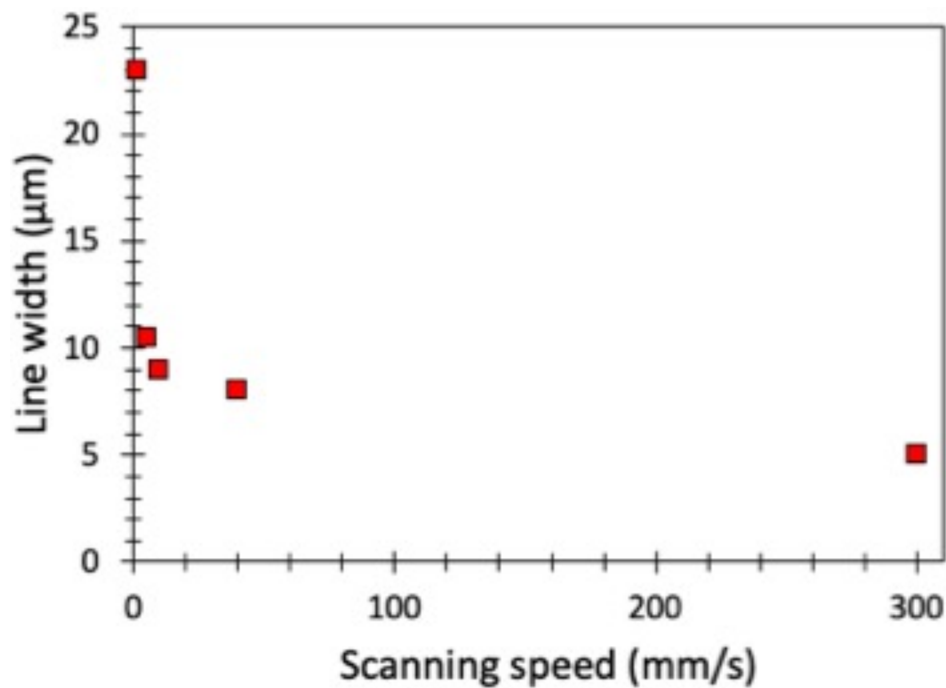

Figure 6.16: *Scanning speed as function to lines widths.*

Atomic force microscopy (AFM) images of the line of dots created using a scanning speed of 300 mm.s^{-1} showed that the elements were actually holes in the Si substrate, similar to what was seen with multiple pulses above (§6.2). One difference here, though, was the appearance of some previously molten material around the holes (fig 6.17a inset).

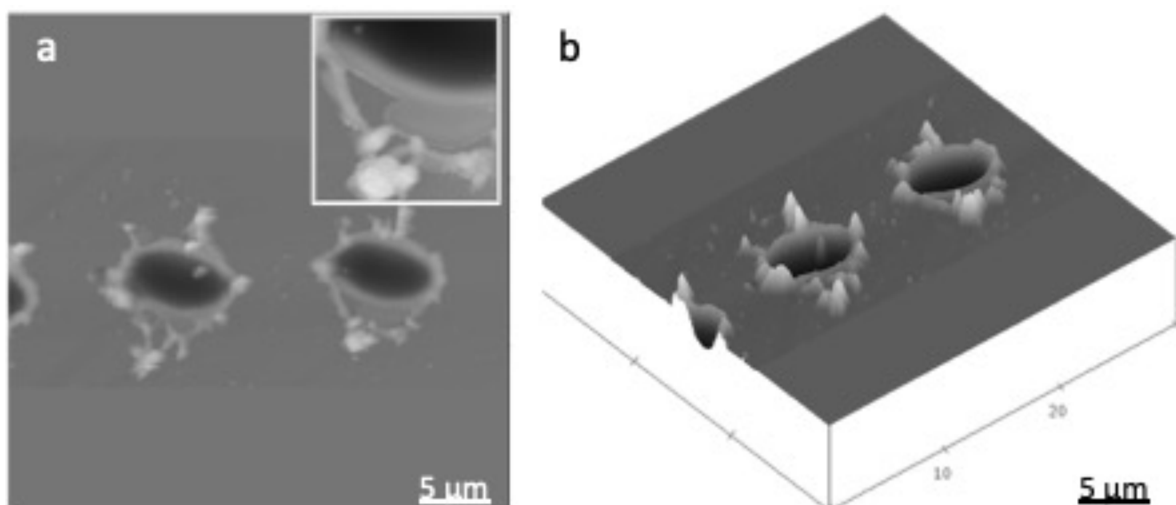

Figure 6.17: *AFM images of separated dots created by LIFT from a 60 nm permalloy film. Inset to part a shows previously molten material around the edge of the dots.*

The effect of pulse energy on the morphology of patterned dots was investigated by creating series of dots using laser pulse energies of 1.4 µJ, 0.60 µJ, 0.40 µJ and 0.20 µJ (corresponding to fluences of 4.3 to 0.8 $J.cm^{-2}$) at a sample scan speed of 140 $mm.s^{-1}$, 220 $mm.s^{-1}$, 250 $mm.s^{-1}$ and 300 $mm.s^{-1}$ and maintaining all other conditions as used previously. AFM images of the resulting acceptor substrate dot regions (Figures 6.17 – 6.21 for pulse energies 1.4 µJ – 0.20 µJ, respectively) showed that holes seen in the acceptor substrate at high pulse energies gradually reduced with lower pulse energies until just surface material remained for the lower pulse energy used (0.20 µJ).

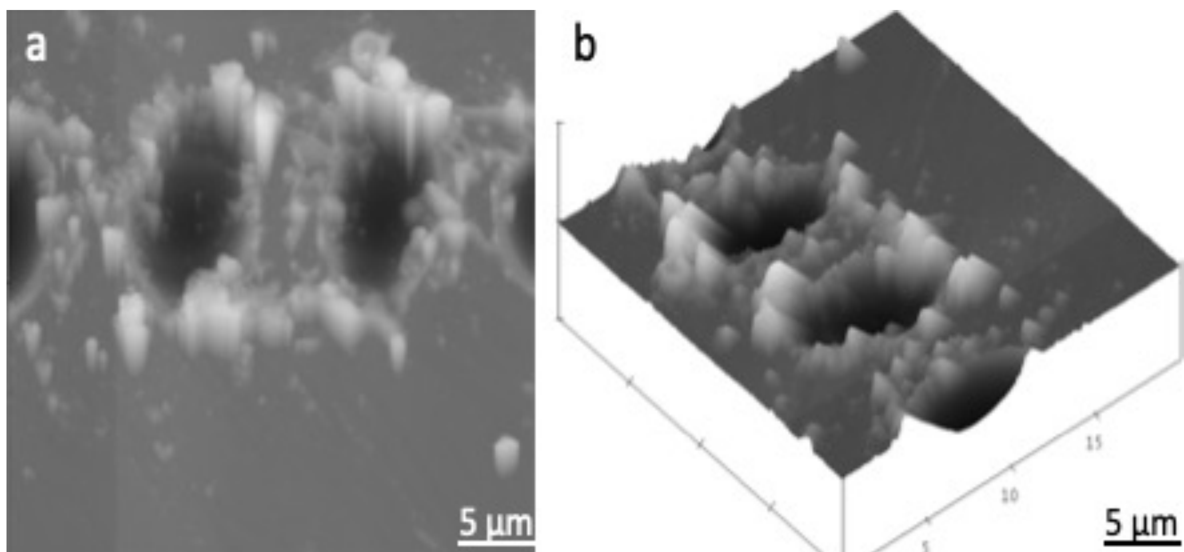

Figure 6.18: *AFM images of dots created by LIFT with scanning speed of 220 mm/s and pulse energy 1.4 µJ, showing holes with 6.5 µm diameter separated by about 1.5 µm.*

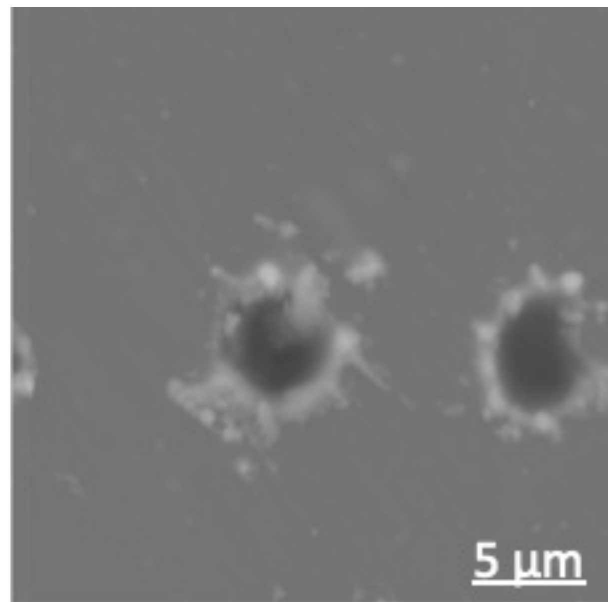

Figure 6.19: *AFM images of line of dots created with scanning speed of 300 mm/s and pulse energy 0.6 µJ, the diameter of dots (holes) 5 µm and separation distance 7 µm.*

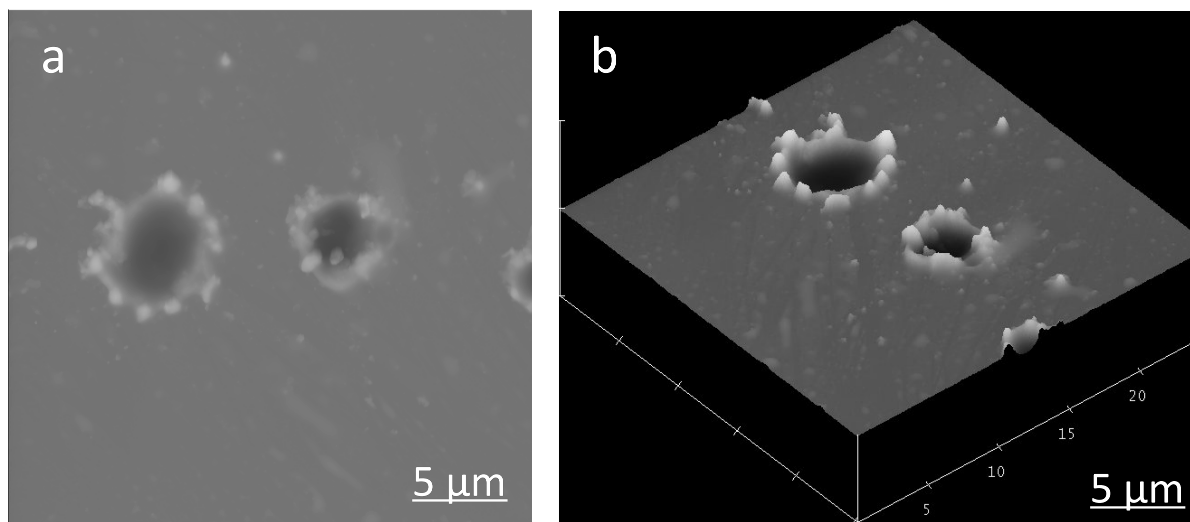

Figure 6.20: *AFM images of dots created by LIFT with a sample scanning speed of 250 mm/s and pulse energy 0.4 µJ. The dots (holes) had a diameter of 4.5 µm and were separated by 7.5 µm.*

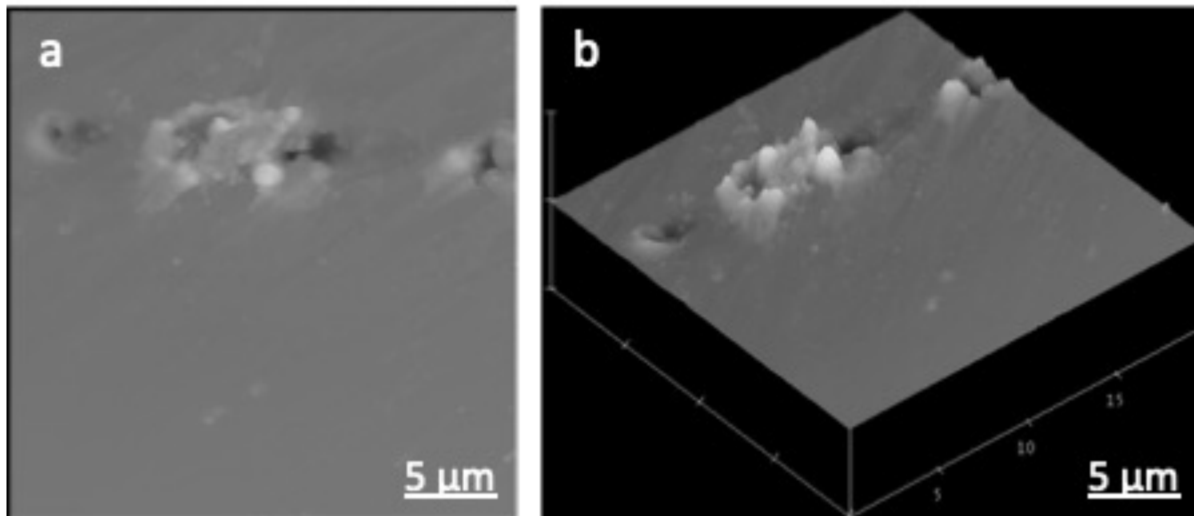

Figure 6.21: *AFM images of line of dots created with scanning speed of 140 mm/s and pulse energy 0.2 µJ. The dots had a diameter of approximately 2.5 µm separated by 2.7 µm.*

The size of the transferred elements or width of etched holes increased with the laser pulse energy (Fig. 6.22). This is due to a non-uniform intensity across the focal laser spot and higher pulse energies resulting in a greater proportion of the laser spot being above the ablation threshold. The range of pulse energies used here resulted in feature sizes from 2.5 μm – 6.5 μm.

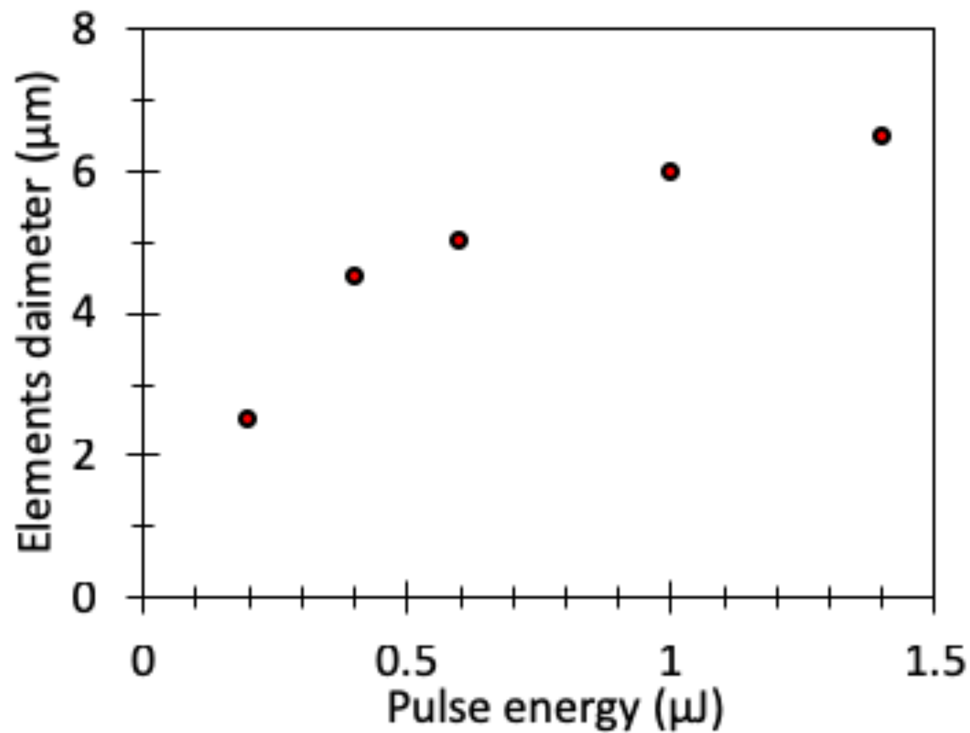

Figure 6.22: *Pulse energy as function to the size of transferred element (hole size).*

The pulse energy was reduced further to 100 nJ and separation introduced between the donor and acceptor substrates, varying from 100 µm to less than 10 µm. For donor-acceptor separations from 40 – 100 μm and 0.1 μJ pulse energy, the transferred material deposited on acceptor substrates appeared as a powder and was easily removed by cleaning as shows in fig 6.23.

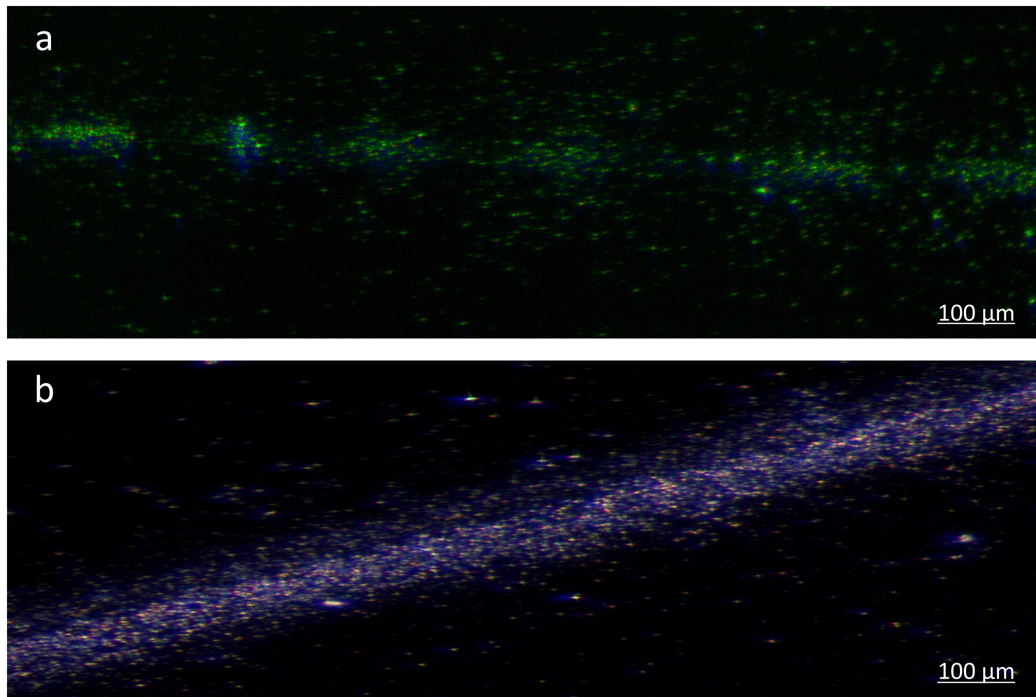

Figure 6.23: *Optical microscopy images of LIFT transferred permalloy on a silicon (acceptor) substrate obtained with laser pulse energy 0.1 µJ and donor-acceptor substrate separation of a) 100 µm and b) 40 µm. The images were taken before cleaning the acceptor substrate.*

The mean free path, λ, of particles in a gas can be calculated by [141].

$$\lambda = \frac{1}{\sqrt{\pi}\pi\theta^2 n} \qquad (6.2)$$

where θ is the particle diameter and ***n*** is the number of molecules per volume.

The equation of state of ideal gases is:

$$PV = nRT \qquad (6.3)$$

where ***R*** is the universal gas constant, ***T*** is temperature, ***V*** is the gas volume and ***P*** is the gas pressure. Given then $n = N/V$, where N is the number of molecules of gas, Eq (6.3) can be written:

$$n = \frac{N_A P}{RT} \qquad (6.4)$$

where N_A is Avogadro's number and R is the universal gas constant. Substituting (6.4) into (6.2) obtains:

$$\lambda = \frac{RT}{\sqrt{2}\pi\theta^2 N_A P} \qquad (6.5)$$

Ni has an atomic radius of 2 Å [142], so using θ = 4 Å, T = 300 K and P = 10^5 Pa gives λ = 5.8×10^{-8} m. This is lower than the donor-acceptor substrates used above and suggests that ablated material will undergo several collisions between the two substrates. This will reduce the kinetic energy of ablated species and cause them to become largely thermalized upon reaching the acceptor substrate. This explains the lack of adhesion seen with transferred material at donor-acceptor separations greater than 40 μm seen above. Also, the shock wave reflected from acceptor is likely to scatter the material during its transfer [130].

To reduce the number of gas-phase collisions (and remove any shock wave effects), the donor-acceptor separation was reduced to less than 10 μm and LIFT operated under vacuum conditions (estimated to be 0.1 Pa), still with a pulse energy of 0.1 μJ. Eq. 6.1 above suggests that the mean free path would have increased to λ = 5.8×10^{-2} m. This resulted in transferred material that was more tightly distributed (Fig. 6.24a) but, upon closer examination, appeared as scattered debris (Fig. 6.24b).

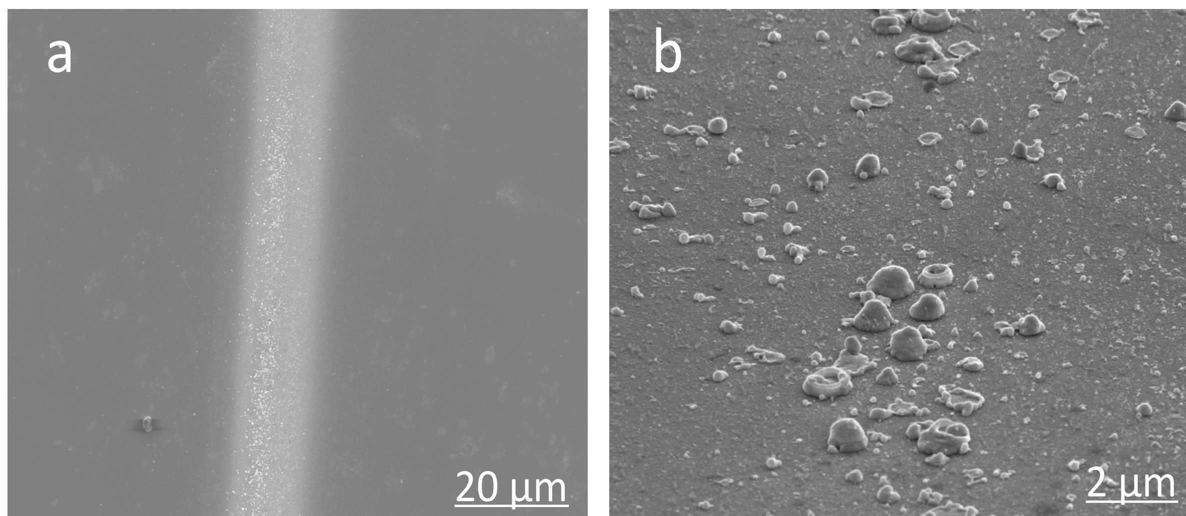

Figure 6.24: *Scanning electron micrographs of transferred 40 nm permalloy on silicon substrate with distance between D/A less than 10 µm with pulse energy 0.1 µJ.*

Even lower pulse energy of 60 nJ was used, still under vacuum, but with the donor and acceptor substrates in contact. The nature of the transferred material is similar to previous attempts with substrate separations less than 10 µm, with it appearing as scattered debris (Fig. 6.25). These debris have out-of-plane dimensions of several hundred nanometres while the donor substrate showed relatively uniform removal of the 40 nm thick permalloy film (Fig. 6.26). This suggest that the transferred material formed a liquid, either in the gas phase or on the acceptor substrate surface, and formed droplets due to surface tension before solidifying after cooling.

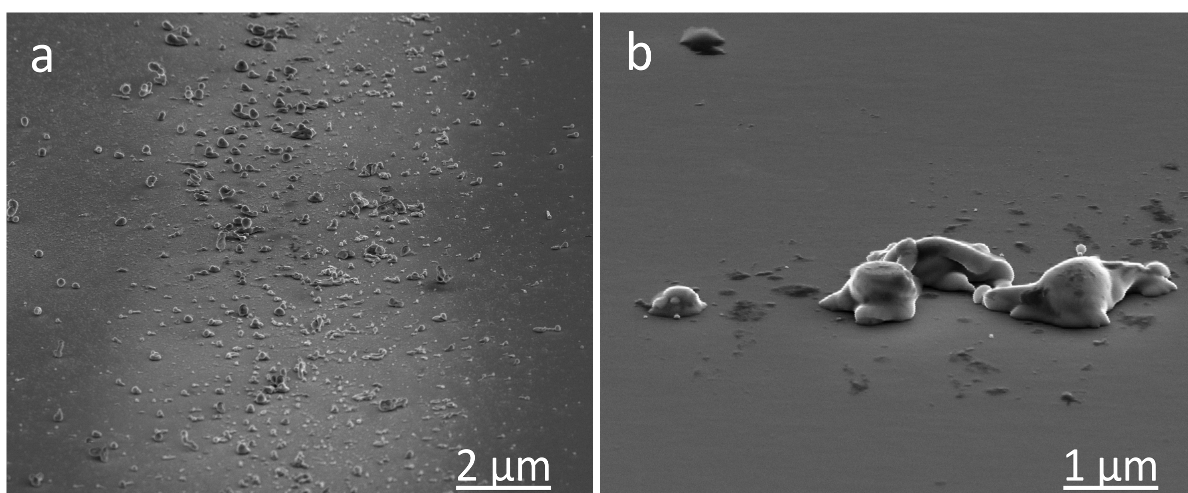

Figure 6.25: *Scanning electron micrographs of transferred 40 nm permalloy on silicon substrate without distance between D/A using pulse energy 60 nJ.*

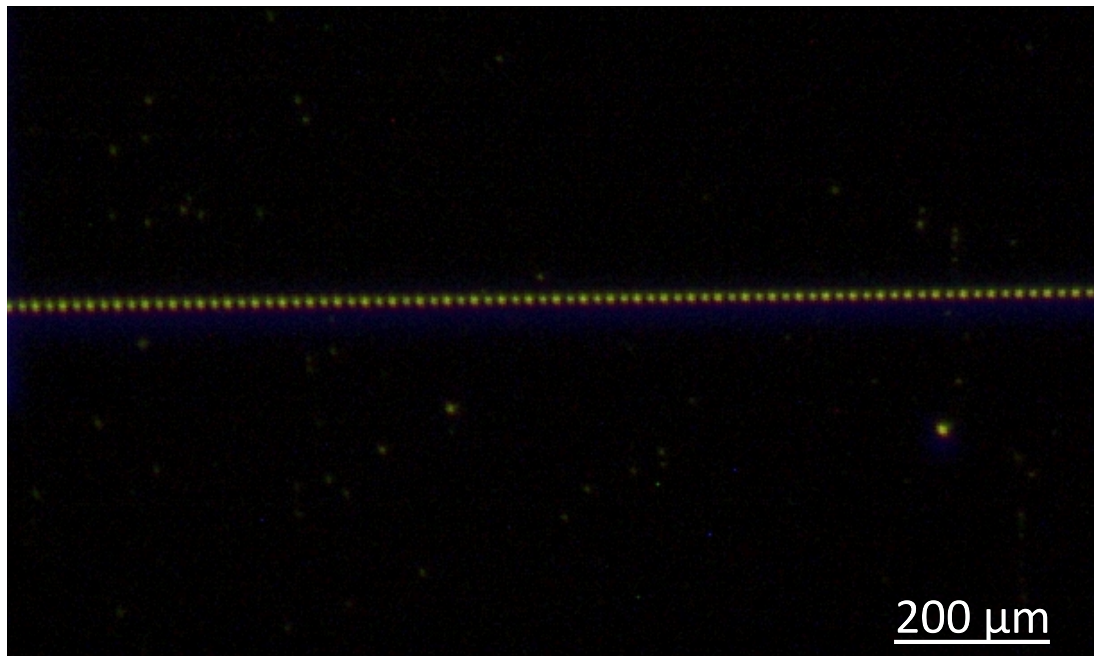

Figure 6.26: *Optical microscopy images of donor substrates following LIFT ablation (40 nm thick permalloy) using pulse energy 60 nJ.*

The nature of the material transfer was also investigated by performing LIFT on 40 nm thick permalloy onto a glass acceptor substrate (instead of silicon), with and without separation between the donor and acceptor substrates. The transferred material (Fig. 6.27) again appeared as a distribution of debris but closer analysis (Fig. 6.27b) shows that the transferred objects were smoother than previously. This suggests that either the different surface energy of glass compared to silicon promotes greater balling of the material and / or the lower thermal conductivity of glass (1 W. m^{-1}. K^{-1} [143]) compared to silicon (130 W. m^{-1}. K^{-1} [143]) causes slower cooling rates and gives transferred atoms greater opportunities to reach minimum-energy positions by forming the more spherical structures. The thermal conductivity of metallic permalloy (9630 W. m^{-1}.K^{-1} [144]) is much higher and, assuming this remains the case for its liquid state, this will cool readily if a sufficiently conductive external heat sink (such as the acceptor substrate) is available.

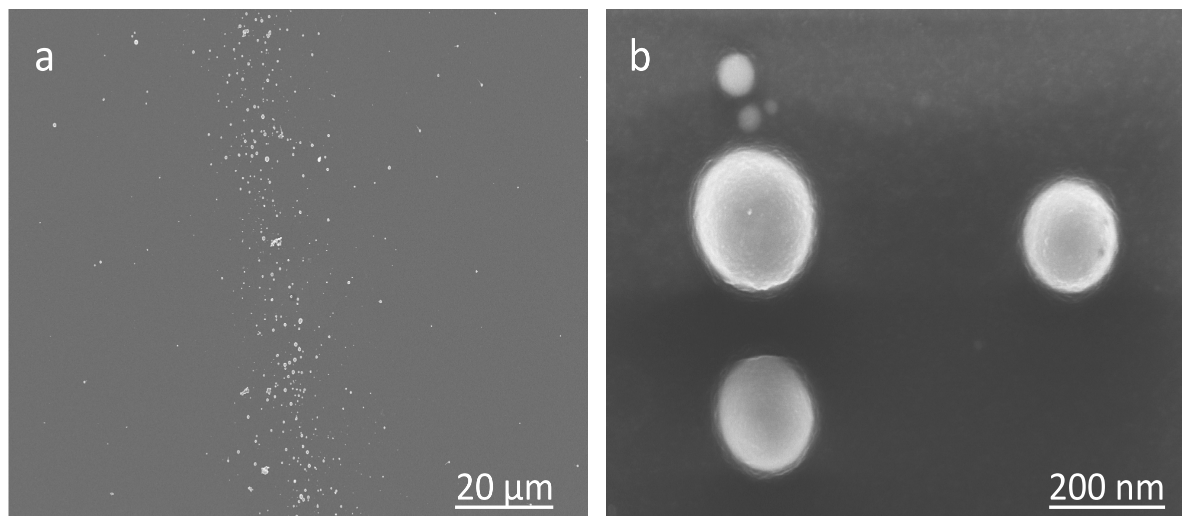

Figure 7.27: *Scanning electron micrographs of transferred 40 nm permalloy on glass substrate without distance between D/A using pulse energy 60 nJ.*

Attempts to transfer magnetic materials using linear command with thicker films from 50 nm – 90 nm with various pulse energies were also made but with similar results to those from 20 nm and 40 nm thick films shown above.

6.5 Summary

In this chapter, we have presented the main attempts to transfer permalloy thin film material as patterned structures with the Laser Induced Forward Transfer (LIFT) process using three laser systems. Multiple and single laser pulses at each transfer point were investigated (using commands 'linear' and 'Dwell' in the A3200 sample position control software). The film thickness, scanning speed, pulse energy, distance between donor and acceptor substrate, operating LIFT under vacuum or atmospheric conditions and the acceptor material were varied. However, none of this allowed the thin film morphology to be transferred to the acceptor substrate and the permalloy appeared as debris particles. LIFT performed at atmospheric pressure resulted in weak adherence to the acceptor substrate. This appeared to be due to a low mean free path of ablated species and their consequent thermalization before deposition, and was overcome by conducting the experiment in a vacuum. The size of these particles suggested that the permalloy melts either in the gas-phase following ablation or on the acceptor substrate before solidifying into droplets. A lower thermal conductivity substrate

(glass rather than silicon) resulted in more spherical droplets, which is consistent with slower cooling through the melting point and consequently longer for atoms to have high surface mobility and become arranged into positions to minimise droplet surface energy. Where measured, no ferromagnetic response could be measured by MOKE but the droplets may be superparamagnetic. This could be tested in future with larger areas of deposition with a highly sensitive magnetometry technique such as with a superconducting quantum interference device magnetometer (SQUID). Attempts to reduce the energy of ablated species through larger donor-acceptor substrate separations at atmospheric pressure resulted in a loss of particle adhesion to the acceptor substrate.

As motioned in §4.5.3, LIFT was used successfully to form wide range of materials from metals to biomaterials. That can refer to strong possibility to transfer magnetic materials successfully in the future using new parameters as in following.

In future a very high thermal conductivity substrate could allow deposited material to become cooled quickly and prevent or minimise surface mobility of ablated species. The free surface energy of the acceptor material or a coating on the acceptor could be adjusted to promote the LIFT deposited material to form a film when in the liquid state. Alternatively, the donor film design could be adjusted to include a low melting point sacrificial underlayer *"Dynamic Release Layer*" (DRL) to permalloy that absorbs the incident laser light and ablates, transferring the overlying permalloy layer as a solid layer. This has been used previously to transfer for instance: polymer [130], [145], aluminium [97], and liposomes and DNA[130]. A similar effect might be achievable with a single layer of permalloy that is thicker than its optical absorption depth at the laser wavelength, with the permalloy closest to the substrate exploding into the gas phase and forcing the surface regions towards the acceptor substrate as a solid. Of course, other magnetic materials could be investigated, particularly if they have different melting points or liquid surface energy to permalloy. It might also be possible to adjust the laser source to avoid heating the ablated species, wither with ultra-violet (UV) wavelengths or being able to use single ultra-short (femtosecond) pulse lengths. This wasn't possible here due to the high pulse repetition rate of the Ti: sapphire laser and would require a pulse picker to achieve. The benefit of being able to achieve LIFT patterning of magnetic materials remains extremely rapid fabrication of microstructures. Although many difficulties

were encountered here, the route may still be achieved in future.

All the previous challenges faced in this part of the project, the solutions and results we obtained, and suggestions for future work are summarised in the flowchart in fig 6.28.

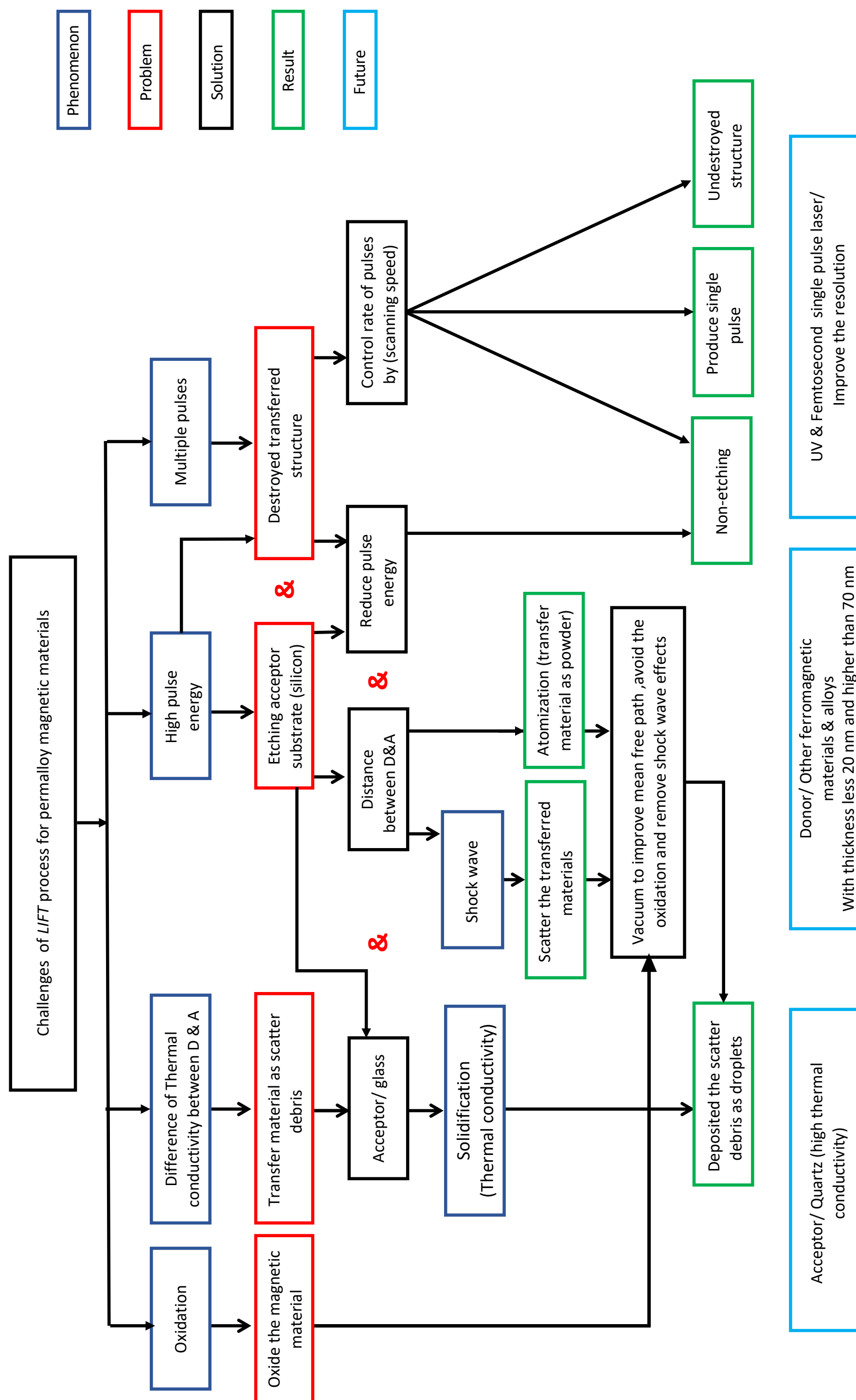

Figure 6.28: *Simple flowchart of: phenomena, problems, solutions and results that were seen for transfer of permalloy magnetic materials by LIFT as well as suggested future actions.*

Chapter 7: Laser direct writing subtraction (LDW-) fabrication of magnetic structures

7.1 Introduction

This chapter presents the results of laser direct writing-subtraction (*LDW-*) of micro/nano-scale permalloy structures. One-dimensional (1D), two-dimensional and (2D) structures were fabricated and tested by fMOKE and imaged with optical microscopy, AFM and SEM. The 1D structures show a width dependent coercivity, while various 2D magnetic structures, including arrays of squares, rectangles and rhombic structures also show a shape-dependent magnetisation response. These are all fabricated by using pulsed laser ablation to remove unwanted regions of a thin film, which allows user-defined arrays covering from almost 1 mm^2 up to over 2 mm^2 to be fabricated in a single dry processing step taking just 10 – 85 s. Millimetre-length permalloy wires of different micro-scale widths are also patterned and their width-dependent magnetisation response measured using anisotropic magnetoresistance (AMR) and tested by fMOKE and imaged with optical microscopy. This demonstrates the potential of *LDW-* rapid fabrication of magnetic structures to create magnetic field sensors with tailored sensitivity.

7.2 One-dimensional magnetic structures

Micro/nano-scale magnetic wires were fabricated from permalloy thin films using the Alphalas diode-pumped solid state (DPSS) 800 picosecond pulse width laser system (see §5.3.2). After initial studies of the capabilities of this approach, structures were fabricated systematically with a range of wire widths, sample scanning speed, film thickness, number of wires, laser fluence and pulse overlap ratio. The wires fabricated are connected with the thin membrane at the ends.

7.2.1 Initial attempts of 1D structure fabrication

The initial attempts investigated the capability of the ps pulse width laser system to fabricate 1D magnetic structures with high resolution in the shortest time possible as well as controlling the overlap between laser pulses. The magnetic properties of patterned structures were measured using the fMOKE system (see §5.5.1).

The first attempt to fabricate magnetic wires used a pulse energy of 1.43 μJ and a pulse repetition rate of about 3.5 kHz. This gave an ablation spot diameter of about 4 μm which corresponds to a fluence of approximately 11 J.cm^{2}. The sample scanning speed was adjusted to control the laser pulse overlap on films (see §5.3.4). An array of 50 magnetic wires of length 3.00 mm was fabricated from a 90 nm thick permalloy film (on glass) by creating ablation lines separated by 6.00 μm (Fig. 7.1) and using a sample scanning speed of 10 mm.s^{-1} to create 30% pulse overlap. The magnetic structures were created by the untouched material between the ablation lines. The ablation spot diameter and overlap ratio were measured by AFM of the structure in fig 7.2.

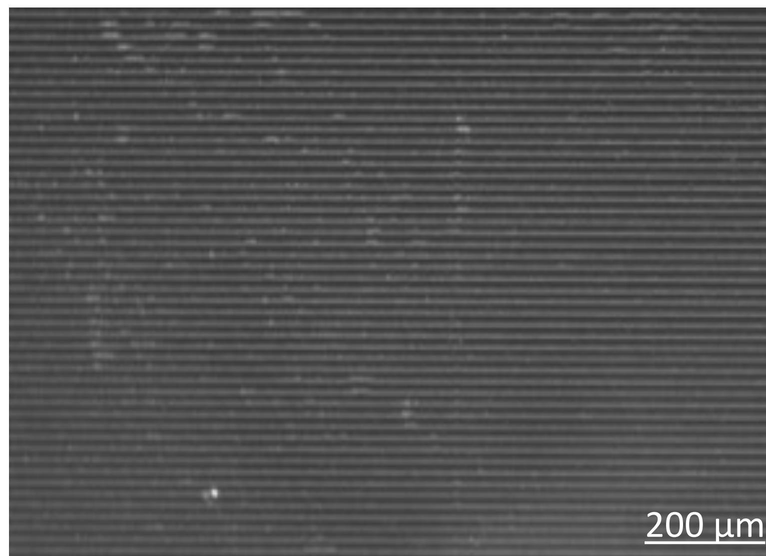

Figure 7.1: *Optical microscopy image of part of an array of 50 permalloy wires fabricated by LDW-, with each wire of approximately 4 μm width. The light regions are the magnetic material while the dark regions are ablated areas.*

Closer inspection of the wires by AFM revealed that the wire edges had an undulating profile (see §5.4.1). The phase difference between undulations on opposite wire sides was

random, due to the precise location of laser pulses not being controlled. The wires had an average from 2.0 μm maximum width of 2.1 μm and an average minimum width of 1.3 μm, i.e. a maximum difference in wire width of about 1.7 μm. Variation in wire width because the undulation side profile of wire as explained in § 5.4.1 as shown in AFM images of this magnetic wires (Fig. 7.2). The time required to fabricate this 300 μm x 3 mm array was just 25 s.

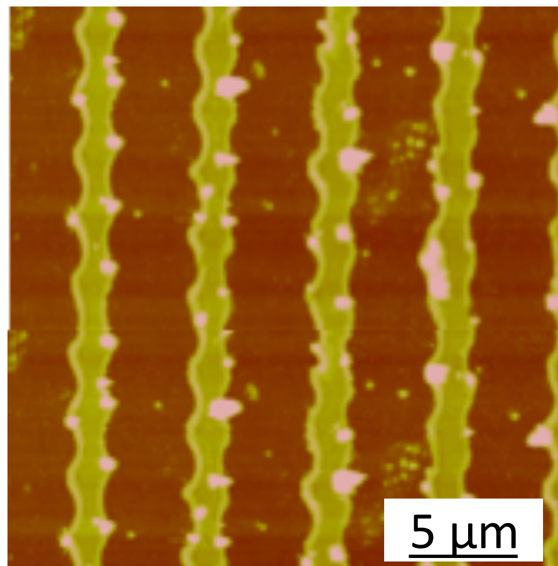

Figure 7.2: *AFM images of permalloy wires created by LDW- using a sample scanning speed of 10 mm/s, ablation line separation of 6 μm and laser pulse overlap of 30%. The light regions are the magnetic wires while the dark are ablated areas.*

An array of narrower wires was fabricated to investigate the effect of laser system parameters further. The array was again made up of 50 wires of length 3.00 mm but the distance between the ablation lines was reduced to 3.0 μm. The pulse energy was adjusted to 30 nJ and pulse repetition rate to about 5 kHz, which allowed an ablation spot of approximately 1.85 μm diameter, to be achieved and average wire widths of about 1.15 μm (Fig. 7.3). The scanning speed used here was 5.0 mm. s^{-1}, which gave a pulse overlap ratio of about 46% but increased the array fabrication time to 43 s. The non-linear increase in the time of fabrication will be discussed below.

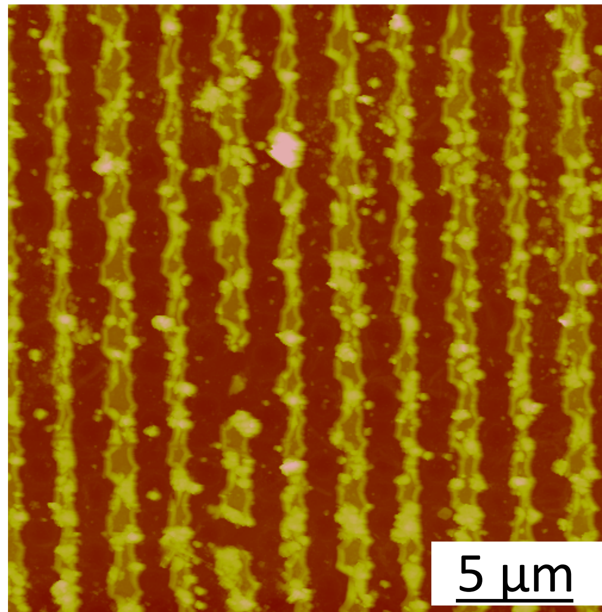

Figure 7.3: *AFM image of permalloy wires created by LDW- fabrication using a sample scanning speed of 5 mm/s, ablation line separation of 2.9 µm, ablation spot diameter of 1.85 µm and pulse overlap of 46%. The light regions are the permalloy structure while the dark regions are ablated areas.*

Figure 7.4 shows a section analysis of an AFM scan and Fig. 7.5a 3D optical image from wires of different widths. This shows that the edges of fabricated structures are generally thicker than the thin film they were fabricated from. This appears to be either due to re-deposition of ablated species and/or some breaking or twisting of the film at the edges of the ablation spot. These are likely to be affected by the optical geometry adopted here of passing the laser beam through the glass substrate onto the rear of the magnetic thin film, which results in the greatest energy density being absorbed at the film-substrate interface, rather than at the surface for direct irradiation of the film. The AFM section analyses showed that the edge profile height was greater for narrower wires (1.15 µm width compared to 1.7 µm width). This may have been due to the edge features on either side of the wire coalescing for the narrower features.

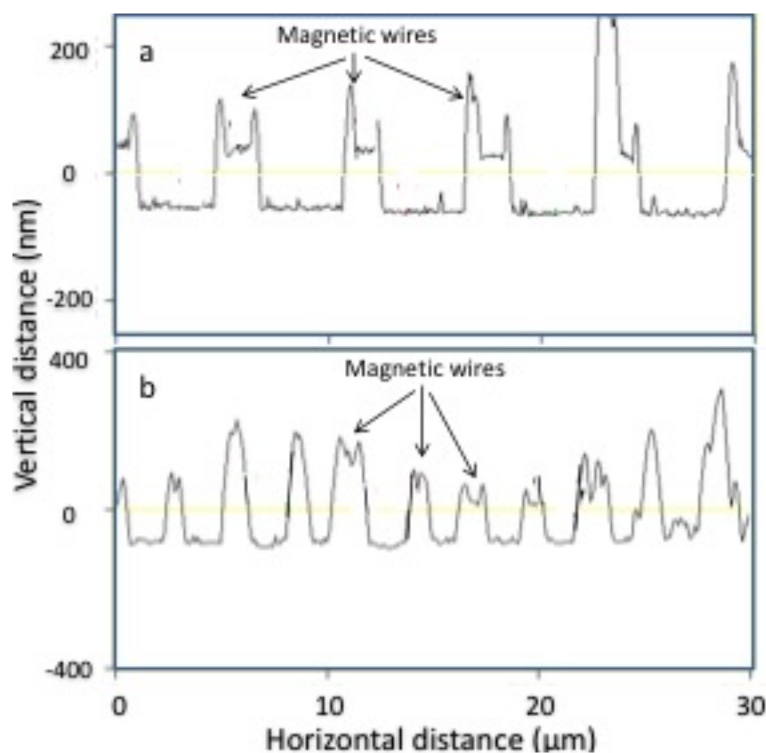

Figure 7.4: *Atomic force microscopy section analysis of a) 1.7 µm and b) 1.15 µm wide permalloy wires fabricated by LDW-.*

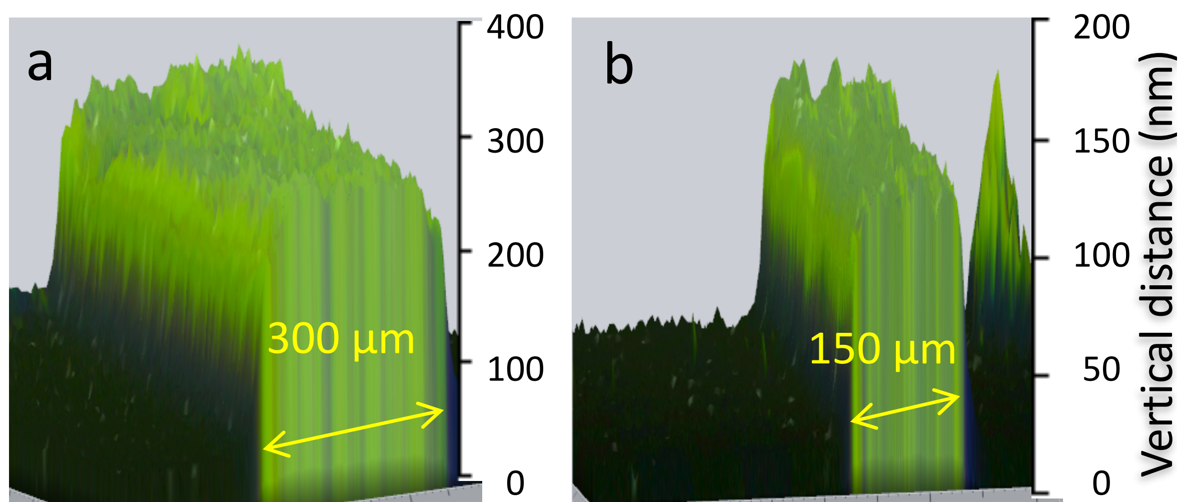

Figure 7.5: *Three dimensional optical microscope images of LDW- fabricated magnetic wires with widths a) 1.7 µm and b) 1.15 µm.*

The magnetic properties of 90 nm thick permalloy thin film and micro-scale structures shown in Figs. 7.2 and 7.3 were measured using the fMOKE system. The measurements were performed with both the fMOKE sensitivity direction (in the longitudinal Kerr configuration)

and the applied magnetic field were applied parallel to each other, along the wire long (magnetic easy) axis and short (magnetic hard) axis to study the effect of shape anisotropy for both magnetic wires.

The magnetisation hysteresis loop in Fig 7.6. was measured from a thin film region of the permalloy sample. The low coercivity of 4 Oe confirms that the film was behaving as a soft ferromagnetic material, as expected (see § 2.4.1).

The long axes hysteresis loops of the magnetic structures showed a characteristic easy axis magnetic response, taking a square shape with coercivity of 16 Oe for the 1.7 µm wire width (Fig. 7.7a) and 39 Oe for the 1.15 µm wire width (Fig. 7.8a). The hysteresis loop obtained from the short axis direction of the wider wire array (Fig. 7.7b) showed near-zero remanence and a shape consistent with hard axis behavior. The equivalent loop from the array of narrower wires offered poor signal-to-noise ratio.

These loop shapes demonstrate that shape anisotropy was responsible for determining the magnetic behaviour (i.e. the demagnetizing field along the long axis is weaker than along short axis as explained in §2.2.2 and §2.5.1). Furthermore, the increase in magnetic coercivity from 16 Oe for the 1.7 µm wide wires to 39 Oe for the 1.15 µm wide wires also demonstrates the dominant influence of shape anisotropy [146]. This indicates that the fabrication method was successful in creating each wire as a single magnetic entity.

A hysteresis loop measured from 50 magnetic wires of width 1.15 µm (Fig. 7.8a) showed additional low field steps because of a contribution to Kerr signal from the surrounding thin film. Hereafter, therefore, the number of patterned wires within an array was increased to at least 75. Figure 7.8b shows the hysteresis loop obtained from the short axis direction of the wires array.

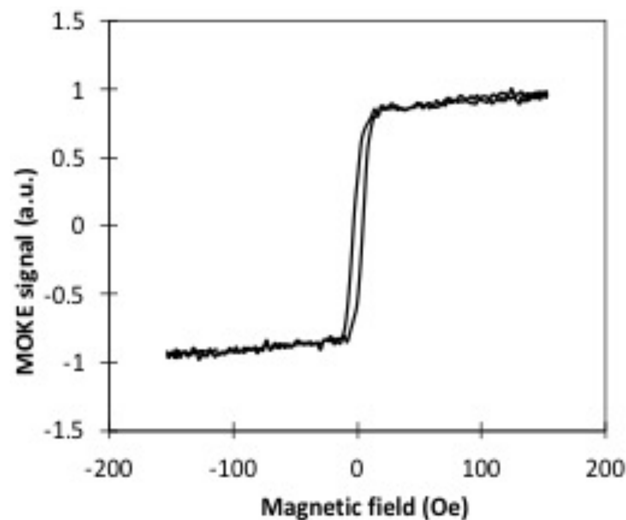

Figure 7.6: *Magnetisation hysteresis loop of 90 nm thick permalloy thin film measured by fMOKE.*

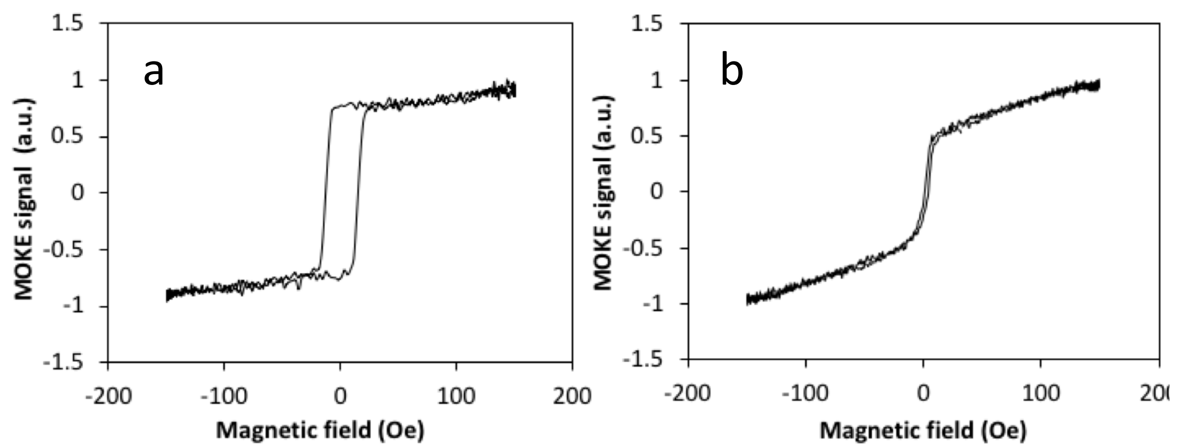

Figure 7.7: *Magnetisation hysteresis loops of magnetic wire arrays with wire width of 1.7 µm along a) long axis and b) short axis.*

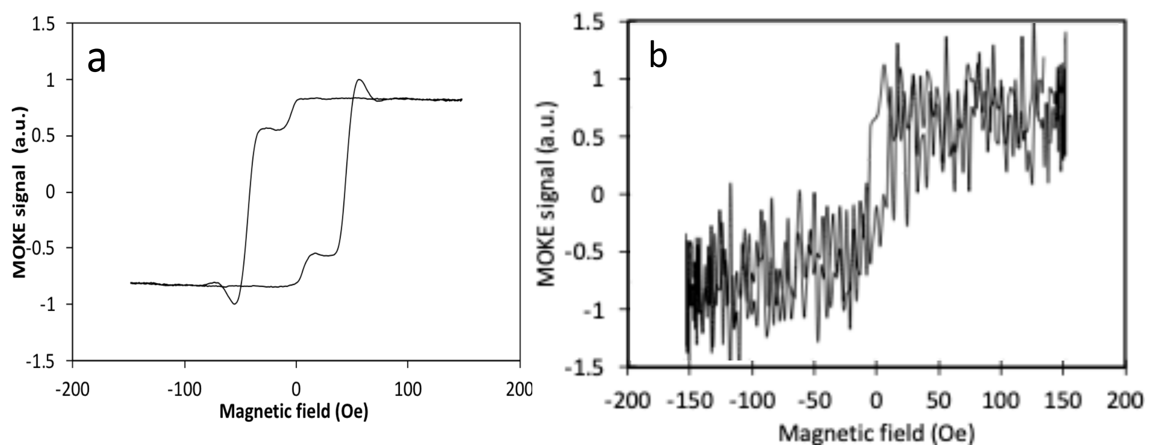

Figure 7.8: *Magnetisation hysteresis loops of magnetic wire arrays with wire width of 1.15 µm along a) long axis and b) short axis.*

7.2.2 Width variation of magnetic wires

Arrays of magnetic wires of different widths were fabricated from a 90 nm thick permalloy thin film (on glass) by *LDW-* using the 800 picosecond pulse length system and varying the centre-to-centre spacing between ablation lines between 2.0 μm and 8.6 μm. These were fabricated using a laser fluence just above the 350 mJ.cm^2 ablation threshold (pulse energy 10 nJ, pulse repetition rate 6 kHz), which gave an ablation spot diameter of 1.85 μm. The sample scanning rate was controlled to be 7.5 mm. s^{-1} which gave a laser pulse overlap of 30%.

Figures 7.9 to 7.23 shows SEM images of parts of each wire array. The undulations in wire edges are again clear. Non-ablated material is also seen along the ablation lines. This is likely to be a consequence of choosing a laser fluence close to the ablation threshold and shot-to-shot variations in the laser pulse energy causing the incident fluence to sometimes be lower than the threshold value. There is also a degree of possibly re-deposited material, as seen above. However, the wire structures are nonetheless clear in all structures. Figure 7.24 shows the wire width (measured as an average of the minimum and maximum wire widths for each array) as a function of ablation line separation. The wire widths were as large as 6.75 μm for the 8.6 μm ablation line separation (Fig. 7.9) and as narrow as 150 nm for the 2 μm ablation line spacing (Fig. 7.23).

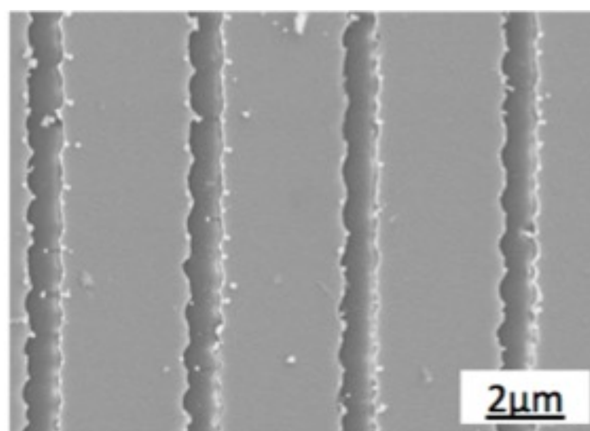

Figure 7.9: *Scanning electron micrograph of permalloy wires with an LDW- ablation line separation of 8.6 μm and wire width 6.75 μm.*

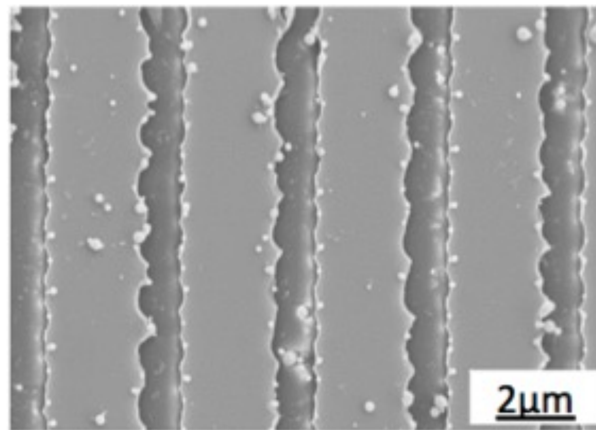

Figure 7.10: *Scanning electron micrograph of permalloy wires with an LDW- ablation line separation of 5.6 µm and wire width 3.75 µm.*

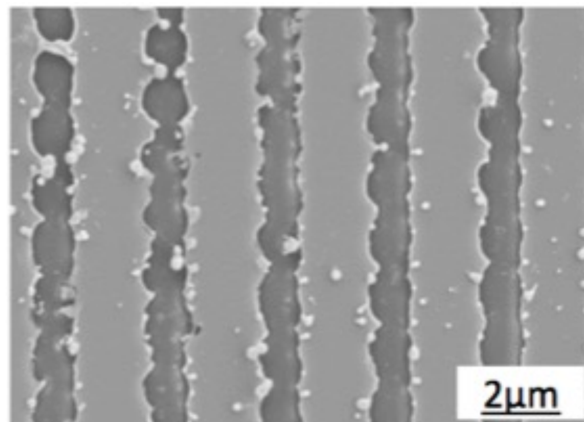

Figure 7.11: *Scanning electron micrograph of permalloy wires with an LDW- ablation line separation of 4.6 µm and wire width 2.75 µm.*

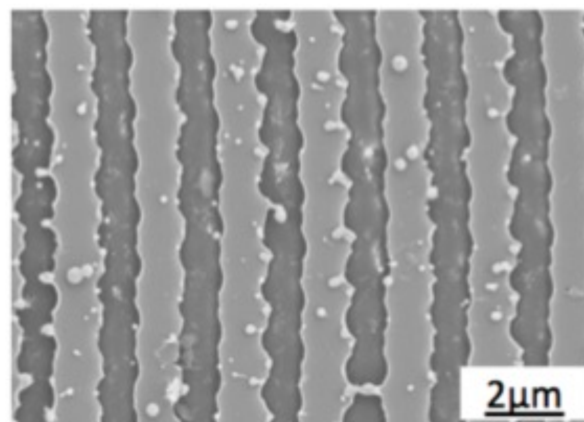

Figure 7.12: *Scanning electron micrograph of permalloy wires with an LDW- ablation line separation of 3.6 µm and wire width 1.75 µm.*

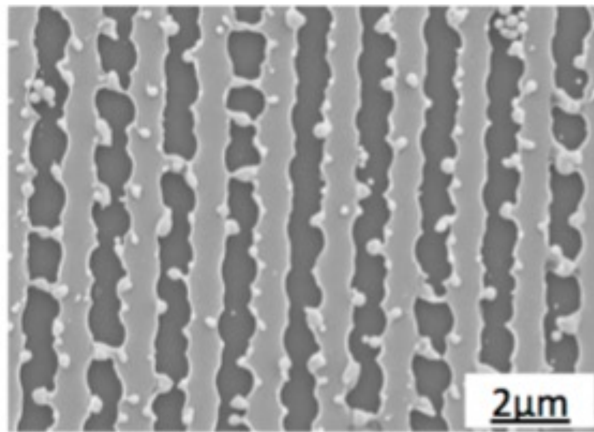

Figure 7.13: *Scanning electron micrograph of permalloy wires with an LDW- ablation line separation of 3.1 µm and width 1.25 µm.*

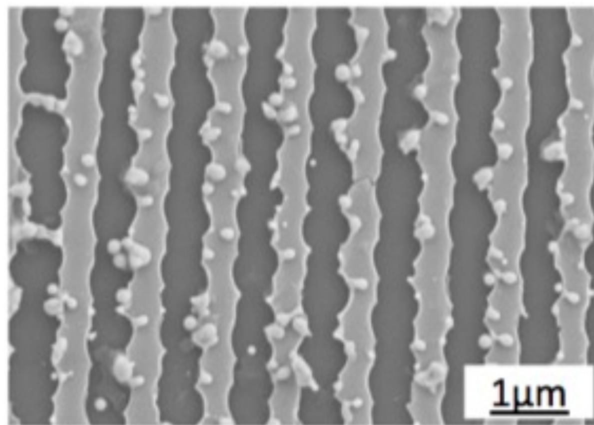

Figure 7.14: *Scanning electron micrograph of permalloy wires with an LDW- ablation line separation of 3.0 µm and wire width 1.15 µm.*

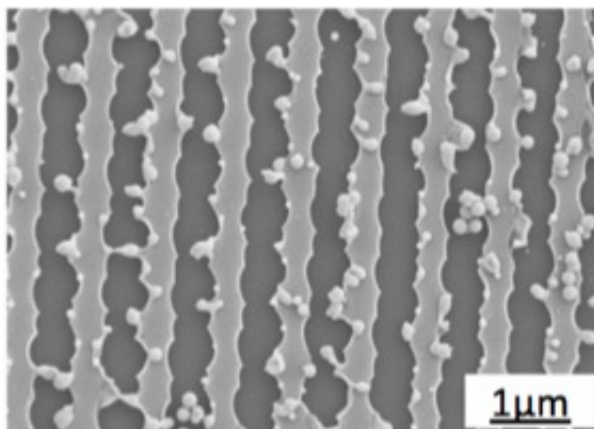

Figure 7.15: *Scanning electron micrograph of permalloy wires with an LDW- ablation line separation of 2.8 µm and wire width 950 nm.*

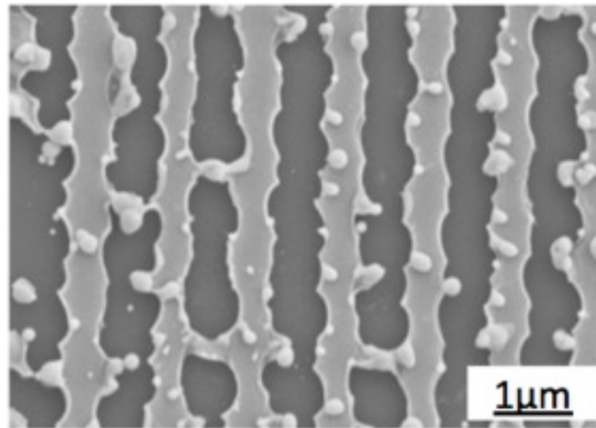

Figure 7.16: *Scanning electron micrograph of permalloy wires with an LDW- ablation line separation of 2.7 μm and wire width 850 nm.*

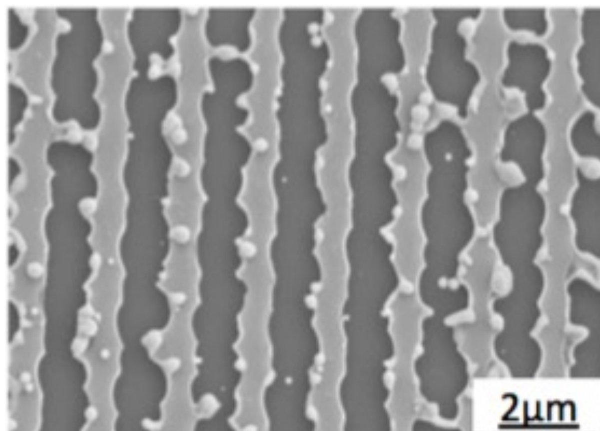

Figure 7.17: *Scanning electron micrograph of permalloy wires with an LDW- ablation line separation of 2.6 μm and wire width 750 nm.*

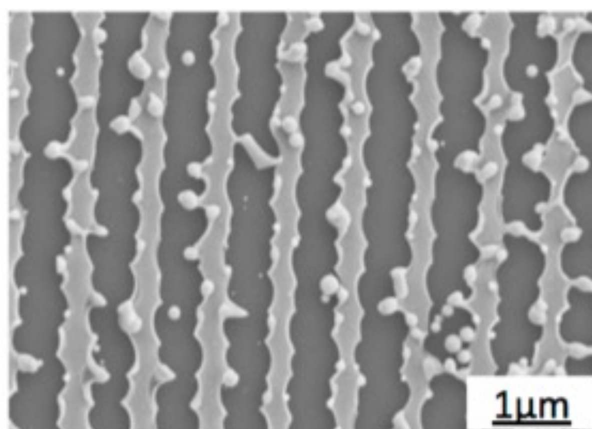

Figure 7.18: *Scanning electron micrograph of permalloy wires with an LDW- ablation line separation of 2.5 μm and wire width 650 nm.*

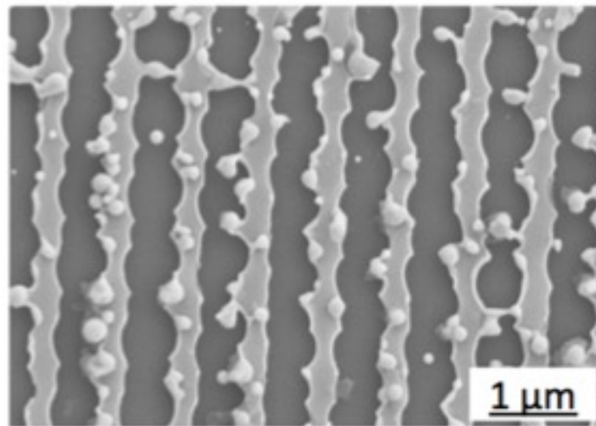

Figure 7.19: Scanning electron micrograph of permalloy wires with an LDW- ablation line separation of 2.4 µm and wire width 550 nm.

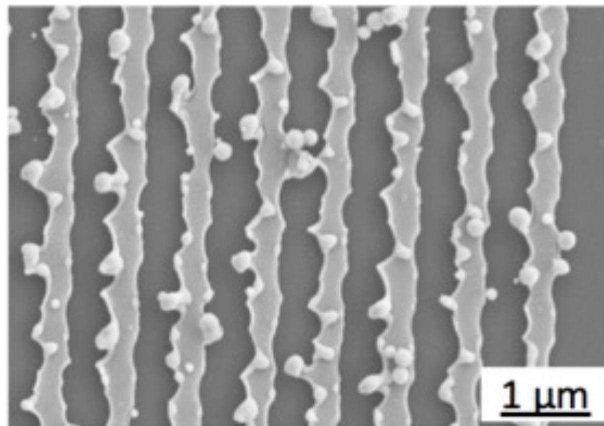

Figure 7.20: *Scanning electron micrograph of permalloy wires with an LDW- ablation line separation of 2.3 µm and wire width 450 nm.*

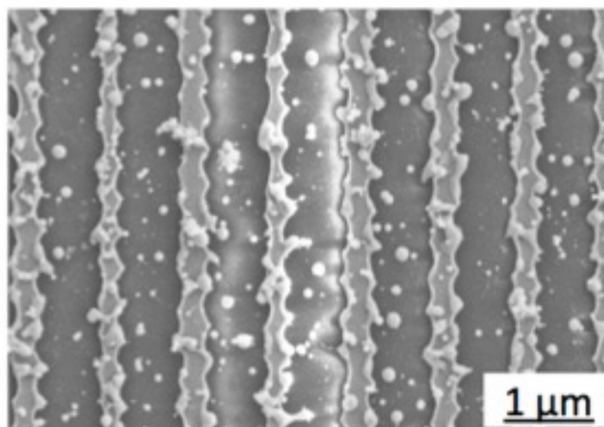

Figure 7.21: *Scanning electron micrograph of permalloy wires with an LDW- ablation line separation of 2.2 µm and wire width 350 nm.*

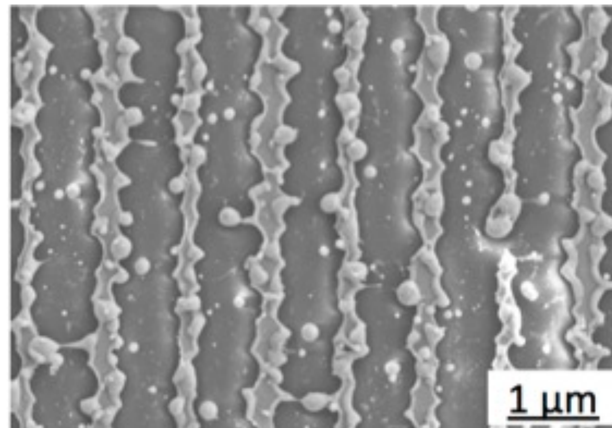

Figure 7.22: *Scanning electron micrograph of permalloy wires with an LDW- ablation line separation of 2.1 µm and wire width 250 nm.*

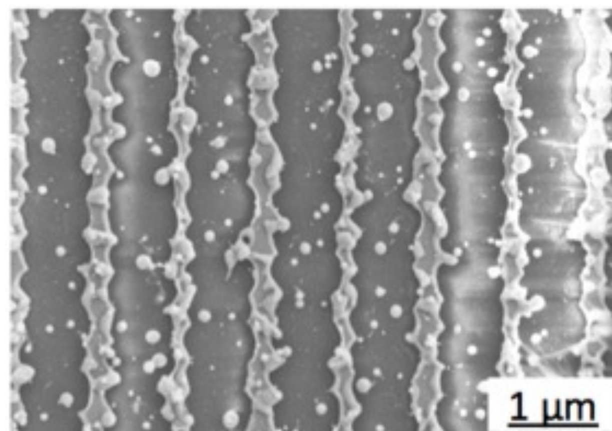

Figure 7.23: *Scanning electron micrograph of permalloy wires with an LDW- ablation line separation of 2.0 µm and wire width 150 nm.*

The undulating edge structure was measured to have an amplitude of 125 nm for all wire widths, although this results in a disproportionate loss of definition for narrower wires. The degree to which edge structure was present was characterised by a width variation parameter, ***a,*** defined as the ratio of the minimum and maximum wire widths measured across multiple positions, so that a = 1 for parallel edges and a < 1 for wave-like edges. The with variation parameter is plotted as a function of ablation line width in Fig. 7.24. This makes clear the precipitous loss of wire definition (low values of a) as the ablation line spacing approaches the same value as the ablation spot diameter. The reduced width of wires formed using more closely spaced ablation lines necessarily creates a larger relative width variation and, therefore, reduced values of a.

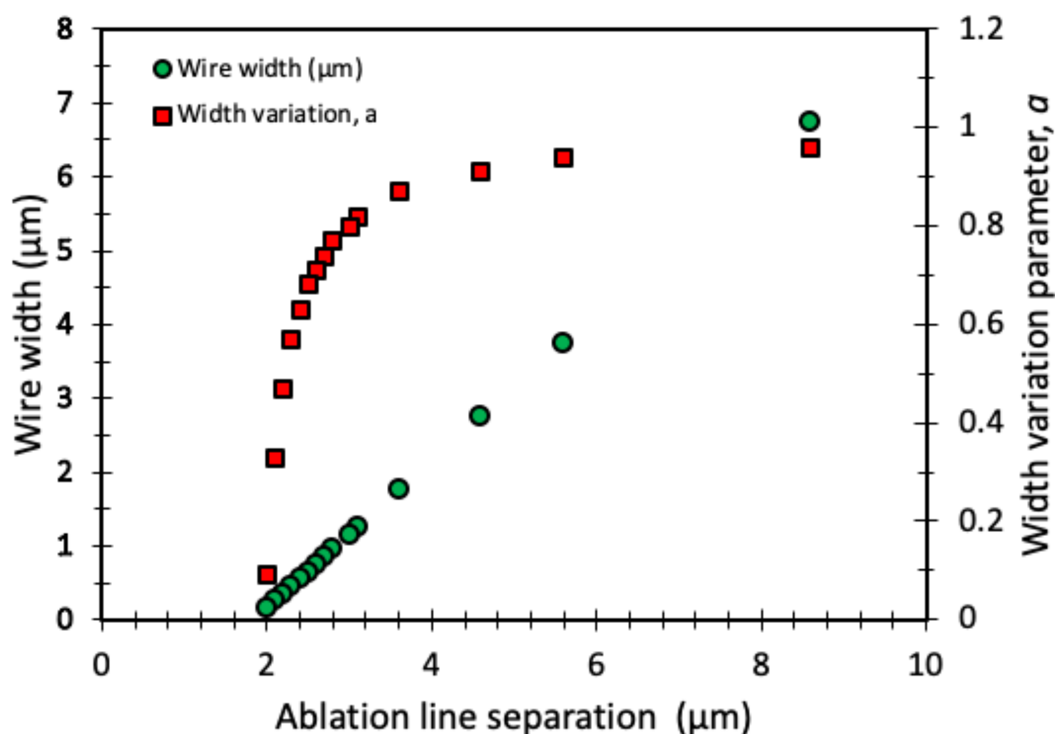

Figure 7.24: *Width of LDW- fabricated wires (squares) and width variation parameter, a (circles), as a function of ablation line separation (using 1.85 µm diameter ablation spot and 30% laser pulse overlap). Wire width is the average of minimum and maximum measured wire widths, while a is the ratio of the minimum to maximum wire widths.*

Figure 7.25 (a to j) shows magnetisation hysteresis loops measured by fMOKE obtained from the wire arrays for wire widths from 6.75 µm down to 650 nm. These were obtained with the Kerr sensitivity direction and applied field along the wires' long axis. All loops have notable easy axis character with sharp magnetisation reversal transitions, which indicates that the fabricated structures by LDW- exhibit strong shape anisotropy and may reverse via rapid propagation of domain walls injected from the adjoining film. The low field steps observed in the narrowest wires (Fig. 7.25 i to j) are due to detection of Kerr signal from the surrounding film, which contributes a relatively large signal compared to that of the small structures

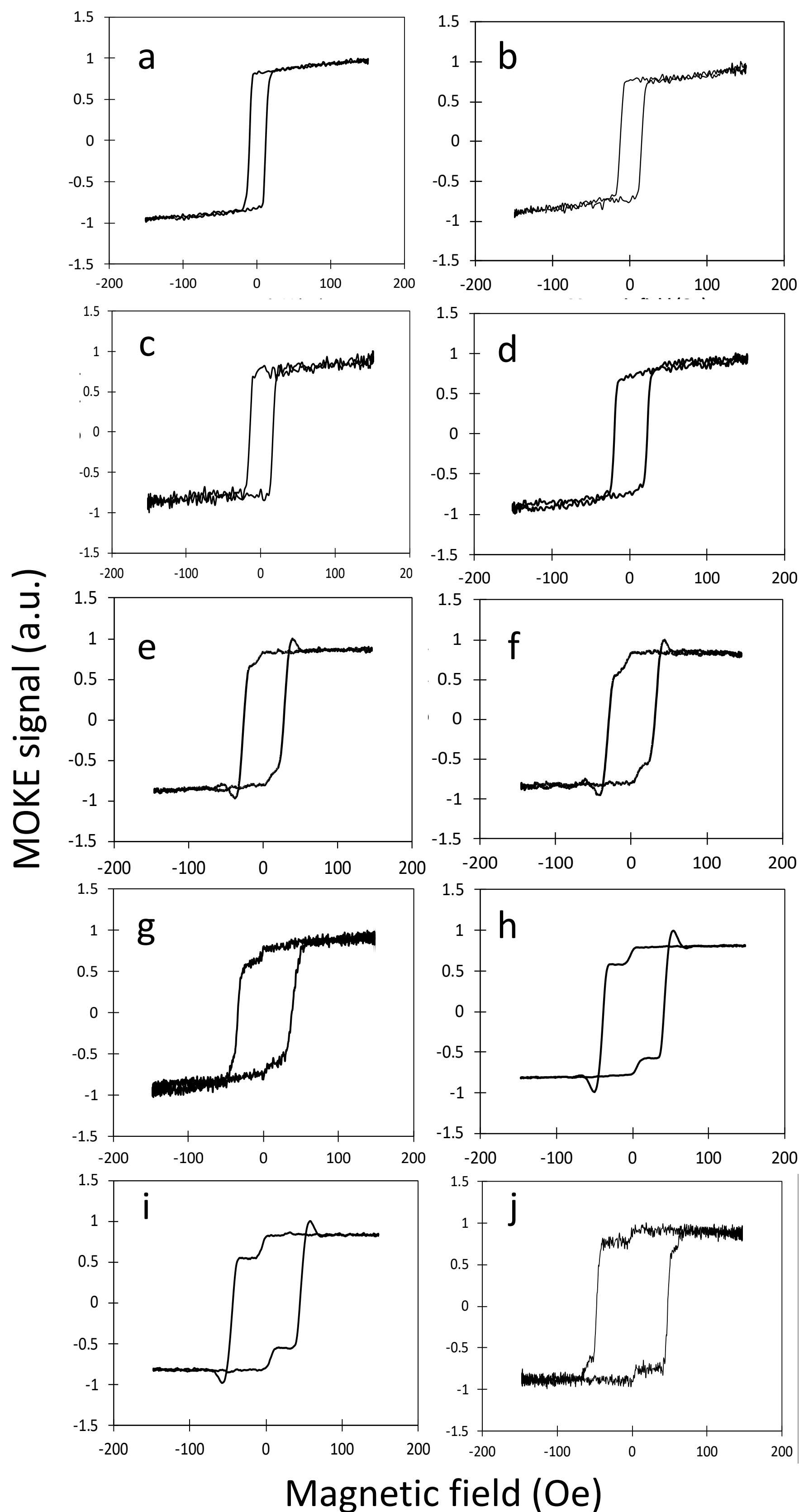

Figure 7.25: *MOKE hysteresis loops of LDW- fabricated permalloy wires of width (a)6.75µm, (b) 3.75µm, (c)2.75µm, (d)1.75µm, (e) 1.25 µm, (f) 1.15 µm, (g) 950 nm, (h) 850 nm, (i) 750 nm and (j) 650 nm.*

Figures (7.26 a to e) shows MOKE loops obtained from even narrower wires, down to 150 nm in width. Despite the apparently poor physical appearance of these structures (Fig. 7.19 to 7.23) the magnetisation reversal transitions in hysteresis loops remain reasonably sharp until the very narrowest case (Fig. 7.26 e), which nonetheless retains a remanence close to M_s.

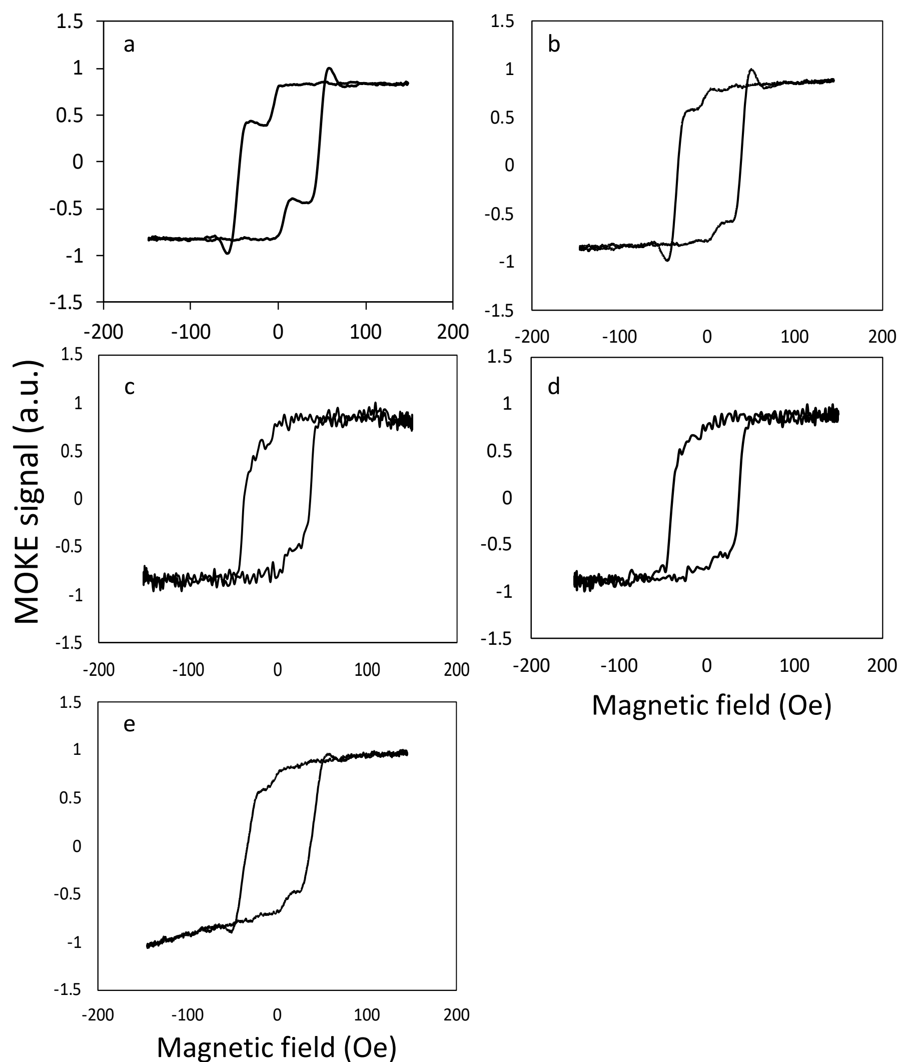

Figure 7.26: *MOKE hysteresis loops of LDW-fabricated permalloy wires of width (a) 550nm, (b) 450nm, (c) 350nm, (d) 250nm and (e) 150 nm.*

The coercivity of the wires was found to be proportional to the inverse of wire width for structures at least 650 nm wide (Fig. 7.27). This is commonly observed for well-defined soft ferromagnetic wire structures [147] but is perhaps surprising to see here given the edge profile of the laser-patterned wires. However, coercivity falls with wire width below 650 nm as the definition of the wire edges becomes increasingly poor due to re-deposited and some un-ablated areas of thin film materials. This is likely to result in increased domain wall pinning and strong local variations in shape anisotropy that soften these regions (seen as the gradual change in magnetisation in the approach to the sharp reversal events seen in Figs. 7.26 d and e).

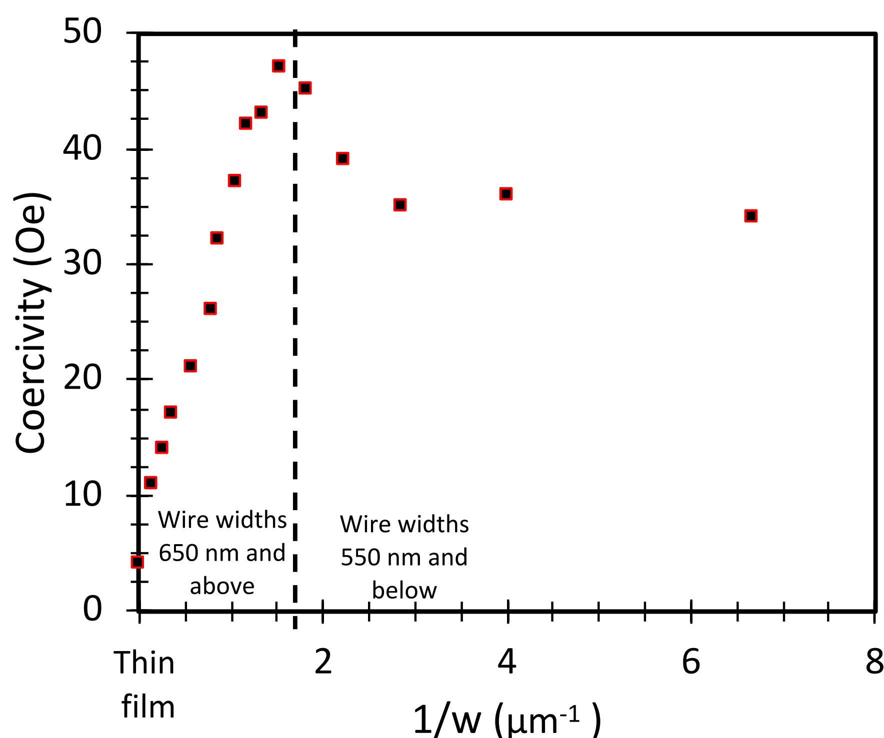

Figure 7.27: *Magnetic coercivity as function of inverse wire widths.*

This fabrication of these arrays is extremely rapid. For example, with the scan speed used of 7.5 mm. s^{-1}, the time required to fabricate 75 magnetic wires each of dimensions 550 nm × 4.0 mm was, in principle, 40s. In practice, this increased to about 85 s due to the time required to change the scan direction at the end of each line (requiring acceleration and deceleration phases). Fig 7.28 shows total fabrication time for patterning the arrays of different widths. The difference in fabrication time is slight, varying between approximately 84.5 and

87 s for the narrowest and widest wires, respectively, but the greatest rate of change is for wire widths up to 1.25 µm (due to control of stage acceleration and deceleration). Beyond this, there are only very small differences in fabrication time.

These considerations give an average effective fabrication rate here of 3.5 mm. s^{-1}. Higher repetition rate, scan speed and, for larger structures, larger focal spot size will also have a marked impact on the fabrication speed. The fabrication speed will also depend on the sample design and the degree to which different scan directions are required. An increased laser spot overlap could reduce the limit of 650 nm wire width seen here for well-described hysteresis behaviour but will increase the fabrication time of arrays. However, given the considerable proportion of time taken in moving between ablation lines (responsible for over half the fabrication time here), the increased of fabrication time can be reduced by fabricate narrower wires (higher resolution).

In general, the average fabrication time of each magnetic wire within an array of length 4 mm using a scanning speed 7.5 mm. s^{-1} was just 1.14 s.

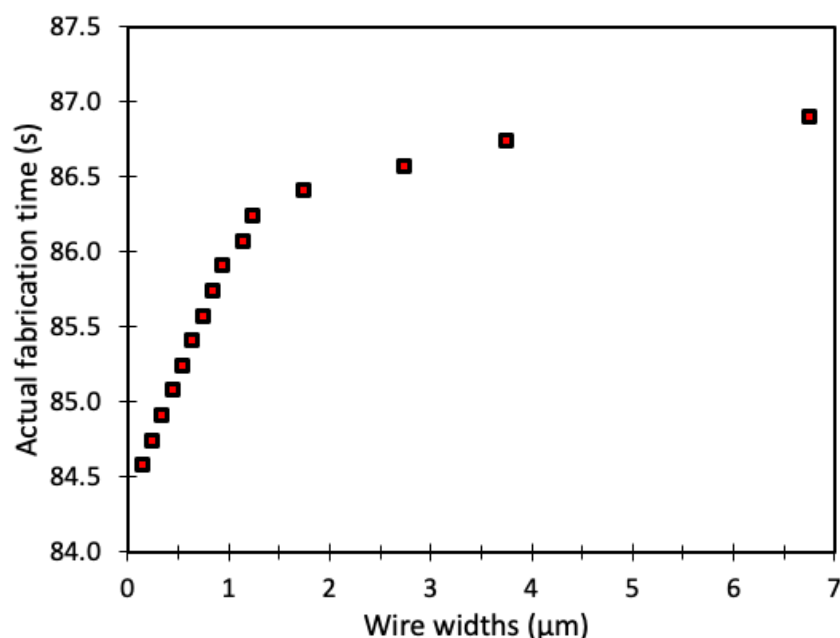

Figure 7.28: *Wire width as function of actual and designed fabrication time.*

7.3 Two-dimensional micro/nano-scale magnetic structures

The previous section described the fabrication of arrays of 1D structures (wires) from permalloy thin films by *LDW*- by rastering a sample during application of a series of laser pulses and adjusting, i.e. controlling the sample scan speed along one axis direction and stepping in the other axis direction between ablation line generation.

Here, the approach is developed further by controlling the sample position along both orthogonal in-plane axes during application of laser ablation pulses to create arrays of isolated two-dimensional (2D) micro/nano-scale magnetic elements of different shapes and aspect ratios.

The details of the laser ablation procedure are described in §5.3.2. Briefly, square and rectangular structures were fabricated from a 90 nm thick permalloy thin film on a glass substrate by using equal (for squares) or different (for rectangles) centre-to-centre distances between ablation lines in orthogonal directions ***x*** and ***y*** (§Fig. 5.14). The ratio of ablation line spacing controlled the aspect ratio of fabricated elements. Alternatively, the sample translation stages were controlled to create series of ablation lines at oblique angles to each other in to create rhombic elements (§Fig. 5.16).

The 800 ps pulse length laser system was used to fabricate the 2D structures. The parameters used here were 10 nJ laser pulse energy, 6 kHz pulse repetition rate, 1.85 μm ablation spot size and a sample scan speed during ablation of 7.5 mm. s^{-1}. This gave a pulse overlap ratio of 30% and, therefore, similar edge profiles and limitations to the 1D wires described above. Each array was made by using 76 laser ablation lines in each direction (i.e. the same number as in §7.2.2 above to create 75 wires). This created an array of 75 x 75 elements, so 5625 in total. Each ablation line was 1 mm long to reduce the stage scanning time compared to the 4 mm 1D wires created above. The proportion of the 1 mm wire lengths that became part of the final 2D array depended on the ablation line separation used in the other set of ablation wires. Figure 7.29 shows an optical microscopy image of an array of rectangular elements, each with an aspect ratio of 1.5.

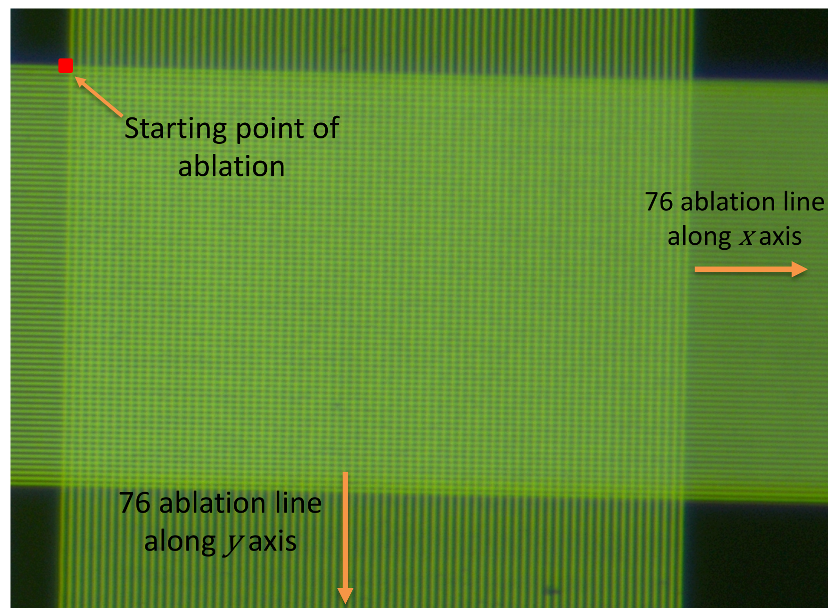

Figure 7.29: *Optical microscopy image of 5625 (75 x 75) rectangular elements with aspect ratio 1.5 (1.9 µm x 2.9 µm) fabricated by LDW- from a permalloy thin film. The full size of array is 281 µm x 365 µm. The black regions are the magnetic elements while the green regions are ablated areas.*

Figure 7.30 shows an SEM image of an array of elements created with identical orthogonal ablation line spacing of 3.75 µm. This resulted in approximately square 1.9µm x 1.9µm elements. The structures again have a curved edge profile due to the 30% laser pulse overlap, although this is less evident than was the case for the longer wires.

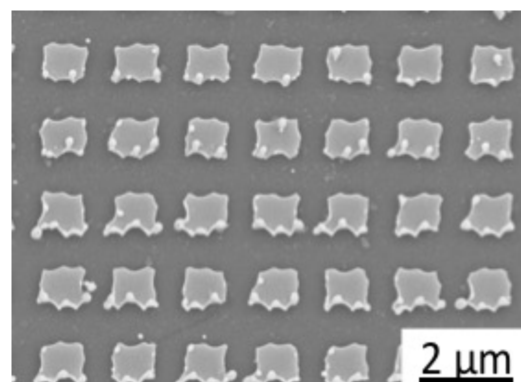

Figure 7.30: *Scanning electron micrograph of permalloy square element array, with each element approximately 1.9 µm x 1.9 µm.*

Figures 7.31 to 7.35 shows SEM images of arrays of rectangular elements fabricated with an ablation line spacing of 3.75 μm in one direction (horizontal in Fig 7.29) and 4.75, 5.75, 6.75, 7.75 and 9.85 μm in the orthogonal direction, respectively. This resulted in rectangular elements with a short side of 1.9 μm and long sides of length 2.9 μm, 3.9 μm, 4.9 μm, 5.9 μm and 8 μm giving aspect ratios of 1.5, 2.1, 2.6, 3.1 and 4.2 respectively. Edge profile distortions due to the 30% pulse overlap are visible with all structures but are particularly evident for the higher aspect ratio structures and, for these, appear to be very similar to those observed with 1D wires in §7.2.2 above.

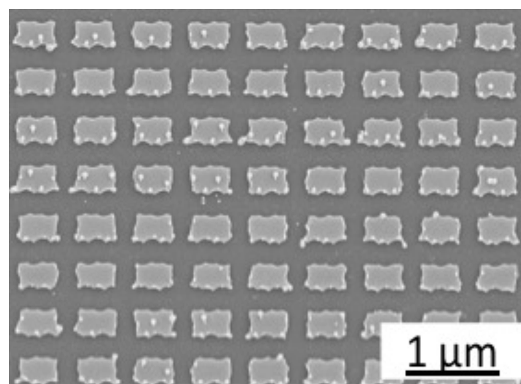

Figure 7.31: *Scanning electron micrographs of permalloy squares elements array with size of 1.9 µm x 2.9 µm.*

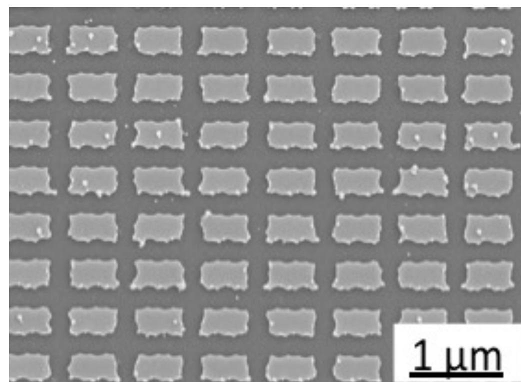

Figure 7.32: *Scanning electron micrograph of LDW- fabricated rectangular permalloy elements, each 1.9µm x 3.9µm.*

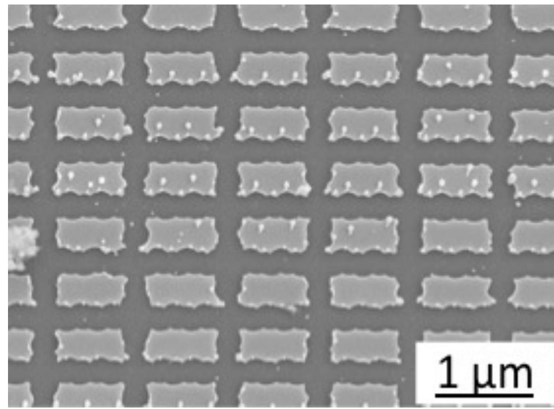

Figure 7.33: *Scanning electron micrograph of LDW- fabricated rectangular permalloy elements, each 1.9µm x 4.9µm.*

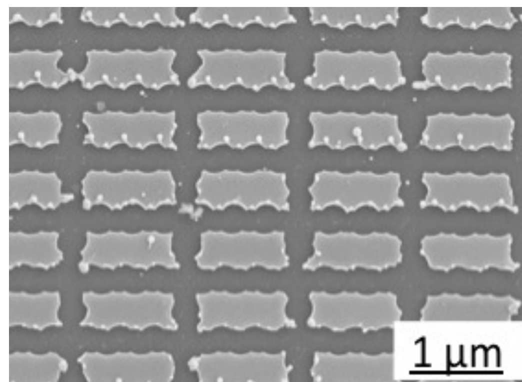

Figure 7.34: *Scanning electron micrograph of LDW- fabricated rectangular permalloy elements, each 1.9µm x 5.9µm.*

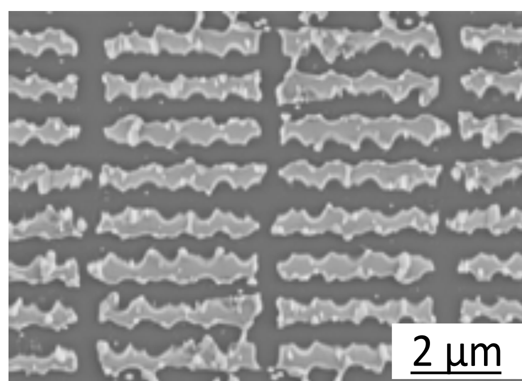

Figure 7.35: *Scanning electron micrograph of LDW- fabricated rectangular permalloy elements, each 1.9 µm x 8 µm.*

Rhombic elements were created with non-orthogonal sets of ablation lines. Figure 7.36 shows one such array created using an angle θ = 71.5° between two ablation line sets and lines within each set having a centre-to-centre separation of 3.75 μm. This resulted in structures with major and minor axis lengths 12 μm and 3μm, respectively, and was fabricated in an array measuring 364 μm x 1039 μm, making 0.189 mm^2 in area.

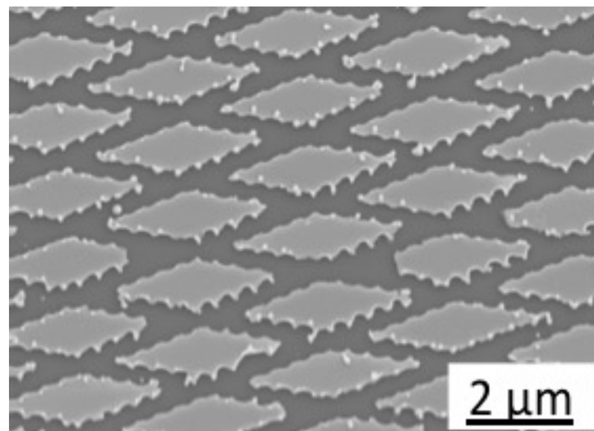

Figure 7.36: *Scanning electron micrographs of permalloy rhombus elements array with of short axes lengths 3μm x long axes lengths 12μm.*

Magnetisation hysteresis loops were obtained by fMOKE along two directions for each of the 2D structure arrays. These were along the long and short sides of rectangular elements, the major and minor axis of rhombic elements and parallel to the sides and diagonals of square elements.

The hysteresis loops obtained from along the long axis of the patterned elements (or along the side of square elements; Fig. (7.37 to 7.43a) showed sensitivity to the element geometry. However, the square and rectangular elements with aspect ratios 1.5, 2.1, 2.6 and 3.1 all exhibited very low remanence (7.37 to 7.41a), possibly due to the formation of a closure domain structure [10]. However, the hysteresis loops from rectangular elements with aspect ratio of 4.2 and rhombus elements with aspect ratio of 4 had strong easy axis character with coercivities of 12 Oe and 14 Oe, respectively, and sharp magnetisation reversal transitions (7.42a and 7.43a). It is well known that shaped ends to elements helps to stabilise magnetic domains by reducing the magnetostatic energy of single domain structure.

The higher coercivity of the rhombic structures is consistent with this and indicates that *LDW*- can produce 2D micro-scale elements with sufficiently high quality edge definition to allow shape effects to be dominant. The square shape of the hysteresis loop from rectangular elements with an aspect ratio of 4.2 appears to be a threshold value for the thickness of permalloy used here and the length scale of the fabricated elements.

This shape anisotropy is also reflected in the hard axis hysteresis loops, which generally have low remanence and a near-linear magnetisation dependence to magnetic fields at low fields (Fig. 7.38b to 7.43b). This is similar to the hysteresis loops obtained along the diagonal directions of square elements (Fig. 7.37) and the loop obtained in the minor (short) axis direction of rhombic elements (Fig. 7.43b). Many of the hard axis loops showed an anomalous signal in the approach to remanence that exceeded the saturation $M_s = \pm 1$. This is likely to be due to a degree of domain re-orientation at these points accompanied by signal contributions from either the transverse MOKE effect (sensitive to magnetisation transverse to the optical plane of incidence) or Voigt effect (sensitive to M^2 along the longitudinal direction)[148].

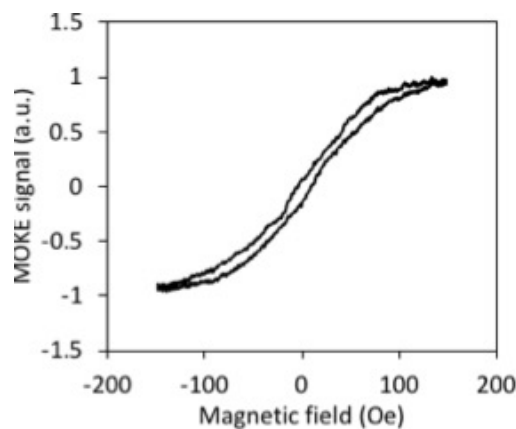

Figure 7.37: *MOKE hysteresis loops of permalloy squares elements array with size of 1.9μm x 1.9μm.*

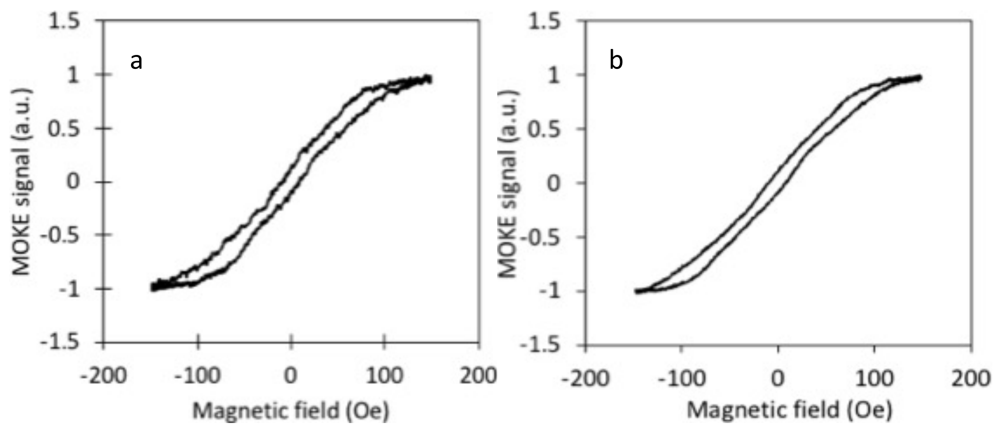

Figure 7.38: *a) MOKE hysteresis loops of permalloy rectangles elements array with size of 1.9µm x 2.9µm with aspect ratio 1.5 and b) MOKE M-H curve obtained by applied the Y magnetic field along the short axes (hard axes).*

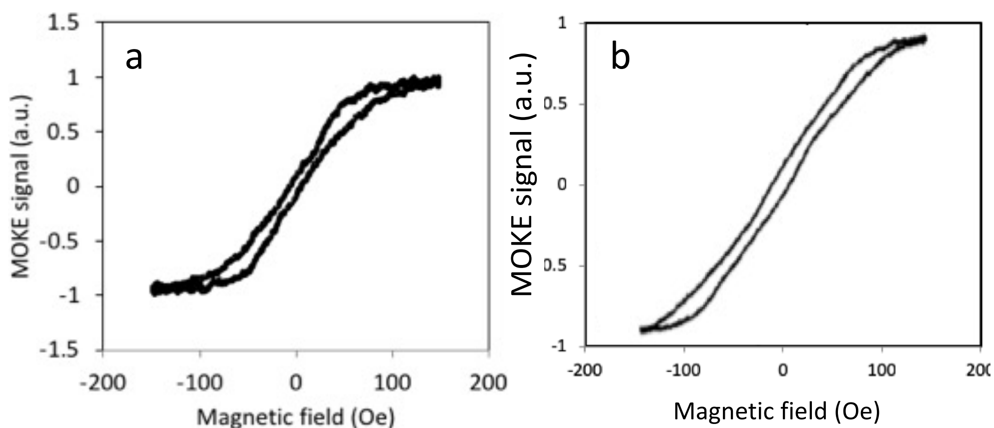

Figure 7.39: *MOKE hysteresis loops of permalloy rectangles elements array with size of 1.9µm x 3.9µm with aspect ratio 2.1 and b) MOKE M-H curve obtained by applied the Y magnetic field along the short axes (hard axes).*

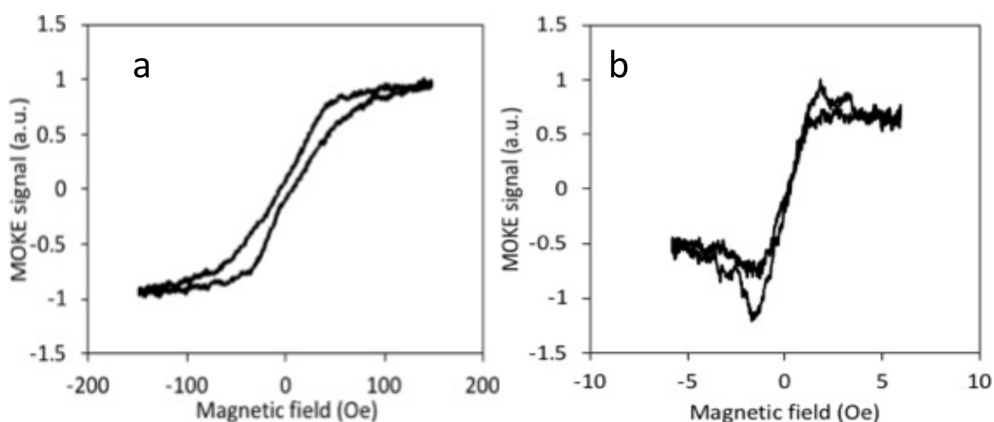

Figure 7.40: *MOKE hysteresis loops of permalloy rectangles elements array with size of 1.9µm x 4.9µm with aspect ratio 2.6 and b) MOKE M-H curve obtained by applied the Y magnetic field along the short axes (hard axes).*

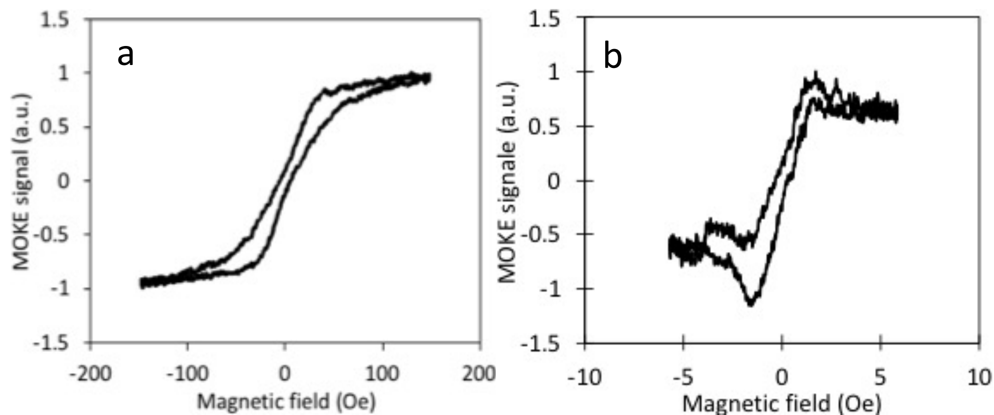

Figure 7.41: *MOKE hysteresis loops of permalloy rectangles elements array with size of 1.9µm x 5.9µm with aspect ratio 3.1 and b) MOKE M-H curve obtained by applied the Y magnetic field along the short axes (hard axes).*

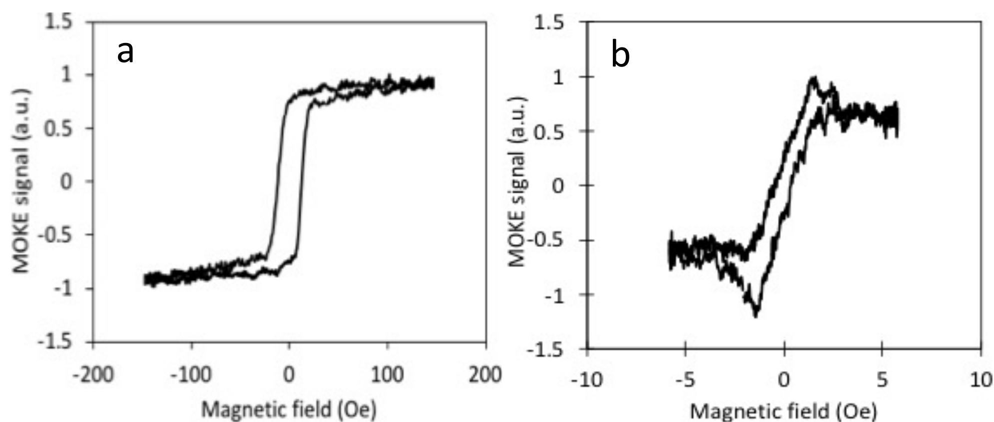

Figure 7.42: *MOKE hysteresis loops of permalloy rectangles elements array with size of 1.9 µm x 8 µm with aspect ratio 4.2 and b) MOKE M-H curve obtained by applied the Y magnetic field along the short axes (hard axes).*

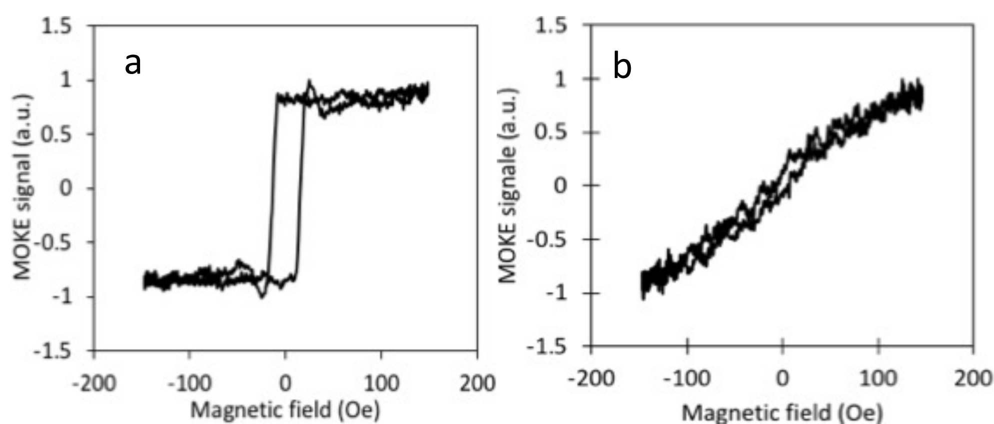

Figure 7.43: *MOKE hysteresis loops of permalloy rhombus elements with short axes lengths 3µm x long axes lengths 12µm with aspect ratio 4.0 and b) MOKE M-H curve obtained by applied the Y magnetic field along the short axes (hard axes).*

The time required to fabricate the array regions (and ignoring the additional length of ablation lines that didn't form part of an array as in Fig. 7.29) of 5625 elements was linearly dependent on the element size and, hence, the overall array size (Fig. 7.44). The array of 1.9 μm x 1.9 μm square elements investigated here (covering 0.079 mm^2 in total) was fabricated in less than 15 s (of the total 46 s required to fabricated the two sets of 76 ablation lines, each 1 mm long), or 2.7 ms per element. This increased to about 48 s for the 1.9 μm x 8.0 μm elements, covering 0.21 mm^2. The actual fabrication time of 2D magnetic structures is more than double the time to fabricate a 1D array over an equivalent area because (a) two sets of ablation line scans are required and (b) the extra time to change scan direction at the end of each ablation line is also doubled.

The average fabrication time of the 2D structures created here can be calculated as 200 $s.mm^{-2}$. However, this depends on the number and length of ablation lines used.

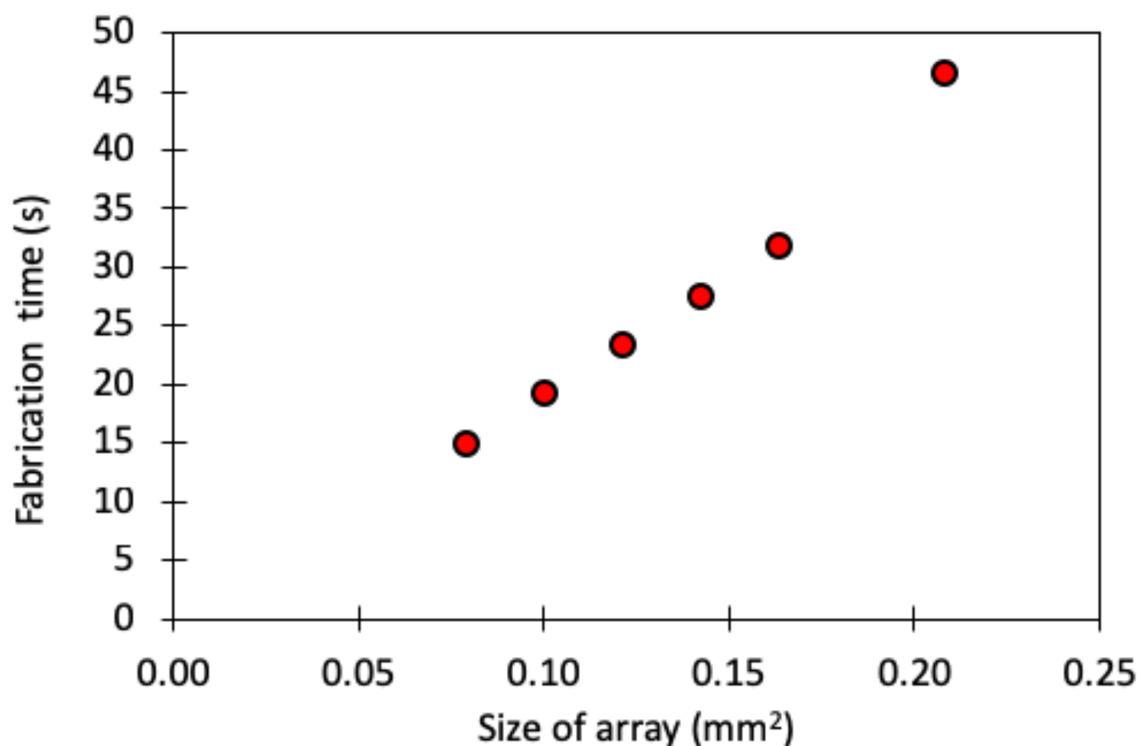

Figure 7.44: *LDW- fabrication time of arrays of square and rectangular elements as function of the array size.*

7.4 Anisotropic magnetoresistance (AMR) measurements of LDW-structures

A 25 nm thick permalloy thin film on glass was patterned by LDW- using the 800 picosecond pulse length system to investigate the magnetoresistance behaviour of magnetic structures fabricated by the laser direct writing. Ablated channels in the thin film defined the wires, which remained in contact at their ends with un-patterned film regions. The wires had different widths but length fixed at 0.5 mm to allow for the 1 mm spacing between the probe needles for performing resistivity measurements. The fabrication process used a laser fluence of 0.6 J.cm^{-2}, pulse energy 125 nJ and pulse repetition rate 40 kHz. These parameters were chosen to increase the laser ablation spot diameter to approximately 5 μm using the 0.3 NA objective lens in order to increase the areal fabrication rate since a large amount of material had to be removed to define the separated wires. The sample scanning speed was controlled to be 6 mm.s^{-1} which gave a laser pulse overlap of 97% and, in principle, smoother wire edges. However, to ensure removal of all magnetic material between wires, the distance between ablation lines was reduced to 1.5 μm to create an overlap between ablation lines (centre to centre) of 70% (Fig. 7.45).

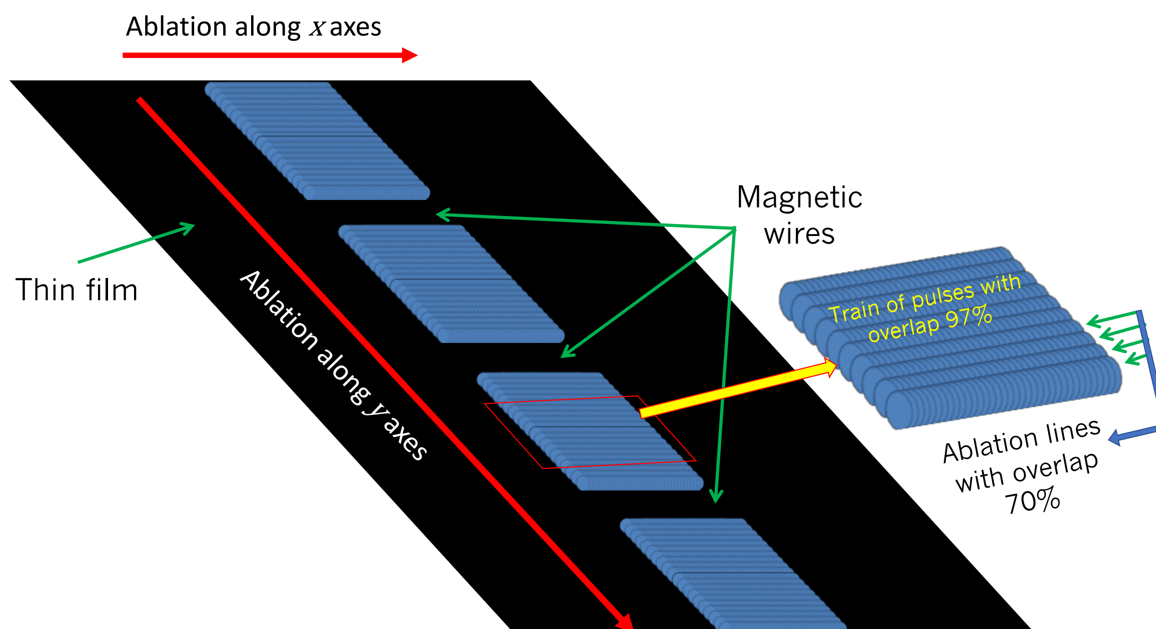

Figure 7.64: *Illustration of fabrication of AMR sensors patterned by laser ablation lines along the x axis. The blue areas show the ablation lines with overlap of 70% and pulses overlap of 97%. The black regions are magnetic film/wires.*

Three wires were fabricated on each sample, with wires separated by 1.16 μm to 1.64μm. The wires were nominally identical on each sample but varied in width between different samples. The wire widths and aspect ratios used to study their effect on the MR response are shown in Table 7.1.

Table 7.1 *Fabricated AMR sensors with range of aspect ratios.*

Aspect ratio (AR)	Wire width (mm)	Wire length (mm)	wires separated mm)
1	0.5	0.5	1.16
2	0.25	0.5	1.41
5	0.1	0.5	1.56
10	0.05	0.5	1.61
20	0.025	0.5	1.64

Fig 7.46 shows optical microscopy images of the three-wire structures with different of aspect ratios and 0.5 mm length, as noted in Table 7.1.

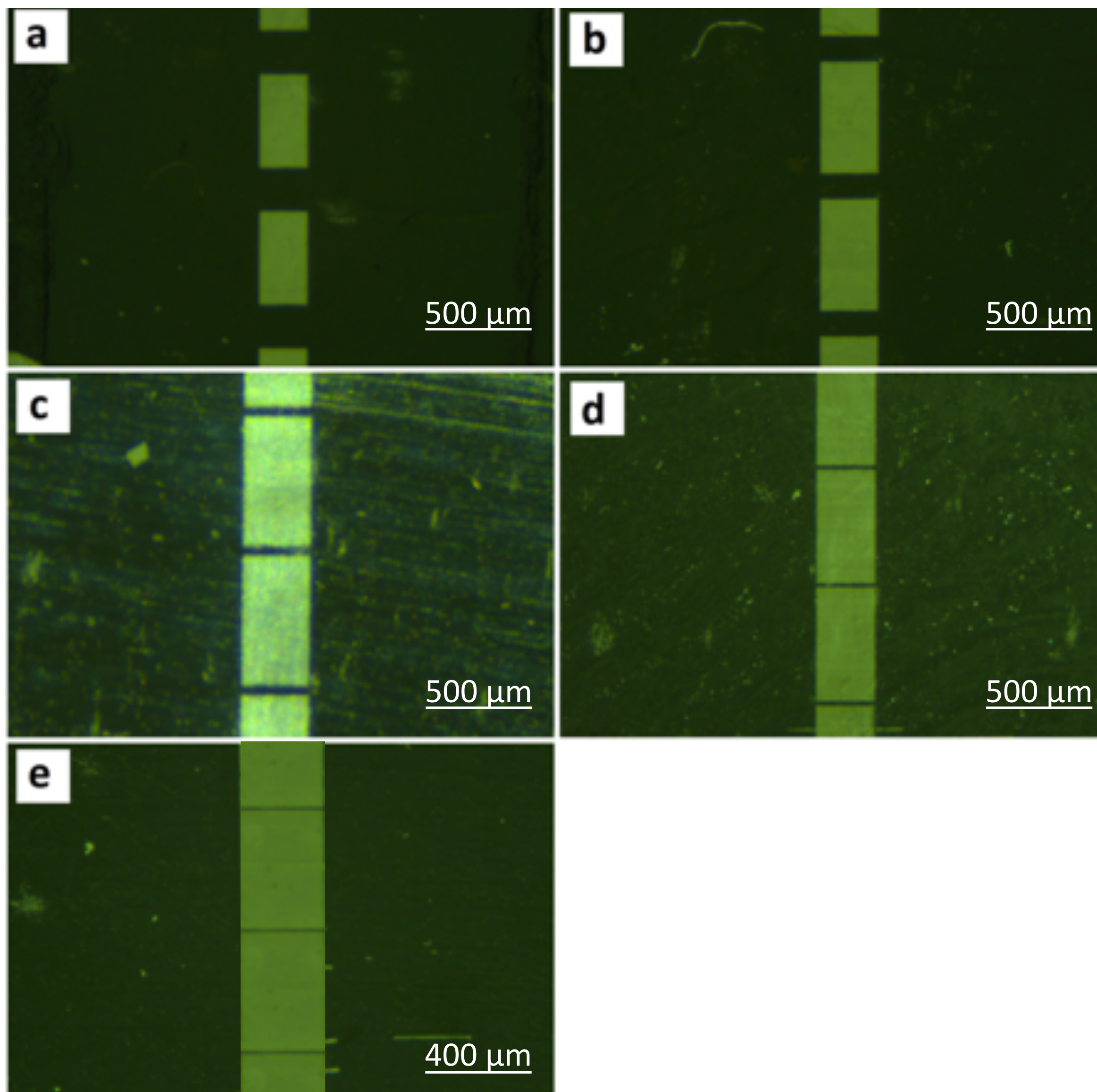

Figure 7.46: *Optical microscopy image of permalloy structures of three wires defined from a thin film with wire length of 0.5 mm and aspect ratios (AR) of: a) 1, b) 2, c) 5, d) 10 and e) 20. The black regions are the magnetic elements and thin film while the green regions are ablated areas.*

Magnetisation hysteresis loops were obtained by fMOKE along two directions for each of the magnetic wire designs. The magnetic field was applied along the long and short sides of fabricated structures. As expected, the hysteresis loops obtained from the long axis and short axis of the patterned sensors (Fig. 7.47 and 7.48) showed an increasingly anisotropic response to applied magnetic field as the aspect ratio increased. The long-axis hysteresis loops for structures with AR ≥ 2.0 have easy-axis character with sharp transitions, which may indicate magnetisation reversal via rapid propagation of domain walls injected from the adjoining film.

The short-axis hysteresis loops show hard axis character, although the reversal mechanisms often appears to be a mixture of magnetisation rotation and domain wall motion..

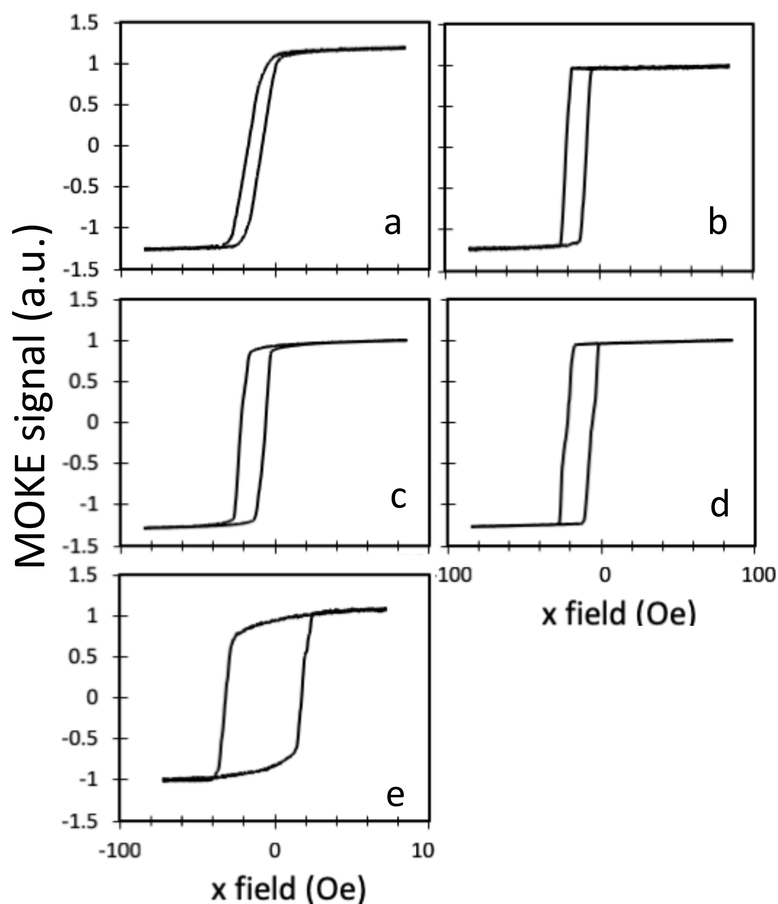

Figure 7.47: *MOKE hysteresis loops obtained by applying magnetic field along the long (easy axis) of LDW-fabricated permalloy wires with aspect ratio: a) 1.0, b) 2.0, c) 5.0, d)10 and e) 20.*

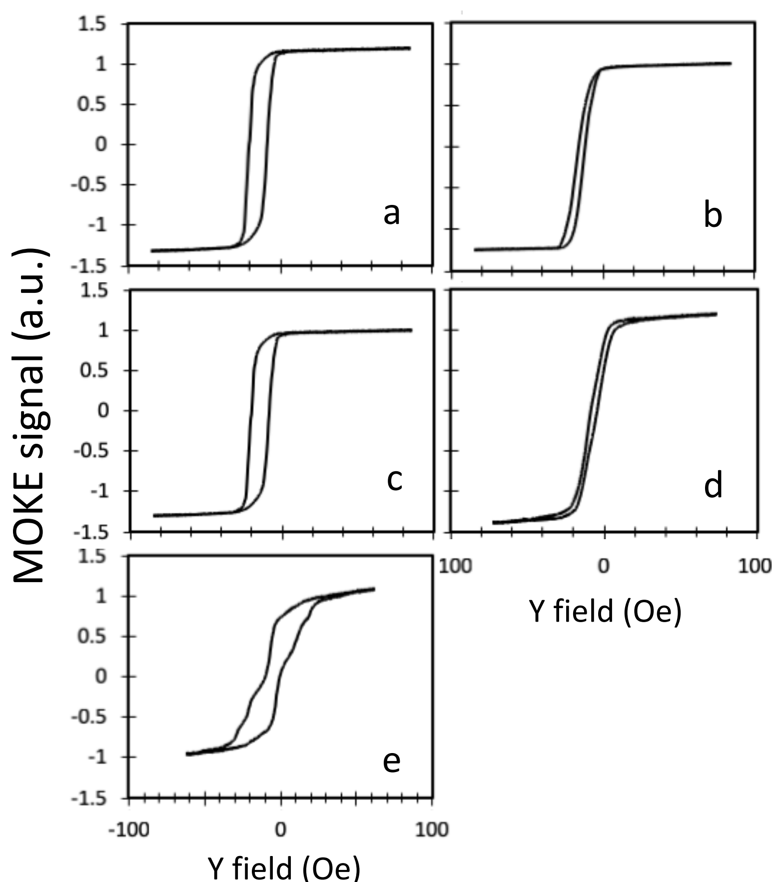

Figure 7.48: *MOKE hysteresis loops obtained by applying magnetic field along the short (hard axis) of LDW-fabricated permalloy wires with aspect ratio: a) 1.0, b) 2.0, c) 5.0, d)10 and e) 20.*

The coercivity of the wires was found to increase with aspect ratio (Fig. 7.49). The coercivity obtained by applied field along easy axis of MR sensors increased smoothly for aspect ratios 1 to 10 from 2 Oe to 4 Oe then increased rapidly to 24 Oe for aspect ratio 20, these results agreed with the previous result of magnetic wire that discussed before (§7.2.2).

The anisotropy field values of hard axis increased linearly with increasing of aspect ratios (Fig 7.50) from 11 Oe to 95 Oe as expected due to need to high magnetic field to reach the saturation, however, the shape of hysteresis loop similar to hysteresis loop of easy axis except the loop of aspect ratio 20 lost the ideal shape and like to hysteresis loops of rectangles elements (fig 7.40 and 7.41).

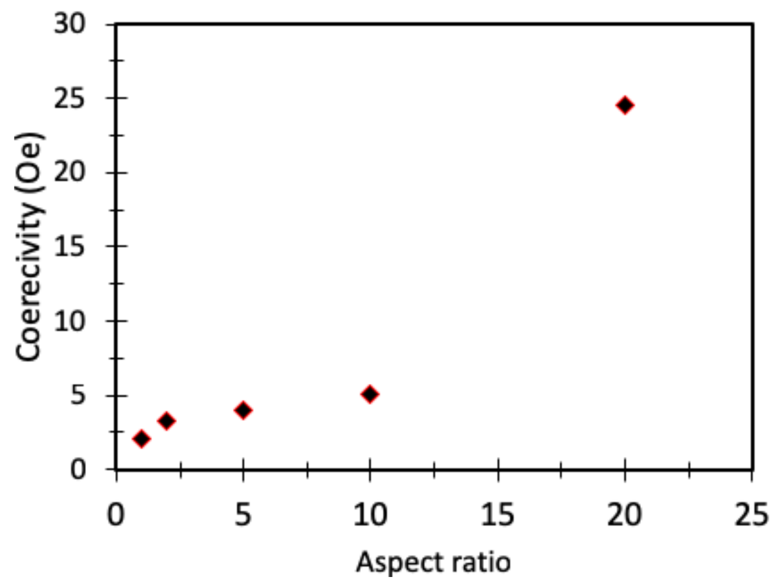

Figure 7.49: *Magnetic coercivity as function of wire aspect ratio.*

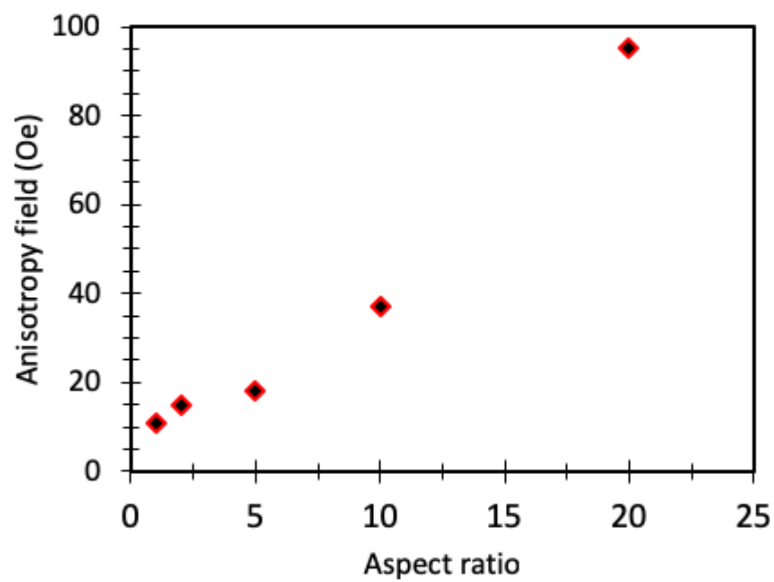

Figure 7.50: *Anisotropy field as a function of wire aspect ratio.*

7.4.1 Anisotropic Magnetoresistance Measurements

AMR measurements were obtained by contacting the thin film regions either side of the wires and measuring their resistance while applying magnetic field either parallel and perpendicular to the wire long axes.

The AMR measurements were carried out by using electric currents of 0.05, 0.1, 0.5, 0.9 and 1 mA for aspect ratios 1, 2, 5, 10, 20, respectively, and at frequencies of between 1.0 and 1.1 kHz.

The AMR ratios can be calculated using Eq 5.9 based on knowledge of different values of resistance, ***R***. Translating this for measurement of voltage (e.g. by a lock-in amplifier). Using Ohm's law ***R* = *V* / *I***, where ***V*** is a voltage and ***I*** current, Eq 5.9 can be written as:

$$MR = \frac{\left(\frac{V_H}{I_H} - \frac{V_0}{I_0}\right)}{\left(\frac{V_0}{I_0}\right)} \qquad (7.1)$$

where V_H is voltage picked up when apply the magnetic field and V_0 when remove the magnetic field. The experiments here were conducted with constant current, so $I_H = I_0$ and Eq 7.1 becomes:

$$MR = \frac{V_H - V_0}{V_0} \qquad (7.2)$$

The permalloy wires showed a clear AMR response to applied magnetic field across the range of aspect ratios, as shown in Figs 7.51 to 7.60. The calculated MR values are shown in Fig. 7.61 and reached up to 0.31% for current applied parallel and 0.32% for current applied perpendicular to the lowest aspect ratio wires. This is lower than the 4% expected for bulk or thin film permalloy [149], most probably due to the significant contribution of the thin film regions beyond the wire ends. MR ratios were somewhat erratic as the aspect ratio varied when measured with field applied along the wire lengths. This is perhaps due to domain wall-based magnetisation reversals leading to ill-defined MR signals and to different wires in each set of three undergoing reversal at slightly different applied fields.

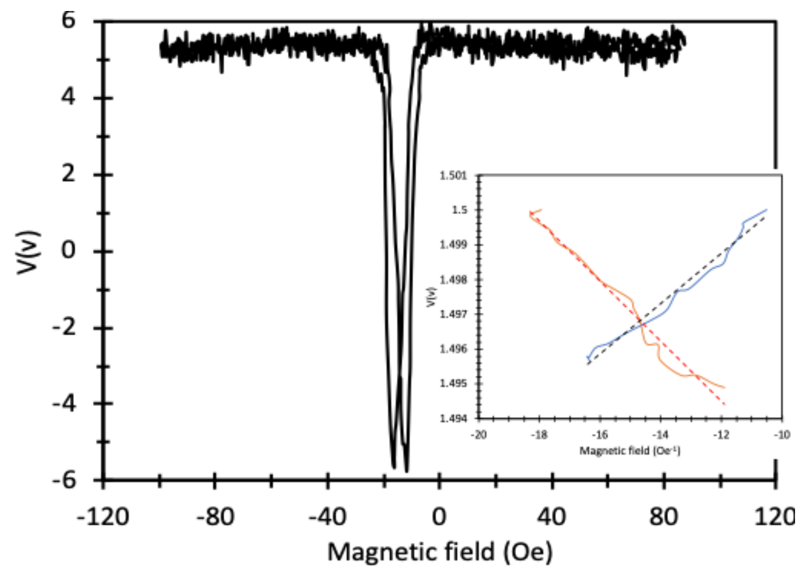

Figure 7.51: *AMR loop of permalloy wires with aspect ratio 1.0 with magnetic field applied parallelly to current flow direction. The inset shows a magnified region of the signal crossing area with linear fits to the transitions in each direction.*

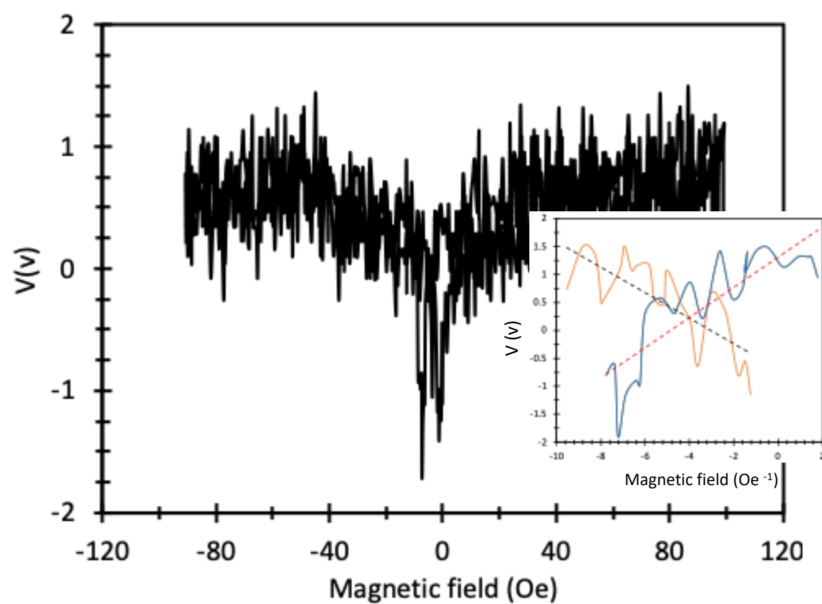

Figure 7.52: *AMR loop of permalloy wires with aspect ratio 2.0 with magnetic field applied parallelly to current flow direction. The inset shows a magnified region of the signal crossing area with linear fits to the transitions in each direction.*

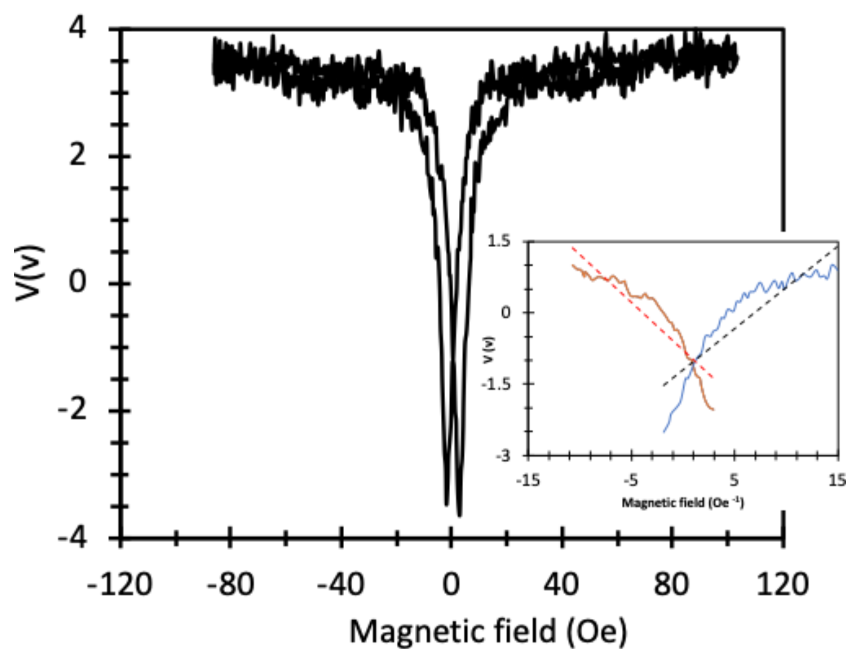

Figure 7.53: *AMR loop of permalloy wires with aspect ratio 5.0 with magnetic field applied parallelly to current flow direction. The inset shows a magnified region of the signal crossing area with linear fits to the transitions in each direction.*

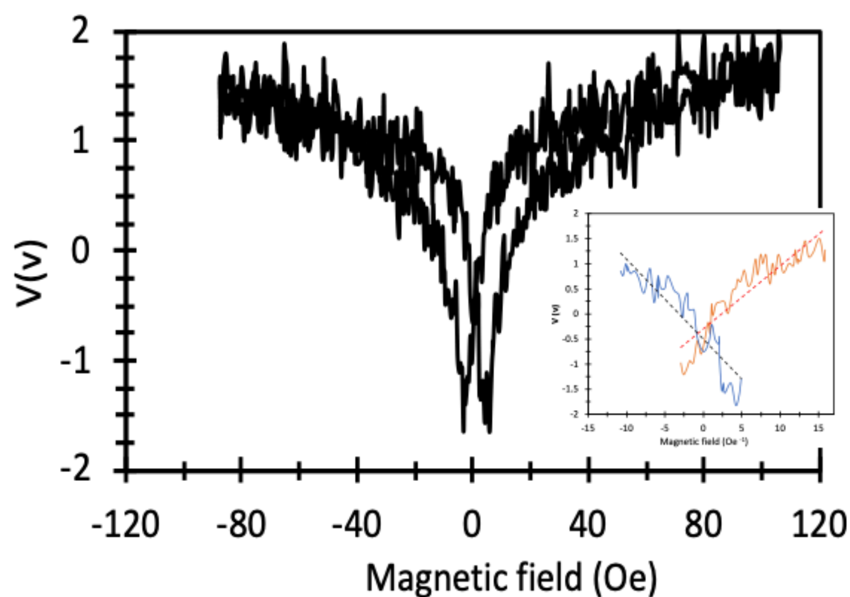

Figure 7.54: *AMR loop of permalloy wires with aspect ratio 10.0 with magnetic field applied parallelly to current flow direction. The inset shows a magnified region of the signal crossing area with linear fits to the transitions in each direction.*

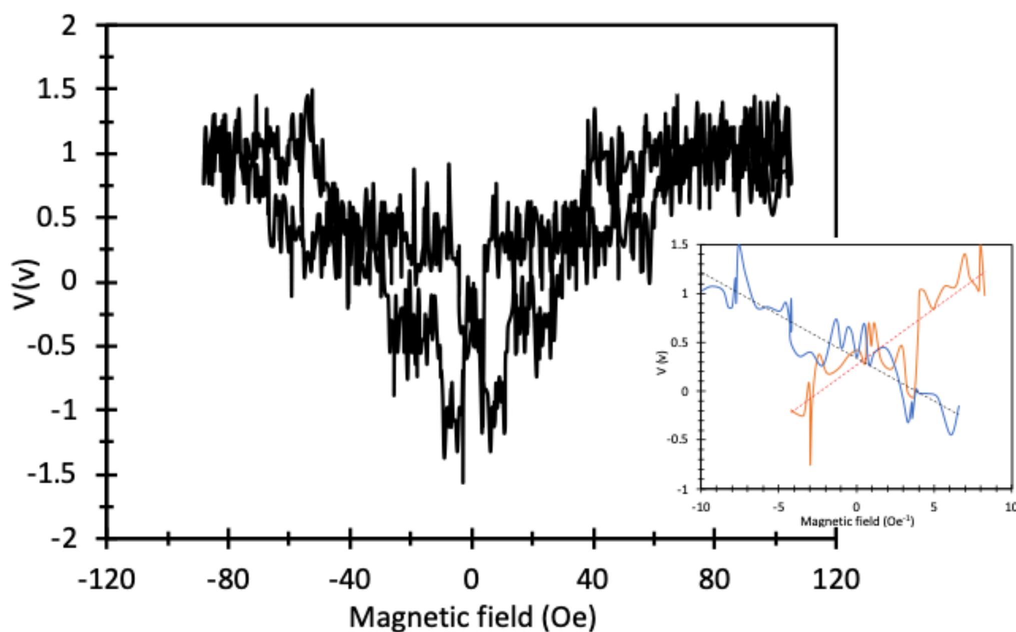

Figure 7.55*: AMR loop of permalloy wires with aspect ratio 20.0 with magnetic field applied parallelly to current flow direction. The inset shows a magnified region of the signal crossing area with linear fits to the transitions in each direction.*

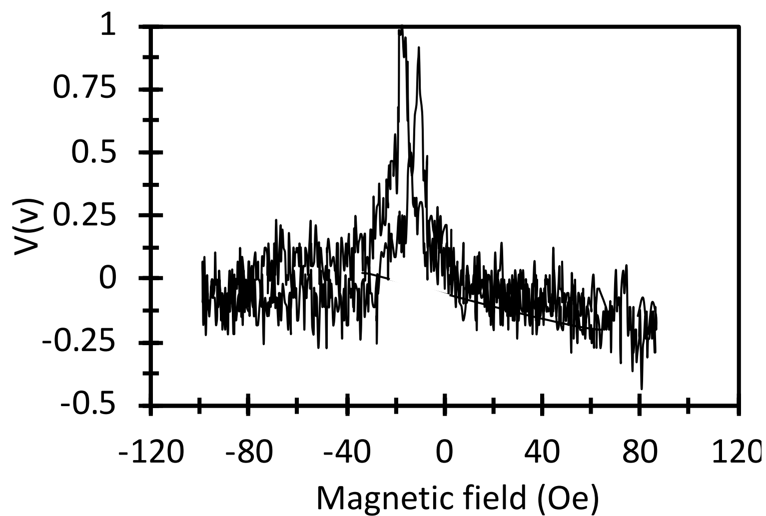

Figure 7.56*: AMR loop of permalloy wires with aspect ratio 1.0 with magnetic field applied perpendicularly to current flow direction. The inset shows a magnified region of the signal crossing area with linear fits to the transitions in each direction.*

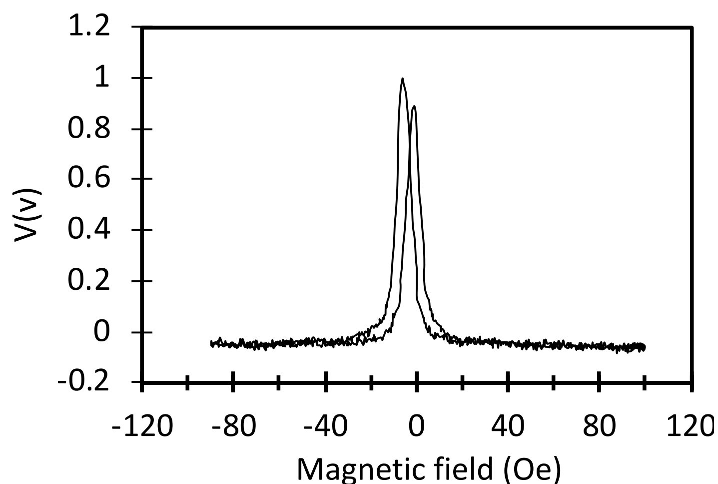

Figure 7.57*: AMR loop of permalloy wires with aspect ratio 2.0 with magnetic field applied perpendicularly to current flow direction. The inset shows a magnified region of the signal crossing area with linear fits to the transitions in each direction.*

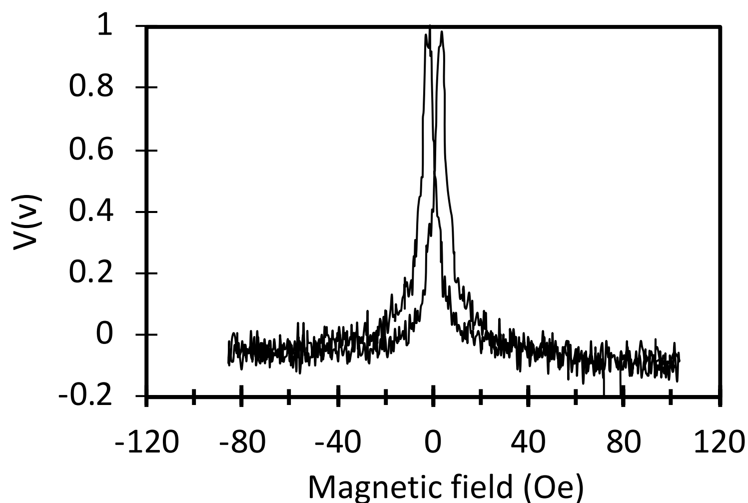

Figure 7.58*: AMR loop of permalloy wires with aspect ratio 5.0 with magnetic field applied perpendicularly to current flow direction. The inset shows a magnified region of the signal crossing area with linear fits to the transitions in each direction.*

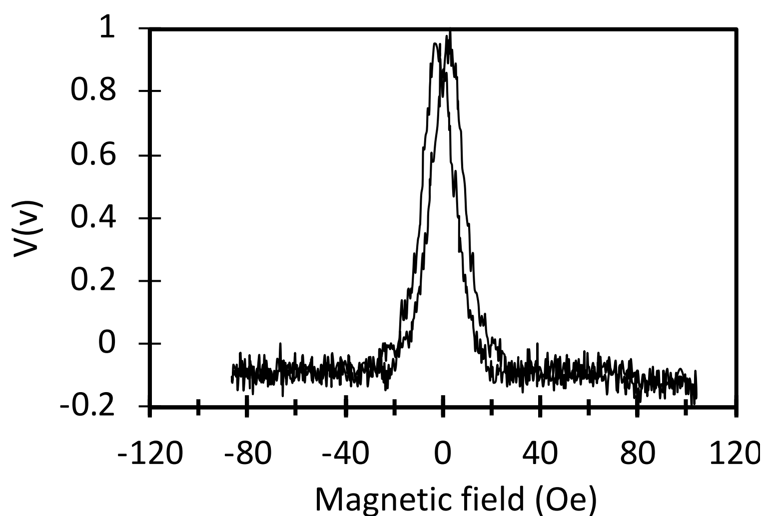

Figure 7.59*: AMR loop of permalloy wires with aspect ratio 10.0 with magnetic field applied perpendicularly to current flow direction. The inset shows a magnified region of the signal crossing area with linear fits to the transitions in each direction.*

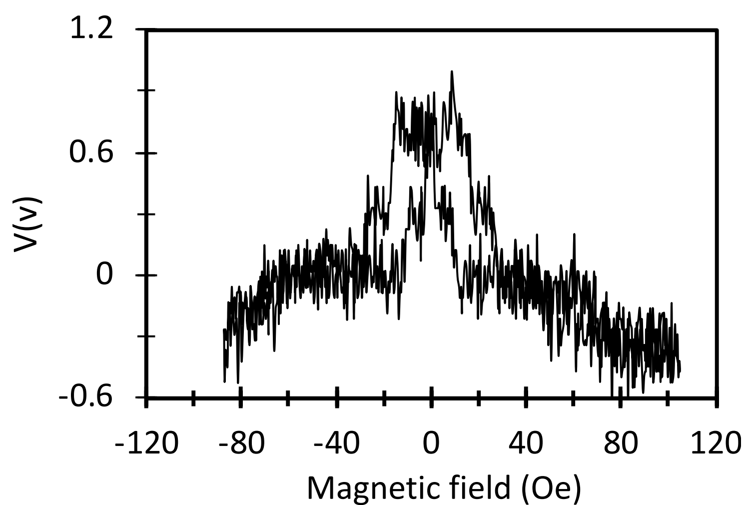

Figure 7.60*: AMR loop of permalloy wires with aspect ratio 20.0 with magnetic field applied perpendicularly to current flow direction. The inset shows a magnified region of the signal crossing area with linear fits to the transitions in each direction.*

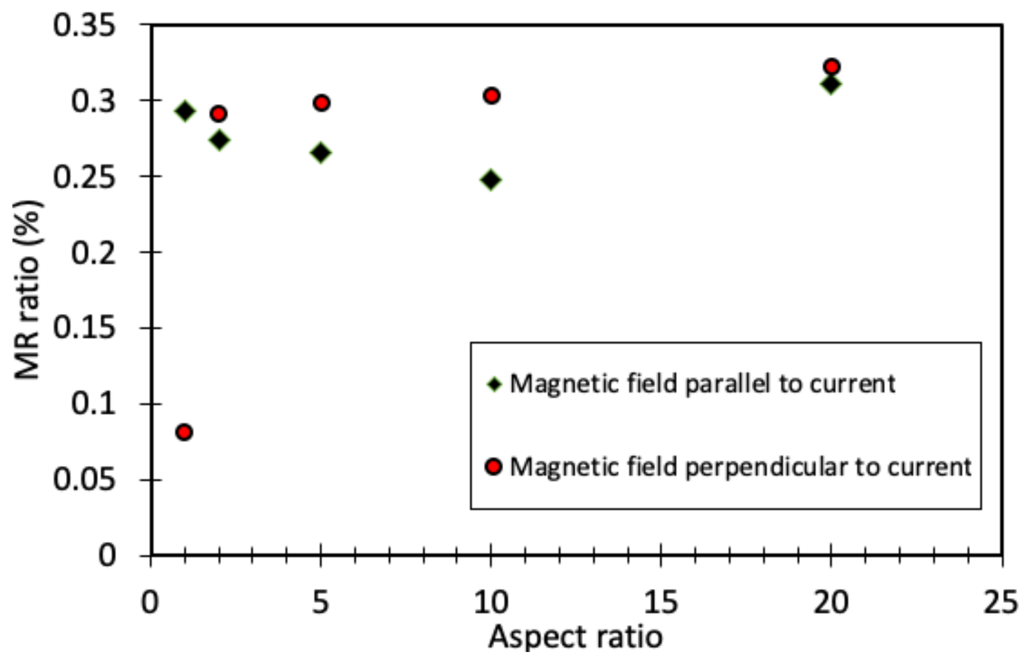

Figure 7.61*: MR ratio as function to aspect ratios of MR sensors (three wires) with applied magnetic field in parallel and perpendicular to current flow direction.*

The sensitivity of the structures was calculated from MR loops as the average gradient of MR as a function of applied field at zero magnetic field, as shown on Figure as shows in fig 7.62. The sensitivity values will show the effect of changing the magnetic field on the electric resistance based on Ohm law ($R = V/I$). Therefore, these part (internal curves) of MR loops were highlighted in the sub-figures of 7.51 to 7.55.

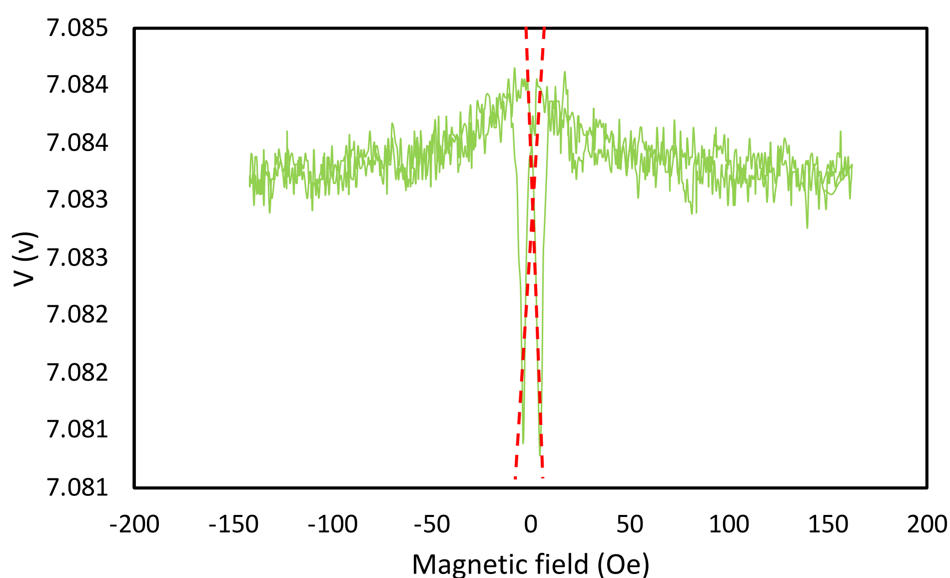

Figure 7.62*: The calculation method of sensitivity of the structures from MR loops.*

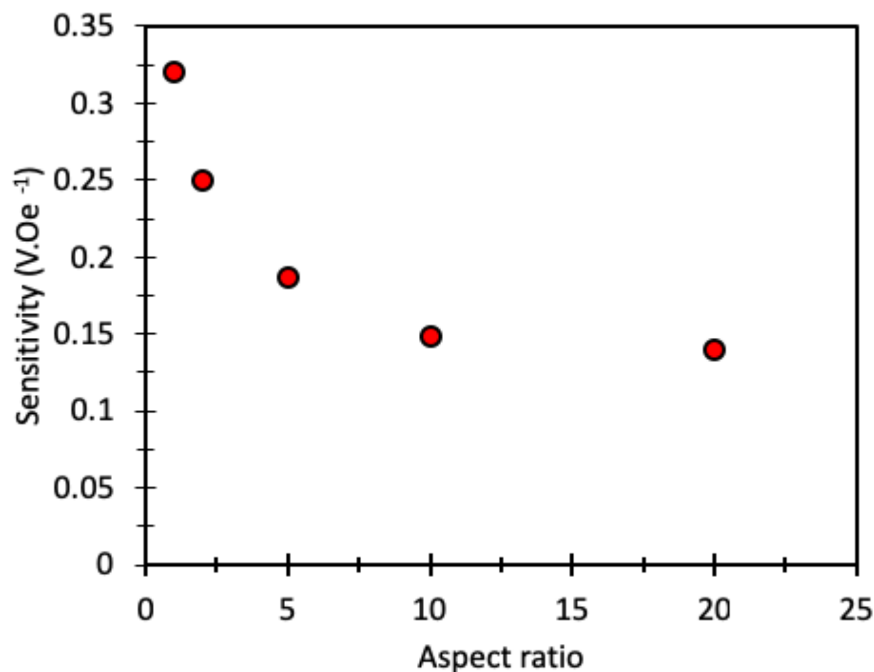

Figure 7.63*: Sensitivity as function to aspect ratios of MR sensors (three wires) with applied magnetic field in parallel to current flow direction.*

Figure 7.63 shows that the field sensitivity of the AMR signal decreases with increased wire aspect ratios. This tunable sensitivity could be valuable in the manufacture of magnetic field sensors [150] in which appropriate sensitivity could be determined to a variable level at the point of fabrication, rather than having to fabricate films of different materials.

The average time required to fabricate each sample was 9.3 minutes. This is a relatively short time to pattern a sensor with dimensions of 7mm × 5mm. The overall ablation area ranged from 2.0 mm^2 for wires with AR = 1 to 3.1 mm^2 for wires with AR = 20. These areas were removed by creating 3666 ablation lines (for AR = 1 wires), each offset by 1.5. The number of ablation lines increased with increase in the aspect ratio in order to remove additional areas of the thin film, up to be 4616 ablation lines for AR = 20 wires. Fig 7.64 show the actual time required to pattern wires with aspect ratios from 1 to 20.

Future MR sensors based on LDW- fabricated wires could be made even more quickly than those here by restricting the overall size of the patterned magnetic thin film, using larger

laser spots or even mask-based wide-field exposure. The ease with which wire sensitivity can be varied with defined width could be highly attractive to manufacturers seeking a common fabrication route to creating sensors for different field strength environments.

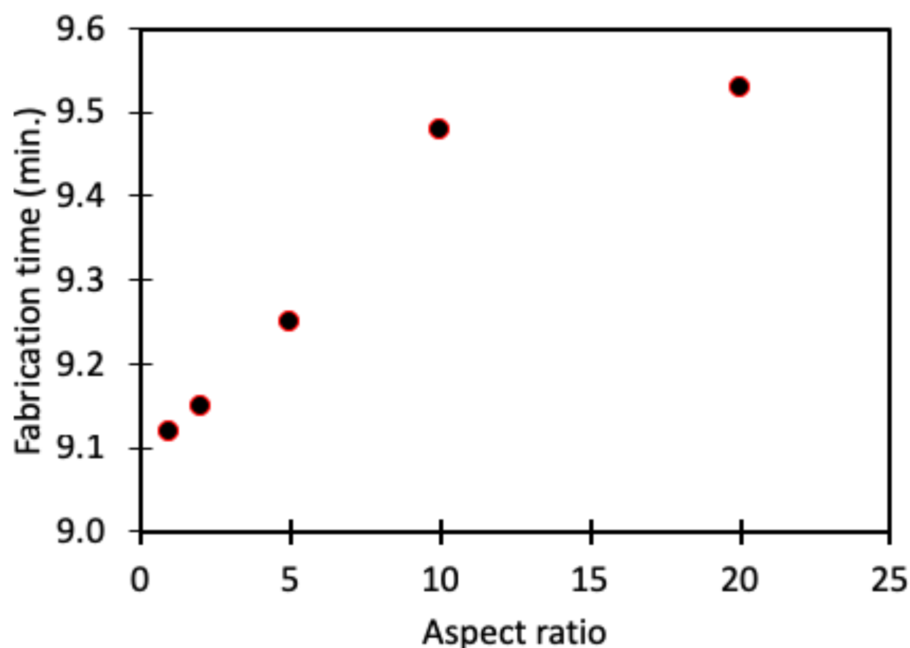

Figure 7.64*: Actual fabrication time as function of aspect ratio of the three-wire structures.*

7.5 Summary

This chapter has presented patterning of a 90 nm-thick permalloy thin film into one- and two-dimensional structures using subtractive Laser Direct Writing (LDW-) with 800 picosecond laser systems. Arrays of wires with a range of widths from 150 nm to 6.75 µm were fabricated by controlling the distance between laser ablation lines. The two-dimensional structures included arrays of squares, rectangles with a range of aspect ratios, and arrays of rhombic elements. Multiple (three) wires were also patterned with range of aspect ratios (1, 2, 5, 10, and 20) but with a length of just 0.5 mm to fit within a magnetoresistance measurement cell. All these structures were tested by focussed magneto-optical Kerr effect magnetometry and by electrical measurements to determine their AMR response to applied magnetic field and the effect of geometrical shape (aspect ratio). This demonstrated a field sensitivity of AMR that is tuneable by fabricated geometry that might be useful in field sensor applications. The experiments here used large magnetic fields to saturate the sensors during each field sweep and future experiments should also consider small-magnitudes of field only in order to test

their reproducibility under these conditions. In general, LDW- can reduce the fabrication time and cost of fabricating nano/micro-scale structures very significantly compared with other techniques; for example, the average time to fabricate a set of 75 wires of length 4 mm was between 84 and 87 s depending on the wire width and was achieved without any chemicals, masks or any other special requirements.

Chapter 8: Conclusions and Future Work

8.1 Conclusion

This project has demonstrated two types of laser direct writing, subtractive laser direct writing (LDW-) and laser-induced forward transfer (LIFT), to fabricate micro/nano-scale magnetic structures.

Attempts to transfer permalloy thin film material as patterned structures with the LIFT process were carried out using three laser systems. Multiple and single laser pulses at each transfer point were investigated and the film thickness, scanning speed, pulse energy, distance between donor and acceptor substrate, and the acceptor material were varied. However, none of this allowed the thin film morphology to be transferred to the acceptor substrate and the permalloy appeared as debris particles. The size of these particles suggested that the permalloy melts either in the gas-phase following ablation or on the acceptor substrate before solidifying into droplets. A lower thermal conductivity substrate (glass rather than silicon) resulted in more spherical droplets, which is consistent with slower cooling through the melting point and consequently longer for atoms to have high surface mobility and become arranged into positions to minimise droplet surface energy. No ferromagnetic response could be measured by magneto-optical Kerr effect magnetometry but the droplets may be superparamagnetic. Attempts to reduce the energy of ablated species through larger donor-acceptor substrate separations at atmospheric pressure resulted in a loss of particle adhesion to the acceptor substrate. LIFT remains a promising technique to transfer and pattern magnetic material, given the excellent results with other types of material achieved in the literature, but realising this will require overcoming several important factors.

LDW- ablation was used to fabricate micro/nano-scale magnetic structures from 90 nm thick permalloy thin films. The scanning speed and laser repetition rate were controlled to give a 30% overlap between neighbouring focused laser spots. This overlap produced an undulating profile to the edges of fabricated magnetic wires that became relatively more pronounced for narrower wires. Wires from several micrometres to 150 nm in width were fabricated although wire widths less than 650 nm had significant levels of additional material between wires. Similarly, wider wires (650 nm or more) exhibited clear uniaxial behaviour and a magnetic coercivity proportional to the inverse of wire width, varying between 11 Oe to 47 Oe, with the highest coercivity obtained for the wire width of 650nm.

Two-dimensional magnetic structure arrays of squares, rectangles of different aspect ratios and rhombic elements were also patterned using LDW-. These elements demonstrated shape-sensitive magnetic behaviour with increasing the shape aspect ratio and how simple control of the bi-axial positioning of a sample during LDW- processing can result in a wide range of structure designs.

LDW- was also successfully used to pattern 25 nm permalloy thin film samples to allow anisotropic magnetoresistance (AMR) measurements. The AMR results measured with magnetic field applied either parallel or perpendicular to the wires showed a clear dependence on wire width. This indicates that LDW- can be used to fabricate magnetic field sensors with a response that can be tuned during the fabrication process.

The LDW- fabrication process of magnetic structures was extremely rapid. Fabrication rates of 3.5 mm. s^{-1} were achieved for one-dimensional structures, which meant that 75 wires dimensions 550 nm × 4.0 mm could be produced in as little as 85 s. Two-dimensional structures with low-micrometre dimensions were fabricated with an average fabrication time of 4.7×10^{-4} s per element, e.g. an array of 5625 structures could be achieved in 15 s. Different laser systems with higher repetition rates will allow these rates to be increased tenfold many times over.

In general, LDW- offers many benefits in the fabrication of nano/micro-scale structures. This process offers speed, simplicity with no use of wet chemicals, low cost, one-step processing, user-defined pattern generation and high throughput. This is a unique combination of features among patterning techniques and makes LDW- particularly suitable for prototyping or even industrial manufacturing of low numbers of magnetic elements with magnetic properties tuned at the point of writing.

8.2 Future work

There are various ways in which the techniques discussed here could be developed further in order to improve their utility.

LDW- fabrication has proved here to be the simplest and most straightforward of the laser writing approaches available. Future experiments will extend the demonstrated range of versatility of this approach, including considering different magnetic materials, understanding the role and limitations of film thickness, attempting to achieve narrower structures with well-described properties (e.g. inverse relationship between coercivity and wire width), the effect of different pulse overlaps, narrower wires for AMR sensors, and new two-dimensional structures with higher aspect ratios. It is already possible to consider wider application of LDW- structures, for example to act as magnetic field sources via domain walls or end domains for trapping superparamagnetic beads for biological techniques [151], [152]. The processing speed of LDW- fabrication might also be improved significantly using a mask and wide-field, single laser pulse fabrication of an entire substrate. Reducing the laser wavelength, e.g. to ultra-violet wavelengths, will offer greater definition of structures but, for point-by-point fabrication, will increase significantly the fabrication time of structures due to the increased number of ablation pixels required.

Transferring magnetic materials by LIFT proved to be challenging but we were able to learn much about the issues being faced from observation of the morphology of transferred material that informs future work. Use of an acceptor substrate with higher thermal conductivity than considered here will probably allow transferred material to condense faster

and reduce its surface mobility and avoid droplet formation. Use of a higher vacuum inside the transfer cell may reduce or remove completely any shockwave effect and reduce the subsequent damage of deposited material. Use of thicker films or films with sacrificial underlayers may allow ablation of the uppermost magnetic film region without it heating significantly, perhaps transferring while remaining in the solid state. Alternatively, thinner films may allow improved resolution of magnetic structures. LIFT remains appealing firstly as it offers even faster fabrication times than LDW- because it depends simply on the area of the structures rather than the area of material that should be cleared. The additive nature of LIFT also means that it might be suitable for multi-layer deposition or three-dimensional fabrication by ablating different, non-ablated regions of donor substrates, either of identical or different materials.

This project used optical techniques to fabricate (LDW-) and characterise (MOKE) the magnetic structures. Other optical analytical techniques are also available, for example the use of scattering (such as laser speckle analysis) to characterise sample morphology [153], [154]. It may be possible to integrate the processes using multiple lasers and optical systems to allow characterisation to be performed during the fabrication process. This could also extend to electrical measurements, e.g. resistance or AMR measurements to provide feedback on the degree of tuning of magnetic field sensors.

The results of this work give confidence to pursuing the further development of direct laser writing of magnetic structures that may see it becoming a mainstream fabrication technique of use to researchers and industrial manufacturers.

Appendix A

DVAR $SPEED	
DVAR $SPACING 'DEFINES A WORD	
$SPACING = x.xxx	All in mm
$SPEED = xxx	The speed F, in mm/s
PSOCONTROL X RESET '	Resets the shutter command
PSOCONTROL X OUTPUT 1 1 '	Defines shutter output
DWELL x.xxx	Holds for x.xxx seconds, will wait at that spot
ENABLE X Y Z	Turn on servo loop control for the axes
ABSOLUTE	
G90	
G1 X xx.xxx Y xx.xxx Z xx.xxx F = 7.5	This is the starting position, all in mm, the speed F, in mm/s
INCREMENTAL	
METRIC	Tells the stage to move relative to its current
SECONDS	
F = $SPEED	
PSOCONTROL X ON	Opens the shutter
REPEAT 76	Repeats everything between this and endrpt (end repeat).
LINEAR X 4.00	LINEAR X moves in X direction by x.xxx mm
PSOCONTROL X off	Close the shutter
LINEAR Y 0.00x	LINEAR Y moves in Y direction. The Y value varying from 0.002 mm to 0.0086mm to control the wires widths.
PSOCONTROL X ON	
LINEAR X –4.00	For opposite direction
PSOCONTROL X OFF	
'ENDRPT	

Appendix B

DVAR $SPEED	
DVAR $SPACING 'DEFINES A WORD	
$SPACING = x.xxx	All in mm
$SPEED = xxx	The speed F, in mm/s
PSOCONTROL X RESET '	Resets the shutter command
PSOCONTROL X OUTPUT 1 1 '	Defines shutter output
DWELL x.xxx	Holds for x.xxx seconds, will wait at that spot
ENABLE X Y Z	Turn on servo loop control for the axes
ABSOLUTE	
G90	
G1 X xx.xxx Y xx.xxx Z xx.xxx F = 7.5	This is the starting position, all in mm, the speed F, in mm/s
INCREMENTAL	
	Tells the stage to move relative to its
METRIC	current
SECONDS	
F = $SPEED	
PSOCONTROL X ON	Opens the shutter
REPEAT 76	Repeats everything between this and endrpt (end repeat).
LINEAR X x.00	LINEAR X moves in X direction by x.xxx mm
PSOCONTROL X off	Close the shutter
LINEAR Y 0.00375	LINEAR Y moves in Y direction by 0.00375 mm
PSOCONTROL X ON	
LINEAR X -x.00	For opposite direction
PSOCONTROL X OFF	
'ENDRPT	
G1 X xx.xxx Y xx.xxx Z xx.xxx F = 7.5	This is the starting position of scanning along Y axes.
INCREMENTAL	
METRIC	
SECONDS	
F = $SPEED	
PSOCONTROL X ON	
REPEAT 76	
LINEAR x 2.00	
PSOCONTROL X off	
LINEAR X 0.00375	LINEAR X moves in X direction. The X value varying from 0.00375 mm to 0.00985mm to control the aspect ratio (elements widths).

```
PSOCONTROL X ON
LINEAR Y -x.00
PSOCONTROL X OFF
'ENDRPT
```

Appendix C

Command	Description
DVAR $SPEED	
DVAR $SPACING 'DEFINES A WORD	
$SPACING = x.xxx	All in mm
$SPEED = xxx	The speed F, in mm/s
PSOCONTROL X RESET '	Resets the shutter command
PSOCONTROL X OUTPUT 1 1 '	Defines shutter output
DWELL x.xxx	Holds for x.xxx seconds, will wait at that spot
ENABLE X Y Z	Turn on servo loop control for the axes
ABSOLUTE	
G90	
G1 X xx.xxx Y xx.xxx Z xx.xxx F = 7.5	This is the starting position, all in mm, the speed F, in mm/s
INCREMENTAL	
	Tells the stage to move relative to its
METRIC	current
SECONDS	
F = $SPEED	
PSOCONTROL X ON	Opens the shutter
REPEAT 76	Repeats everything between this and endrpt (end repeat).
LINEAR X x.xx Y x.xx	LINEAR X moves in X direction by x.xxx mm
PSOCONTROL X off	Close the shutter
LINEAR Y 0.00375	LINEAR Y moves in Y direction by 0.00375
PSOCONTROL X ON	mm
LINEAR X -x.00 Y -x.xx	For opposite direction
PSOCONTROL X OFF	
'ENDRPT	
G1 X xx.xxx Y xx.xxx Z xx.xxx F = 7.5	This is the starting position of scanning along Y axes.
INCREMENTAL	
METRIC	
SECONDS	
F = $SPEED	
PSOCONTROL X ON	
REPEAT 76	
LINEAR X x.xx Y x.xx	
PSOCONTROL X off	
LINEAR X 0.00375	LINEAR X moves in X direction. The X value varying from 0.00375 mm to 0.00985mm to control the aspect ratio (elements widths).

```
PSOCONTROL X ON
LINEAR Y -x.xx X x.xx
PSOCONTROL X OFF
'ENDRPT
```

Appendix D

DVAR $SPEED	
DVAR $SPACING 'DEFINES A WORD	
$SPACING = x.xxx	All in mm
$SPEED = xxx	The speed F, in mm/s
PSOCONTROL X RESET '	Resets the shutter command
PSOCONTROL X OUTPUT 1 1 '	Defines shutter output
DWELL x.xxx	Holds for x.xxx seconds, will wait at that spot
ENABLE X Y Z	Turn on servo loop control for the axes
ABSOLUTE	
G90	
G1 X xx.xxx Y xx.xxx Z xx.xxx F = 7.5	This is the starting position, all in mm, the speed F, in mm/s
INCREMENTAL	
METRIC	Tells the stage to move relative to its current
SECONDS	
F = $SPEED	

"For dots? X? ARRAY"

REPEAT xx	Repeats everything between this and endrpt for x times (end repeat).
REPEAT x	
PSOCONTROL X ON	Opens the shutter
DWELL x.xxx	holds for x.xxx seconds
PSOCONTROL X OFF	
LINEAR X x.xxx	
ENDRPT	
LINEAR X -(x*x.xxx)	
LINEAR Y x.xxx	
PSOCONTROL X OFF	Close the shutter
ENDRPT	

References

[1] F. Hrouda, "Magnetic anisotropy of rocks and its applicability in geology and geophysics," *Geophys. Surv.*, vol. 5, pp. 37–82, 1982.

[2] M. Shinkai, "Functional magnetic particles for medical application," *J. Biosci. Bioeng.*, vol. 94, no. 6, pp. 606–613, 2002.

[3] Q. A. Pankhurst, N. T. K. Thanh, S. K. Jones, and J. Dobson, "Progress in applications of magnetic nanoparticles in biomedicine," *J. Phys. D. Appl. Phys.*, vol. 42, no. 22, p. 224001, 2009.

[4] P. I. Nikitin, P. M. Vetoshko, and T. I. Ksenevich, "Magnetic Immunoassays," *Sens. Lett.*, vol. 5, no. 1, pp. 296–299, 2007.

[5] J. P. and B. M.-B. and F. Schick, "Geometry and extension of signal voids in MR images induced by aggregations of magnetically labelled cells," *Phys. Med. Biol.*, vol. 51, no. 18, p. 4707, 2006.

[6] A. Arani, A. Eskandari, P. Ouyang, and R. Chopra, "A novel high amplitude piezoceramic actuator for applications in magnetic resonance elastography: a compliant mechanical amplifier approach," *Smart Mater. Struct.*, vol. 26, no. 8, p. 87001, 2017.

[7] D. K. Wood, K. K. Ni, D. R. Schmidt, and A. N. Cleland, "Submicron giant magnetoresistive sensors for biological applications," *Sensors Actuators A Phys.*, vol. 120, no. 1, pp. 1–6, 2005.

[8] M. V. and A. Hernando, "A soft magnetic wire for sensor applications," *J. Phys. D. Appl. Phys.*, vol. 29, no. 4, p. 939, 1996.

[9] K.H.J. BUSCHOW, *Handbook of Magnetic Materials*, 1st editio., vol. 16. Amsterdam.: (Elsevier, Amsterdam., 2011.

[10] N. A. Spaldin, *magnetic materials fundamentals and application*, Second edi., no. 2. CAMBRIDGE UNIVERSITY PRESS, 2014.

[11] G. R. View, "Global Magnetic Sensor Market Size , Share | Industry Report ... Global Magnetic Sensor Market Size , Share | Industry Report ...," *Grand veiw Research.*, 2018. .

[12] R. Dixon, "Magnetic sensors refresh in new automotive economy - IHS Technology," *IHS Markit*, 2018. [Online]. Available: https://technology.ihs.com/604792/magnetic-sensors-refresh-in-new-automotive-economy. [Accessed: 23-Aug-2018].

[13] D. Banks, "Femtosecond laser induced forward transfer techniques for the deposition of nanoscale, intact, and solid-phase material," 2008.

[14] C. B. Arnold and A. Piqué, "Laser Direct-Write Processing," *MRS Bull.*, vol. 32, no. January, pp. 9–15, 2007.

[15] B. D. Cullity and C. D. Graham, *Introduction to Magnetic Materials, Second Edition - Cullity - Wiley Online Library*, Second Edi. 2008.

[16] Northridge California state university, "Magnetism MSE 630 Fall." Northridge California state university, California state, p. 22, 2008.

[17] B. D. Cullity and C. D. Graham, *Introduction to Magnetic Materials*, Second Edi. United States of America: John Wiley & Sons, 2008.

[18] U. Cambridge, "Ferromagnetic Materials," *University of Cambridge*, 2008. [Online].

Available: https://www.doitpoms.ac.uk/tlplib/ferromagnetic/index.php. [Accessed: 24-May-2017].
[19] T. H. E. Nature and O. F. Magnetism, “electricalengproject.blogspot.co.uk/2013/02/electronics- tutorial-about-magnetism.html,” *ELECTRICAL ENGINEERING AND PROJECTS*, 2013. .
[20] “Hard disk drive,” *www.pctechguide.com/hard-disks/hard-disk-hard-drive-operation*. .
[21] S. Chikazumi, C. D. Graham, and S. Chikazumi, “Physics of ferromagnetism.” Oxford University Press, Oxford; New York, 1997.
[22] R. Kodama, “Magnetic nanoparticles,” *J. Magn. Magn. Mater.*, vol. 200, no. 1–3, pp. 359–372, 1999.
[23] S. Franssila, *Introduction to microfabrication*, vol. 54. John Wiley and Sons, 2004.
[24] M. Madou, *Fundamentals of Microbabrication: The Science of Miniaturization*, 2nd ed. Boca Raton, FL: CRC Press, 2002.
[25] C. Hu, “Device Fabrication Technology,” in *Modern Semiconductor Devices for Integrated Circuit*, First Edit., Prentice Hall, 2009, pp. 59–88.
[26] A. Guimarães, “The Basis of Nanomagnetism,” in *Principles of Nanomagnetism SE - 1*, Second edo., Springer Berlin Heidelberg, 2009, pp. 1–20.
[27] D. K. Wood, K. K. Ni, D. R. Schmidt, and A. N. Cleland, “Submicron giant magnetoresistive sensors for biological applications,” *Sensors Actuators, A Phys.*, vol. 120, no. 1, pp. 1–6, 2005.
[28] A. Sobczak-Kupiec *et al.*, “Magnetic nanomaterials and sensors for biological detection,” *Nanomedicine Nanotechnology, Biol. Med.*, vol. 12, no. 8, pp. 2459–2473, 2016.
[29] Q. A. P. and N. T. K. T. and S. K. J. and J. Dobson, “Progress in applications of magnetic nanoparticles in biomedicine,” *J. Phys. D. Appl. Phys.*, vol. 42, no. 22, p. 224001, 2009.
[30] Q. A. Pankhurst, J. Connolly, S. K. Jones, and J. Dobson, “Applications of magnetic nanoparticles in biomedicine,” *J. Phys. D. Appl. Phys.*, vol. 36, no. 13, pp. R167–R181, 2003.
[31] D. Qin, Y. N. Xia, J. a Rogers, R. J. Jackman, X. M. Zhao, and G. M. Whitesides, “Microfabrication, microstructures and microsystems,” *Microsyst. Technol. Chem. Life Sci.*, vol. 194, pp. 1–20, 1998.
[32] M. Combs, C., & Nichols, “Introduction to micro-/nanofabrication,” in *Nanostructures, Micro-/Nanofabrication and Materials*, vol. 91, no. 23–24, Springer handbook of nanotechnology, 2012, p. 1140.
[33] X. -a. Zhao, “Reaction of thin metal films with crystalline and amorphous Al2O3,” *Journal of Vacuum Science & Technology A: Vacuum, Surfaces, and Films*, vol. 4, no. 6. p. 3139, 1986.
[34] H. O. Pierson, W. A. Publishing, and N. York, *HANDBOOK OF CHEMICAL VAPOR DEPOS I TION (CVD) by*, no. Cvd. 199AD.
[35] R. W. Mann, L. a. Clevenger, P. D. Agnello, and F. R. White, “Silicides and local interconnections for high-performance VLSI applications,” *IBM J. Res. Dev.*, vol. 39, no. 4, pp. 403–417, 1995.
[36] J. I. Martín, J. Nogués, K. Liu, J. L. Vicent, and I. K. Schuller, “Ordered magnetic nanostructures: Fabrication and properties,” *J. Magn. Magn. Mater.*, vol. 256, no. 1–3, pp. 449–501, 2003.
[37] G. Szulczewski, S. Sanvito, and M. Coey, “A spin of their own,” *Nat. Mater.*, vol. 8, no. 9, pp. 693–695, 2009.

[38] P. P. Faraday and L. University, *An Introduction to MEMS*, no. January. Loughborough, Leics: PRIME Faraday Partnership, 2002.

[39] M. Madou, “Non-lithography Applications,” in *Micromanufacturing*, K. F. Ehmann, D. Bourell, M. L. Culpepper, T. J. Hodgson, T. R. Kurfess, M. Madou, K. Rajurkar, and R. Devor, Eds. Dordrecht: Springer Netherlands, 2007, pp. 111–120.

[40] J.-P. Halain *et al.*, “The dual-gain 10 µm back-thinned 3k×3k CMOS-APS detector of the solar orbiter extreme UV imager,” in *Space Telescopes and Instrumentation 2014: Ultraviolet to Gamma Ray*, 2014, p. 91443I.

[41] X. Wang and B. Wolfs, “A high-dynamic range (HDR) back-side illuminated (BSI) CMOS image sensor for extreme UV detection,” in *Proc. SPIE 8298, Sensors, Cameras, and Systems for Industrial and Scientific Applications XIII*, 2012, vol. 8298, no. January, p. 82980B–82980B–8.

[42] C. M. Weber, C. N. Berglund, and P. Gabella, “Mask cost and profitability in photomask manufacturing: An empirical analysis,” *IEEE Transactions on Semiconductor Manufacturing*, vol. 19, no. 4. pp. 465–474, 2006.

[43] K. Lewotsky, “Masking Costs,” *SPIIEE’’ss ooeemaaggaazziinnee*, vol. c, no. February, p. 1, 2004.

[44] J. Sturtevant *et al.*, “14-nm photomask simulation sensitivity,” in *P30th European Mask and Lithography Conference, 2014, Dresden, Germany*, 2014, no. October 2014.

[45] R. Gladhill, K. H. Nakagawa, R. Gladhill, and K. H. Nakagawa, “Photomask manufacturability and pattern fidelity for curvilinear structures Richard,” in *SPIE Photomask Technology + Extreme Ultraviolet Lithography, 2018, Monterey, California, United States Downloaded*, 2018, no. October 2018.

[46] J. Koch *et al.*, “Maskless nonlinear lithography with femtosecond laser pulses,” *Appl. Phys. A Mater. Sci. Process.*, vol. 82, no. 1 SPEC. ISS., pp. 23–26, 2006.

[47] M. Z. Mohammed, A.-H. I. Mourad, and S. A. Khashan, “Maskless Lithography Using Negative Photoresist Material: Impact of UV Laser Intensity on the Cured Line Width,” *Lasers Manuf. Mater. Process.*, vol. 5, no. 2, pp. 133–142, Jun. 2018.

[48] A. O. Adeyeye, J. A. C. Bland, C. Daboo, D. G. Hasko, and H. Ahmed, “Optimized process for the fabrication of mesoscopic magnetic structures,” *J. Appl. Phys.*, vol. 82, no. 1, p. 469, 1997.

[49] M. Vähä-Nissi, T. Hirvikorpi, T. Mustonen, M. Karppinen, and A. Harlin, “Thin film deposition techniques - Steps towards more sustainable packages,” in *International Conference on Nanotechnology for the Forest Products Industry 2010*, 2010, p. 1,394 (2 Vols).

[50] W. Park, J. Rhie, N. Y. Kim, S. Hong, and D. S. Kim, “Sub-10 nm feature chromium photomasks for contact lithography patterning of square metal ring arrays,” *Sci. Rep.*, vol. 6, no. December 2015, pp. 1–6, 2016.

[51] M. J. Jackson, *Microfabrication Using X- ray Lithography BT - Micro and Nanomanufacturing*, First. Boston, MA: Springer US, 2007.

[52] E. & V. N. Crowe, “E-beam Lithography vs . X-ray Lithography,” Maryland, 2009.

[53] K. Early, M. L. Schattenburg, and H. I. Smith, “Absence of resolution degradation in X-ray lithography for λ from 4.5nm to 0.83nm,” *Microelectron. Eng.*, vol. 11, no. 1, pp. 317–321, 1990.

[54] G. V. and S.-J. Kim, G. Venugopal, S.-J. Kim, G. Beata, and M. Andrzej, “Nanolithography,” in *Advances in Micro/Nano Electromechanical Systems and Fabrication Technologies*, K. Takahata, Ed. london: In Tech, 2013, p. 234.

[55] Defense Advanced Research Projects Agency (DARPA), “The LIGA process.” .
[56] P. B. Fischer and S. Y. Chou, “IO nm electron beam lithography scanning electron microscope and sub-50 nm overlay using a modified,” *Appl. Phys. Lett., Vol. 62, No. 23, 7 June 1003*, vol. 62, no. June, pp. 6–8, 1993.
[57] K. K. B. Hon, L. Li, and I. M. Hutchings, “Direct writing technology—Advances and developments,” *CIRP Ann. - Manuf. Technol.*, vol. 57, no. 2, pp. 601–620, 2008.
[58] V. R. Manfrinato *et al.*, “Aberration-Corrected Electron Beam Lithography at the One Nanometer Length Scale,” *Nano Lett.*, vol. 17, no. 8, pp. 4562–4567, 2017.
[59] Y. Chen, “Nanofabrication by electron beam lithography and its applications: A review,” *Microelectron. Eng.*, vol. 135, pp. 57–72, 2015.
[60] B. Bercic, “Introduction to Electron Beam Lithography,” 2006. [Online]. Available: http://www-f7.ijs.si/uploads/images/SPIN - OFF TEHNOLOGIJE/Electron_Beam_Lithography.pdf.
[61] F. WATT, A. A. BETTIOL, J. A. VAN KAN, E. J. TEO, and M. B. H. BREESE, “ION BEAM LITHOIONGRAPHY AND NANOFABRICATION: A REVIEW,” *Int. J. Nanosci.*, vol. 04, no. 03, pp. 269–286, Jun. 2005.
[62] F. WATT, A. A. BETTIOL, J. A. VAN KAN, E. J. TEO, and M. B. H. BREESE, “ION BEAM LITHOGRAPHY AND NANOFABRICATION: A REVIEW,” *Int. J. Nanosci.*, vol. 04, no. 03, pp. 269–286, Jun. 2005.
[63] M. Erdmanis, P. Sievilä, A. Shah, N. Chekurov, V. Ovchinnikov, and I. Tittonen, “Focused ion beam lithography for fabrication of suspended nanostructures on highly corrugated surfaces,” *Nanotechnology*, vol. 25, no. 33, 2014.
[64] S. Kang, “Application of Soft Lithography for Nano Functional Devices,” *Intechopen.Com*, no. February, pp. 403–426, 2010.
[65] Y. N. Xia and G. M. Whitesides, “Soft lithography,” *Annu. Rev. Mater. Sci.*, vol. 37, no. 5, pp. 551–575, 1998.
[66] C. M. Sotomayor Torres, “Alternative lithography,” *Mater. Sci.*, p. 446, 2002.
[67] M. Krogh, “My Little Guide to Soft Lithography,” Linköping, Sweden., 2007.
[68] S. P. Li, W. S. Lew, J. A. C. Bland, M. Natali, A. Lebib, and Y. Chen, “Intrinsic anisotropy-defined magnetization reversal in submicron ring magnets,” *J. Appl. Phys.*, vol. 92, no. 12, pp. 7397–7403, 2002.
[69] A. Pimpin and W. Srituravanich, “Reviews on micro- and nanolithography techniques and their applications,” *Eng. J.*, vol. 16, no. 1, pp. 37–55, 2012.
[70] A. Latif, “Nanofabrication using focused ion beam,” University of Cambridge, 2000.
[71] I. Utke, P. Hoffmann, and J. Melngailis, “Gas-assisted focused electron beam and ion beam processing and fabrication,” *J. Vac. Sci. Technol. B Microelectron. Nanom. Struct.*, vol. 26, no. 4, p. 1197, 2008.
[72] G. Xiong, D. a. Allwood, M. D. Cooke, and R. P. Cowburn, “Magnetic nanoelements for magnetoelectronics made by focused-ion-beam milling,” *Appl. Phys. Lett.*, vol. 79, no. 21, pp. 3461–3463, 2001.
[73] Y. O. Katsumi Suzuki, Shinji Matsui, *Sub-Half-Micron Lithography for ULSIs*. Cambridge University Press, 2000.
[74] G. Binning and R. Heinrich, “The Scanning Tunneling Microscope,” *Sci. Am.*, vol. 253, no. 2, pp. 50–56, 1985.
[75] G. Binnig and C. F. Quate, “Atomic Force Microscope,” *Phys. Rev. Lett.*, vol. 56, no. 9, pp. 930–933, 1986.
[76] A. A. Tseng, A. Notargiacomo, and T. P. Chen, “Nanofabrication by scanning probe

microscope lithography: A review," *J. Vac. Sci. Technol. B Microelectron. Nanom. Struct.*, vol. 23, no. 3, p. 877, 2005.

[77] R. Garcia, A. W. Knoll, and E. Riedo, "Advanced scanning probe lithography," *Nat. Nanotechnol.*, vol. 9, no. 8, pp. 577–587, 2014.

[78] P. Mendes and T. Richardson, "Fabrication of Gold Micro- and Nanostructures by Photolithographic\nExposure of Thiol-Stabilized Gold Nanoparticles," *Nano Lett.*, vol. 6, no. 3, pp. 345–350, 2006.

[79] G. Yoon, I. Kim, S. So, J. Mun, M. Kim, and J. Rho, "Fabrication of three-dimensional suspended, interlayered and hierarchical nanostructures by accuracy-improved electron beam lithography overlay," *Sci. Rep.*, vol. 7, no. 1, pp. 1–8, 2017.

[80] Z. W. Xu, F. Z. Fang, Y. Q. Fu, S. J. Zhang, T. Han, and J. M. Li, "Fabrication of micro/nano-structures using focused ion beam implantation and XeF_2 gas-assisted etching," *J. Micromechanics Microengineering*, vol. 19, no. 5, p. 054003, 2009.

[81] G. Feiertag *et al.*, "Fabrication of photonic crystals by deep x-ray lithography," *Appl. Phys. Lett.*, vol. 71, no. 11, pp. 1441–1443, 1997.

[82] D. Qin, Y. Xia, and G. M. Whitesides, "Soft lithography for micro- and nanoscale patterning," *Nat. Protoc.*, vol. 5, no. 3, pp. 491–502, 2010.

[83] F. S. S. Chien, C. L. Wu, Y. C. Chou, T. T. Chen, S. Gwo, and W. F. Hsieh, "Nanomachining of (110)-oriented silicon by scanning probe lithography and anisotropic wet etching," *Appl. Phys. Lett.*, vol. 75, no. 16, pp. 2429–2431, 1999.

[84] I. B. Divliansky *et al.*, "Fabrication of two-dimensional photonic crystals using interference lithography and electrodeposition of CdSe," *Appl. Phys. Lett.*, vol. 79, no. 21, pp. 3392–3394, 2001.

[85] C. B. Arnold and A. Piqué, "L aser Direct-Write Processing," *MRS Bull.*, vol. 32, no. 1, pp. 9–15, 2007.

[86] Technology and Applications Center Newport Corporation, "Workstation for Laser Direct-Write Processing," Irvine, California, USA, 39, 2009.

[87] A. Alasadi, F. Claeyssens, and D. A. Allwood, "Laser direct writing (LDW) of magnetic structures," *AIP Adv.*, vol. 056322, 2018.

[88] M. Brown and C. Arnold, *Fundamentals of Laser-Material Interaction and Application to Multiscale Surface Modification*, Second edi., vol. 135. Springer Berlin Heidelberg, 2010.

[89] M. J. Weber, *Handbook of Laser Wavelengths*, 1st Editio., vol. 16. Boca Raton: CRC PRESS LLC, 1998.

[90] M. J. Beesley, *Lasers and their applications*. london: Taylor and Francis, 1978.

[91] P. E. Dyer and R. J. Farley, "Dynamics of laser-induced periodic surface structures in excimer laser ablation of polymers," *J. Appl. Phys.*, vol. 74, no. 2, p. 1442, 1993.

[92] B. N. Chichkov, C. Momma, S. Nolte, F. von Alvensleben, and A. Tünnermann, "Femtosecond, picosecond and nanosecond laser ablation of solids," *Appl. Phys. A Mater. Sci. Process.*, vol. 63, no. 2, pp. 109–115, 1996.

[93] J. Byskov-Nielsen, "Short-pulse laser ablation of metals : Fundamentals and applications for micro-mechanical interlocking," University of Aarhus, 2010.

[94] G. Paltauf and P. E. Dyer, "Photomechanical processes and effects in ablation," *Chem. Rev.*, vol. 103, no. 2, pp. 487–518, 2003.

[95] S.-T. K. von der Linde D, "Physical mechanisms of short pulse laser ablation," in *Applied Surface Science*, 1999, vol. 3734, pp. 1–10.

[96] I. Zergioti *et al.*, "Microdeposition of metal and oxide structures using ultrashort laser

pulses," *Appl. Phys. A Mater. Sci. Process.*, vol. 66, no. 5, pp. 579–582, 1998.

[97] J. S. Stewart, T. Lippert, M. Nagel, F. Nüesch, and A. Wokaun, "Laser-induced forward transfer using triazene polymer dynamic releaser layer," *AIP Conf. Proc.*, vol. 1278, pp. 789–799, 2010.

[98] P. Delaporte and A.-P. Alloncle, "Laser-induced forward transfer: A high resolution additive manufacturing technology," *Opt. Laser Technol.*, vol. 78, pp. 33–41, 2016.

[99] C. Schneider and T. Lippert, "Laser ablation and thin film deposition," in *ChristofW. Schneider and Thomas Lippert Abstract*, vol. 139, P. Schaaf, Ed. Berlin, Heidelberg: Springer Berlin Heidelberg, 2010, pp. 89–112.

[100] J. Reif, "Basic physics of femtosecond laser ablation," in *Laser-Surface Interactions for New Materials …*, A. Miotello and P. M. Ossi, Eds. Berlin, Heidelberg: Springer Berlin Heidelberg, 2010, pp. 19–41.

[101] A. I. Kuznetsov, R. Kiyan, and B. N. Chichkov, "Laser fabrication of 2D and 3D metal nanoparticle structures and arrays," *Opt. Express*, vol. 18, no. 20, p. 21198, 2010.

[102] W. M. Steen and M. J., *Laser Material Processing*, vol. 1, no. 0. 2010.

[103] J. Hoffman *et al.*, "The effect of laser wavelength on the ablation rate of carbon," *Appl. Phys. A Mater. Sci. Process.*, vol. 117, no. 1, pp. 395–400, 2014.

[104] J. Byskov-Nielsen, J.-M. Savolainen, M. S. Christensen, and P. Balling, "Ultra-short pulse laser ablation of metals: threshold fluence, incubation coefficient and ablation rates," *Appl. Phys. A*, vol. 101, no. 1, pp. 97–101, 2010.

[105] F. Belloni *et al.*, "Laser ablation threshold of cultural heritage metals," *Conf. Lasers Electro-Optics Eur. - Tech. Dig.*, vol. 0150, no. July, pp. 2–7, 2007.

[106] R. J. Baseman, N. M. Froberg, J. C. Andreshak, and Z. Schlesinger, "Minimum fluence for laser blow-off of thin gold films at 248 and 532 nm," *Appl. Phys. Lett.*, vol. 56, no. 15, p. 1412, 1990.

[107] K. H. Leitz, B. Redlingshöer, Y. Reg, A. Otto, and M. Schmidt, "Metal ablation with short and ultrashort laser pulses," *Phys. Procedia*, vol. 12, no. PART 2, pp. 230–238, 2011.

[108] C. R. Phipps *et al.*, "Laser interaction with materials: introduction," *Appl. Opt.*, vol. 53, no. 31, p. LIM1, 2014.

[109] E. G. Gamaly, a. V. Rode, B. Luther-Davies, and V. T. Tikhonchuk, "Ablation of solids by femtosecond lasers: Ablation mechanism and ablation thresholds for metals and dielectrics," *Phys. Plasmas*, vol. 9, no. 3, p. 949, 2002.

[110] V. G. N. and A. V Nesterov, "Influence of beam polarization on laser cutting efficiency," *J. Phys. D. Appl. Phys.*, vol. 32, no. 13, p. 1455, 1999.

[111] I. A. Choudhury and S. Shirley, "Laser cutting of polymeric materials: An experimental investigation," *Opt. Laser Technol.*, vol. 42, no. 3, pp. 503–508, 2010.

[112] G. Li, S. Hu, H. Tang, and B. Chen, "Laser repeat drilling of alumina ceramics in static water," *Int. J. Adv. Manuf. Technol.*, 2018.

[113] X. D. Wang *et al.*, "Laser drilling of stainless steel with nanosecond double-pulse," *Opt. Laser Technol.*, vol. 41, no. 2, pp. 148–153, 2009.

[114] R. J. von Gutfeld and R. T. Hodgson, "Laser enhanced etching in KOH," *Appl. Phys. Lett.*, vol. 40, no. 4, pp. 352–354, Feb. 1982.

[115] G. Yoo, H. Lee, D. Radtke, M. Stumpf, U. Zeitner, and J. Kanicki, "A maskless laser-write lithography processing of thin-film transistors on a hemispherical surface," *Microelectron. Eng.*, vol. 87, no. 1, pp. 83–87, 2010.

[116] R. R. Benoit, D. M. Jordan, G. L. Smith, R. G. Polcawich, S. S. Bedair, and D. M.

Potrepka, "Direct-Write Laser Greyscale Lithography for Multi-Layer Lead Zirconate Titanate Thin Films," *IEEE Trans. Ultrason. Ferroelectr. Freq. Control*, p. 1, 2018.
[117] P. Peyre *et al.*, "Surface modifications induced in 316L steel by laser peening and shot-peening. Influence on pitting corrosion resistance," *Mater. Sci. Eng. A*, vol. 280, no. 2, pp. 294–302, 2000.
[118] C. Scolaro, A. Visco, L. Torrisi, N. Restuccia, and E. Pedullà, "Modification induced by laser irradiation on physical features of plastics materials filled with nanoparticles," *EPJ Web Conf.*, vol. 167, pp. 1–6, 2018.
[119] S. Shaikh *et al.*, "Femtosecond laser induced surface modification for prevention of bacterial adhesion on 45S5 bioactive glass," *J. Non. Cryst. Solids*, vol. 482, pp. 63–72, 2018.
[120] J. Bohandy, B. F. Kim, F. J. Adrian, and a. N. Jette, "Metal deposition at 532 nm using a laser transfer technique," *Journal of Applied Physics*, vol. 63, no. 4. pp. 1158–1162, 1988.
[121] J. Bohandy, B. F. Kim, and F. J. Adrian, "Metal deposition from a supported metal film using an excimer laser," *J. Appl. Phys.*, vol. 60, no. 4, p. 1538, 1986.
[122] C. S. and T. Lippert, "Laser ablation and thin film deposition.," in *Laser Processing of Materials: Fundamentals, Applications and Developments*, 1st ed., J. J. P. Z. W. H. W. R.Hull C. Jagadish R.M. Osgood, Ed. Stockholm, Sweden: Springer Series, 2010, pp. 89–112.
[123] M. L. Levene, R. D. Scott, and B. W. Siryj, "Material Transfer Recording," *Appl. Opt.*, vol. 9, no. 10, p. 2260, 1970.
[124] A. Piqué *et al.*, "Anovel laser transfer process for direct writing of electronic and sensor materials," *J. Mater. Res.*, vol. 15, no. 9, p. S279–S284 (1999), 1999.
[125] A. Piqué, "Laser-Induced Forward Transfer of Functional Materials: Advances and Future Directions," *J. Laser Micro/Nanoengineering*, vol. 9, no. 3, pp. 192–197, 2014.
[126] N. Mir-Hosseini, M. J. J. Schmidt, and L. Li, "Growth of patterned thin metal oxide films on glass substrates from metallic bulk sources using a Q-switched YAG laser," *Appl. Surf. Sci.*, vol. 248, no. 1–4, pp. 204–208, 2005.
[127] a Klini, P. a Loukakos, D. Gray, a Manousaki, and C. Fotakis, "Laser induced forward transfer of metals by temporally shaped femtosecond laser pulses.," *Opt. Express*, vol. 16, no. 15, pp. 11300–11309, 2008.
[128] R. Pohl, M. Jansink, G. R. B. E. Römer, and A. J. Huis in 't Veld, "Solid-phase laser-induced forward transfer of variable shapes using a liquid-crystal spatial light modulator," *Appl. Phys. A Mater. Sci. Process.*, vol. 120, no. 2, pp. 427–434, 2015.
[129] D. P. Banks *et al.*, "Femtosecond laser induced forward transfer for the deposition of nanoscale transparent and solid-phase materials," pp. 1–9, 2009.
[130] A. Palla-Papavlu, V. Dinca, T. Lippert, and M. Dinescu, "Laser induced forward transfer for materials patterning," *Rom. Reports Phys.*, vol. 63, no. SUPPL., pp. 1285–1301, 2012.
[131] a. Klini, a. Mourka, V. Dinca, C. Fotakis, and F. Claeyssens, "ZnO nanorod micropatterning via laser-induced forward transfer," *Appl. Phys. A Mater. Sci. Process.*, vol. 87, no. 1, pp. 17–22, 2007.
[132] W. A. Tolbert, I.-Y. Sandy Lee, M. M. Doxtader, E. W. Ellis, and D. D. Dlott, "High-speed color imaging by laser ablation transfer with a dynamic release layer: fundamental mechanisms," *J. imaging Sci. Technol.*, vol. 37, no. 4, pp. 411–421, 1993.
[133] D. W. Piston, "Choosing objective lenses: the importance of numerical aperture and

magnification in digital optical microscopy.," *Biol. Bull.*, vol. 195, no. April, pp. 1–4, 1998.
[134] A. Piqué, H. Kim, R. C. Y. Auyeung, I. Beniam, and E. Breckenfeld, "Laser-induced forward transfer (LIFT) of congruent voxels," *Appl. Surf. Sci.*, vol. 374, pp. 42–48, 2016.
[135] M. N. and T. Lippert and 5.4.1, "Nanomaterials : Processing and Charalterization with Lasers," in *Nanomaterials: Laser-Induced Nano/Microfabrications (A)*, 2012, pp. 35–66.
[136] "Pellin Broca Prism," *http://www.thorlabs.com/newgrouppage9.cfm?objectgroup_id=3217&gclid=CMeX2P29icoCFSoEwwodYxsHyg/ accesed 20/11/2015*. .
[137] P. Weinberger, "John Kerr and his effects found in 1877 and 1878," *Philos. Mag. Lett.*, vol. 88, no. 12, pp. 897–907, 2008.
[138] D. C. andRPCowburn N. D A Allwood, Gang Xiong, "Magneto-optical Kerr effect analysis of magnetic nanostructures," *J. Appl. Phys.*, vol. 36, pp. 2175–2182, 2003.
[139] R. C. O'Handley, *Modern Magnetic Materials: Principles and Applications*, Illustrate. Canada: John Wiley & Sons., 1999.
[140] C. Reig, M. D. Cubells-Beltrán, and D. R. Muñoz, "Magnetic field sensors based on Giant Magnetoresistance (GMR) technology: Applications in electrical current sensing," *Sensors*, vol. 9, no. 10, pp. 7919–7942, 2009.
[141] D. TABOR, *Gases, loquids and solids and other states of matter*, THIRD EDIT. Cambridge: Cambridge University Press, 1991.
[142] Lenntech Water treatment & purification, "Chemical properties of nickel." [Online]. Available: https://www.lenntech.com/periodic/elements/ni.htm. [Accessed: 29-Oct-2018].
[143] T. E. ToolBox, "Thermal Conductivity of common Materials and Gases." [Online]. Available: https://www.engineeringtoolbox.com/thermal-conductivity-d_429.html. [Accessed: 26-Aug-2018].
[144] Goodfellow, "Technical Information - Nickel/Iron." [Online]. Available: http://www.goodfellow.com/catalogue/GFCat4I.php?ewd_token=0uPVTu12RVNKSAlp9SMkO1j77c8SbM&n=t97rpMZXIPRxgvv0vzQSm1lRCD4i9k&ewd_urlNo=GFCat411&Catite=NI299100&CatSearNum=2. [Accessed: 26-Aug-2018].
[145] P. Schaaf, *Laser Processing of Materials*. 2010.
[146] W. C. Uhlig, M. J. Donahue, D. T. Pierce, and J. Unguris, "Direct imaging of current-driven domain walls in ferromagnetic nanostripes," *J. Appl. Phys.*, vol. 105, no. 10, pp. 1–7, 2009.
[147] D. M. Burn, E. Arac, and D. Atkinson, "Magnetization switching and domain-wall propagation behavior in edge-modulated ferromagnetic nanowire structures," *Phys. Rev. B - Condens. Matter Mater. Phys.*, vol. 88, no. 10, pp. 1–8, 2013.
[148] R. Hubert, Alex, Schäfer, *Magnetic Domains The Analysis of Magnetic Microstructures*, 1st ed., vol. 3, no. 2. Springer-Verlag Berlin Heidelberg, 1998.
[149] C. C. Wang, S. B. Kumar, S. G. Tan, M. B. a. Jalil, and G. C. Han, "Magnetoresistance calculation in current-perpendicular-to-plane giant magnetoresistance spin valves with current-confined paths," *J. Appl. Phys.*, vol. 105, no. 1, p. 013909, 2009.
[150] M. Vázquez, A. Hernando, and M. V. and A. Hernando, "A soft magnetic wire for sensor applications," *J. Phys. D. Appl. Phys.*, vol. 29, no. 4, pp. 939–949, 1996.
[151] G. Vieira *et al.*, "Magnetic Wire Traps and Programmable Manipulation of Biological

Cells," *Phys. Rev. Lett.*, vol. 103, no. 12, pp. 16–19, 2009.
[152] T. Byvank, "Separating Magnetically Labeled and Unlabeled Biological Cells within Microfluidic Channels," The Ohio State University, 2012.
[153] L. C. Leonard and V. Toal, "Roughness measurement of metallic surfaces based on the laser speckle contrast method," *Opt. Lasers Eng.*, vol. 30, no. 5, pp. 433–440, 1998.
[154] H. J. Tiziani, "Optical methods for precision measurements - An invited paper," *Opt. Quantum Electron.*, vol. 21, no. 4, pp. 253–282, 1989.